Some Theoretical Studies on High-Speed Optical Devices

A Thesis Submitted in Partial Fulfillment For the Degree of

Doctor of Philosophy

In the Faculty of Engineering

Goa University

By

Gaitonde Jaya Venktesh

Research Centre in Electronics and Telecommunication Engineering

GOA COLLEGE OF ENGINEERING, FARMAGUDI

PONDA, Goa University, Goa

December 2022

Declaration

I, **Gaitonde Jaya Venktesh** hereby declare that this thesis represents work which has been carried out by me and that it has not been submitted, either in part or full, to any other University or Institution for the award of any research degree.

Place: Taleigao Plateau **Gaitonde Jaya Venktesh**

Date:

Certificate

I hereby certify that the above Declaration of the candidate, **Gaitonde Jaya Venktesh** is true and the work was carried out under my supervision.

Dr. Rajesh B. Lohani

Principal, Goa Engineering College

Professor, Electronics and Telecommunication Department,

Goa Engineering College (Govt. of Goa), Farmagudi-Ponda-Goa, 403401.

Acknowledgement

First of all, I would like to thank the almighty, God, for his blessings, for giving me the right wisdom to complete this research, and for paving out the way in case of any struggles.

Secondly, I would extend my deep sense of gratitude towards my guide, Prof. Dr. Rajesh B. Lohani for inculcating in me the right spirit and attitude towards research, and the right technique, and for his continued motivation towards research. He guided me out in case of technical difficulties through the basics and conceptualizations, and suggested me the right options for journal and conference publications.

I would also like to thank the other DRC members, Prof. Dr. K. R. Pai and Prof. Dr. H. G. Virani for their continued valuable advise, comments, suggestions, and support during the entire course of the research process. They helped me in channelizing my research work.

Further, I would convey my thanks to Dr. M. S. Krupashankara, Principal, Goa Engineering College for giving constant support.

I am deeply indepted to my senior Professors, Assoc. Prof. Dr. Shajahan Kutty, Assoc. Prof. Dr. Nitesh Guinde, Asst. Prof. Chetan Dessai, and Prof. Dr. R. P. R. C. Aiyar for their technical support and suggestions.

I am grateful to my fellow colleagues, Dr. Neha Karanjkar, Asst. Prof. Devendra Sutar, Asst. Prof. Shrinivas Joshi, Asst. Prof. Vrushali Kelkar, Asst. Prof. Tejas Pathak, Mr. P. R. Satarkar, Mrs. Remya Pillai, Mr. Kishan Konnanavar, Mr. Sunit Fulari, Mr. Sudhir Rawat, Ms. Shruthi Adpaikar, and Mr. Vishnu Singh for their help and support.

I sincerely thank my organization, Goa Engineering College (Goa University),

Prof. M. K. Deshmukh (Bits Pilani, Goa Campus), and Prof. Dr. Vasantha M.H (NIT, Goa) for allowing me to avail commercial software facilities in their domain.

I would thank Prof. Dr. V. N. Shet, and Prof. Dr. J. A. Laxminarayana, for their valuable suggestions.

I thank Mr. Sunay Pai, Prof. Milind Sakhardande and Mr. Ketan Naik for their help.

A special thanks to my family colleague Mr. Ravindra Yaragatti for his help towards English language editing in writing research papers and his consistent support.

Finally, I am grateful to my family, my relatives, and my well wishers for their moral support, motivation, and help towards my research.

Abstract

This thesis embodies the work on optimization of Optical Field Effect Transistor (OPFET) or optically-controlled Metal-Semiconductor Field Effect Transistor (MESFET) for optical communication and other related applications. OPFET has been known for its inherently high gain-bandwidth product apart from its significantly fast response speed. Here, extensive simulation results have been presented which cover the different aspects of optimization. The optimization procedures involve manipulating the structural dimensions, using different channel and gate materials, choosing different illumination models, varying the external control factors such as bias, optical power, wavelength, and modulation frequency. A semi-analytical method is employed using MATLAB software to evaluate the OPFET characteristics. These results have been validated with experiments reported elsewhere and Visual TCAD software simulations. This research establishes an important relationship between 3-dB bandwidth and gate length i.e. the 3-dB bandwidth of OPFET increases with gate length with other factors kept constant, whereas the device dimensions and doping concentration are subject to scaling rules. It proves graphically that the 3-dB bandwidth is directly proportional to the depletion width sensitivity, which increases at the gate length increases or as the doping concentration decreases.

The work performs structural, material, and illumination model optimization of the OPFET detector-cum-amplifier for Visible-Light Communication (VLC) applications. A wide range of medium to long gate lengths (3 μm to 25 μm); semiconductor materials involving Si, InP, and GaAs; gate materials involving Indium-Tin-Oxide (ITO) and gold (Au); and illumination models featuring buried-gate front-illumination, generalized model, and surface-gate back-illumination have been considered for optimization. The work has been extended in the Ultraviolet (UV) domain with gate lengths from 3 μm to 8 μsm; semiconductor materials

such as GaN, 6H-SiC, and ZnO; gate materials such as Au, ITO, and Silver-Oxide (AgO_2); and illumination models involving buried-gate front- and back-illumination, generalized model, and surface-gate front-illumination. In the UV domain, the device has also been studied for high dynamic range imaging or high resolution imaging applications. To indicate the robustness of the device towards electro-migration failure, the reliability of OPFET illumination models has been evaluated.

The visible/UV and infrared/visible contrast features of GaAs and In0.53Ga0.47As back-illuminated OPFETs, switching and frequency responses of GaAs OPFET models, potential of GaN OPFET for microwave/terahertz detection, and the different operating frequency ranges of GaAs back-illuminated OPFET detector have been studied.

Further, the gate Schottky junction of OPFET has been modeled for the first time for photodetection applications under UV and visible illumination and bias-selective dual-mode operation of OPFET has been proposed for functioning in diode mode and transistor mode. The potential of OPFET as a photodetector, oscillator, amplifier as well as gain and phase-shifting element in smart antenna for optically-driven 5G applications has been demonstrated. The OPFET has also been studied under solar ($AM0$) illumination for solar energy harvesting, laser-power beaming, and solar-based communication applications.

This work establishes the feasibility of graphene as a semiconductor material for OPFET structure. The basic characteristics of graphene OPFET are computed and analyzed under dark and illumination. Furthermore, the graphene OPFET is structurally optimized and studied under incident solar illumination. The results have been contrasted with graphene FET.

Last but not the least, the simple, accurate, and computationally efficient Finite-Difference Method (FDM) has been proposed as a numerical method for modeling the OPFET device.

Introduction/Motivation

There is a huge demand for high-speed optical devices in the present arena, due to immunity of optical domain to electromagnetic interference and the availability of wide spectrum bandwidth. More specifically, the three modes of optical communication i.e. Visible-Light Communication (VLC), Ultraviolet-Communication (UVC), and Infrared-Communication (IRC) are emerging as promising alternatives to RF/5G communication, since RF/5G technology suffers from congested bandwidth, regulatory spectrum use, and interference with nearby RF access points. These issues can be resolved by opto-electronic integration with RF electronics or using the optical domain alone. Further, very high speeds are possible with optical communication than RF/5G communication due to the ultrafast dynamics of optical sources (Lasers and Light-Emitting Diodes (LEDs)) and photodetectors (photodiodes, transistors, and Photomultiplier Tubes (PMTs)). Also, the optical signal provides an additional degree of freedom to control the device characteristics, thus catering to a diversity of applications. Optimization is a powerful means to enhance the performance of any system or device. This is where, the simulation and modeling tools have a great significance and can provide a great deal of insight into the device internal physics and characteristics. The heart of any optical communication system or any standalone optical set-up is the photodetector. Thus, it is imperative to critically improve the performance of photodetector so that maximum throughput is delivered by the system. The Optical Field-Effect Transistor (OPFET) or optically-controlled Metal-Semiconductor Field-Effect Transistor (MESFET) –based photodetector is certainly a high potential device due to its inherently high gain-bandwidth product. In this thesis, the performance of OPFET is optimized considering various detector parameters such as responsivity, 3-dB bandwidth, gain, External Quantum Efficeincy (EQE), detectivity, unity-gain cut-off frequency (f_T), Linearity and Dynamic Range (LDR), dark current, rejection ratios etc. to suit various communication and other related applications.

Contents

List of Figures

List of Tables

Chapter 1

Literature Survey with Gap Analysis

1.1 OPFET as an Optically-Controlled Device

OPFET has been extensively studied in the past several decades for its potential use as photodetectors, optically-controlled amplifiers, oscillators, and switches. In the late 1970s, OPFET was identified as a fast as well as sensitive optical detector with the detection mechanism being photoconductivity [12, 13]. In the 1980s, the photoeffects on the common source and common-drain microwave GaAs OPFET oscillators were studied revealing that the optically-induced oscillation frequency shift in common-source mode is approximately five times larger than the common-drain mode [14]. Later, Forrest et al. (1982) [15] explained more precisely the relative contributions from the photoconductive and photovoltaic effects. The authors stated that at low frequencies, the prevalent mechanism is photoconductivity, whereas at high or microwave frequencies, the photovoltaic effect dominates when the gate bias resistance is high. De Salles (1983) [7] demonstrated theoretical and experimental findings on GaAs opaque gate MESFET under illumination showing close agreement. Significant variation of gain of amplifier and frequency of oscillator were achieved with a little change in optical power. The optical injection locking of oscillator was also demonstrated. Two alternative structures i.e. the back-illuminated and buried-gate MESFETs were proposed for enhanced absorption in the device active region. Mizuno (1983) [9] investigated

the microwave performance of GaAs MESFET under illumination showing that the drain current, S-parameters, and gain variation with optical power similar to that with the gate-to-source voltage. The author, as a consequence of this phenomenon, presented the functioning of optical/FM and optical/AM microwave transformers, and optically switched amplifier. In 1984, Sun et al. [16] experimentally reported the optical tuning and optical switching features of GaAs MESFET oscillators. The highest tuning ranges were observed by using common source mode followed by common gate mode and common drain mode. The light influence on the S-parameters and transconductance of GaAs OPFET was studied (1985) [8]. Maximum effect was observed on the parameter S_{21} when biased near the pinch-off point. At lower gate voltages in the reverse bias regime, the transconductance was unaffected with illumination. The transconductance decreased at higher gate voltages whereas it increased near the pinch-off voltage. Later on, Papaionannou et al. (1986) [17] demonstrated some effects of optical radiation on the GaAs OPFET wherein they explained the relative contributions from the hole traps in the channel, device geometry, and backgating. The trapping of holes (minority carriers) determined the low frequency response; mid-frequency response was due to the trap-free lifetime, whereas the amplified photovoltage at the gate junction through the transconductance of the device determined the high frequency response. Simons et al. (1986) [18] analytically obtained the photovoltage and the sensitivity of the drain-to-source current to illumination for InP and GaAs MESFETs, GaAs PBT, and $Al_{0.3}Ga_{0.7}As$/GaAs HEMT devices. It was observed that the GaAs MESFET and GaAs PBT exhibit larger sensitivity than InP MESFET, whereas the AlGaAs/GaAs HEMT delivered the largest sensitivity. Further, the design is discussed for the realization of GaAs MESFET SPST switch controlled optically with high isolation and low insertion loss. In 1987, Darling et al. [19] described experimentally the large signal performance of epitaxial GaAs OPFET with uniform doping. Electrical bias, optical flux, position, and spot size-dependent optical gain was analyzed

and it was concluded that the governing dc gain phenomena are the transit time photoconductivity along with a variation in the pinch-off voltage through the photovoltaic effect. Blanchflower et al. (1989) [20] showed that the accurate control of the phase and frequency of a GaAs MESFET oscillator can be achieved by the combination of optical injection locking and closed-loop optical frequency tuning. Lakshmi et al. (1990) [21] computed and analyzed the photoresponse of enhancement mode GaAs OPFET in two modes: (i) the usual mode wherein the energy of photon is higher than the bandgap with the light flux high enough to create above turn-on threshold conduction and (ii) the subthreshold mode with the photon energy between that of the Schottky barrier height and the bandgap of the material. In the second mode, the device functions by internal photoemission from gate metal to the semiconductor. It was observed that in the usual mode, the square root of the drain current under illumination varies as the logarithm of the incident flux, whereas in the sub-bandgap mode, the photocurrent directly changes with the increase in light intensity. Later on, Mishra et al. (1990) [22] theoretically studied the effect of optical illumination and surface recombination on the performance of ion-implanted GaAs OPFET. The results depicted the drain-to-source current sensitivity to optical illumination, which reduced to some extent with surface recombination. Further, the threshold voltage is observed to decrease in enhancement mode and increase under depletion mode due to photogeneration, while surface recombination reverses the effect. In 1992, Chakrabarti et al. [23] reported the characteristics of an ion-implanted GaAs OPFET using a semi-numerical model. The previous model was corrected for by including the dependence of the depletion widths on the channel voltage and the photovoltage generated at the Schottky gate. Highly sensitive saturation drain current was observed under illumination with the photogenerated carriers being negligible compared to the doping charge and the dominant photovoltaic effect at low to medium fluxes. In 1994, Chakrabarti et al. [24] demonstrated the switching characteristics of OPFET using analytical techniques by considering

(i) the photovoltage generated across the gate junction, (ii) the excess photogenerated charge in the gate depletion region for calculation of the gate-to-source capacitance, (iii) effect of illumination on the minority carrier lifetime, and (iv) the various losses of the incident optical radiation due to reflections at various interfaces. The results showed that the OPFET parameters significantly change with illumination. The RC time constant and the unity-gain cut-off frequency were improved with illumination. These parameters were studied as a function of doping concentration and gate length providing usefulness for designing. The parameters tended to saturate at higher optical flux densities due to the saturation of the photovoltaic and photoconductive effects. A time-dependent analysis of the characteristics of ion-implanted GaAs OPFET was carried out (1994) [25]. The study considered the light turning on and off at a time $t = 0$ as a reference. The parameters reach their steady state value after increasing with time upon light being turned on. Upon turning off the light, the parameters decrease with time and settle to their corresponding dark condition values. The time is less under on condition than that under off condition. Further, Pal et al. (1996) [26] suggested a rule for scaling the ion-implanted GaAs OPFET. They considered a 1-D model and the rule was consistent with the 2-D modeling analysis even for the devices with a short channel. These rules serve as a guideline to miniaturise and integrate OPFET in an appropriate manner. A complete analytical model was presented accounting for the photovoltaic and photoconductive effects, surface recombination effect, illumination-dependent lifetime, photovoltaic effect at the channel-substrate junction, semi-insulating nature of the substrate, and losses of optical flux at various interfaces (1996) [27]. This model also included the effect of photogeneration in the substrate region. It was concluded that substrate photogeneration significantly affects the RC time constant and the unity-gain cut-off frequency of OPFET. Zebda et al. (1997) [28] used a perturbation technique to study the time varying characteristics of ion-implanted GaAs OPFET. The device was modeled considering the photogenerated concentration-

dependent carrier lifetime. The gate-to-source capacitance, threshold voltage, and the current-voltage characteristics were studied as a function of frequency and bias voltages. It was observed that the capacitance, threshold voltage, and drain current decreased with the increase in modulation frequency. Saxena et al. (1998) [29] discussed the analytical modeling and dc performance of a generalized ion-implanted GaAs MESFET model, showing enhanced response as compared to opaque gate OPFET due to the photovoltages generated at the Schottky junction and the active layer-substrate junction. It is observed that the radiation has a strong influence on the channel conductance, photovoltages, and the transconductance. A numerical model of an ion-implanted GaAs OPFET was presented (1998) [30] based on physics by considering the channel photoconductive effect, and the gate Schottky and the channel-substrate barrier photovoltaic effects. The position-dependent channel voltage and depletion width variations at the gate and the channel-substrate barriers were estimated for a non-uniform doped channel. It was observed that the channel voltage increases with illumination due to the photovoltaic effect. The photovoltage generated at the channel-substrate junction is much more enhanced as compared to that at the gate barrier. The gate-to-source capacitance and transconductance are observed to decrease with increase in the reverse gate voltage and increase under illumination for a fixed gate voltage. Further, Shubha et al. (1998) [31] presented an analytical model for an ion-implanted opaque gate GaAs OPFET. The photovoltages generated across the gate junction and the channel-substrate junction greatly influence the device characteristics. Under the dark condition and low optical power, the current saturates at a larger value of drain-to-source voltage beyond 1.0 V due to the non-linearity imposed by the impurity profile. The effect of illumination and biasing voltages on the channel conductance and transconductance of the device were studied. In 2000, Bose et al. [32] investigated the illumination effects on the threshold voltage of short channel GaAs OPFET with non self-aligned architecture. They presented a new analytical model by solving 2-D Poisson's equation by

implementing Green's function technique. The illumination shifts the threshold voltage increasingly in the negative direction due to generation of excess carriers, constituting a large current and acting as a leakage current. Later on, Roy et al. (2000) [33] evaluated and discussed analytically, the frequency-dependence of OPFET under back-illumination showing significant enhancement over previously reported research on front-illumination. Both the photovoltages were unaffected up to 100 GHz, after which there was a roll-off with frequency. The drain-to-source current decreased at higher frequencies due to roll-off of carrier lifetime with frequency. Increasing the active layer thickness increased the drain current. Transconductance was observed to be lower for higher frequency at a particular gate-to-source voltage. The transconductance increases gradually as the device mode is switched from depletion to enhancement mode. Further, Verma et al. (2001) [34] evaluated the dc characteristics of buried-gate GaAs OPFET under dark and front illumination. They observed enhanced performance compared to OPFET under front-illumination and back-illumination with surface gate. The device will be suitable for optical communication and optical computing. A new integrated optoelectronic device was presented based on a n-GaAs OPFET and a p-AlGaAs/p-GaAs/n^+-AlGaAs surface emitting double heterostructure light emitting diode (DH-LED) vertically integrated on a p^+-GaAs substrate and separated by a semi-insulating (SI) GaAs layer (2004) [35]. They referred this device to as a light-source integrated OPFET (LSI-OPFET). The LED generates the optical radiation when biased which is fed to the OPFET as back-illumination. The bias current of the LED serves as the controlling parameter of the intensity of back-illumination, and hence the control of gate-to-source, gate-to-drain capacitances and the transconductance of OPFET. The proposed device is demonstrated for designing common-source and common-drain microwave oscillators. Narsimha Murty et al. (2006) [36] presented a novel analytical model for evaluating the light-dependent S-paramters of GaAs OPFET. It was observed that the light has significant effect on S_{11} and S_{21} parameters, whereas the effect is

insignificant on the S_{12} and S_{22} parameters. Also, it was noticed that in the near pinch-off region, the effect of light on S_{11} and S_{21} parameters is very prominent. In 2006, Jit et al. [37] studied analytically the effects of illumination on the high pinch-off microwave n-GaAs OPFET oscillators in the common-source and common-drain configurations. The investigation simulates the variations in the gate-to-source and gate-to-drain capacitances by the developed photovoltage at the Schottky junction under illumination to study the optical effects on the oscillation frequency of the oscillators. It was observed that in the common-source configuration, the oscillation frequency is greatly modulated by the gate-to-source capacitance, whereas in the common-drain configuration, the oscillation frequency is sensitive to the gate-to-drain capacitance. Chattopadhyay et al. (2007) [38] presented an analytical model to investigate the optically-controlled characteristics of Si OPFET considering diffusion process of doping. The results were compared to that of ion-implanted OPFET showing degradation of drain current due to larger ion-implantation process-induced defects. The dc parameters such as drain-to-source current, switching response, threshold voltage, and gate capacitances were computed under dark and illumination. It was observed from the simulations that the threshold voltage shows linear reduction when the impurity flux density in case of diffusion process is increased. Under dark condition, the OPFET functions as an enhancement mode device for specific low densities and as a depletion mode device for specific high densities. Further, the threshold voltage decreases to more negative values under illumination. The light-induced carriers tend to shift the device mode to depletion regardless of the doping concentration.

1.2 Comparison of OPFET with APD

The OPFET usually provides higher gain-bandwidth product than APD because of the internal gain of the phototransistor using the photovoltaic effect which is amplified through the transconductance of the device, along with its high speed

operation emanating from fast generation, transport, and collection of carriers using drift mechanism of transport with no limiting factors except series resistance to some extent at lower to moderate intensities. At higher intensities, the photoconductive effect significantly adds to the gain but with the adverse effect of reduced speed. On the other hand, APD works on the principle of impact ionization at high reverse bias voltages which provide high multiplication gain. However, as the gain increases with increased ionization, simultaneously the avalanche build-up time increases which limits its speed and bandwidth. Hence, the APD provides high gain (>100) upto 1-3 GHz after which the gain reduces significantly. Thus, the APD offers inferior gain-bandwidth product. Whereas, OPFET has the tendency to provide gain from (10^2-10^{11}) with speed ranging from 2 MHz to >10 GHz. Discussing about noise characteristics, in APD, as the avalanche process creates many fluctuations of generated carriers, the SNR can degrade, through excess noise created. Whereas, in OPFET, the noise can be easily controlled by optimizing the resistive components, thus, suppressing the Johnson noise as well as reducing the gate leakage current noise and reducing capacitances. Since the gain of OPFET is high, the SNR is enhanced as compared to APD. Because of the transistor gain, the responsivity and sensitivity is higher in OPFET. The speed and response time of APD varies from μs to ns, whereas the response speed of OPFET is usually from ns to ps for high performance devices.

1.3 Visible-Light Photodetectors

Monolithic integration of photodetectors and transistors in Opto-Electronic Integrated Circuit (OEIC) receivers offer several advantages such as improved response, greater functionality, and manufacturability, suppression of the input capacitances and bond-wire inductances enhancing the response speed and sensitivity, and ease of manufacturing. Heterojunction bipolar transistors (HBTs)

employed in OEICs have the advantage of producing fast transistor with easily implemented optical lithography. In [39], K. D. Pedrotti et al. (1991) demonstrated monolithically integrated GaAs PIN-HBT OEIC with a bandwidth of 13 GHz at 0.8 μm wavelength enabling up to 17 Gbit/s data rate operation. The PIN photodiode showed a FWHM pulse response of 25 ps corresponding to a 3-dB bandwidth of 35 GHz. A dark current of 40 nA at a -3 V bias was observed. The responsivity was 0.244 A/W corresponding to EQE of 35.6%.

Optical interconnects with low cost and wide-bandwidth are necessary for productive opto-electronic systems such as that of computer chips. Two most important components of a receiver are the photodetector and the low noise amplifier. The choice of these components depends upon the technology maturity, ease of monolithic integration, and sensitivity, noise, and frequency response performance. A. A. Ketterson et al. (1993) [40], demonstrated the performance of 0.85 μm-sensitive OEIC photoreceiver based on GaAs/InGaAs/AlGaAs pseudomorphic MODFET and MSM PD. The quarter-micrometer MODFETs had f_{Ts} of 70 GHz which were implemented in a two-stage trans-impedance amplifier. The results revealed a trans-impedance amplifier bandwidth of 14 GHz and a receiver bandwidth of 11 GHz, which were the largest reported bandwidths so far for monolithic OEIC receivers. Thus, the superior receiver performance can be obtained through the opto-electronic monolithic integration of low-capacitance PD i.e. MSM, and high-performance FETs i.e. sub-micrometer MESFETs or MODFETs in a TZ design. The MSM PD exhibits a 3-dB bandwidth of 9 GHz and a responsivity of 0.6 A/W.

The simplified growth and fabrication processes of the MSM PD and MESFET amplifier provide viable solutions for low cost manufacturing technology. The MSM PD structure consisting of interdigitated metal fingers is consistent with the MESFET gate metal process enabling their integration in monolithic OEIC receivers. The typical responsivities of MSM PDs are 0.2 A/W sufficient for short-distance communication. C. G. Shih et al. (1996) [41] presented a 1 Gb/s GaAs

OEIC receiver integrating MSM-PD and 0.6 μm gate length D-mode MESFET technology. The MSM PD showed a maximum 3-dB bandwidth of 8 GHz and a detector capacitance of 45 fF at a finger width of 1 μm and finger spacing of 2 μm. The corresponding values for 2 μm and 3 μm width and spacing were 6.2 GHz and 33 fF and for 3 μm and 5 μm width and spacing were 4.2 GHz and 29 fF. The overall receiver bandwidth was 1.2 GHz.

Fast and sensitive PIN-finger PD with broadband response from UV to NIR was realized in integrated Si modified 0.5 μm BiCMOS technology (A. Nemecek et al. (2005)) [42]. The finger structure was created by using a finger anode with p^+-doping decorated in a thick intrinsic region with low n^--doping placed within an n^+-doped region. In the finger structure design, the spacing between p^+-fingers allows effective carrier separation and extraction due to the low-doping-induced high field intrinsic region with fast drift enhancing the quantum efficiency and bandwidth. An increase in the reverse-bias voltage increases the built-in potential, extending the space-charge region towards the substrate, causing faster drift and thus, increasing the speed. The designed PD shows responsivities of 0.25 A/W, 0.43 A/W, and 0.27 A/W at 410 nm, 660 nm, and 850 nm wavelengths respectively due to the finger structure and large intrinsic region. The capacitance decreases as reverse-bias is increased till complete depletion of the active region. The photodiode, at 410 nm wavelength and 17 V reverse bias exhibited a simulated rise time/fall time of 116 ps/98 ps, measured response times of 228 ps/211 ps and a 3-dB bandwidth of 1.34 GHz. The corresponding values at 660 nm were: 140 ps/126 ps, 88 ps/187 ps, and 3 GHz, and at 850 nm were: 247 ps/205 ps, 285 ps/215 ps, and 2.21 GHz.

The advantages of perovskite-based films are the long carrier lifetime and diffusion length, with very high External Quantum Efficiency (EQE) in the spectrum 300 to 800 nm, and a low trap and defect concentration within the bandgap, reducing the leakage dark current. The absorption coefficient of these hybrid films is of the order of 10^4 cm^{-1}, implying that the thickness of the active layer

can be only a few hundred nanometers for complete light absorption, which in turn reduces the transportation distance for the photocarriers and increases the speed. L. Dou et al. (2014) [43] presented a solution-processed hybrid perovskite photodetector based on the following combinations: ITO-coated glass, above which an organic/inorganic hybrid $CH_3NH_3PbI_{3-x}Cl_x$ layer was sandwiched between PEDOT:PSS (hole-transportation p-type layer) and PCBM (electron-transportation n-type layer). To suppress the dark current and the carrier recombination significantly under reverse bias, a hole-blocking contact buffer layer based on poly[(9,9-bis(3′-(N,N-dimethylamino)propyl)-2,7-fluorene)-alt-2,7-(9,9-dioctylfluorene)] (PFN) was introduced. Al was utilized as a top electrode. The device exhibited a good rectification ratio of $\sim 10^5$ ($\pm$1 V) and a very large detectivity of 8×10^{13} Jones at -0.1 V. When the bias was reduced to 0 V, the detector was self-powered with an increased detectivity of 4×10^{14} Jones since the dark current is reduced. The device showed a broadband photoresponse from 300 to 800 nm with a maximum EQE of 80%. The detector also showed an excellent linear response over a wide range of optical power densities corresponding to an *LDR* of larger than 100 dB, comparable with Si photodetectors (120 dB) and larger than other photodetectors such as InGaAs (66 dB). A maximum 3-dB bandwidth of 3 MHz was obtained using a 0.01 cm^2 area device with rise time of 180 ns and fall time of 160 ns. The active-layer optimum thickness for achieving simultaneous high *EQE*, small dark current, and fast response speed was around 300 nm. The device was studied at an optical wavelength of 550 nm.

Semi-polar and non-polar InGaN/GaN multiple quantum-well (MQW)-based devices show narrower emission linewidth, lower efficiency droop, shorter carrier lifetime, and higher temperature-stability than the traditional c-plane (polar) devices. With these advantages, C. H. Kang et al. (2019) [44] demonstrated 1.55 Gbits/s VLC operation with a 3-dB bandwidth of semi-polar InGaN/GaN μ-PD of 347 MHz at -10 V bias at 405 nm wavelength as compared to their previous work on c-plane devices demonstrating 3.2 Gbit/s operation with a 3-dB PD

bandwidth of 71.5 MHz. The previous work used orthogonal frequency-division multiplexing, which needs larger computational effort for obtaining high data rate capacity. So in the present work, the authors used a simple non-return-to-zero on-off keying modulation scheme. The investigated detector exhibited a significant responsitivity of 0.191 A/W, and a low dark current of 1.6 pA at -10 V bias at 400 nm. The detector also presented wavelength-selective characteristics (340-420 nm) with substantial rejection ratio (53-fold), thus providing low noise and high SNR characteristics. A detectivity of 3.41×10^{12} $cmHz^{1/2}W^{-1}$ was obtained at 0 V bias at 400 nm and reduced to 1.89×10^{12} $cmHz^{1/2}W^{-1}$ at -10 V bias. Traditional Si-based PDs have wide coverage in VLC systems due to their low cost and CMOS compatibility. However, their broadband absorption hinders their performance in wavelength-selective and high SNR VLC communication links. Also, their responsivity is low (< 0.1 A/W) at or below 400 nm wavelengths due to lower absorption depths. The compositionally tunable Group-III-nitride-based PDs can overcome the drawbacks of these Si PDs. However, the previously reported Group-III-nitride PDs were characterized as separate devices and not demonstrated in VLC systems.

1.4 Ultraviolet Photodetectors

Solar-blind response with 100 times enhancement of UV response over visible response was achieved in Schottky and np-diamond diodes when measured in the wavelength range 120 nm to 600 nm (1991) [45].

UV photodetectors were built on 6H-SiC photodiodes with two different structures: SiC Schottky barrier structures and SiC shallow p-n junctions (1992) [46]. The responsivity of Schottky barrier photodetectors was 0.15 A/W at 215 nm, whereas that of p-n junction photodetectors was 0.13 A/W at 225 nm. These high sensitivities were supported by low leakage currents and the detectors could be used in high temperature environments. For p-n junctions, it was observed

that shortening the active-layer thickness of n-layer shifts the photoresponse maximum towards short wavelengths. Further, rendering the n-layer thickness same as the space charge thickness drives the UV sensitivity to a maximum.

The various advantages of GaN-based compounds are the high breakdown strength enhancing scaling and frequency response of transit time-limited devices. Further, employing high voltages reduces the depletion capacitance at the Schottky contacts. Low leakage currents improve the Signal-to-Noise Ratio and allow high-temperature operation. High electron peak velocity and large optical photon energies are crucial for transient transport. Large photo-absorption depths avoid surface recombination and surface scattering. The inherent benefits of MSM photodiodes are fabrication ease, fabrication process compatibility with that of FETs, high bandwidth potential, and lower capacitance. With this scenario, Joshi et al. (1994) [47] reported on the high-speed response of GaN MSM photodetectors based on Monte Carlo computations with inclusion of hole and electron transport, electric field effects, circuit loading and the dependence on intensity. The transient impulse response favorably compares with a 0.25 μm GaAs MSM device, with better performance at lower intensities. At higher intensities, performance enhancement is realizable by raising the applied voltage and through ballistic regime operation at electric fields around 150 kV/cm. A bandwidth of about 100 GHz was realized.

GaN photoconducting UV sensors fabricated by electron cyclotron resonance molecular beam epitaxy with interdigitated electrodes were reported (1995) [48]. The detector exhibited a high responsivity of 125 A/W, a gain-quantum efficiency product of 600 at 254 nm and 25 V. The device showed fast response of the order of 20 ns corresponding to 25 MHz bandwidth. A sharp long wavelength cut-off at 365 nm was observed in the spectral response, whereas the response remained constant in the range 200 nm to 365 nm.

High-speed photodetectors are vital in missile tracking and intercept, as well

as in space-based optical communications. Usually, GaN-based photodetectors exhibit slow response due to high density of traps. Carrano et al. (1998) [49] overcame this issue by fabricating high-quality single-crystal based GaN MSM UV photodetector and with transit time-limited response. The device showed a fast rise time of ∼23 ps corresponding to a 3-dB bandwidth of ∼16 GHz. A slow component was observed in the temporal and frequency response due to the slower hole drift velocity of GaN.

ZnO is a wide bandgap material (E_g=3.3 eV) suitable for UV detection with high radiation robustness for harsh environments. It has a large exciton binding energy (60 meV) showing potential for low-threshold blue/UV lasers which can be integrated with photodetectors. However, p-n junction based devices are difficult to realize due to the lack of reliable p-type ZnO. Thus, only MSM UV detectors with either ohmic or Schottky contacts were reported. Alloying MgO with ZnO results in $Mg_xZn_{1-x}O$ with the same material benefits as pure ZnO but with composition-dependent tunable bandgap. This opens it up for applications such as solar UV radiation monitoring, airborne missile warning systems, and ultra-high temperature flame detection. Yang et al. (2001) [50], for the first time reported on the high quality epitaxial $Mg_xZn_{1-x}O$s films on c-plane sapphire by pulse laser deposition, as well as fabricated and characterized photoconductive MgZnO UV MSM detectors. $Mg_{0.34}Zn_{0.66}O$ thin films were grown with a bandgap of 4.05 eV. The MSM detector exhibited a large responsivity of 1200 A/W at 308 nm at 5 V bias, and UV/visible rejection ratio (R_{308} nm/R_{400} nm) of more than 4 orders of magnitude. Fast rise times of 8 ns and slow fall times of 1.4 μs were recorded. The rise time was limited by the excitation laser which possessed a Full Width Half Maximum ($FWHM$) of 4 ns. The slow component in the fall time was attributed to the excess lifetime of trapped holes in n-type semiconductors, which in turn resulted in large responsivity. The origin of traps is related to the device processing-induced surface damage or the interface states associated with the Wurtzite-cubic phase separation and alloy fluctuation.

Solar-blind photodetectors are crucial for applications such as engine/flame monitoring, missile warning and tracking, covert space-to-space communication, and chemical/biological agent detection. AlGaN-based solar-blind detectors have been thoroughly studied with MSM structures exhibiting low dark current, low noise, and high responsivity. The highest 3-dB bandwidth of solar-blind MSM photodetector to date was 100 MHz. This value was also one order lower than that using Schottky photodetectors. Thus, N. Biyikli et al. (2003) [51] demonstrated multi-gigahertz bandwidth (5.4 GHz) solar-blind AlGaN-based MSM detectors fabricated on Metal-Organic Chemical Vapour Deposition (MOCVD)-grown epitaxial $Al_{0.38}Ga_{0.6}2N$ layers. The dark current leakage densities were below $1{\times}10^{-6}$ A/cm^2 at 40 V reverse bias. The device exhibited a peak photoresponse of 1.26 A/W at 264 nm accounted by photoconductive gain mechanism. Also, a three orders of magnitude rejection of visible light at 350 nm was obtained.

Previously published reports on monolithic opto-electronic integration of photodetectors and transistors were basically in the InP, Si, or GaAs material systems. M. Mikulics et al. (2011) [52] reported on the integration of opto-electronic circuit in the GaN material system using MSM photodetector and MESFET amplifier. These components were integrated in coplanar strip lines in the GaN/AlN/SiC material system. Ultrafast response was obtained with MSM photodetector with a response time as short as 0.9 ps and a 3-dB bandwidth of 410 GHz. The ultrafast response was attributed to the existence of carrier traps in the GaN layer that were formed due to the relatively low molecular beam epitaxy (MBE) growth temperature of 650 °C. The MESFET amplified the 6 mV peak signal from MSM photodiode into 35 mV peak signal with a 4 ps wide response. The comparatively slower response of MESFET was due to the limitation by the input capacitance. The 3-dB bandwidth of MESFET was 55 GHz, much larger than the expected value of frequency cut-off of GaN MESFET, primarily due to the very high maximum frequency of oscillation (f_{max}) representing the power gain of MESFET as opposed to f_T which corresponds to current gain. At low frequencies, the OEIC

exhibits ten times higher response than just the MSM diode, and delivers a power gain up to 150 GHz.

The disadvantage of conventional PIN or MSM diodes is that obtaining high internal quantum efficiency (IQE) from UV to NIR is difficult on account of the large absorption depth of silicon at high wavelengths. Various approaches were utilized to overcome this issue based on reach-through structures; arsenic diffusion within the p-type Si substrate; graded doping epitaxial region and rear-side surface field in a rear-side illuminated CMOS sensor; using pinned photodiode topology and providing two new regions in the standard process; utilizing molecular beam epitaxy technology; and using lateral trench structures. A. Ali et al. (2016) [53] further improved the IQE of the device using through silicon via (TSV) connection in the MSM device in CMOS technology. The TSV connection is created by first etching a trench, and filling that trench with a conductive metal. The employment of TSV contact within silicon substrate forms a Schottky junction, which develops a large radial electric field distributed uniformly in the space charge region. The advantage of the Schottky contact is that it allows the phenomenon of photoemissive detection at photon energies lower than the bandgap, thus enabling high IQE in a wide spectral region. Also, this contact in TSV configuration overcomes the drawback of large absorption depth of Si at high wavelengths. The authors obtained a minimum IQE of 98.24% in the 300 nm-1000 nm spectral region at 3 V bias, with a dark current of 83.8 fA, a 3-dB bandwidth of 41.4 GHz, and a maximum cross talk noise of 57.73%. The other proposed photodetector with a TSV included inside a p-well diffused in an n-substrate showed a 3-dB bandwidth of 635.6 GHz and a maximum cross talk noise of 0.37%.

Given the high cost and limited detectivity ($< 5\times10^{13}$ Jones) of GaN, Si, or SiC p-n junction UV photodetectors, and the low UV/visible rejection ratio, large and bulky nature, and high operating voltage of the PMTs, research efforts have been devoted to the development of organic-inorganic lead halide perovskite

materials-based photodetectors with comparatively lower cost, and showing excellent detectivity (10^{13}-10^{14} Jones), a large *LDR* (over 100 dB), and fast speed of response (in the microseconds range). Despite this progress, their detectivity is lower compared to PMT due to the absence of efficient gain mechanism, and their toxicity along with environmental instability. Hence, D. Shao et al. (2020) [54] fabricated a visible-blind perovskite-polymer hybrid photodetector based upon the combination of 1,1-bis[(di-4-tolyamino)phenyl]cyclohexane(TAPC) and novel wide-bandgap, vacancy-ordered, Pb-free inorganic perovskite: Cs_2SnCl_6 doped with Nd^{3+} nanoparticles (NPs) (Cs_2SnCl_6: Nd^{3+}). This detector exhibited high speed, large detectivity, and large *LDR*. This superior response is attributed to the electron confinement effect resulting in interfacial charge-controlled hole injection. The device showed a high rectification ratio of 6362 for the dark current at $\pm$5 V, a high photocurrent-to-dark current ratio of $\sim 10^6$ at -15 V at 280 nm. Further, it exhibited a maximum photoresponse of 2103.8 A/W and *EQE* of $7.01\times10^5\%$ at 372 nm wavelength. A *LDR* of 118 dB under 280 nm UV illumination was observed. The 3-dB bandwidth was recorded to be $\sim$300 kHz with rise time and decay times of 2.5 and 1.8 μs, respectively. The detectivity was measured to be $\sim 6.3 \times 10^{15}$ Jones at 372 nm. Moreover, this UV photodetector is environmentally stable.

1.5 Graphene and Graphene-based Photodetectors

Photodetectors based on traditional semiconductors such as Si and InGaAs suffer from low transmittance, non-resilience, limited spectrum, low resolution, and CMOS-inconsistency. The excellent optical and electronic properties, mechanical resilience, and wafer-scale development and consolidation of two dimensional materials viz. Transition metal dichalcogenides (TMDs), graphene, and their unified systems can overcome the above limitations. 2D heterostructure photodiodes provide ultrafast and broad visible to infrared response. Ultrasensitiveness and

broadband photodetection can be registered using 2D hybrid systems-based phototransistors when integrated with other systems such as perovskites, quantum dots, plasmonic nanostructures, or organic materials. Further, integration of 2D PDs with Si and CMOS-based systems can lead to high performance, broadband detection, low cost, and imaging modalities [55].

Photodetectors can be classified as photodiodes, photoconductors, and phototransistors. Photodiode either administers the built-in electric field via a p-n junction or a metal-semiconductor Schottky junction. Ultrahigh mobility of graphene leads to ultrafast response from picoseconds to nanoseconds, and high bandwidth in the GHz range [56] in graphene photodiodes. However, the External Quantum Efficiency (EQE) of photodiodes is below 100% except in Avalanche photodiodes (APDs), wherein impact ionization occurs near breakdown resulting in multiplication gain, but at the expense of high voltages of 50-100 V. 2D materials viz. MoS_2, InSe, and BP-based APDs offer multiplication gains of 100-1000 [57]. Photoconductors provide gain by the movement of photoexcited electrons or holes several times across the source and drain ohmic electrodes before their recombination when an external field is applied across the electrodes with the gain defined by the ratio of carrier lifetime to the transit time. While the prolonged lifetime of one type of carriers due to the trapped sites results in high gain, this conversely degrades the temporal and frequency response.

There exist noise-related issues in photodiodes and photoconductors. To address these issues as well as provide high gain and simultaneous large bandwidth, phototransistors are employed. As an extension of the photoconductor, the phototransistor consists of a third gate terminal, wherein a thin dielectric electrically isolates the gate from the channel in 2D material-based photodetectors [58]. The charge density can be controlled and varied by the gate bias through the field effect and the dark current can be restrained using depletion mode operation.

The 2D photodetectors without gain can be classified into 2D PDs with photo-

induced bolometric and thermoelectric effects and 2D photodiodes in heterostructure configuration based on photovoltaic effect. Carrier transport in graphene being dominated by hot carriers and the electron-electron interactions being strong, the photothermoelectric effect is exhibited by p-n junctions in graphene [59]. Certain PDs in metal-graphene-metal (MGM) configuration reported dominance by photovoltaic effect [60]. Graphene photothermoelectric detectors showed high bandwidth of 40 GHz, but limited responsivity of 6.1 mA/W on account of the low absorption and non-existence of gain [56]. Graphene with its feeble phonon-electron coupling and small electronic heat capacity when incorporated in bolometers as bilayer graphene exhibited high sensitivity (33 $fWHz^{-1/2}$) at 5 K and ($>$ 1 GHz) very fast speeds at 10 K [61]. 2D heterojunction photodiodes are grown either by locally doping through chemical modifications or electrostatic interactions or by using transfer processes in both planar and orthogonal directions. These devices are characterized by ultrafast response but without gain. The sandwich structures based on Gr-TMD-Gr out-of-plane configurations were investigated for use as a photodetector. Graphene served as transparent electrode in the top and bottom positions for extracting charges, whereas the TMD absorbed photons and assisted in the transport of carriers. The advantages of the materials utilized were the capability of TMDs of strong interactions between light and matter and the possibility of tuning the Fermi level of graphene based on the bias applied. For example, Gr-Ws2-Gr structure showed good performance with sensitivity of 0.1 A/W and EQE above 30% [62].

Since the earlier type of PDs showed limited responsivities and gains, 2D hybrid PDs were demonstrated. The photoresponse depends on the photoconductive gain from the difference between the majority carrier electron transit time and the minority carrier hole lifetime. For further enhancement of photoresponse, techniques such as surface doping [63], sensitizations with quantum dots (QDs) [64], perovskites [65], or metal nanostructures [66] were employed. The cost of photoconductive gain is the 1 kHz order or lower bandwidth. These types

of PDs suffice for steady state spectroscopy, sensing, and video imaging applications. The photogating effect in graphene detectors can be enhanced using the combination of optical waveguides, optical microcavities, and the plasmonic field proliferation. Other methods are sensitizing graphene hybrid phototransistors with colloidal quantum dots (CQDs), other 2D materials, organic materials, perovskites etc.

CQDs have distinct properties viz. strong light absorption, UV to short wave infrared (SWIR) broad absorption range, and quantum confinement effect-induced tunable bandgap by changing size. The detector is formed by covering monolayer or bilayer graphene with a thin film of CQDs. Upon illumination, the photogenerated holes move toward graphene and undergo drift toward drain by voltage bias. The electrons remain trapped in the quantum dot layer. The photogating effect is the result of the trapped carriers whereby the conductance of graphene is modulated by these charges, and the Dirac point is shifted to higher back-gate voltage. The detectors of hybrid graphene-PbS CQDs show high quantum efficiency of 25%, high gain up to 10^8 (responsivity of 10^7 A/W) in the SWIR region up to 1.6 μm. Also fast video-imaging speed (<10 ms) and high detectivity of 10^{13} Jones were obtained [64]. Integration of CQD photodiode on top of a graphene phototransistor and biasing the CQDs film, the depletion width and the charge collection efficiency is raised by the extra electrical field normal to the graphene-CQDs interface. EQE exceeding 70%, Linear Dynamic Range (LDR) of 110 dB, and 3-dB bandwidth of 1.5 kHz were attained [67].

Graphene FETs (GFETs) act as excellent transducers on account of the very sensitive channel currents to variations in potential and charge densities at graphene channel or interfaces. This feature is enabled by the shift in the Dirac point depending upon the gate and graphene work-function difference, charge density and type at the graphene-substrate interface, and the level of impurity doping [68]. The ultrahigh mobility of graphene results in high speed operation of GFET photodetectors, which outperform Si MOSFETs and exhibit comparable performance

to the InP or GaAs HEMTs in terms of cut-off frequency.

Under visible light illumination of 532 nm wavelength, the responsivity of GFETs can reach to ∼10 mA/W [60]. Using hybrid GFETs, higher photoresponse is possible due to the combination of high absorption characteristics of other semiconductor materials and the ultrahigh carrier mobilities of graphene. Using PbS QDs on graphene, produced visible responsivities of $\sim 2.8 \times 10^3$ A/W at a negative gate bias and $\sim 1.7 \times 10^3$ A/W at a positive gate bias [69]. The mechanism of detection was characterized by the efficient transfer of photogenerated holes in the PbS QDs into the conductive graphene channel, enhancing hole density in the p-doped region and reducing electron density in the n-doped region. The variation in carrier densities leads to the photocurrent. The high carrier mobilities of graphene are vital in achieving the high responsivities.

Even more efficient absorption of light is possible with organic materials than inorganic semiconductors. For instance, graphene-chlorophyll hybrid FET exhibited a high responsivity of 10^6 A/W and a high gain of 10^6 electrons per photon at 683 nm wavelength [70]. The hole transfer from chlorophyll to graphene is electrostatically prominent and creates significant charge separation in the hybrid film. The electrons maintained in the chlorophyll layer act as a negative gate voltage and produces field-effect p-type doping in graphene. Even further improvement was attained using one of the family of TMDs i.e. MoS_2. MoS_2 possesses strong light absorption of (1×10^7 /m) in the visible region. Ultrahigh responsivities of 5×10^8 A/W at room temperature under 635 nm illumination were recorded using MoS_2/graphene bilayer film based GFETs [71].

On the other hand, UV photodetectors based on hybrid GFETs with combination of wide bandgap oxide semiconductors such as TiO_2 and ZnO and graphene, integrated the high UV absorption characteristics of oxides and the high carrier mobilities in graphene. ZnO QDs/graphene hybrid GFETs recorded responsivities and gains up to 10^4 A/W and 10^4 respectively [72]. Adsorption of oxygen

molecules from air on the surface of ZnO QDs attract electrons in ZnO QDs forming negatively charged anions. The electron-hole pairs are generated in ZnO QDs upon illumination, and the holes travel toward the surface and release the adsorbed oxygen anions turning into oxygen molecules. The electrons proceed toward the graphene channel and create n-type doping in graphene.

1.6 Overview of Modeling Methods for OPFET

In relation to device physics, modeling refers to solving a partial differential equation (PDE) with the solution representing the relationship between the cause and the effect in the presence of numerous causal factors. Applying suitable boundary and initial conditions as well as appropriate assumptions are imperative in the PDE solving process. Analytical methods of solution give close to exact answers being directly representing the various attributes involved as well as existence of fewer errors. In contrast, numerical methods are based upon approximations. The disadvantages of analytical methods are their limited applicability due to the modeling complexity involved, non-existence of analytical solution in certain cases, and the requirements of regular geometry, equation linearity, constant coefficients etc. The two main broad classifications of numerical techniques are the deterministic and the stochastic methods. Deterministic method always produces the same output for a given input. Whereas, the stochastic method can produce different outputs for the same input based on the number of times the computation is carried out and other factors, and relies on statistical principles [73]. The stochastic methods such as the widely used Monte Carlo method [74], although suited to complex environments is overlooked due to its inherent statistical error and the necessity of performing a group of calculations. Hence deterministic methods are preferred. The three main categories of deterministic methods are the Finite-Difference Method (FDM), Finite-Volume Method (FVM), and Finite-Element Method (FEM).

Finite-Difference Method (FDM) is based on the concept of finite differences so that the PDE should be satisfied over a set of interconnected points (within the domain area) called as nodes [73]. For solving the PDE, it should satisfy the suitable boundary conditions. The finite differences are framed based upon the Taylor series expansions. The advantages of the FDM approach are their simplistic nature, and adaptability to any form of PDEs. Further FDMs are advantageous in terms of stability, convergence, and accuracy for 1D systems [75]. Also, manipulation of geometry and performing local calculations is straightforward due to the uniformity of the spatial relation to neighbouring nodes [76]. FDM also offers higher-order approximations, and hence higher-order accuracy [77]. However, it has a drawback of non-handling complex geometries in various dimensions. Also, the FDM approach does not easily handle material discontinuities, and cannot produce local grid refinements.

Finite-Volume Method (FVM) enables approximating the PDE over finite-sized control volumes rather than at points. This approach allows to create cells of arbitrary structure, although regular geometries are used traditionally such as convex polygons (in 2D) or polyhedrons (in 3D). The cells are bounded by planar surfaces (in 3D) and straight edges (in 2D). The data is stored in the centroid of the cells, and the perpendicular gradients at the faces are based upon the approximations of the cell center values of the dependent variable. The Taylor series expansions are used traditionally for this purpose. Unlike FDM method, where PDE is solved directly, in FVM approach, the PDE is solved by first integrating it over the control volume, and then approximated and solved. Further, due to the absence of cell centers at the boundaries, the boundary conditions cannot be directly satisfied. Hence, the solutions obtained using FVM method are known as weak form solutions [73]. One remarkable feature of the FVM method is the conservation property. The property physically stems from the fact that the net rates of the quantities leaving and that being produced within the control volume are the same. The strength of the FVM method lies on the flux computation only

at the cell boundaries, holding also for non-linear problems. The adaptive mesh refinement is possible with FVM approach. FVM method utilizes constant shape functions, and inherently conserves current, and hence solves for the current density of charge carriers with utmost accuracy. However, the FVM approach suffers from the disadvantage as compared to the FDM and FEM approaches of not able to make the approximating functions of higher order [78].

Finite-Element Method (FEM) relies on the variation of parameters approach [79]. It involves converting the strong PDE form to weak form, and then using finite-sized elements to discretize and obtain solution to the weak form problem. The weak form is obtained by multiplying the PDE with test function, and then performing integration of the equation over the complete computational domain. The suitable boundary conditions need to be applied. The finite-sized elements chosen could be traditionally of convex elements, namely that of arbitrary polygons in 2D or arbitrary polyhedrons in 3D. In the past, triangular elements in 2D and tetrahedral elements in 3D were preferable due to the simple mathematical structures. The FEM method involves describing the solution and the test function in each element by a linear combination of basis functions with undetermined coefficients. The mathematical processing results in a linear system of algebraic equations, and should be solved to give the undetermined coefficients, and finally the solution of the dependent variable. The attractive feature of the FEM method is that it allows the manipulation of the type and degree of the basis functions. The accuracy enhancement can be carried out either by h-adaptivity (reduction of the element size), p-adaptivity (increasing the basis function degree) or by a combination of the two (hp-adaptivity), which is not possible in FVM and FDM methods [73]. Further, the FEM approach enables faster computation than the FVM method due to fewer degrees of freedom. Also, combining with other physics interfaces is straightforward and allows differentiation of the variables using the d operator. One more feature of the FEM method is its energy conservation and not current conservation. In the linear FEM approach, there

is poor current conservation, whereas in the log formulation, it is much better but inferior as compared to the FVM approach. The quasi-Fermi level approach works better for wide bandgap systems or low temperature environments. The density gradient formulation offers quantum physics computations with the drift-diffusion method. The additional advantages of the FEM method are its general nature, the freedom to increase the order of elements for accurate physical fields approximation, and the adaptive mesh refinement. Mixed formulations are possible with FEM method and can be straightforwardly handled. Both FEM and FVM approaches are suited for curved and irregular geometries. The disadvantage of the FEM method is the quite involved and advanced mathematics behind it, and requires mathematical expertise for its implementation. On the other hand, FVM and FDM methods are relatively straightforward in implementation [78, 80].

1.7 Gap Analysis

Optical control of MESFET has a crucial advantage over other technologies:

- With OPFET, simultaneous detector-cum-amplifier operation is possible.
- It offers inherently high gain-bandwidth product.
- It has the capability to achieve simultaneous high gain, bandwidth, responsivity, *EQE*, detectivity, *LDR*, sensitivity, f_T, and low switching time, power dissipation, and operating voltage.
- OPFET provides a large number of degrees of freedom to tune the device characteristics such as structure, material, illumination model, modulation frequency, bias, optical power, wavelength etc.
- In other devices especially photodiodes, there is a trade-off between various parameters and simultaneous superior values of all parameters are not possible.

- Its high gain-bandwidth product caters to long-haul optical communication applications.
- As compared to diodes, there is an extra terminal (gate) to control (optically and electrically) the device characteristics.
- Diversity of applications are possible using OPFET-based optical systems.
- There is a lot of scope for improvement in OPFET performance through optimization.
- OPFET operating as a high-speed photodetector or an optical demodulator, has many attractive advantages such as low noise, low bias voltage, medium internal gain, wide dynamic range, wide spectral response, resistive output impedance, and others. In MESFET, the channel current is controlled by a Schottky gate, which has a much bigger coupling capacity with the semiconductor conductive channel, and accordingly better gate-control ability. Also, MESFETs can be easily fabricated and integrated.
- OPFET gives the possibility of bias-dependent dual-mode operation of the device. (Schottky junction diode mode or transistor (OPFET) mode).
- Some extra processing/addition/new structures/complex structures etc. are needed to improve the performance in other devices.
- OPFET can cater to wide number of applications so that large scale integration and fabrication possible.
- In most of the other devices, either of photovoltaic or photoconductive effects dominate, whereas in OPFET, the maximum sensitivity could be achieved through both effects simultaneously at high optical power levels.
- In OPFET, photoemissive effect can be administered when the photon energy is below the bandgap but above the Schottky barrier height, but in most of the other devices, it is absent.

- Disadvantage of High Electron Mobility Transistor (HEMT): The need for precise growth methods for HEMT increases the fabrication cost.

Visible-Light Communication (VLC) has gained tremendous importance in recent years as a promising alternative to RF-based communication. With the growing demand for higher communication bandwidth, the RF with its narrow bandwidth is insufficient to cater to the requirements. With a spectrum range of 385 THz to 800 THz, VLC's bandwidth is a thousand times larger than the RF spectrum. The important benefits of VLC are cost efficiency, energy efficiency, and unregulated large bandwidth [81]. Its potential applications include Li-Fi (Light-Fidelity) Networks, robots in hospitals, vehicle to vehicle communication, information displayed on signboards, and underwater communication [82].

VLC receivers require photodetectors with high sensitivity, large bandwidth, and low dark current. Presently, the state-of-art photodetectors being employed in VLC include the p-i-n photodiodes [83, 84, 85] and avalanche photodiodes (APDs) [86, 87, 88, 89, 90]. The p-i-n photodiodes provide high-speed detection but without amplification. APDs offer gain upto a modulation frequency of 1 GHz, beyond which the photocurrent gain reduces significantly. In certain cases, the APDs may also require amplification depending upon applications. Further, photodiodes require high bias voltages for operation. The 3-dB bandwidth of photodiodes limits the VLC system bandwidth. But the raw data rate transferable in a VLC link can far exceed the VLC system bandwidth or detector bandwidth. For detectors with low bandwidths, the data rates can be maximized by adding an adaptive equalizer to the presented analog front end at the receiver [91].

High-performance Optoelectronic Integrated Circuit (OEIC) receivers for visible light communication are a technology that monolithically integrates optoelectronic and electronic devices on a common semiconductor substrate. Against discrete devices, OEICs offer advantages of multifunction capabilities, better speed and noise performance, besides the use of fewer components. These advantages

enable a simpler assembly procedure, as well as more compact and reliable systems at low cost [92]. At present, OEIC receivers use separate detector and amplifier components for VLC, resulting in increased cost and system complexity. The most commonly used amplifiers for VLC are the transimpedance amplifiers (TIAs) [83, 84, 85, 86, 87, 88, 89, 90, 91] with high bandwidth and low noise [93]. GaAs Optical Field-Effect Transistor (OPFET) or optically-controlled Metal–Semiconductor Field-Effect Transistor (MESFET) is a device capable of the dual functions of detector and amplifier. It is compatible with OEICs and can provide high gain and large bandwidth along with a high unity-gain cutoff frequency (fT). In addition, in contrast to its photodiode counterparts, it has an added advantage of operating at lower bias voltages. Reference [94] studied OPFET-based OEIC receivers in the InGaAs material system at 1.6 μm wavelength operation. The study showed that the OPFET-based detector-cum-amplifier exhibits higher sensitivity at 10 Gb/s and 20 Gb/s data rates than other combinations of photodetectors and amplifiers. These latter combinations included p-i-n photodiodes, APDs, Metal–Semiconductor-Metal (MSM) photodiodes, MESFET, High-Electron Mobility Transistor (HEMT), Heterojunction Bipolar Transistor (HBT), and Metal–Insulator-Semiconductor Field-Effect Transistor (MISFET). The study has stimulated interest in exploring MESFET-based detector-cum-amplifier at other wavelengths of operation.

The authors have come across no reported work in the literature survey undertaken by them on the optimization of OPFET devices in regard to any application. Moreover, the optimization of these devices can assist in achieving specific VLC requirements or specifications in addition to improving their overall performance. GaAs buried-gate front-illuminated OPFET device has been studied as a highly sensitive photodetector as compared to front- and back-illuminated surface-gate OPFETs [34]. Buried-gate OPFET has the distinguishing features of the gate being buried into the channel and channel side illumination. These features obviate the requirement of a transparent gate. Elimination of the requirement of

transparent gate results in zero wastage of light at the metal film and thereby improves responsivity. To the best of our knowledge, buried-gate OPFET has not yet been explored as a detector-cum-amplifier in regard to any application.

On the other hand, Ultraviolet (UV) reflectance imaging is a well-known application in biomedical engineering. It requires photodetectors with high visible/UV contrast ratios along with high visible sensitivity and low dark current. There is no much information available on the visible/UV contrast features of any photodetector. The contrast ratio should be high in order to appropriately control the ambient visible light in the presence of background UV radiation during imaging and enabling erroneous Both the applications have one thing in common: they need photodetectors operating in the visible range. Three most featured materials capable of operating in the visible region include Si, GaAs, and InP. These possess distinct electrical and optical properties which motivate one to conduct research using these materials. One potential candidate to cater to high gain-bandwidth product applications is a phototransistor or a photoFET. Optical Field Effect Transistor (OPFET) or optically controlled Metal-Semiconductor Field Effect Transistor (MESFET) has been a widely studied device over the past few decades for its applications as photodetectors, optically-controlled amplifiers, oscillators, and switches [7, 9, 12, 24, 29, 31, 33, 34, 95, 96]. However, the research lacks the assessment or the impact of the OPFET device incorporating these materials from the optimization point of views i.e. material and structural optimization. Further, analysis of the attained results and the correlation of the detector responses with the material and the structural parameters can substantiate further research.

Also, no significant research has been reported so far on the applications of GaAs OPFET or AlGaAs/GaAs High Electron Mobility Phototransistor (PHEMT) as photodetector-cum-amplifier. Known studies neither investigate in depth nor analyze the bandwidth performance and its optimization. For long haul communications, the very high responsivity of OPFET gives it an edge over the

reported devices. In high data rate VLC applications, even with lower 3-dB and detection-cum-amplification bandwidths in some cases, the OPFET devices have higher gain-bandwidth product. An additional advantage is that a single device acts as a detector-cum-amplifier as compared to other OEIC receivers, which employ distinct detectors and amplifiers. Published reports on the GaAs-based detectors and amplifiers in OEIC receivers are several years old. Most of the reported research on InP-based OEIC receivers is limited to the 1.33–1.55 μm infrared region.

Ultraviolet (UV) photodetectors are useful in applications such as chemical, environmental and biological analysis and monitoring, flame and radiation detection, astronomical studies, missile detection and optical communication [97]. Typical harsh environment applications of the UV photodetectors are solar observations, ultraviolet (UV) astronomy, military defence, automatization, short-range communications security as well as environmental and biological researches [98]. Suitable materials for these applications involve wide-band-gap materials viz. GaN, SiC, and ZnO. These materials possess high saturation velocities, high breakdown voltages, mechanical robustness to harsh environments, and good dielectric strength sufficing for such purposes. Significant studies are underway towards the improvement of performances of the various detectors. Devices such as Metal-Semiconductor-Metal (MSM), photoconductors, photodiodes, phototransistors, Schottky-barrier, nanostructure, hybrid, organic, etc are the various detectors in this arena. Photodetectors employ photoconductive, photovoltaic or photoemissive effect or a combination of all to convert light signals into electrical signals. The state-of-art photodetectors employed in UV communication include mainly the photomultiplier tubes (PMTs) and the avalanche photodiodes (APDs) [99, 100, 101, 102, 103]. PMTs offer high gain and low dark current but are bulky and fragile. APDs are miniaturized and exhibit high gain. However, they are expensive. These devices offer gigahertz or sub-gigahertz bandwidth. Photodetectors utilized for other applications such as photoconductors,

MSM photodiodes, Schottky diodes, p-n junction detectors, and p-i-n detectors have significant trade-off between either of gain, bandwidth, response speed, detectivity, dark current or exhibit lower gains than the transistor photodetectors [104, 105, 106, 107]. Combination of the excellent properties of the wide-band-gap materials and the FETs can fulfill much of the requirements of the UV industry. To the authors' best knowledge, there has been lack of optimization procedures in such structures towards UV applications. The buried-gate structure employed in various devices, in general, is known for its high speed, power and stability. It is one of the most sensitive models of OPFET for photodetector applications. Besides that, and a few more contributions, there has been no notable published work on such devices, especially concerning optimization.

Traffic security is an important scenario for various outdoor applications [108]. These include Vehicle-to-Vehicle (V2V) and Vehicle-to-Infrastructure (V2I)-based systems. These systems are implemented by using techniques such as pulse position (PPM)/variable PPM (VPPM), on–off keying (OOK) [109], and orthogonal frequency division multiplexing (OFDM) [110]. The road accidents can be prevented by employing these (V2V and V2I) Intelligent Transportation Systems (ITS). Further, these can control, ease, and mobilize the traffic which are widely dispersed in the entire world. Apart from vehicular communication, buildingtobuilding (B2B) simplex and duplex VLC communications [111] can be established in bank buildings, campuses, and headquarters to enable access to data, information, and media. The Li-Fi application can be extended by utilizing street and park lights as access points implemented in either hybrid or aggregate systems [112]. The solar panels can be deployed to simultaneously harvest energy and act as a communication receiver [113]. In V2I communication system, the traffic lights are used as VLC transmitters, whereas in V2V system, the headlights and rear lights act as transmitting sources [108]. Generally arrays of LEDs are employed as optical sources in these applications.

In VLC V2V and V2I systems, the commercially used detectors are either pixel

image sensors, single photosensitive elements (photodiodes (PDs)) or a matrix of PDs (cameras) [108]. Compared to image sensors and camera devices, the single PDs offer advantages of very high speed, high sensitivity, low noise, very low system complexity, very low sensor complexity, low energy consumption, and low production cost. The drawback is that these PDs cannot carry out spatial separation of the sources. This feature may not be needed in many of the applications. Hence, single PDs have a significant edge over that of image sensors and camera devices. This functionality of PDs can be further enhanced by employing FET-based photodetectors.

V2V and V2I communications [114] should possess fast switching, and high gain-bandwidth product photodetectors. The presently available devices are based on the p-i-n, avalanche photodiodes (APDs), Metal–Semiconductor- Metal (MSM) PDs, and Schottky PDs as photodetectors [41, 89, 90, 115]. They employ various kinds of Field Effect Transistors (FETs) as amplifiers to form Opto-Electronic Integrated Circuit (OEIC) receivers. These devices operate at nanoseconds to picoseconds speed range but are inferior in terms of gain-bandwidth product.

The disadvantage of the communication system presented in [114] and the detectors/amplifiers currently used is that the transmitters and receivers have to be aligned. Further, the vehicles need to be close to each other with a constant distance between them. These systems work only when the vehicles have stopped and fail under the naturalmovement of cars.

To foster these challenges, there is a need for a detector/amplifier combination which can detect very weak signals resulting from the natural motion of cars along with high-speed operation.

The major advantage of OPFET is the high gain-bandwidth product enabling long haul communications, thus, greatly increasing the transmitting distances and allowing flexibility in the traffic lighting and communication systems. The

most widely investigated material system for this device has been GaAs. GaAs possesses high electron mobility, high carrier saturation velocity, moderately high absorption coefficient in the visible region, short lifetime of holes in n-type material and long electron lifetime.

5G and beyond 5G i.e. 6G communications are the emerging technologies for mobile-based and other related telecommunications. The frequency spectrums used by 5G are the sub-6 GHz (450 MHz to 6 GHz), and the millimeter-wave frequencies (24.250 GHz to 52.600 GHz), and also include unlicensed spectrum. Further, there may be frequencies in the 5925 to 7150 MHz range and 64 GHz to 86 GHz range [116]. 6G and higher versions may use the 95 GHz to 3 THz bands [117]. 5G and 6G communications have been expected to offer high capacity, security, connectivity, and quality links apart from low latency and low power consumption networks [118, 119, 120]. But, communicating in the RF domain alone has several limitations such as restricted spectrum band, regulatory spectrum use, and interference with nearby RF access points [121]. Thus, operating in the optical domain or an integration of RF and optical wired or wireless communication is the expected viable solution. Optical wired communication is achieved with the deployment of optical fibers and can provide high capacity links of around 100 Gbps or higher [122]. Optical wireless communication uses visible, infrared or ultraviolet light as a propagation media. This is broadly classified as visible light communication (VLC), Light-Fidelity (Li-Fi), optical camera communication (OCC), free space optical communication (FSOC), and light detection and The ultimate data rate of the communication system is limited by the 3-dB bandwidth of the photodetector used at the receiving end. The state-of-art photodiodes used for communication have limited gain-bandwidth product which also restricts transmission distance.

Graphene is an emerging 2-D material with outstanding properties such as high optical transmittance, high mechanical flexibility, high robustness, bias-dependent tunable work function, ultra-high carrier mobility, light weight, high

saturation velocity, zero effective mass of carriers, excellent chemical/physical stability etc. Because of the absence in bandgap in monolayer graphene under zero bias conditions, it is considered a semi-metal. It forms an excellent transparent electrode apart from its outstanding resilience to adverse environments such as high temperatures. GaAs is a semiconductor with moderate bandgap, high saturation velocity, high mobility, moderate to high optical absorption coefficients, and short minority carrier lifetime. It also has the potential to withstand certain high temperatures [123]. Thus, the combination of graphene and GaAs as electrode-semiconductor materials certainly have the edge over other commonly used materials under hostile environments like elevated temperatures. These environments are typical of automotive, space, and aeronautics 5G applications.

The control of adaptive antennas can be achieved either electronically or optically. The optical control has the advantages of higher bandwidth and lower losses as compared to electronic control [124]. Further, electrical beam-forming require bulky devices [125]. Optical phased arrays allow fast, stable, and precise beam steering [126]. Integration of photonics with electronics leads to low-cost, compact, and light-weight solutions with immunity towards electromagnetic interference [127]. Further, optical control provides additional degrees of freedom as compared to electronic control such as optical power, wavelength, and the way in which the device is illuminated (illumination model). This increases the given data and helps in greater and efficient control of the dynamically steered phased array antenna.

The solar cells are used in applications such as toys, calculators, watches, electric fences, remote lighting systems, water pumping, water treatment, emergency power, portable power supplies, satellites, and space vehicles. These devices used as arrays are powerful converters of renewable source of energy i.e. sun (solar energy) into electricity. Generally, solar cells are based on diodes i.e. p-n junction photodiodes, Schottky diodes, p-i-n diodes, heterojunction diodes etc and in some cases phototransistors such as Bipolar Junction Transistors (BJTs) and

Heterojunction Bipolar Transistors (HBTs) with large areas since capacitance and response times are of less importance. However, the response times may be important for some specific applications and when the conversion time is to be kept short. Apart from this, solar cells can be used as receivers in laser power beaming applications [128]. Power beamed to a photovoltaic array could power a satellite, an orbital transfer vehicle or a lunar base. Understanding solar cell response to the pulsed output of a free-electron laser (FEL) is important for evaluation of power-beaming applications. In this case, the switching and capacitances are of vital significance. Various device structures with different materials have been widely investigated over the past several decades [129, 130, 131, 132] which have delivered significant solar responses. However, to the best of the authors' knowledge, no work addresses the performance of FET-based detectors for solar cell applications.

There are numerous efforts towards Visible Light Communication under background solar illumination using solar cells [133, 134, 135, 136]. However, they either fail under high solar intensity or the system data rate is restricted to tens of Mbits/s. Further, these systems require separate Laser Diodes (LDs) or Light-Emitting Diodes (LEDs) as sources for communication purposes. As an alternative, we suggest to use modulated sunlight for communication. This idea has been implemented in [137, 138]. The modulated sunlight was first utilized in space communication [139]. Communication bandwidth of up to 10 MHz is recorded with further enhancement possible through optimization. The sunlight communication system is even now in its infancy. Instead, of simple photodiodes and photosensors used in [137, 138] to detect modulated sunlight, we can employ a FET based photodetector such as Metal-Semiconductor Field Effect Transistor (MESFET), also called as Optical Field Effect Transistor (OPFET).

Graphene is an excellent material for opto-electronic applications and the present photodetectors/modulators based on graphene include mainly Graphene MOSFET (Metal-Oxide Semiconductor Field Effect Transistor), metal-graphene-

metal PDs, plasmonic PDs, heterostructure PDs, etc [56, 71]. However, the progress of graphene devices is hindered by the high metal-graphene contact resistance, Fermi level pinning in metal-graphene contacts, low absorption in monolayer graphene, and the absence of bandgap in monolayer graphene [140, 141, 142, 143]. Surface treatments, modifying fabrication processes, edge-contacts, introduction of defects in graphene surfaces, UV/ozone treatments, O2 low power plasma treatments, rapid thermal annealing, increased surface bonding of metal and graphene, lowering barrier height, and increasing the doping density in graphene by biasing etc. are some of the methods used to lower the contact resistance in metal-graphene contacts [144, 145, 146, 147, 148]. The Fermi level pinning in metal-graphene contacts can be reduced by Surface Charge Transfer Doping, construction of 2D/metal vdWs (Van-der Waals) contacts, or creating edge contacts [149]. Reduced quantum efficiencies due to low absorption can be increased by utilizing graphene in transistor configuration, proliferation of hot carriers through Photo-thermoelectric effect (PTE), hot carrier-induced resistance change through biased Photo-bolometric effect (PBE), and/or by integrating graphene with other semiconductors or quantum dots [64, 150, 151, 152]. The issue of zero bandgap in monolayer graphene can be overcome by biasing bilayer graphene, constrainment of graphene in one dimension to produce graphene nanoribbons (GNRs) or quantum dots, or by chemically modifying graphene [153]. These issues were the main reasons for non-exploration of graphene-based MESFET for a diversity of applications. Since the research shows that these issues can be resolved by suitable means (may not be completely), graphene MESFET has come into the limelight. The notable feature of the graphene MESFET is that the high dipole capacitance at the interface of metal and graphene can induce significant sensitivity to applied gate bias as well as high magnitude of carrier density very suitable for intra-band absorption based photodetection, and modulation. Further, the high dipole capacitance induced large carreir density in graphene creates a highly intensified electric field between contacted and non-

contacted graphene as well as large temperature, conductivity, potential, and resistance gradients greatly suited for photovoltaic (PV), photo-bolometric (PB), and photo-thermoelectric (PT) current responses. Thus, graphene-MESFET has a great scope for opto-electronic applications and there are also a lot of degrees of freedom for optimization.

Chapter 2

Objectives and Main Contributions of Research

2.1 Objectives

The objectives of this research are:

- Optimization of high speed optical devices as detector cum amplifier in optical communications application based on OEIC receivers. Proposing a new model for the optimized high speed optical device.
- Investigating the feasibility of the use of different materials than the existing ones for the device.

2.2 The Main Contributions of Research

The main contributions and observations of this research are as follows:

- The OPFET device, in overall, shows better gain-bandwidth performance than the state of art devices such as p-i-n photodiodes, PMTs, APDs, and integrated PDs-FET/HBT configurations.
- The proposed study remarkably shows/establishes an important relationship between gate length and 3-dB bandwidth in OPFET (with the structural dimensions and the doping concentration subject to scaling rules) is that the bandwidth increases with the elongation of gate length at least for medium

to long gate length devices. The principle behind this finding is that as the gate length increases, the doping concentration reduces (according to scaling rules). Further, the depletion width sensitivity to applied illumination increases as the doping cocnentration decreases. It is pointed out for the first time that the frequency response curve widening is directly related to the depletion width sensitivity enhancement under photovoltaic conditions when the limiting factors such as series resistances and photoconductive effects are kept to a minimum. This fact occurs irrespective of other negative factors such as decrease in magnitude of doping concentration, and increase in the gate length itself. The reduction in depletion width sensitivity at higher doping concentrations is explainable by the fact that for a fixed photovoltage generated, since the higher doping concengtration means occupying higher energy bands, more energy is required to attain the same sensitivity. The relatively new aspect of relating the depletion width sensitivity to the bandwidth of the device is demonstrated graphically in the proposed research.

- The effective cancellation of the barrier height by the induced photovoltage; compensation of the higher depletion width sensitivity occuring at lower barrier height devices by the lower photovoltages in these devices; de-ionization of the space charge ions by the photocondcutive electrons in the gate depletion region; effect of squared lifetime term as opposed to the non-squared lifetime term in the equation for photogenerated hole density on the 3-dB bandwidth (the squared lifetime term produces steeper frequency response as opposed to non-squared lifetime term which reduces the bandwidth); the dominance of the higher photovoltage magnitude over the gentler roll-off rate arising from non-squared lifetime term at lower intensities whereas the roll-off rate is comparable to the photovoltage magnitude in short lifetime devices such as GaAs OPFET ($\tau_p = 10^{-8}$ s) and dominates at higher inten-

sities; the large photovoltage reducing the depletion width beyond the zero point, thus maintaining the roll-off point of photovoltage with frequency at a wider location increasing the bandwidth; at intensities where photovoltaic and photoconductive effects are comparable, the net bandwidth is dependent upon the relative contributions of the two effects not only at the dc frequency but also at or near the 3-dB point; the device parameters are closely related to the individual contributions from the saturation and conductance components of current; are some of the relatively new aspects encountered which can have significant effect on the OPFET characteristics.

- At higher intensities, in most of the cases, negative sensitivity is registered since the high photoconductive effect increases the voltage drop across the series resistance which completely depletes the channel and eliminates photovoltaic effect.

- The external factors applied as well as the intrinsic material properties, the photoconductive, photovoltaic, and the series resistance effects can explain the performance of OPFET.

- In many cases, there is a compensation of the effects arising due to one set of material parameters with the other set of parameters, thus showing comparable performance.

- It has been investigated from the simulations that the buried-gate structures have lower series resistances under dark than the surface-gate structures of same dimensions, and hence higher dark current (in-line with reported lietrature).

- The response times increase with the elongation of the gate length since although the drain current rises with gate length, the space charge increases at a greater rate.

- It has been observed that the depletion width sensitivity is higher when the dielectric constant is lower with other factors constant.

- The photovoltaic response of Schottky junction in GaN OPFET in the UV region is higher than the photoconductive response since the photovoltage-induced forward thermionic emission current is high compared to the reverse drift-diffusion photocurrents.

- The Schottky junction in MESFET offers greater 3-dB bandwidth under high background lighting conditions as opposed to MESFET itself which offers greater 3-dB bandwidth under low background lighting. This occurs when the gate length is sufficiently high (subject to scaling rules) so that the doping concentration is reduced and becomes comparable or lesser than the photogenerated excess carrier density, thus the effect of illumination on the minority carrier lifetime is perceived which reduces the hole lifetime. This lowered lifetime as well as lesser contributions from the photoconductive reverse drift and slow diffusion currents result in the increased bandwidth in Schottky junction in MESFET under high background lighting. In the OPFET device, the bandwidth is low at these intensities owing to the presence of slow photoconductive effect.

- Both transconductance and gate to source capacitance increase with gate length, but the rate of rise of capacitance is higher resulting in decrease of unity-gain cut-off frequency.

- Both transconductance and gate to source capacitance increase with optical power, but the transconductance increases at a higher rate causing an increase of unity-gain cut-off frequency with optical power.

- Depletion width sensitivity and 3-dB bandwidth or the frequency response curve have one-to-one correspondence with each other.

- The responsivity decreases with an increase of gate length.

- Photovoltage remains constant with gate length (for GaAs OPFET).
- Generalized and buried-gate front-illuminated models have been perceived as highly sensitive models at lower intensities. At higher intensities, the surface gate back-illuminated and the buried-gate back-illuminated models deliver higher photoresponse.
- Graphene OPFET delivers good terahertz detection-cum-modulation and photovoltaic performance at high gate bias levels and considerable mid-infrared photoconductive performance at low bias levels. Whereas, graphene FET shows better mid-infrared photoconductive performance.
- The frequency response study of the OPFET device for example of GaAs OPFET at different flux densities suggesting the different frequency ranges of operation can be stored in the form of a look-up table. The different frequency responses at various flux densities serve to indicate the relative contributions of the photovoltaic and photoconductive effects as a function of frequency and thus, can be used to tune the device to appropriate frequencies. The look-up table can be used to access the desired frequency depending upon the application for RF/microwave/terahertz imaging specctroscopy and the frequency response can also be crucial for photodetector application.
- For OPFET photodetector in 5G smart antenna applications, the device dimensions, gate to source voltage, drain to source voltage can be the control factors for variabl gain, variable phase detectors with large extent of variation. On the other hand, optical power and choice of illumination model can be the control factors for constant gain, variable phase detectors but the extent of variation is less within 10 to 20 degrees. The gain and phase tend to decrease with device dimensions as well as with gate voltages, except the gain which tends to increase at higher drain voltages. The gain and phase

significantly increased with the increase in the drain voltage whereas they decreased with the increase in optical power except at higher drain voltages where there is a slight increase in gain.

- In the UV region, in the case of 6H-SiC buried-gate OPFET, there is no significant effect of the elevated temperatures on gain, responsivity, switching time, and detectivity, except the 3-dB bandwidth which decreases as the temperature increases. The GaN buried-gate OPFET models when compared tgo ZnO and 6H-SiC models show that GaN models in overall exhibit better performance, with the SiC OPFET showing superior gain-bandwidth performance, and the ZnO OPFET is perceived as a high optical power detector.

- The OPFET devices show high solar energy harvesting efficiencies as well as wider 3-dB bandwidths under modulated solar illumination than the state of art devices used in solar communication.

- In the buried-gate front-illuminated OPFET, as the dimensions increase, the photovoltaic charge tends to reduce whereas the photocondcutive charge tends to increase. The depletion width sensitivity rises with the elongation of gate length and saturates at longer gate lengths.

- Surface-gate devices exhibit higher *LDR* than buried-gate devices due to lower dark current, thus showing potential towards high dynamic range or high resolution imaging.

Chapter 3

Theory/OPFET Models

3.1 Structure of OPFET and its Equivalent Circuit

Optically-controlled Metal-Semiconductor Field Effect Transistor also known as OPFET (Optical Field Effect Transistor) is a transistor structure based on the metal-semiconductor contact wherein the field effect is obtained from the depletion region formed between the metal gate and the underlying semiconductor acting as a capacitance. The device consists of N-type moderate doping of the channel layer on slightly p-type semi-insulating substrate. The channel is epitaxially grown on the substrate. Two highly doped n_+ regions are diffused on both sides of the channel layer to form the source and the drain. The source and drain metal ohmic contacts composed of metal are made on these n_+ regions. The gate metal forming a Schottky contact is laid down on the channel layer. These steps utilize lithography and lift-off techniques for fabrication.

The OPFET is characterized by various illumination models: (i) **Surface-gated front-illuminated OPFET** wherein the surface gate is transparent or semi-transparent to light and the illumination is allowed to enter the device through the metal gate-contact shown in Fig.3.1a. (ii) **Generalized OPFET** is a superset of the front-illuminated OPFET in which the spacings between the gate and source as well as the gate and drain are illuminated in addition to the metal

gate (see Fig.3.1b).(iii) **Opaque-gate OPFET** is another subset of the Generalized Model wherein the gate is made opaque i.e. the illumination only falls in the spacings (refer Fig.3.1c). (iv) **Buried-gate front-illuminated OPFET** represents the OPFET model with gate buried into the channel and the illumination enters the device through the front-surface of the active layer shown in Fig.3.1d and the gate is made opaque.(v) **Buried-gate back-illuminated OPFET** is similar to the buried-gate front-illuminated OPFET in terms of structure but differs from the way of illumination. This device is illuminated from the rear side through the substrate by inserting a fiber up to the gate-substrate interface (see Fig.3.1e) with the gate being transparent or semi-transparent. (vi) **Surface-gated back-illuminated OPFET (without substrate effect)** refers to the model wherein the metal gate contacts the front active-layer surface but the radiation is allowed to fall through the rear side of the active layer by inserting a fiber up to the active-layer substrate interface shown in Fig.3.1f.(vii) **Surface-gated back-illuminated OPFET (with substrate effect)**: This model is similar to the previous model except that the fiber is inserted partially into the substrate (see Fig.3.1g).

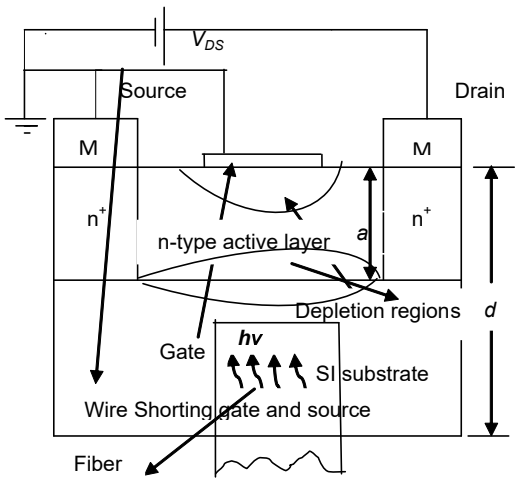

(g) Back-iluminated OPFET (with substrate effect)

Figure 3.1: Schematic structures of OPFET illumination models

The equivalent circuit of OPFET is presented in Fig.3.2. In Fig.3.2, g_d is the

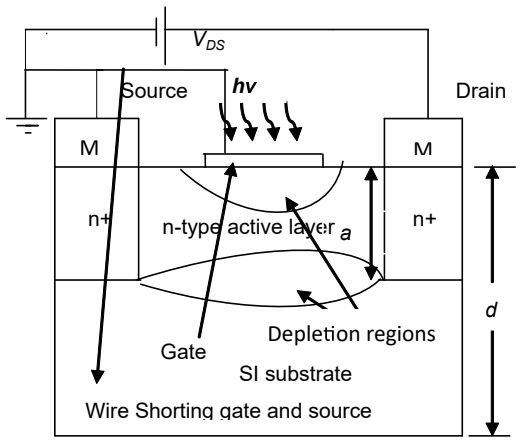

(a) Front-illuminated OPFET

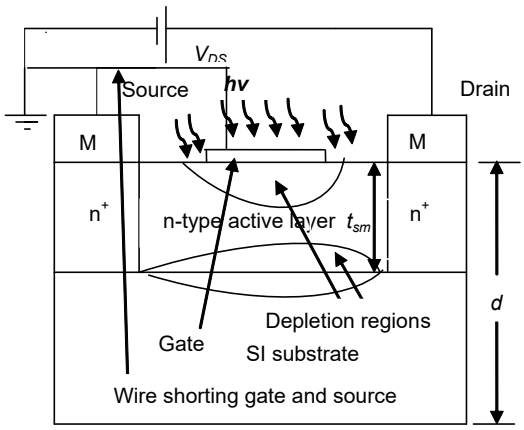

(b) Generalized OPFET

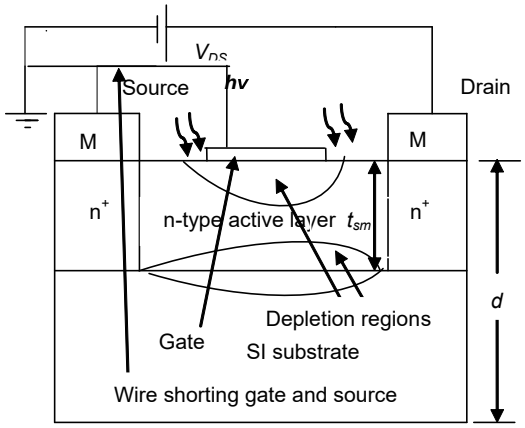

(c) Opaque-gate OPFET

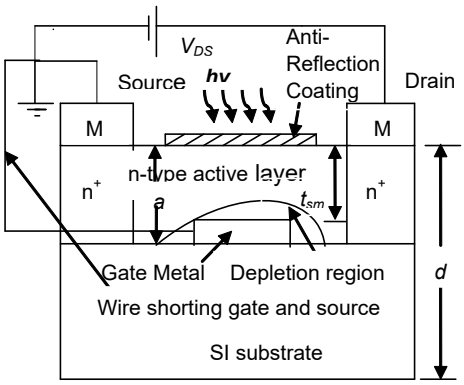

(d) Buried-gate front-iluminated OPFET

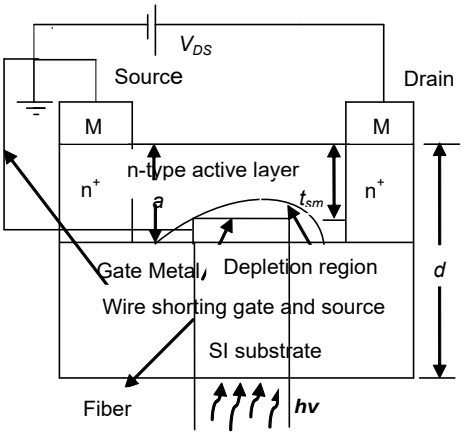

(e) Buried-gate back-iluminated OPFET

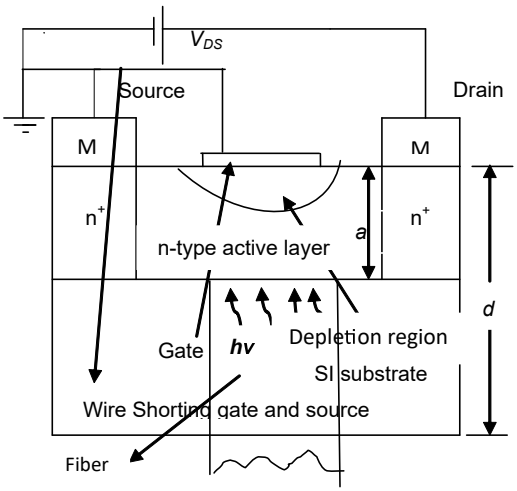

(f) Back-iluminated OPFET (without substrate effect)

Figure 3.1: Schematic structures of OPFET illumination models

channel conductance; g_m is the transconductance; v_{gs} is the gate-to- source voltage; C_{gs}, C_{ds}, and C_{gd} are the gate-to-source, drain-to-source, and gate-to-drain capacitances respectively; R_s and R_d are the parasitic series source and drain resistances respectively; R_g is the gate resistance; R_i is the internal gate resistance; L_g, L_s, and L_d are the parasitic series gate, source and drain inductances respectively.

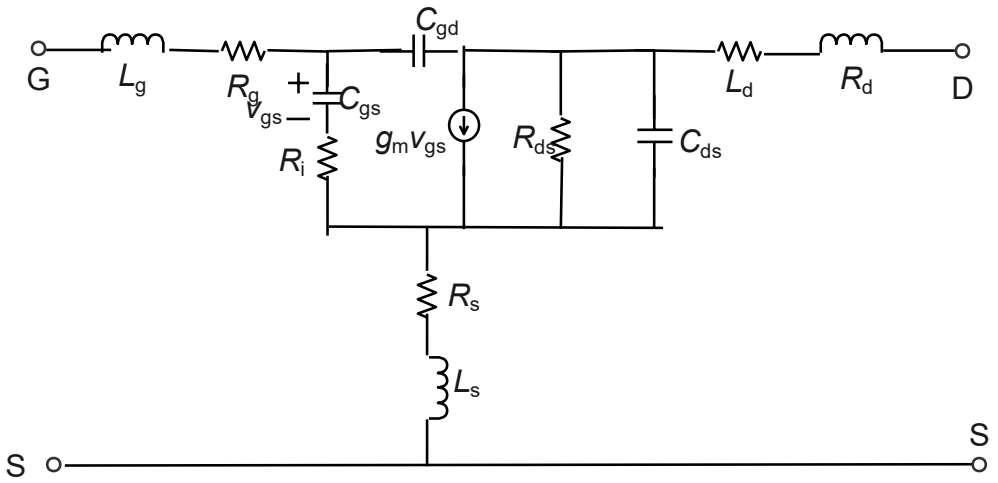

Figure 3.2: Equivalent circuit of OPFET

3.2 Brief Operation of OPFET

Under Dark: The MESFET operates either in enhancement mode (normally-off mode) or depletion mode (normally-on mode). The gate bias modulates the device characteristics by controlling the width of the depletion regions at the Schottky junction and the active layer-susbtrate junction. When the gate voltage is above the threshold voltage, the positive bias applied between drain and source attracts electrons from the channel towards the drain terminal thereby producing the drain-to-source current depending upon the effective active-layer thickness. With a small applied drain bias below the pinch-off voltage, the drain current increases linearly with the drain voltage (linear or ohmic region). In this region, the channel acts as a resistance. As the drain voltage approaches pinch-off, the device exhibits non-linear behaviour (pinch-off region). At this point, the channel

at the drain side of the gate is pinched-off. With the further increase in the drain voltage, the current tends to saturate to a constant value (saturation region). The total depletion of the channel which was initially at the drain end at the pinch-off point, increases towards the source as the drain voltage increases such that the electrons move at their saturation velocity to maintain constant current. In the enhancement mode, the device is off under zero gate bias i.e. the channel is fully pinched-off. Thus, the application of a positive gate bias shrinks the depletion region and allows the current between drain and source. The threshold voltage is positive for normally-off MESFET. In the depletion mode, the device is on even under zero gate bias. The application of a negative voltage extends the depletion region towards the semi-insulating substrate thus limiting the current.

Under Illumination: When the incident light with photon energy greater than the bandgap of the semiconductor is allowed to fall on the device, the radiation will be absorbed in the neutral (channel and substrate) regions and the depletion (Schottky junction and active layer-susbtrate) regions depending upon the illumination model employed. In the front-illuminated OPFET, the absorption will occur in all the regions except the sidewalls of the gate depletion region, whereas in the generalized model, the absorption will take place in all the regions including the sidewalls. In the opaque-gate OPFET, the absorption regions are similar to the generalized model except the depletion region below the gate. In the buried-gate front-illuminated OPFET, the absorption occurs in the neutral channel and Schottky junction depletion regions. Since the gate is opaque, the radiation does not pass to the substrate region. In the buried-gate and surface-gate back-illuminated (without substrate effect) configurations, the absorption regions are same as that of the buried-gate front-illuminated model. In the surface-gate back-illuminated model, the absorption occurs in the neutral channel, part of the neutral substrate, the Schottky junction depletion and the active layer-substrate depletion regions. Upon absorption, electron-hole pairs are generated in the respective regions. The photogenerated electrons are driven towards the channel

while the holes travel in the opposite direction. With the applied drain bias, the electrons produce drain-to-source current (photoconductive effect). The holes crossing the junction develop a photovoltage decreasing the depletion width and in turn, increasing the drain-to-source current (photovoltaic effect). In the models where substrate effect is involved, since the substrate is made semi-insulating and the channel is moderately doped, the p-n junction depletion width at the channel-substrate interface extends completely into the substrate whereas the depletion width is zero on the channel side. The photovoltage generated across the p-n junction depletion region has no effect on the detector characteristics. The drain-to-source current is limited by the voltage drop developed across the series resistances. Under modulated optical signal, wherein the light is modulated by a signal of frequency ω, the lifetime of carriers will also be modulated as also the generation rate, and the photogenerated carriers by the same frequency. Thus, the drain to source current will also be modulated. When the photon energy is less than the bandgap but greater than the Schottky barrier height, the OPFET operates by internal photoemission of metal electrons into the semiconductor giving rise to a photocurrent.

3.3 Brief Operation of Schottky junction in OPFET

Under Dark: Under low to moderately-doped conditions at room temperature, the transport mechanism prevailing across the Schottky junction is thermionic emission. The Fermi level difference between the semiconductor and the metal enables the transfer of electrons from the semiconductor to the metal until the equilibrium is established. This leaves behind immobile positive donor ions which collectively form a depletion layer or region at the metal-semiconductor interface presenting a barrier to the further flow of electrons into the metal. This barrier is represented in the theory in terms of the Schottky barrier height or the built-in potential. Under the dark condition, with applied forward bias, the current

initially rises with voltage and eventually saturates at higher forward voltages due to contribution from the parasitic series resistance. When the reverse bias is applied, the current rises with voltage at the very low values of voltage and saturates at its reverse saturation current density value at the higher voltages. The reverse saturation current density depends upon the parameters such as the absolute temperature, the Richardson constant, and the barrier height.

Under illumination: Under illumination, with photon energy greater than the bandgap, the device can be operated in either the photovoltaic mode or the photoconductive mode. The incident illumination is absorbed in the channel and the depletion regions creating electron-hole pairs. The holes advance toward the junction while the electrons travel in the direction of the channel. The holes generated in the depletion region are enabled to cross the Schottky junction by the built-in electric field in the depletion region producing a photovoltage. With the gate shorted to the source (zero bias or the photovoltaic mode), this photovoltage acts as a positive bias constituting a forward current. The photocurrent generated is significant subject to considerable photovoltage owing to the forward-bias operation and the low dark current resulting in high responsivities. The dependence of this photocurrent on the modulation frequency is due to the frequency variation of the photovoltage with frequency and more specifically due to the modulation of the hole lifetime with frequency. The drift and the diffusion phenomena also constitute a photocurrent which tends to reduce the forward photocurrent when its contribution is comparable to the forward current since these currents flow in the reverse direction. The drift photocurrent is due to the separation and drift of the photogenerated carriers in the gate depletion region by the built-in electric field in this region which are eventually collected at the contacts. The diffusion photocurrent arises from the diffusion of the minority carriers (holes) generated in the neutral channel region within their diffusion length to the edge of the depletion region which are then drifted by the electric field towards the junction and collected at the contacts. The photovoltage reduces the depletion

width, hence, the drift photocurrent is also slightly reduced. The diffusion photocurrent decreases for both low and high values of the depletion width and there exists an optimum depletion width at which the diffusion photocurrent is maximum. The drift phenomenon is much faster than the diffusion phenomenon in terms of the response time since the drift occurs in the presence of electric field. Both these processes depend upon the modulation frequency owing to the influence of the photovoltage, in turn, the depletion width on these processes. The drift photocurrent initially is constant for the lower frequencies and increases at the higher frequencies due to the increase in the depletion width owing to the lower photovoltage developed at the higher frequencies. However, the variation of the diffusion photocurrent with the frequency is determined by whether the increase in the depletion width with frequency ranges below or above the optimum depletion width at which the diffusion photocurrent is maximum. Another contribution to the frequency variation of this current emanates from the modulation of the hole lifetime with the frequency. The net combined effect of the two contributions will define the overall frequency variation of the photocurrent. In the reverse bias mode i.e. with a suitably large negative voltage applied across the gate and the source terminals, the depletion area for photogeneration is significantly increased resulting in considerable drift current while the diffusion current depends upon the criteria described earlier. In this mode, the drift of carriers due to the built-in electric field in the depletion region is assisted by the field generated owing to the applied reverse bias, thus, enabling faster operation. The photovoltage has no effect on the thermionic emission current since the device is operating at its reverse saturation current density. However, it can affect the drift and the diffusion currents depending upon the negative voltage applied through a reduction in the depletion width. Since the device is operating in the reverse bias mode (photoconductive mode) where the contributions are from the drift and the diffusion photocurrents only, the currents involved are much lower than that in the forward bias mode, and hence, the responsivities that can be attained

are lower. The dark current is low but comparatively higher than that in the zero bias mode. When the photon energy is less than the bandgap, but greater than the Schottky barrier height, the device functions by internal photoemission of metal electrons into the semiconductor.

The OPFET device working and physics is illustrated in the energy band diagrams presented below:

The following parameters are defined:

E_C=Conduction band; E_i=Intrinsic Fermi Level; E_{Fm}=Metal Fermi Level; E_V=Valence band; E_F=Fermi Level; V_{bi1}=Channel-substrate Built-in potential

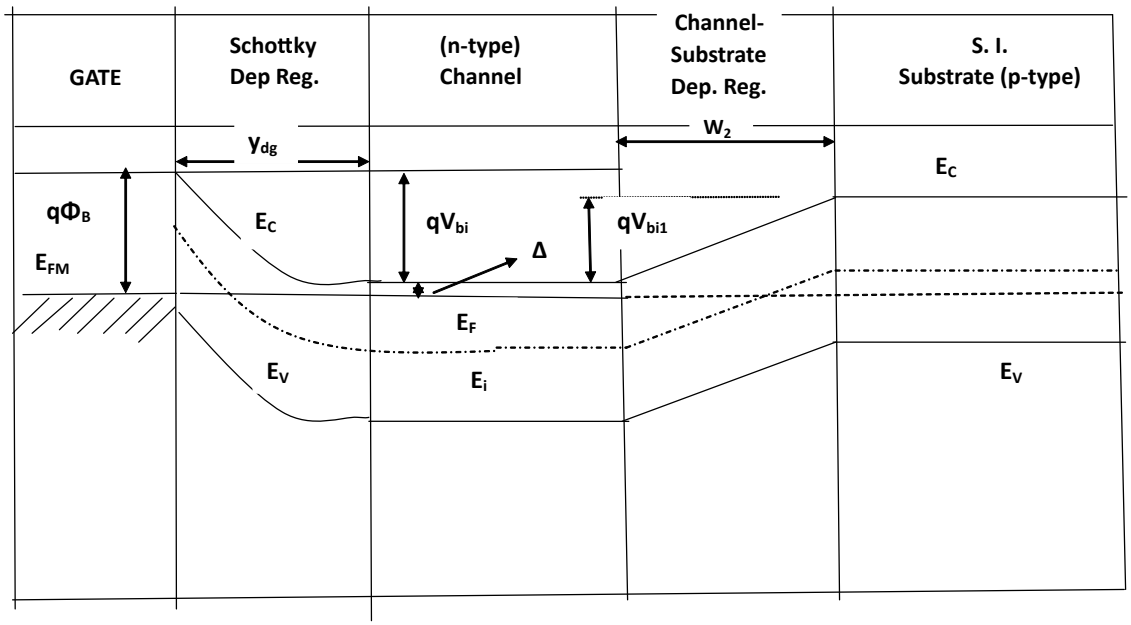

Figure 3.3: Energy-band diagram of OPFET under dark and without bias

The energy band diagrams presented show the interaction between the various regions of the OPFET device under dark and illumination with and without bias. The two basic building blocks within the OPFET device are the metal-semiconductor contact i.e. the gate-channel junction and the p-n junction at the interface of channel and substrate. Under dark and no bias conditions, the metal gate upon forming intimate contact with the n-type semiconductor channel, the energy bands modify themselves to adapt the changes occurring due to transfer of charges thus, attaining equilibrium. The gate-semiconductor contact is a rectifying contact i.e. it allows the current to flow in one direction and blocks

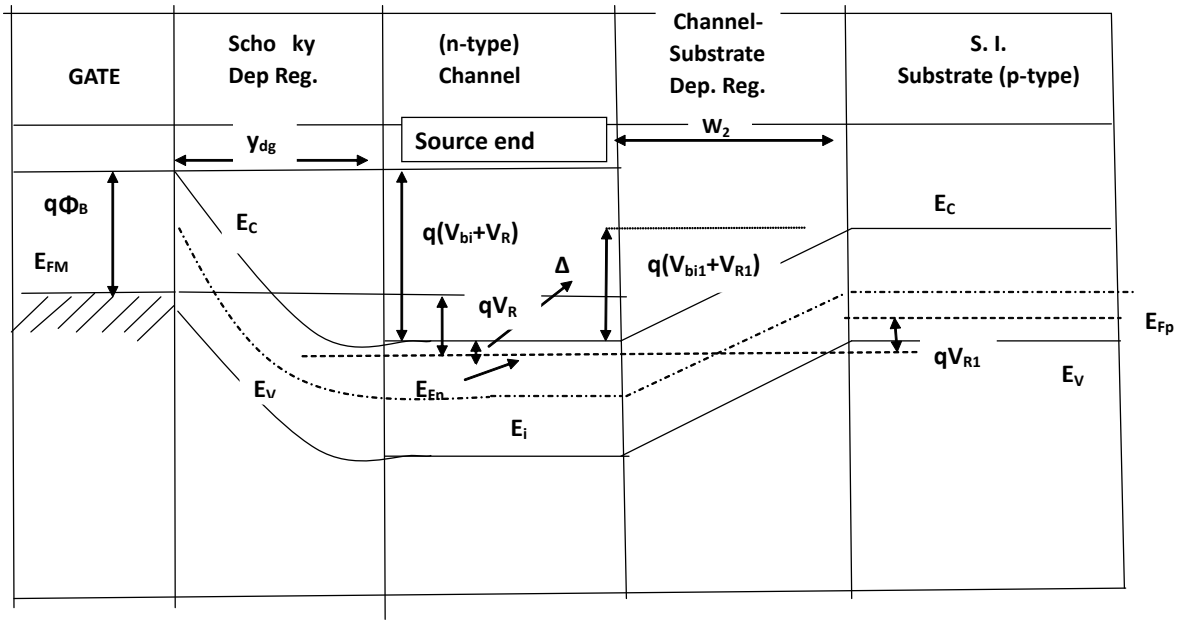

Figure 3.4: Energy-band diagram of OPFET under dark and with bias (at source end)

$$V_R(Reverse) = v_{gs} + I_{dss} \times R_s$$

$$V_{R1}(Reverse) = -v_{bs} + I_{dss} \times R_s$$

E_{Fn} and E_{Fp}=Quasi Fermi Levels for channel and substrate respectively
v_{bs}=Substrate bias

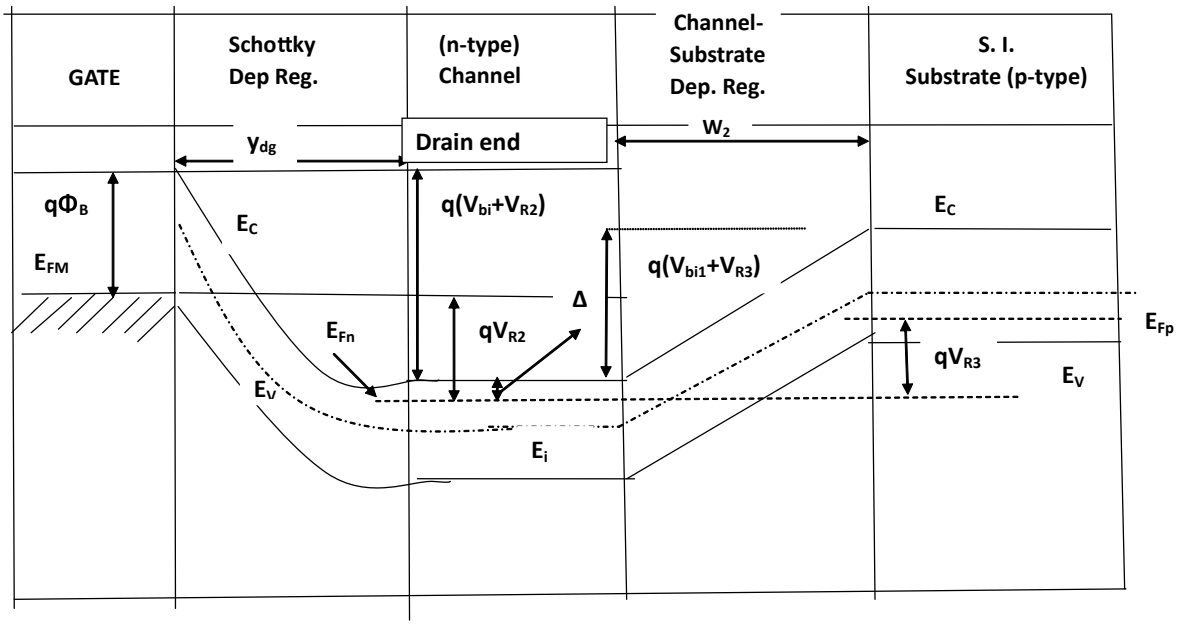

Figure 3.5: Energy-band diagram of OPFET under dark and with bias (at drain end)

$$V_{R2}(Reverse) = v_{gs} + V_{DS} + I_{dss} \times R_s$$

$$V_{R3}(Reverse) = -v_{bs} + V_{DS} + I_{dss} \times R_s$$

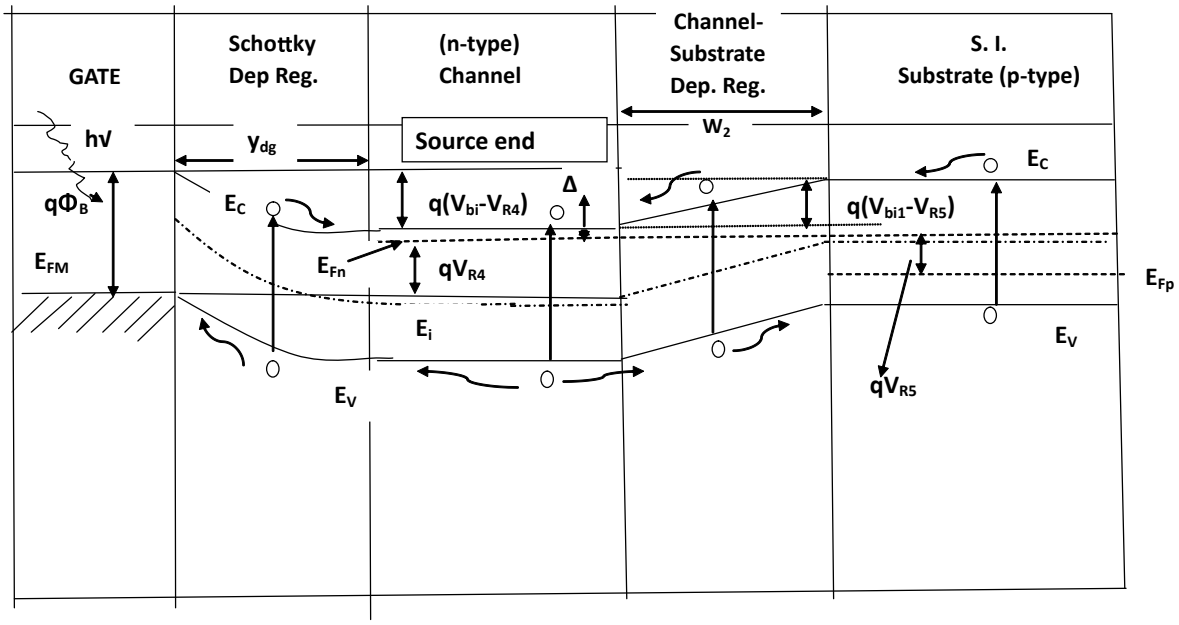

Figure 3.6: Energy-band diagram of OPFET under illumination and with bias (at source end)

$$V_{R4}(Forward) = -v_{gs} + V_{OP1} - I_{dss} \times R_s$$

$$V_{R5}(Forward) = v_{bs} + V_{OP2} - I_{dss} \times R_s$$

V_{OP2}=Photovoltage generated across the channel-substrate junction

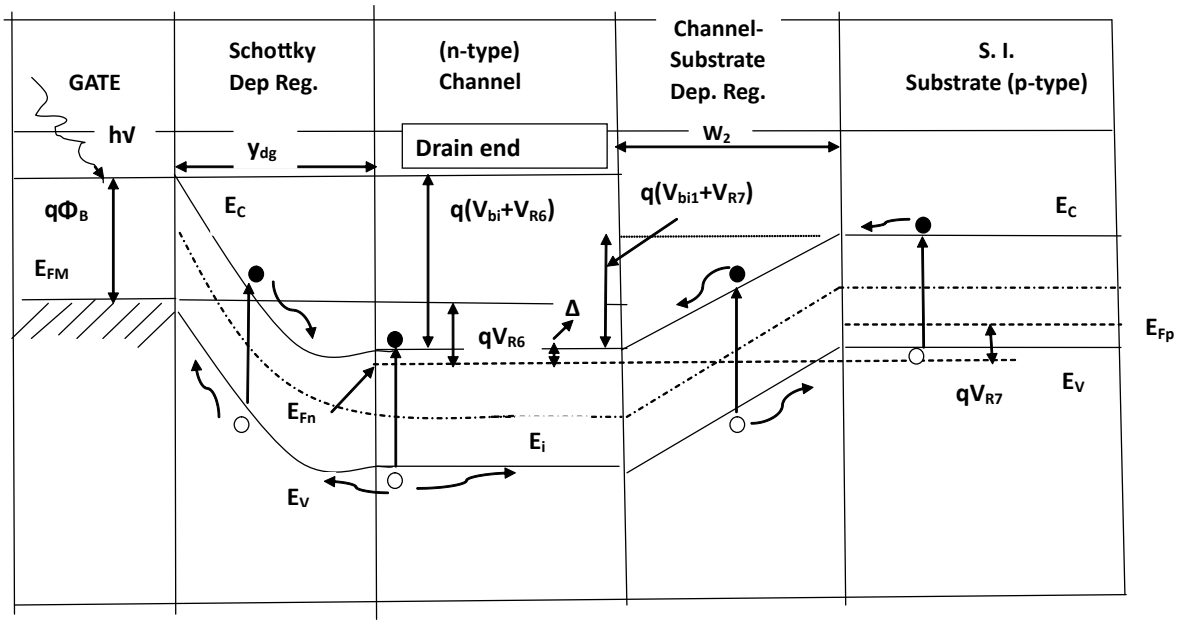

Figure 3.7: Energy-band diagram of OPFET under illumination and with bias (at drain end)

$$V_{R6}(Reverse) = v_{gs} + V_{DS} - V_{OP1} + I_{dss} \times R_s$$

$$V_{R7}(Reverse) = -v_{bs} + V_{DS} - V_{OP2} + I_{dss} \times R_s$$

the current in the reverse direction. For rectifying contacts, the work function of metal is greater than that of the semiconductor which means that the semiconductor Fermi level is at a higher position than that of the metal. To bring the system in equilibrium, the electrons from the highest occupied states in the conduction band of the semiconductor move into the metal till the semiconductor Fermi level is aligned with that of the metal. The movement of electrons from semiconductor to metal leaves behind positive ionized donor charges near the metal-semiconductor contact extending into the semiconductor forming a region devoid of mobile carriers called as the depletion region. This transfer of electrons creates at the interface on the semiconductor side a layer of positive charges whereas a layer of negative charges is formed on the metal side. An electric field is established pointing from semiconductor to metal and correspondingly a potential barrier opposing this electric field to prevent further transfer of electrons. This potential barrier is called as the built-in voltage or contact potential. Since the separation between the conduction band edge and the Fermi level increases with decreasing electron concentration and in thermal equilibrium Fermi level remains constant throughout, the conduction band edge bends up. The existence of varying potential from the edge of the depletion region up to the contact establishes a non-zero electric field within this region and linearly increasing from the edge up to the contact which creates the band bending. In other words, the band bending represents a potential barrier i.e. the contact potential which the electrons from the semiconductor have to overcome to move into the metal. On the other hand, the electrons from the metal see a barrier Φ_B to move into the semiconductor called as the Schottky barrier height. This parameter is given by the difference between the metal work function and the electron affinity of the semiconductor. The equilibrium is established when the diffusion of electrons from the semiconductor to metal is exactly balanced by the drift of electrons generated by the electric field representing the separation of charges at the interface of gate and semiconductor. The greater the doping density of the channel

the smaller is the depletion width.

Similarly, when the n-type channel is in intimate contact with the semi-insulating p-type substrate, transfer of carriers occurs to bring the system in equilibrium. The majority carrier electrons from channel diffuse into the substrate whereas the majority carrier holes from the substrate diffuse into the channel where they recombine with oppositely charged carriers. This movement causes a region of positively charged ions near the junction extending into the channel and a region of negatively charged ions on the substrate side. This region which is devoid of mobile carriers is called as the depletion region. An electric field is established from the channel to substrate preventing further diffusion of carriers. The movement of carriers occurs until the diffusion of carriers is exactly balanced by the drift of carriers driven by the electric field separating the charges and the Fermi levels of both the sides are aligned. This alignment of the Fermi levels causes the conduction and valence bands in the depletion region to band upwards from the channel to substrate. A built-in potential or a potential barrier is developed across the junction which opposes the electric field separating the charges. Since the channel is moderately doped and the substrate is of high resistivity, the built-in potential across the channel-substrate junction is lesser being directly proportional to the doping densities of both the sides. However, the semi-insulating substrate creates wider depletion region on the substrate side and shorter depletion region on the channel side.

The above description represents the state in equilibrium with no applied bias and under dark condition. In realistic device such as OPFET, with the applied bias, the equilibrium is disturbed which creates the longitudinal drain-to-source current to flow through the control of the depletion width in the lateral direction by using gate and substrate bias. The OPFET is either operated in zero gate bias mode or small to moderate reverse gate bias mode to facilitate separation and col-

lection of photocarriers generated within the depletion regions thus, contributing to photocurrent. With applied drain-to-source bias across the device, the channel voltage almost linearly varies from 0 at the source end to V_{DS} at the drain end. Thus, there is a gradual increase in the depletion widths from the source end until the drain end. This drain bias or channel voltage acts as a reverse bias across the gate-channel junction as well as the channel-substrate junction over and above the reverse gate bias and voltage drop across the series resistance in the case of gate junction and voltage drop across the series resistance in the case of channel-substrate junction. This net reverse biases acting across the junctions tend to widen the band bending, increase the potential barrier and widen the depletion widths. Thus, the dark current is significantly suppressed. With the reverse voltage acting across the gate junction, some more electrons from the neutral channel region are pushed deeper into the semiconductor thus, increasing the amount of positive donor ions and widening the space charge region. Thus, the potential barrier seen by the electron in the channel is the built-in voltage plus the reverse bias applied whereas the metal electron sees the same barrier as earlier (Φ_B). It is only the energy bands which are shifted in response to the disturbance in equilibrium whereas the relative position of the Fermi level with respect to the conduction band in the neutral region remains the same decided by the doping density of the n-type semiconductor. In the case of channel-substrate junction, when the bias is applied, the Fermi level in case of zero bias condition splits into two quasi-Fermi levels: one for the n-type semiconductor and one for the p-type substrate. The quasi-Fermi level for the channel is lowered with respect to that for the substrate by an amount equal to the reverse voltage applied. More of electrons from the n-side are pushed deeper into the channel whereas holes from p-side are attracted deeper into the substrate thus, widening the depletion region and reducing the diffusion current flow from substrate to channel.

The equilibrium is also disturbed when the device is illuminated with pho-

ton energy greater than the bandgap of the semiconductor. The case we have considered is a simple front-illuminated OPFET where the light enters the device through the transparent gate contact. With photon energy greater than the bandgap, electron-hole pairs are generated in the depletion regions as well as the neutral regions of the OPFET device. Since electric field is present in both the depletion regions, this field separates the electron hole pairs generated within these regions. The holes move towards the junctions whereas the electrons move towards the channel. The crossing of holes across the junctions creates a forward leakage photocurrent which can be modelled as a forward photovoltage superimposed over the applied gate and substrate voltages. The separation and collection of carriers also contribute a reverse drift current and a reverse diffusion current (arising from diffusion of minority carriers from channel/substrate to the edge of the depletion regions which are eventually drifted across the junctions). These reverse drift/diffusion currents tend to reduce the forward current, however, their magnitude is comparatively lower in most of the cases and hence the forward current remains unaffected. The generation of the photovoltages across the junctions tend to reduce the potential drop across the depletion regions thus, the electrons and holes in the channel and substrate respectively see a lower barrier as well as reduced bending of the energy bands. Hence, these changes result in diffusion of electrons from the channel to the metal side to make up for the reduced barrier. The same diffusion of carriers occurs across the channel-substrate junction. The depletion widths are greatly reduced as compared to their dark values, thus, the drain-to-source current is enhanced when a positive drain-to-source bias is applied. The photovoltage developed across the gate junction is amplified by the OPFET through the transconductance of the device. The above phenomena can be collectively called as photovoltaic effects. The photovoltaic effects are characterized by shifting of the energy bands.

One more effect which contributes to photocurrent is the photoconductive ef-

fect. Here, after the generation of free electron-hole pairs in the various regions, the majority carrier photogenerated electrons increase the conductivity of the device by shifting the Fermi level closer to the conduction band. Thus, when a positive drain-to-source voltage is applied across the device these carriers are drifted across the drain and source terminals generating a photoconductive current.

3.4 Modeling of OPFET

For surface-gated OPFETs, the space charge region extension in the channel measured from the surface is written as,

$$y_{dg} = \left[\frac{2\epsilon}{qN_{dr}}(\phi_B - \Delta + v(x) - v_{gs} - V_{OP1})\right]^{\frac{1}{2}} \tag{3.1}$$

where N_{dr} is the doping concentration, Φ_B is the Schottky barrier height, Δ is the position of Fermi level below the conduction band, ϵ is the permittivity of semiconductor, V_{OP1} is the photovoltage generated across the Schottky junction and v(x) is the channel voltage which varies from 0 at the source end to V_{DS} at the drain end. V_{DS} is the drain to source voltage and v_{gs} is the gate to source voltage.

For buried-gate OPFETs, y_{dg} is written as:

$$y_{dg} = t_{sm} - \left[\frac{2\epsilon}{qN_{dr}}(\phi_B - \Delta + v(x) - v_{gs} - V_{OP1})\right]^{\frac{1}{2}} \tag{3.2}$$

where t_{sm} is the effective active layer thickness.

3.4.1 Photovoltage calculation in the front-illuminated, buried-gate front-illuminated, generalized, and opaque-gate OPFET models

In the gate depletion region, the hole continuity equation is written as:

$$\frac{\partial p}{\partial y} + \frac{p}{v_y \tau_p} - \frac{\alpha \phi e^{-\alpha y}}{v_y} = 0 \tag{3.3}$$

where p is the hole density, v_y is the carrier saturated velocity, α is the absorption coefficient, Φ is the photon flux density, $\tau_{\omega p}$ is the hole lifetime under ac condition, and y is the distance from surface towards the substrate.

Its analytical solution is given as:

$$p(y) = A_1 + \alpha\phi\tau_{\omega p}B_1\left[1 - \frac{1}{(1-\alpha v_y\tau_{\omega p})}\right]e^{-\frac{y}{v_y\tau_{\omega p}}} \tag{3.4}$$

where

$$A_1 = \frac{\alpha\phi\tau_{\omega p}}{(1-\alpha v_y\tau_{\omega p})}e^{-\alpha y} \tag{3.5}$$

$$B_1 = e^{-(\alpha-\frac{1}{v_y\tau_{\omega p}})y_{dg}} \tag{3.6}$$

using the boundary condition at $y = y_{dg}$,

$$p = \alpha\Phi\tau_{\omega p}e^{-\alpha y_{dg}} \tag{3.7}$$

Then the photovoltage is calculated as:

$$V_{OP1} = \frac{kT}{q}ln\left[1 + \frac{qv_y p(0)}{J_{s1}}\right] \tag{3.8}$$

for front-illuminated OPFET.

$$V_{OP1} = \frac{kT}{q}ln\left[1 + \frac{qv_y p(t_{sm})}{J_{s1}}\right] \tag{3.9}$$

for buried-gate front-illuminated OPFET.

$$V_{OP1} = \frac{kT}{q}ln\left[1 + \frac{qv_y Z(\pi/4(r_1^2+r_2^2)p(0) + Lt_{sm}p(0))}{ZLt_{sm}J_{s1}}\right] \tag{3.10}$$

for the generalized model of OPFET.

$$V_{OP1} = \frac{kT}{q}ln\left[1 + \frac{qv_y Z(\pi/4(r_1^2+r_2^2)p(0))}{ZLt_{sm}J_{s1}}\right] \tag{3.11}$$

for opaque-gate OPFET,

where $p(0)$ is the hole density computed at $y = 0$, $p(t_{sm})$ is the hole density computed at $y = t_{sm}$, J_{s1} is the reverse saturation current density across the Schottky junction, q is the electronic charge, k is the Boltzmann constant and T

is the temperature. Z is the gate width and L is the gate length. r_1 and r_2 are the depletion region widths at the source and drain sides of the gate respectively, given by:

$$r_1 = y_{dg}(v(x) = 0) \tag{3.12}$$

and

$$r_2 = y_{dg}(v(x) = V_{ds}) \tag{3.13}$$

3.4.2 Photovoltage calculation in the surface-gate and buried-gate back-illuminated OPFET models

The hole continuity equation for back-illumination in the depletion region is represented as follows:

$$\frac{\partial p}{\partial y} + \frac{p}{v_y \tau_p} - \frac{\alpha \phi e^{-\alpha(t_{sm}-y)}}{v_y} = 0 \tag{3.14}$$

Its analytical solution can be expressed as:

$$p(y) = \frac{\alpha \phi \tau_{\omega p}}{(1 + \alpha v_y \tau_{\omega p})} e^{-\alpha(t_{sm}-y)} \tag{3.15}$$

where the constant arising while solving the continuity equation is assumed zero from physical condition. Then, the photovoltage is calculated as:

$$V_{OP1} = \frac{kT}{q} ln \left[1 + \frac{q v_y p(0)}{J_{s1}}\right] \tag{3.16}$$

for surface gate back-illuminated OPFET.

$$V_{OP1} = \frac{kT}{q} ln \left[1 + \frac{q v_y p(t_{sm})}{J_{s1}}\right] \tag{3.17}$$

for buried-gate back-illuminated OPFET. For surface-gate back-illuminated OPFET (with substrate effect), t_{sm} in Eq.3.14 and 3.15 should be replaced by d, the effective surface-to-substrate thickness.

3.4.3 Photogenerated electron density calculation in the neutral channel region for front-illuminated, buried-gate front-illuminated, generalized, and opaque-gate OPFET models

The electron continuity equation in the channel region is expressed as

$$\frac{\partial^2 n}{\partial y^2} - \frac{n}{D_n \tau_{\omega n}} + \frac{\alpha \Phi e^{-\alpha y}}{D_n} = 0 \tag{3.18}$$

Here n is the electron density, D_n is the diffusion constant of electrons, $\tau_{\omega n}$ is the lifetime of electrons under ac condition. The solution of Eq.3.18 is given by:

$$n(y) = \alpha \Phi \tau_{\omega n} A_2 e^{-\frac{y}{L_{n\omega}}} - B_2 \tag{3.19}$$

where

$$A_2 = \left[1 + \frac{1}{(\alpha^2 L_{n\omega}^2 - 1)}\right] \tag{3.20}$$

and

$$B_2 = \frac{\alpha \Phi \tau_{\omega n}}{(\alpha^2 L_{n\omega}^2 - 1)} e^{-\alpha y} \tag{3.21}$$

$L_{n\omega}$ is the ac diffusion length of electrons:

$$L_{n\omega} = (D_n \tau_{\omega n})^{1/2} \tag{3.22}$$

The boundary condition used is at $y = 0$,

$$n = \alpha \Phi \tau_{\omega n} \tag{3.23}$$

3.4.4 Photogenerated electron density calculation in the neutral channel region for surface-gate and buried-gate back-illuminated OPFET models

The continuity equation in the neutral channel region is given by:

$$\frac{\partial^2 n}{\partial y^2} - \frac{n}{D_n \tau_{\omega n}} + \frac{\alpha \Phi e^{-\alpha (t_{sm} - y)}}{D_n} = 0 \tag{3.24}$$

Its solution is obtained as:

$$n(y) = \alpha\Phi\tau_{\omega n}A_2 e^{-\alpha(t_{sm}-y_{dg})}e^{-\frac{(y_{dg}-y)}{L_{n\omega}}} - B_3 \tag{3.25}$$

where A_2 is given by Eq.3.20 and B_3 is stated as:

$$B_3 = \frac{\alpha\Phi\tau_{\omega n}}{(\alpha^2 L_{n\omega}^2 - 1)}e^{-\alpha(t_{sm}-y)} \tag{3.26}$$

The boundary condition used is at $y = y_{dg}$,

$$n = \alpha\Phi\tau_{\omega n}e^{-\alpha(t_{sm}-y_{dg})} \tag{3.27}$$

For surface-gate back-illuminated OPFET (with substrate effect), t_{sm} in Eq.3.24 and 3.25 should be replaced by d, the effective surface-to-substrate thickness.

3.4.5 Photogenerated electron density calculation in the depletion region for the front-illuminated, buried-gate front-illuminated, generalized, and opaque-gate OPFET models

The electron continuity equation in the depletion region is represented as:

$$\frac{\partial n}{\partial y} - \frac{n}{v_y\tau_{\omega n}} + \frac{\alpha\Phi e^{-\alpha y}}{v_y} = 0 \tag{3.28}$$

The solution of the above equation is given by:

$$n(y) = \frac{\alpha\Phi\tau_{\omega n}e^{-\alpha y}}{(1 + \alpha v_y\tau_{\omega n})} \tag{3.29}$$

3.4.6 Photogenerated electron density calculation in the depletion region for the surface-gate and buried-gate back-illuminated OPFET models

The electron continuity equation is expressed as:

$$\frac{\partial n}{\partial y} - \frac{n}{v_y\tau_{\omega n}} + \frac{\alpha\Phi e^{-\alpha(t_{sm}-y)}}{v_y} = 0 \tag{3.30}$$

The solution of the above equation is given by:

$$n(y) = \frac{\alpha\Phi\tau_{\omega n}e^{-\alpha(t_{sm}-y)}}{(1 - \alpha v_y\tau_{\omega n})} \tag{3.31}$$

3.4.7 Drain to source current calculation

In general, the total conducting charge is expressed as,

$$Q_n = Q_d + Q_{ch} + Q_{dep1} + Q_{dep2} \tag{3.32}$$

Here Q_d is the charge due to doping; Q_{ch}, Q_{dep1} and Q_{dep2} are the charges due to photogeneration in the channel, Schottky junction depletion region and the substrate depletion region respectively.

Then Q_n can be evaluated as:

$$Q_n = \int_{y_{dg}}^{t_{sm}} N_{dr} + \int_{y_{dg}}^{t_{sm}} n_{ch} + \int_{0}^{y_{dg}} n_{dep1} + \int_{t_{sm}}^{d} n_{dep2} \tag{3.33}$$

where n_{ch}, n_{dep1} and n_{dep2} are the photogenerated electron densities in the channel, Schottky junction depletion region and substrate depletion region respectively. The charge equation 3.33 is applicable to the front-illuminated, back-illuminated (with substrate effect), and generalized OPFET models.

For buried-gate models, the charge is calculated as:

$$Q_n = \int_{0}^{y_{dg}} N_{dr} + \int_{0}^{y_{dg}} n_{ch} + \int_{y_{dg}}^{t_{sm}} n_{dep1} \tag{3.34}$$

For surface-gate back-illuminated model (without substrate effect), the charge is given as:

$$Q_n = \int_{y_{dg}}^{t_{sm}} N_{dr} + \int_{y_{dg}}^{t_{sm}} n_{ch} + \int_{0}^{y_{dg}} n_{dep1} \tag{3.35}$$

The charge in the case of opaque-gate OPFET is computed as:

$$Q_n = \int_{y_{dg}}^{t_{sm}} N_{dr} + \int_{y_{dg}}^{t_{sm}} n_{ch} + \int_{t_{sm}}^{d} n_{dep2} \tag{3.36}$$

All the integrations concerned with the computation of charge are performed numerically using the Trapezoidal method. The total drain to source current is then calculated using the model described in [30]:

$$I_{ds} = I_{dss} tanh(\eta V_{DS}) + \frac{V_{DS}}{R_{sh}} \tag{3.37}$$

The drain to source saturation current is calculated as:

$$I_{dss} = qv_y ZQ_n(0) \tag{3.38}$$

where $Q_n(0)$ is the total conducting charge at the source end in the presence of series resistances. η is the parameter giving the ratio of the drain-to-source conductance evaluated at $V_{DS} = 0$ to the drain to source saturation current. The drain to source conductance can be estimated as

$$G_{CH} = \frac{G_{ch}}{1 + (R_s + R_d)G_{ch}} \tag{3.39}$$

where G_{ch} is the channel conductance evaluated at $V_{DS} = 0$ and is given by

$$G_{ch} = \frac{q\mu Z}{L} Q_n(0) \tag{3.40}$$

$Q_n(0)$ is again the total conducting charge at the source end, however, in the absence of series resistances. R_s and R_d are the series source and drain resistances and R_{sh} is the drain to source shunt resistance.

The parasitic series source and drain resistances involved in the calculation are obtained following a similar procedure as given in [31]. In the case of the generalized and opaque-gate model of the OPFET, the additional components of the current due to the contributions from the sidewalls of the gate depletion region are given as follows: At the source end,

$$I_{dep1s} = \frac{qZ\pi\mu V_{DS}\Phi\tau_{\omega n}(1 - e^{-\alpha r_1})}{4L(1 + \alpha v_y \tau_{\omega n})} \tag{3.41}$$

At the drain end,

$$I_{dep1d} = \frac{qZ\pi v_y \Phi\tau_{\omega n}(1 - e^{-\alpha r_2})}{4(1 + \alpha v_y \tau_{\omega n})} \tag{3.42}$$

3.4.8 Calculation of gate depletion region and sidewall space charge

The net space charge in the gate depletion region can be obtained as:

$$Q_{depsc} = qZ \int_0^L dx \int_0^{y_{dg}} (N_{dr} - n_{dep1}(y))dy \tag{3.43}$$

which is the difference between the doping-induced space charge and the photogenerated electron density in the depletion region since the photogenerated electrons deionize the space charge ions. The above equation is applicable for all the models except opaque-gate model since in this model, there is no generation below the gate.

Similarly, the net space charge in the sidewalls of the gate depletion region is estimated as:

$$\begin{aligned} Q_{sidsc} = &\frac{\pi}{2}\epsilon Z(\Phi_B - \Delta - v_{gs} - V_{OP1}) + \frac{\pi}{2}\epsilon Z(\Phi_B - \Delta - v_{gd} - V_{OP1}) \\ &- qZ\frac{\pi}{4}\Phi\tau_{\omega n}\frac{(1-e^{-\alpha r_1})r_1}{(1+\alpha v_y\tau_{\omega n})} - qZ\frac{\pi}{4}\Phi\tau_{\omega n}\frac{(1-e^{-\alpha r_2})r_2}{(1+\alpha v_y\tau_{\omega n})} \end{aligned} \tag{3.44}$$

where v_{gd} is the gate to drain voltage. In Eq.3.44, the third and fourth terms are applicable only to the generalized and opaque-gate OPFET models since it is only in these models that the photogeneration in the sidewalls takes place. Thus, the total net space charge is:

$$Q_{deptsc} = Q_{depsc} + Q_{sidsc} \tag{3.45}$$

3.5 Modeling of Schottky junction in OPFET

3.5.1 Calculation of Thermionic emission current

The prevailing mechanism of carrier transport across the Schottky junction for moderately-doped semiconductors is Thermionic emission. The equation of Thermionic emission for Schottky junction in OPFET with zero drain bias under illumination is given by:

$$J_{TE} = J_{s1}\left[e^{\left(\frac{q(v_{gs}+V_{OP1}-IR_s)}{kT}\right)} - 1\right] \tag{3.46}$$

where J_{s1} is the reverse saturation current density:

$$J_{s1} = A^*T^2e^{\left[-\frac{q\Phi_B^0+q\Delta\Phi_B(V)}{kT}\right]} \tag{3.47}$$

I is the current through the Schottky junction, A^* is the Richardson constant, $\Delta\Phi_B(V)$ is the voltage-dependent modulation of the Schottky barrier height,

applicable only in the case of graphene metal gate given as:

$$q\Delta\Phi_B(V) = -\frac{1}{2}\frac{h}{2\pi}V_F\sqrt{\frac{\pi\epsilon N_{dr}(V_{bi}+V)}{2qn_0}} \tag{3.48}$$

where h is the Planck's constant, V_F is the Fermi velocity in graphene, V_{bi} is the built-in potential at the Schottky junction ($V_{bi} = \Phi_B - \Delta$), $V = -v_{gs} - V_{OP1} + IR_s$, and n_0 is the graphene extrinsic residual doping density.

3.5.2 Calculation of drift current

In this thesis, we have modeled the Schottky junction in OPFET for the front-illuminated, buried-gate front-illuminated, generalized, and the back-illuminated (without substrate effect) OPFET models.

For the front-illuminated and the generalized models, the drift current is given by:

$$J_{drift} = -q\int_0^{y_{dg}} \alpha\Phi e^{-\alpha y}dy \tag{3.49}$$

Eq.3.49 can be evaluated as:

$$J_{drift} = -q\Phi(1 - e^{-\alpha y_{dg}}) \tag{3.50}$$

For the buried-gate front-illuminated model, the drift current is written by:

$$J_{drift} = -q\int_{y_{dg}}^{t_{sm}} \alpha\Phi e^{-\alpha y}dy \tag{3.51}$$

Eq.3.51 can be computed as:

$$J_{drift} = -q\Phi(e^{-\alpha y_{dg}} - e^{-\alpha t_{sm}}) \tag{3.52}$$

For the surface-gate back-illuminated model, the drift current is stated by:

$$J_{drift} = -q\int_0^{y_{dg}} \alpha\Phi e^{-\alpha(t_{sm}-y)}dy \tag{3.53}$$

Eq.3.53 can be calculated as:

$$J_{drift} = -q\Phi(e^{-\alpha(t_{sm}-y_{dg})} - e^{-\alpha t_{sm}}) \tag{3.54}$$

3.5.3 Calculation of diffusion current

For front-illuminated, generalized, and the buried-gate front-illuminated OPFETs, the diffusion current density is obtained by solving the second order continuity equation for minority carriers density (holes) given by:

$$D_p \frac{\partial^2 p}{\partial y^2} - \frac{p - p_0}{\tau_{\omega p}} + \alpha \Phi e^{-\alpha y} = 0 \tag{3.55}$$

where D_p is the diffusion constant for holes. Eq.3.55 is solved using the boundary conditions: $p = 0$ at $y = y_{dg}$ and $p = p_0$ at $y = \infty$ where p_0 is the equilibrium hole density and the solution is expressed as:

$$\begin{aligned} p = &- \frac{\alpha \Phi \tau_{\omega p} e^{-\alpha y}}{(\alpha^2 L_{p\omega}^2 - 1)} + p_0 \\ &- p_0 e^{\left(\frac{y_{dg} - y}{L_{p\omega}}\right)} + \frac{\alpha \Phi \tau_{\omega p} e^{-\alpha y_{dg}} e^{\left(\frac{y_{dg} - y}{L_{p\omega}}\right)}}{(\alpha^2 L_{p\omega}^2 - 1)} \end{aligned} \tag{3.56}$$

Then, the diffusion current density is obtained as:

$$J_{diff} = -qD_p \left(\frac{\partial p}{\partial y}\right)_{y = y_{dg}} \tag{3.57}$$

It can be evaluated as:

$$J_{diff} = -\left[\frac{q\alpha \Phi L_{p\omega}}{(1 + \alpha L_{p\omega})} e^{-\alpha y_{dg}} + qp_0 \frac{D_p}{L_{p\omega}}\right] \tag{3.58}$$

where $L_{p\omega}$ is the ac diffusion length of holes:

$$L_{p\omega} = (D_p \tau_{\omega p})^{1/2} \tag{3.59}$$

For back-illuminated OPFET, the corresponding continuity equation, hole density, and diffusion current density are expressed respectively as follows:

$$D_p \frac{\partial^2 p}{\partial y^2} - \frac{p - p_0}{\tau_{\omega p}} + \alpha \Phi e^{-\alpha (t_{sm} - y)} = 0 \tag{3.60}$$

$$\begin{aligned} p = &- \frac{\alpha \Phi \tau_{\omega p} e^{-\alpha (t_{sm} - y)}}{(\alpha^2 L_{p\omega}^2 - 1)} + p_0 \\ &- p_0 e^{\left(\frac{y - y_{dg}}{L_{p\omega}}\right)} + \frac{\alpha \Phi \tau_{\omega p} e^{-\alpha (t_{sm} - y_{dg})} e^{\left(\frac{y - y_{dg}}{L_{p\omega}}\right)}}{(\alpha^2 L_{p\omega}^2 - 1)} \end{aligned} \tag{3.61}$$

$$J_{diff} = \left[\frac{q\alpha \Phi L_{p\omega}}{(1 + \alpha L_{p\omega})} e^{-\alpha (t_{sm} - y_{dg})} + qp_0 \frac{D_p}{L_{p\omega}}\right] \tag{3.62}$$

3.5.4 Current due to internal photoemission

Internal photoemissions occur for photon energies between the bandgap energy of the semiconductor and the barrier height of the Schottky junction. In this thesis, the photon energy is considered to be greater than the bandgap, hence no internal photoemission will take place.

3.5.5 Calculation of total current density

The total current density across the illuminated Schottky junction is the sum of the Thermionic emission, drift and diffusion current densities:

$$J_T = J_{TE} + J_{drift} + J_{diff} \tag{3.63}$$

3.6 Scaling rules

The scaling rules for the MESFET device as stated in [154] are reproduced here:

3.6.1 Constant gate length-doping concentration product

$$LN_{dr} = 1.6 \times 10^{17} \tag{3.64}$$

3.6.2 Maximum effective active layer thickness

$$t_{sm(max)} = \frac{L}{\pi} \tag{3.65}$$

3.6.3 Minimum effective active layer thickness

$$t_{sm(min)} = d_0 + 6L_D \tag{3.66}$$

where

$$d_0 = \left| \frac{2\epsilon V_{bi}}{qN_{dr}} \right|^{0.5} \tag{3.67}$$

is the zero-bias gate-depletion width and

$$L_D = \left| \frac{\epsilon kT}{q^2 N_{dr}} \right|^{0.5} \tag{3.68}$$

is the Debye length for the channel material.

3.6.4 Maximum breakdown voltage

$$V_{br} = \frac{4.4 \times 10^{17} (V/m^2)}{N_{dr} t_{sm}} \tag{3.69}$$

3.7 Y-parameters and S-parameters modeling

From the equivalent circuit, the Y-parameters of the intrinsic device have been obtained [36]:

$$Y_{11} = j\omega C_{gd} + \frac{j\omega C_{gs}}{(1 + j\omega C_{gs} R_i)} \tag{3.70}$$

$$Y_{12} = -j\omega C_{gd} \tag{3.71}$$

$$Y_{21} = \frac{g_m e^{-j\omega\tau}}{(1 + j\omega C_{gs} R_i)} - j\omega C_{gd} \tag{3.72}$$

$$Y_{22} = j\omega(C_{gd} + C_{ds}) + 1/R_{ds} \tag{3.73}$$

The intrinsic Y-parameters are converted to intrinsic ABCD-parameters [155]:

$$A = -\frac{Y_{22}}{Y_{21}} \tag{3.74}$$

$$B = -\frac{1}{Y_{21}} \tag{3.75}$$

$$C = -\frac{Y_{12}Y_{21} - Y_{11}Y_{22}}{Y_{21}} \tag{3.76}$$

$$D = -\frac{Y_{11}}{Y_{21}} \tag{3.77}$$

The intrinsic ABCD parameter matrix is multiplied by the ABCD representation of the gate and drain leads as given in [36]:

$$\begin{bmatrix} A & B \\ C & D \end{bmatrix}_{MESFET} = \begin{bmatrix} 1 & R_g + j\omega L_g \\ 0 & 1 \end{bmatrix}_{gate} \begin{bmatrix} A & B \\ C & D \end{bmatrix}_{Intrinsic} \begin{bmatrix} 1 & R_d + j\omega L_d \\ 0 & 1 \end{bmatrix}_{drain} \tag{3.78}$$

The resultant matrix is converted to Z parameters [155]:

$$Z_{11} = -\frac{A}{C} \tag{3.79}$$

$$Z_{12} = -\frac{AD - BC}{C} \tag{3.80}$$

$$Z_{21} = -\frac{1}{C} \tag{3.81}$$

$$Z_{22} = -\frac{D}{C} \tag{3.82}$$

The resulting matrix is added to the Z-matrix of the source to give the complete Z-parameters of the OPFET [36]:

$$\begin{bmatrix} Z_{11} & Z_{12} \\ Z_{21} & Z_{22} \end{bmatrix}_{complete} = \begin{bmatrix} Z_{11} & Z_{12} \\ Z_{21} & Z_{22} \end{bmatrix}_{MESFET} + \begin{bmatrix} R_s + j\omega L_s & R_s + j\omega L_s \\ R_s + j\omega L_s & R_s + j\omega L_s \end{bmatrix}_{source} \tag{3.83}$$

Finally, the Z-parameters are converted to complete S-parameters under suitable source/load impedances [155]:

$$S_{11} = \frac{(Z_{11} - Z_{01}^*)(Z_{22} + Z_{02}) - Z_{12}Z_{21}}{(Z_{11} + Z_{01})(Z_{22} + Z_{02}) - Z_{12}Z_{21}} \tag{3.84}$$

$$S_{12} = \frac{2Z_{12}(R_{01}R_{02})^{1/2}}{(Z_{11} + Z_{01})(Z_{22} + Z_{02}) - Z_{12}Z_{21}} \tag{3.85}$$

$$S_{21} = \frac{2Z_{21}(R_{01}R_{02})^{1/2}}{(Z_{11} + Z_{01})(Z_{22} + Z_{02}) - Z_{12}Z_{21}} \tag{3.86}$$

$$S_{22} = \frac{(Z_{11} + Z_{01})(Z_{22} - Z_{02}^*) - Z_{12}Z_{21}}{(Z_{11} + Z_{01})(Z_{22} + Z_{02}) - Z_{12}Z_{21}} \tag{3.87}$$

where Z_{01} is the source impedance and Z_{02} is the load impedance.

3.8 Design of Optically-controlled Amplifier and Oscillator using S parameters

3.8.1 Design of Amplifier

One important factor which is necessary but not sufficient for unconditional stability [156] is the Rollett's stability factor (K-factor). It should be greater than unity for all frequencies under consideration. It is given by:

$$K = \frac{1 - |S_{11}|^2 - |S_{22}|^2 + |\Delta|^2}{2|S_{12}||S_{21}|} \tag{3.88}$$

where

$$\Delta = S_{11}S_{22} - S_{12}S_{21} \tag{3.89}$$

This parameter should be less than 1 for all operating frequencies. One more additional criterion is that there should be no RHP poles in network terminated with defining impedances.

In case the K-factor is less than 1, then the device is conditionally stable at a particular set of load and source impedances. This can be ensured if the following conditions are satisfied [156]:

No RHP poles in network terminated with defining impedances,

$|S_{22}| < 1$ for all frequencies,

$|\Gamma_{in}| < 1$ for all frequencies,

where

$$\Gamma_{in} = S_{11} + \frac{S_{12}S_{21}\Gamma_L}{1 - S_{22}\Gamma_L} \tag{3.90}$$

is the input reflection coefficient, and

$$\Gamma_L = \frac{Z_{02} - Z_0}{Z_{02} + Z_0} \tag{3.91}$$

is the reflection coefficient of the load. Z_0 is the characteristic impedance of 50 ohms.

3.8.2 Design of Oscillator

One important factor which is necessary but not sufficient for oscillation is the Rollett's stability factor (K-factor). It should be less than unity [157]. The oscillation frequency and the combination of source/load impedances that will produce stable oscillation are determined by the S-parameter characterisation approach. In this approach, the device will produce stable oscillations if the following condition is satisfied [157]:

$$|\Gamma_G||\Gamma_{in}| = 1 \tag{3.92}$$

where

$$\Gamma_G = \frac{Z_{01} - Z_0}{Z_{01} + Z_0} \tag{3.93}$$

is the reflection coefficient of the source. If the condition given by Eq.3.92 is satisfied implies that its dual condition at the other port is also satisfied:

$$|\Gamma_L||\Gamma_{out}| = 1 \tag{3.94}$$

where

$$\Gamma_{out} = S_{22} + \frac{S_{12}S_{21}\Gamma_G}{1 - S_{11}\Gamma_G} \tag{3.95}$$

is the output reflection coefficient. The frequency at which the oscillations conditions are satisfied is the resonance or the oscillation frequency, and the source/load impedances are the resonance or tuned circuits.

3.9 Structure of Graphene OPFET

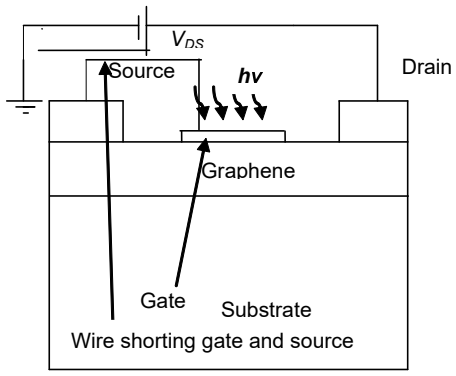

Figure 3.8: Structure of graphene OPFET

The schematic sketch of the transparent gate graphene OPFET (GOPFET) under optical front-illumination is depicted in Fig.3.8. Graphene is grown using either epitaxy [158], Chemical Vapour Deposition (CVD) [159], Reduced Graphene Oxide (RGO) method [160], or mechanical exfoliation [161]. The difference between graphene OPFET and the well known graphene FET (GFET) is the presence of a physical oxide/insulated layer between the gate and graphene acting as a capacitor in graphene FET, which is absent in graphene OPFET and is replaced by an electrical dipole capacitance with equilibrium separation distance of the order of Angstroms as opposed to the sub-micrometer thickness of the oxide layer. Thus, the graphene OPFET is a special case of the graphene FET [162]. The GFET fabrication process is as follows: a) transfer of graphene onto the Si/SiO_2 substrate, b) application of resist coating Poly(methyl methacrylate)(PMMA), c) Physical Vapour Deposition (PVD) of metal (e.g. Ti/Au) on the sample, d) Lift-off, e) Dielectric (Al_2O_3) deposition by Atomic Layer Deposition (ALD), f) application of resist coating (PMMA), g) Using PVD of metal-combination on

the sample, h) Lift-off. The GOPFET fabrication is similar to GFET production except there is no dielectric deposition on the graphene channel instead the PMMA resist coating is adjusted to enable metal gate contact directly onto the graphene.

3.10 Operation of GOPFET

Under Dark: The GOPFET functions analogous to conventional OPFET under dark except that the graphene is a zero bandgap material and the metal gate induces doping into the underlying graphene channel by transfer of carriers (either n- or p-type) depending upon the metal used which results in an interfacial potential step and hence a dipole capacitance. Further, the carrier density below the gate in the graphene channel can be electrically tuned by applying a gate voltage relative to the Dirac point. The device functions by capacitively modulating the charge carrier density in the graphene channel through applied gate voltage which is then collected at the contacts upon the application of drain-to-source voltage. The induced carrier density and hence the current are strong functions of the bias-dependent Fermi level, dipole capacitance, the quantum capacitance, and the diffusion to drift current ratio.

Under illumination: Photovoltaic effect, photoconductive effect, photo-induced thermoelectric effect, field-effect doping and bolometric effect are the various sensing mechanisms in graphene-based photodetectors.

1. Photovoltaic effect The photovoltaic effect results from the generation of photocurrents in the vicinity of metal contact with graphene or in the junctions created by p- and n-regions of graphene [163, 164]. These photocurrents are produced from the generation of excitons in graphene when exposed to light, and the separation of electrons and holes by the built-in electric fields near the junctions.

2. Photoconductive effect This effect contributes due to the inter-band

absorption of the photons with energy greater than twice that of the Fermi level resulting in the generation of electron-hole pairs in the neutral region of graphene rather than in junctions [1]. The generated carriers produce a photocurrent depending upon the bias applied to the source and drain contacts of graphene FETs.

3. Photothermoelectric effect The photothermoelectric effect emanates from the induction of temperature difference when exposed to light, eventually leading to a thermoelectric voltage [5, 165] . Hot carriers are generated upon illumination to form a hot Fermion distribution on account of the slow relaxation of electrons and lattice in graphene and the thermal decoupling of photocarriers from the crystal lattice. The photothermoelectric voltage occurs in the junction of regions with different Seebeck coefficients [5, 166].

4. Field-effect Doping This effect occurs in gated photodetectors such as graphene FETs. The gate voltage-induced variation of the channel current and the trapping of charges at certain interfaces due to this variation is called as field-effect doping. Under light exposure, the trapping of some of the photo-carriers in the channel or at interfaces will lead to electrostatic production of free carriers in graphene. There is a horizontal shift of the transfer curve on account of the change of the effective gate voltage [167].

5. Bolometric effect This effect occurs through thermally-induced heating of the active element under illumination, which alters the resistance of the active element depending upon the temperature [168].

3.11 Modeling of GOPFET/GFET [1, 2]

3.11.1 Carrier statistics

2D density of states in graphene is given by:

$$g_{2D}(\varepsilon) = \frac{2|\varepsilon|}{\pi\hbar^2 V_F^2} \tag{3.96}$$

where ε is the energy, and $\hbar$ is the reduced Planck's constant ($\hbar$=h/(2π)).

Electron density at a chemical potential (μ_c) is given by:

$$n_e(\mu_c) = n_i + \frac{\mu_c^2}{\pi\hbar^2 V_F^2} \tag{3.97}$$

where n_i is the intrinsic carrier concentration in graphene:

$$n_i = \frac{\pi}{6}\left(\frac{k_B T}{\hbar V_F}\right)^2 \tag{3.98}$$

Hole density,

$$n_h(\mu_c) = n_e(-\mu_c) \tag{3.99}$$

Full charge density or charge imbalance is given as:

$$n_s = n_e - n_h \tag{3.100}$$

Total carrier density,

$$N_s = n_e + n_h \tag{3.101}$$

3.11.2 Quantum capacitance

Quantum capacitance of graphene charge sheet is expressed as:

$$C_Q = \frac{2}{\pi}\left(\frac{q^2}{\hbar^2 V_F^2}\right) k_B T \ln\left(2 + 2\cosh\left(\frac{\mu_c}{k_B T}\right)\right) \tag{3.102}$$

3.11.3 Basic equation of graphene planar electrostatics

$$qV_G = \varepsilon_F + \frac{q^2 n_s}{C_{ox}} + \frac{C_{it}}{C_{ox}}\varepsilon_F = m\varepsilon_F + \frac{\varepsilon_F^2}{2\varepsilon_a} \tag{3.103}$$

where V_G is the gate bias applied, $\varepsilon_F = \zeta$ is the proper electric charge-independent chemical potential, C_{it} is the interface trap capacitance, m is the dimensionless ideality factor ($m = 1 + C_{it}/C_{ox}$), and ε_a is the characteristic energy scale,

$$\varepsilon_a = \frac{\pi\hbar^2 V_F^2 C_{ox}}{2q^2} \tag{3.104}$$

C_{ox} is the oxide capacitance ($C_{ox} = \epsilon_{ox}\epsilon_0/d_{ox}$) for GFET and should be replaced by the dipole capacitance ($C_d = \epsilon_p\epsilon_0/z_d$) in the case of GOPFET where ϵ_{ox}

is the oxide dielectric constant, d_{ox} is the oxide layer thickness, ϵ_0 is the free space permittivity, z_d represents the effective distance between the charge sheets of metal gate and graphene ($z_d = d_{eq} - d_0$), d_{eq} is the equilibrium separation distance between gate and graphene, d_0=0.24 nm and $\epsilon_p = 1$ [25].

3.11.4 Self-consistent solution of basic electrostatic equation

Electron Fermi energy as a function of gate voltage:

$$\varepsilon_F = (m^2\varepsilon_a^2 + 2\varepsilon_a q V_G)^{1/2} - m\varepsilon_a \tag{3.105}$$

Charge density,

$$qn_s(V_G) = C_{ox}\left[|V_G - V_{NP}| + V_0\left(1 - \left(1 + 2\frac{|V_G - V_{NP}|}{V_0}\right)^{1/2}\right)\right] \tag{3.106}$$

where V_0 is the characteristic voltage given as,

$$V_0 = \frac{m^2\varepsilon_a}{q} \tag{3.107}$$

and V_{NP} is the voltage corresponding to the electrical charge neutrality point.

3.11.5 Gate and intrinsic channel capacitances

The low frequency gate capacitance,

$$C_G = \left(\frac{1}{C_{ox}} + \frac{1}{C_Q + C_{it}}\right)^{-1} \tag{3.108}$$

Channel capacitance,

$$C_{CH} = \frac{C_{ox}}{1 + \frac{C_{ox}+C_{it}}{C_Q}} \tag{3.109}$$

3.11.6 I-V and amplification characteristics

Drain current,

$$I_D = q\frac{W}{L}D_0 n_s(0)\frac{1+k}{k}\left(1 - e^{\left(-\frac{k}{1+k}\frac{qV_D}{\varepsilon_D}\right)}\right) \tag{3.110}$$

where D_0 is the diffusion coefficient ($=\mu\varepsilon_D/q$), μ is the mobility, ε_D is the diffusion energy,

$$\varepsilon_D = n_{e/h} \Big/ \left(\frac{dn_{e/h}}{d\mu_c}\right) = \varepsilon_F/2 \tag{3.111}$$

k is the ratio of diffusion to drift current which can be shown to be:

$$k = \frac{C_{ox}}{C_Q + C_{it}} \tag{3.112}$$

Transconductance, g_m is given by:

$$g_m = \frac{W}{L}\mu V_D C_{CH} \tag{3.113}$$

Unity-gain cut-off frequency, f_T is expressed as:

$$f_T = \frac{g_m}{2\pi C_G} \tag{3.114}$$

3.11.7 Optical effects: photoinduced carriers

If n_0 is the electron density under dark i.e. radiation field $F_0 = 0$, then under illumination i.e. $F_0 \neq 0$, the electron density becomes

$$n_e = n_0 + \Delta n_e \tag{3.115}$$

From the theory of conservation of charge number, $\Delta n_e = n_h$, hole density under illumination. Thus, $n_e = n_0 + n_h$. The photogenerated electron and hole densities can be expressed as:

$$n_e = \frac{2}{\pi\gamma^2}\int_0^\infty \frac{x}{e^{(x-\mu_e^*)/k_BT}+1}dx \tag{3.116}$$

$$n_h = n_e - n_0 = \frac{2}{\pi\gamma^2}\int_0^\infty \frac{x}{e^{(x+\mu_h^*)/k_BT}+1}dx \tag{3.117}$$

where $\gamma = \hbar V_F$ is the band parameter. Using the mass balance equations, the quasi chemical potentials μ_e^* and μ_h^* for electrons and holes can be determined and then the photo-induced electron and hole densities can be obtained.

3.11.8 Mass balance equation

$$F_{-+}^{co,+} + F_{-+}^{cp,-} = F_{+-}^{co,-} + F_{+-}^{cp,+} \tag{3.118}$$

where

$$F_{\lambda,\lambda'}^{co,\pm} \tag{3.119}$$

describe the absorption (+) and emission (−) of photons and

$$F_{\lambda,\lambda'}^{cp,\pm} \tag{3.120}$$

describe the absorption (−) and emission (+) of phonons.

$$F_{-+}^{co,+} = \frac{q^2 F_0^2}{32\hbar^2\omega} f_- \left(-\frac{\hbar\omega}{2}\right) \left[1 - f_+ \left(\frac{\hbar\omega}{2}\right)\right] \tag{3.121}$$

denotes optical absorption from the valence band to the conduction band, ω is the radiation frequency.

$$F_{+-}^{co,-} = \frac{q^2 F_0^2}{32\hbar^2\omega} f_+ \left(\frac{\hbar\omega}{2}\right) \left[1 - f_- \left(\frac{-\hbar\omega}{2}\right)\right] \tag{3.122}$$

denotes optical emission from the conduction band to the valence band.

$$F_{+-}^{cp,+} = \frac{g^2(N_0+1)}{2\pi\hbar\gamma^2} \int_0^{\hbar\omega_0} dx x(\hbar\omega_0 - x) f_+(x)[1 - f_-(x - \hbar\omega_0)] \tag{3.123}$$

represents phonon emission with transition from the conduction band to the valence band,

$$F_{-+}^{cp,-} = \frac{g^2 N_0}{2\pi\hbar\gamma^2} \int_0^{\hbar\omega_0} dx x(\hbar\omega_0 - x) f_-(-x)[1 - f_+(\hbar\omega_0 - x)] \tag{3.124}$$

represents phonon absorption with transition from the valence band to the conduction band.

$$f_\lambda(x) = [1 + e^{(x-\mu_\lambda^*)/k_B T}]^{-1} \tag{3.125}$$

$\lambda = +1$ denotes conduction band or higher energy band or electron and $\lambda = -1$ denotes valance band or lower energy band or hole, μ_λ^* is the quasi Fermi level

for holes or electrons under illumination.

$$g = \frac{\hbar B b^2}{\sqrt{2\rho\hbar\omega_0}} \tag{3.126}$$

where $\rho = 6.5\times10^{-8}$ g/cm^2 is the areal density of graphene sheet, ω_0=0.196 meV is the optical phonon frequency at the Γ-point, B 2, $b = a/\sqrt{3}$ is the equilibrium bond length in graphene, and

$$N_0 = [e^{\hbar\omega_0/k_BT} - 1]^{-1} \tag{3.127}$$

3.11.9 Inter-band optical conductance

$$\sigma_{inter}(\omega) = 2P_{OP}/F_0^2 = 8\hbar\omega \times \sum_{\lambda,\lambda'} (F_{\lambda,\lambda'}^{co,+} - F_{\lambda,\lambda\prime}^{co,-})/F_0^2 \tag{3.128}$$

where

$$P_{OP} = 4\hbar\omega \times \sum_{\lambda,\lambda'} (F_{\lambda,\lambda'}^{co,+} - F_{\lambda,\lambda\prime}^{co,-}) \tag{3.129}$$

is the energy transfer rate induced by optical absorption in the steady state.

3.11.10 Intra-band optical conductance

$$\sigma_{intra}(\omega) = 2P_{OP1}/F_0^2 = 8\hbar\omega \times F_{\lambda,\lambda}^{co,+}/F_0^2 \tag{3.130}$$

where

$$F_{\lambda,\lambda}^{co,+} = \frac{q^2F_0^2}{8\pi\hbar^4\omega^3}\frac{\omega\tau_\lambda}{(1+(\omega\tau_\lambda)^2)}\int_0^\infty dEEf_\lambda(\lambda E)[1-f_\lambda(\lambda E)] \tag{3.131}$$

specifies intra-band optical absorption in the conduction band ($\lambda = 1$) and valence band ($\lambda = -1$) with τ_λ being the energy relaxation time for an electron or a hole in different bands.

$$P_{OP1} = 4\hbar\omega \times F_{\lambda,\lambda}^{co,+} \tag{3.132}$$

is the energy transfer rate for intra-band absorption.

3.11.11 Photobolometric effect (PBE) [3, 4]

The carriers within graphene stay away from equilibrium with lattice for a comparatively longer time (τ_{el}) than the time required to produce the thermalized distribution between the electrons (τ_{ee}). The inelastic e-e scattering rate under high doping concentration with the Fermi level (E_F) greater than k_BT is given by:

$$\tau_{ee}^{-1} = \frac{\alpha^2(k_BT_e)^2}{\hbar E_F} \tag{3.133}$$

Here T_e is the electron temperature in graphene, and α is defined as

$$\alpha = \frac{q^2}{\epsilon\hbar V_F} = 1 \tag{3.134}$$

This is followed by the electron energy dissipation or relaxation towards the lattice via e-l coupling or by diffusion of electrons far from the heated zone. The e-l scattering rate is defined as:

$$\tau_{el}^{-1}(E_k) = \frac{(E_k - E_F)D^2k_BT_L}{4\rho v_s^2\hbar^3V_F^2} \tag{3.135}$$

where v_s=2.6×10^4 m/s is the phonon velocity in graphene, D=18 eV is the deformation potential, T_L is the lattice temperature, and E_k is the carrier energy.

The resistance ratio $\Delta R/R$, a key performance metric of the graphene-based bolometer is written as:

$$\frac{\Delta R}{R} = \frac{\eta_{abs}P_{in}\tau_{el}}{2E_Fn_sW_1L_1} \tag{3.136}$$

where P_{in} denotes the input power, η_{abs} is the efficiency of absorption, W_1 and L_1 are the width and length of graphene respectively that absorb light, τ_{el} is the electron-lattice scattering time. E_F is related to the carrier density n as $E_F = \hbar V_F(\pi n_s)^{1/2}$.

Incorporating the length (L) and width (W) of the photodetector,

$$\frac{\Delta R}{R} = \frac{\tau_{el}e^{3/2}}{2\hbar V_F\pi^{1/2}}\frac{1}{n_s^{3/2}}(\eta_{abs}P_{in})\frac{(W^{1/2}L^{3/2})}{L_1} \tag{3.137}$$

The PB current is absent under zero bias voltage. With applied bias between the metallic contacts, the variation in graphene resistance can be sensed through the variation of photocurrent flowing across the graphene sheet as:

$$I_{ph} = \Delta I = I_{off} - I_{on} = \frac{V_b}{R} - \frac{V_b}{R + \Delta R} = \frac{\Delta R}{R} \frac{V_b}{R + \Delta R} \tag{3.138}$$

The PB photodetector speed is restricted by the electron-lattice scattering-induced hot carrier relaxation.

The PB effect analysis discussed earlier is mostly true for $\Delta R <$ R. For $\Delta R >$ R, the electron temperature should be calculated directly.

The general PB photocurrent is obtained from the electron temperature ΔT_e and lattice temperature ΔT_L as:

$$I_{ph} = \frac{W}{L} \left(\left. \frac{\partial \sigma}{\partial T_e} \right|_{T_e = T_L = T_s} \Delta T_e + \left. \frac{\partial \sigma}{\partial T_L} \right|_{T_e = T_L = T_s} \Delta T_L \right) \tag{3.139}$$

where $\partial\sigma/\partial T_e$ and $\partial\sigma/\partial T_L$ are the conductivity variation rates with variations in electron and phonon temperatures, and T_s is the initial temperature at equilibrium without radiation field. The absorbed power emanates from light absorption as well as from electrical Joule heating. The Joule heating power is given by $P_{abs} = V_b^2/R$. The heat transfer equation governing the absorbed power-dependence of carrier concentrations and the hot electron temperature (T_e) is stated as:

$$k_e \nabla^2 T_e - g_{e-l}(T_e - T_0) + P^* = 0 \tag{3.140}$$

where g_{e-l} is the electron-lattice thermal coupling ($g_{e-l} = \gamma C_e$), k_e denotes the thermal conductivity of graphene, C_e is the heat capacity of electrons, γ is the cooling rate of electrons towards lattice, T_0 represents the substrate temperature and P^* is the power absorbed by the electrons per unit area.

The thermal conductivity k_e of electrons is given by:

$$k_e = \frac{\pi^2 k_B^2 T_e \sigma}{3q^2} \tag{3.141}$$

where T_e represents the temperature of operation, and σ is the graphene electrical conductivity. The heat capacity of electrons, $C_e = A\gamma T_e$ decides the initial temperature elevation, where A denotes the graphene sheet areal density, and $\gamma = (4\pi^{5/2}k_B^2 n_s^{1/2})/(3hV_F)$ is the Sommerfeld coefficient.

Because of much higher heat capacity of the lattice, C_p, compared to the heat capacity of the electrons, C_e, the absorbed power propels the electron temperature (T_e) above the lattice temperature (T_0).

The heat equation solution is expressed analytically over the detector length as:

$$\Delta T_e(y) = T_e(y) - T_0 = \frac{\sinh((0.5 \times L - |y|)/\xi)P^*\xi^2}{\cosh((0.5 \times L)/\xi)2k_e} \tag{3.142}$$

where ξ is the e-l hot carrier cooling length. The cooling length is represented as $\xi = (k_e/g_{e-l})^{1/2}$. For maximum photobolometric output, the external electrodes should be placed from the photogenerated carriers at a distance exceeding the electron mean free path.

3.11.12 Photothermoelectric effect (PTE) and Photovoltaic effect (PVE) [5]

The carrier multiplication (CM) induced by intrinsically occuring Auger and impact ionization processes of the photogenerated carriers in graphene is even more profilerated by the energy transport mediated by hot carriers which stay at an elevated temperature above that of lattice for a long time due to the inefficient electron cooling towards the lattice.

Hot carrier-based thermoelectric currents show non-monotonic dependence upon the gate voltage with multiple sign changes and is a fingerprint of the carrier multiplication qnd the hot carrier regime. CM process enables fast carrier generation, whereas the carrier drift towards the contacts from the region of excitation is a long charge harvesting stage.

The processes accounted by optical phonons, occuring on picoseconds time scale, become damped when the photoexcited carrier energies fall well below the Debye energy, ω_D=200 meV. For these carriers, the prevalent cooling process is assisted by acoustic phonons, producing a slow cooling rate. For cooling rate defined as $dT_{el}/dt = -\gamma_1(T_{el} - T_0)$, T_{el}=T_0, Reference [169] finds

$$\gamma_1 = \frac{3D^2\mu_c^3}{4\pi^2\hbar^3\rho V_F^4 k_B T_{el}} = \frac{0.87(\mu_c[meV]/100)^3}{T_{el}[K]/300} ns^{-1} \tag{3.143}$$

The energy transport effects prevail over the conventional photovoltaic effect.

The current density in the hot-carrier domain is expressed by the local current density

$$j = \sigma E - e\eta n_x(r)\nabla U_g(r) + \sigma s \nabla T_{el} \tag{3.144}$$

The photovoltaic effect (PVE) is represented by the initial two terms in Eq.3.144 (here n_x is the equilibrium density of photogenerated carriers and η is the mobility at energy ε=$(1/2)hf$, f is the frequency of radiation). The readjustment of carriers with respect to this local photocurrent establishes an electric field $E = -\nabla(\phi - \mu_c/e)$ that propels the current from the excitation region towards the contacts. The final term in Eq.3.144 denotes the thermoelectric current contributed by the gradient of electron temperature. In Eq.3.144, σ and s are the electrical conductivity and Seebeck coefficient respectively. The energy flux which determines the temperature profile is given as:

$$W = (\phi - \mu_c/q)j - \Pi j - k_e \nabla T_{el} \tag{3.145}$$

where $\Pi = sT$ is the Peltier coefficient.

Considering a rectangular domain with width W and length L, with an interface step in carrier density between regions 1 and 2. The two contacts are placed at $y = \pm L/2$ where the photocurrent is collected.

Utilizing the continuity relation $\nabla \cdot J = 0$ and Eq.3.144, the photocurrent is

written as:

$$I = \int_{0}^{W} \int_{-L/2}^{L/2} (s(y)\nabla T_{el} - \sigma^{-1}(y) q\eta n_x \nabla U_g) \frac{dydx}{RW} \tag{3.146}$$

where $R = (\frac{1}{W}) \int_{-L/2}^{L/2} \sigma^{-1}(y)dy$ represents the total resistance, and the contacts are kept at same potentials, $\int_{-L/2}^{L/2} E_y dy = 0$. The first term in Eq.3.146 gives the hot-carrier (HC) contribution through the average elevation of the electron temperature along the interface:

$$I_{(HC)} = \left(\frac{s_1 - s_2}{R}\right) \Delta T, \Delta T = T^{ave}_{el,y=0} - T_0 \tag{3.147}$$

where T_0 denotes the temperature of lattice, s_1 and s_2 represent the Seebeck coefficients in domains 1 and 2, and the notation *ave* specifies the average value over $0 < x < W, y = 0$. The heat transport equation given below determines the spatial profile of T_{el}:

$$\nabla \cdot W + \gamma C_{el}(T_{el} - T_0) = \alpha \varepsilon_0 N, \varepsilon_0 = hf \tag{3.148}$$

where C_{el} is the electron specific heat, γ is the electron cooling rate towards the lattice (Eq.3.143), and N denotes the photon flux absorbed in the laser spot per unit area.

The chemical potentials, $\mu_{1,2}$, and the conductivities, $\sigma_{1,2}$, give the estimate of $(s_1 - s_2)$/R in Eq.3.147 using $R = (\frac{L}{2W}) \left(\frac{\sigma_1 + \sigma_2}{\sigma_1 \sigma_2}\right)$ and the Mott formula

$$s(\mu_c) = -\frac{\pi^2 k_B^2 T}{3q} \frac{1}{\sigma} \frac{d\sigma}{d\mu_c} \tag{3.149}$$

$$\sigma(\mu_c) = \sigma_{min} \left(1 + \frac{\mu_c^2}{\Delta^2}\right) \tag{3.150}$$

where $k_B T \ll \max(\mu, \Delta)$. Here Δ specifies the neutrality region width, and σ_{min} represents the minimum conductivity.

The photovoltaic effect is represented by the second term of Eq.3.146:

$$I_{(PV)} = -\frac{1}{RW} \int \int \sigma^{-1}(r) q\eta n_x(r) \nabla U_g(r) dxdy \tag{3.151}$$

The laser spot size being larger with respect to the depletion width,$l_0 \gg w_d$, the integration in Eq.3.151 simplifies. Setting $eU_g(r) = \mu_c(r)$, using Eq.3.149, and replacing the integration over y by that over μ_c, gives:

$$I_{(PV)} = \frac{\eta\Delta}{\sigma_{min}R}\left(\tan^{-1}\frac{\mu_1}{\Delta} - \tan^{-1}\frac{\mu_2}{\Delta}\right) n_x^{ave}(y=0) \tag{3.152}$$

Since j has zero divergence, we can write Eq.3.145 as:

$$\nabla \cdot W = -\sigma^{-1}|j|^2 - j \cdot \nabla\Pi - \nabla \cdot (k_e \nabla T) \tag{3.153}$$

The first term (quadratic in j) can be ignored. The Peltier cooling effect, described by the second term of Eq.3.153, is substituted in Eq.3.148 giving:

$$-\nabla \cdot (k_e \nabla T_{el}) + \gamma C_{el}(T_{el} - T_0) = \alpha\varepsilon_0 N + j \cdot \nabla\Pi \tag{3.154}$$

Since the Peltier term $j \cdot \nabla\Pi$ spans over a distance of the order of the p-n junction width (typically < 0.1 μm in the devices studied till now), it can be replaced by a delta function source confined at the 1-2 interface.

Eq.3.154 can be simplified by averaging the quantities along the device width $0 < x < W$, $T_{el}^{ave}(y) = (\frac{1}{W})\int_0^W T_{el}(x,y)dx$, $N^{ave}(y) = (\frac{1}{W})\int_0^W N(x,y)dx$.

For cooling length $\xi = (k_e/\gamma C_{el})^{1/2}$ greater than $L/2$, Eq.3.154 can be solved by approximating $\gamma = 0$ producing temperature profile $\delta T_{el}^{ave}(y) = (1-2|y|/L)\Delta T$ with the average temperature elevation along the interface:

$$\Delta T = \frac{\alpha\varepsilon_0 l_0 N_{y=0}^{ave}}{\frac{2}{L}(k_1+k_2) + \frac{T_0}{(RW)}(s_1-s_2)^2} \tag{3.155}$$

This gives the temperature elevation of order ΔT for $\xi > W$ (narrow device) and of order $(W/\xi)\Delta T$ for $\xi < W$ (wide device).

For a general system size L, the solution can be expressed as:

$$\delta T_{el}^{ave}(y<0) = A_1 sinh((y+L/2)/\xi_1) \tag{3.156}$$

$$\delta T_{el}^{ave}(y>0) = A_2 sinh((L/2-y)/\xi_2) \tag{3.157}$$

After the boundary values and derivatives matching at $y = 0$, we get

$$\Delta T = \frac{\alpha \varepsilon_0 l_0 N_{y=0}^{ave}}{\left(\frac{k_1}{\xi_1} \coth \frac{L}{2\xi_1} + \frac{k_2}{\xi_2} \coth \frac{L}{2\xi_2} + \frac{T_0}{RW}(s_1 - s_2)^2\right)} \tag{3.158}$$

The above result agrees with Eq.3.155 for small system size $L \ll \xi_{1,2}$. At large L, it gives a saturated value of:

$$\Delta T = \frac{\alpha \varepsilon_0 l_0 N_{y=0}^{ave}}{\left(\frac{k_1}{\xi_1} + \frac{k_2}{\xi_2}\right)} \tag{3.159}$$

3.12 Theory of Numerical Modeling Methods

3.12.1 Finite-Difference Method (FDM)

The discretization of finite-difference domain is shown in Fig.3.9 [170].

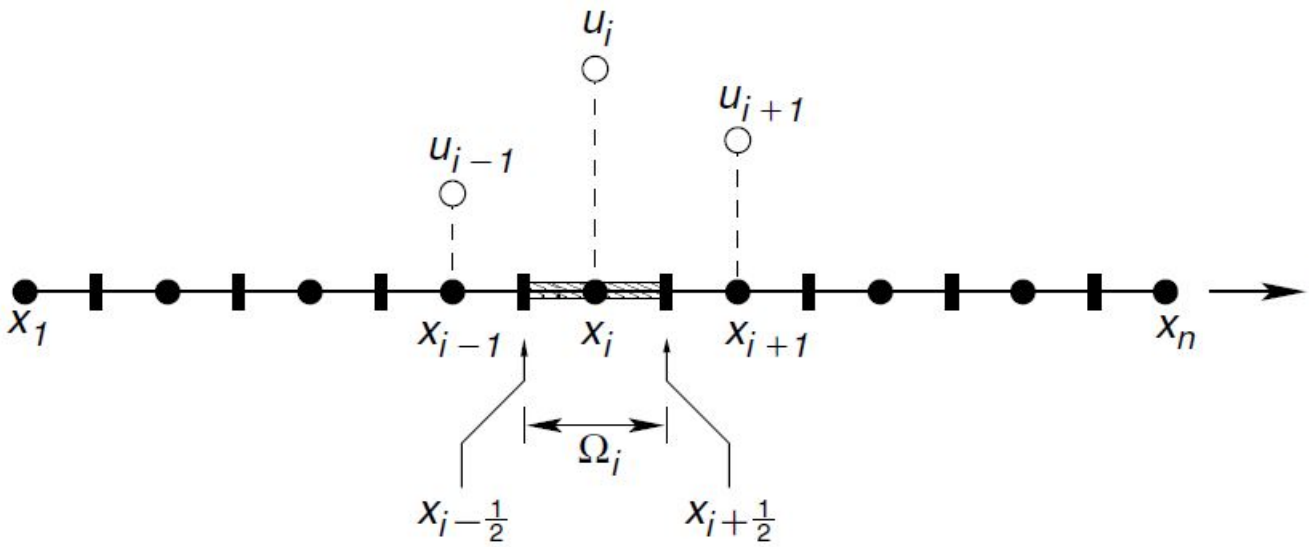

Figure 3.9: The discretization of domain for FDM.

There are many instances where continuous domain representing exact solution has to be replaced by discrete domain giving approximate solution.

For one dimensional case, given the function $u(x)$ and a set of points x_i ; $i = 1,...,N$ as shown in 3.1, the numerical output is represented by a discrete set of function values $u_1,...,u_N$ that approximate u at these points, i.e., $u_i = u(x_i)$; $i = 1,...,N$.

Consider that the points are equidistant along the domain with a distance $\Delta x = x_{i+1}$-x_i; i = 1,...,N-1. Thus, u_{i+1}=$u(x_{i+1})$=$u(x_i + \Delta x)$. This partitioning of the domain is called as a mesh or grid.

The forward, backward and centred finite difference approximations of $u_x|_i$, respectively are defined as [170]:

$$u_x|_i = \frac{u_{i+1} - u_i}{\Delta x} \tag{3.160}$$

$$u_x|_i = \frac{u_i - u_{i-1}}{\Delta x} \tag{3.161}$$

$$u_x|_i = \frac{u_{i+1} - u_{i-1}}{2\Delta x} \tag{3.162}$$

The second order derivative is written as:

$$u_{xx}|_i = \frac{u_{i+1} - 2u_i + u_{i-1}}{\Delta x^2} \tag{3.163}$$

The above approximations are substituted in the partial differential equation representing the physical phenomenon and the resulting matrices-based equation is solved for the unknowns.

3.12.2 Finite-Volume Method (FVM)

The finite volume method approximates the governing PDE over finite-sized control volumes called as cells, rather than at points, as shown in Fig.3.10 [73]. These discrete bounding surfaces are known as cell faces and the cell vertices are called as nodes. All data is saved at the centroids of the cells, known as cell centers.

The finite volume method begins by integration of the governing PDE over the cells forming the computational domain. For Poisson equation $\nabla^2\phi = S_\phi$, this yields

$$\int_{V_i} \nabla^2\phi dV = \int_{V_i} S_\phi dV \tag{3.164}$$

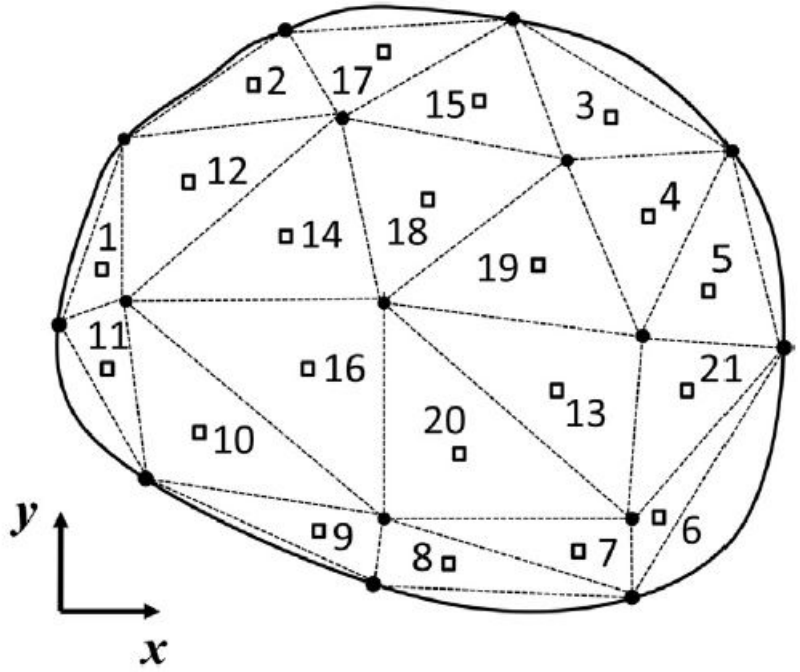

Figure 3.10: 2D Computational Domain and Mesh for FVM

where V_i is the volume of the i-th cell. The volume integral on the LHS of Eq. 3.164 can be simplified by writing the Laplacian, as $\nabla^2\phi = \nabla \cdot \nabla\phi$, and by using the Gauss divergence theorem, to yield

$$\int_{S_i} (\nabla\phi) \cdot \hat{\mathbf{n}} dA = \int_{V_i} S_\phi dV \tag{3.165}$$

where S_i is the surface area of the surface bounding the cell i, and dA is the differential area with outward pointing unit surface normal $\hat{\mathbf{n}}$. The RHS of Eq. 3.165 can be simplified by using the mean value theorem and by considering that the mean value of S_ϕ over the volume V_i is the same as the value of S_ϕ estimated at the cell centroid i. This yields

$$\int_{S_i} (\nabla\phi) \cdot \hat{\mathbf{n}} dA = S_i V_i \tag{3.166}$$

The cells are generally bounded by a set of discretized faces. Therefore, the LHS integral of Eq. 3.166 can be substituted by a summation over the faces enclosing the cell i, to give

$$\sum_{f=1}^{N_{f,i}} \int_{S_f} (\nabla\phi) \cdot \hat{\mathbf{n}} dA = \sum_{f=1}^{N_{f,i}} (\nabla\phi)_f \cdot \hat{n_f} A_f = S_i V_i \tag{3.167}$$

where the index "f " refers to cell faces, $N_{f,i}$ is the total number of cell faces i, and A_f is the area of face f. The quantity, $(\nabla\phi)_f \cdot \hat{n_f}$ gives the average value of the normal component of the gradient of ϕ at face f, i.e., $(\nabla\phi)_f \cdot \hat{n_f} = \frac{1}{A_f} \int\limits_{S_f} (\nabla\phi) \cdot \hat{n} \mathrm{dA}$.

For FVM, the normal gradients at the faces are approximated by the cell center values of ϕ. Conventionally, for this purpose, Taylor series expansions are used. This approximation, followed by substitution into Eq. 3.167, gives a set of discrete linear algebraic equations of the form

$$\sum_{i=1}^{N_C} A_{i,k}\phi_k = S_i V_i \tag{3.168}$$

for all i=1,2,...N_C, where N_C is the total number of cells. In FVM, the PDE is first integrated over the control volume and then approximated and solved.

The quantity under consideration is conserved. These conservation laws may be mathematically represented as $\mathbf{J} = -\Gamma\nabla\phi$, where $\mathbf{J}$ is the flux, ϕ is the driving potential, and Γ is the proportionality constant. If Γ=1, then $\mathbf{J} = -\nabla\phi$, thus Eq. 3.167 may be written as

$$\sum_{f=1}^{N_{f,i}} J_f \cdot \hat{n_f} A_f = -S_i V_i \tag{3.169}$$

Noting that $J_f \cdot n_f$ expresses the transport rate of the quantity under consideration, such as charge, energy, or mass, leaving the control volume through the face f per unit area, the LHS of Eq. 3.169 expresses the net rate that leaves the control volume. Eq. 3.169 represents a fundamental conservation property at steady state.

3.12.3 Finite-Element Method (FEM):

The finite element method is based on the variation of parameters principle, first proposed by Ritz and Galerkin [79]. The method converts the strong form of the PDE to the weak form and then uses finite-sized elements to discretize and solve the resulting weak form problem. The extraction of the weak form begins

by multiplying the PDE with a so-called test function, and then integrating the entire equation over the whole computational domain [73].

$$\int_{V_\Sigma} [\nabla^2 \phi] v dV = \int_{V_\Sigma} S_\phi v dV \tag{3.170}$$

where V_Σ is the volume of the whole computational domain, and v is the test function: $v{=}v(x,y)$ in 2D and $v{=}v(x,y,z)$ in 3D. The test function is a scalar function. Noting that $\nabla \cdot (v\nabla\phi) = v\nabla^2\phi + (\nabla v)\cdot(\nabla\phi)$, Eq. 3.170 may be written as

$$\int_{V_\Sigma} [\nabla \cdot (v\nabla\phi) - (\nabla v)\cdot(\nabla\phi)] dV = \int_{V_\Sigma} S_\phi v dV \tag{3.171}$$

Next, using the Gauss-divergence theorem for the first term of Eq. 3.171, we get

$$\int_{S_\Sigma} (v\nabla\phi)\cdot\hat{n} dA - \int_{V_\Sigma} (\nabla v)\cdot(\nabla\phi)] dV = \int_{V_\Sigma} S_\phi v dV \tag{3.172}$$

where $\hat{n}$ is the outward pointing surface normal on a differential area dA on the enclosing surface of the control volume. The total surface area of the enclosing surface is denoted by $\int_{S_\Sigma}$. Eq. 3.172 presents the generalized weak form of the Poisson equation.

Before applying the finite element method, the computational field is discretized into a set of convex elements as shown in Fig.3.11 [73]. The further step is to represent the solution and the test function in each element by a linear combination of basis functions:

$$\phi(x,y) = \sum_{i=1}^{N} a_i \psi_i(x,y) \tag{3.173}$$

$$v(x,y) = \sum_{i=1}^{N} b_i \psi_i(x,y) \tag{3.174}$$

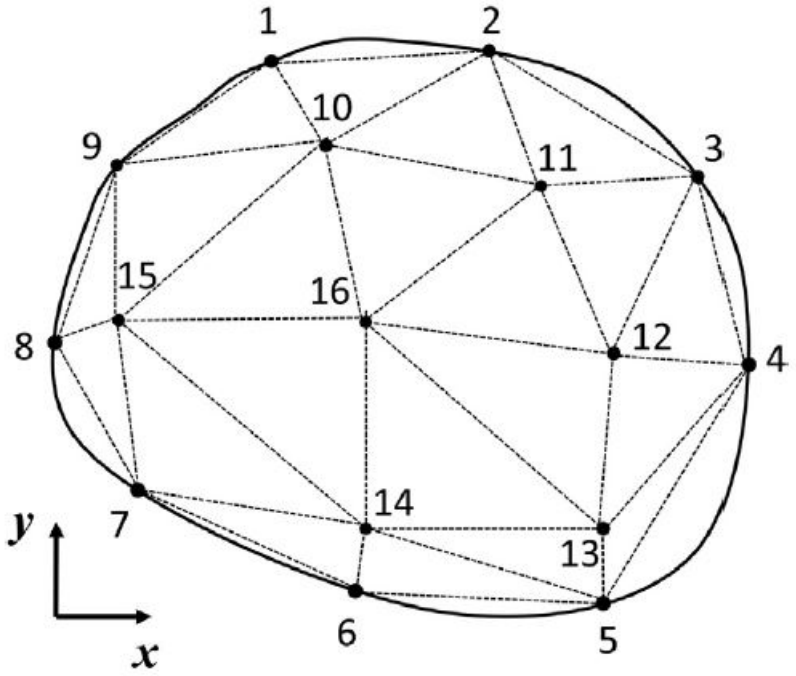

Figure 3.11: 2D Computational Domain and Grid for FEM

where N is the number of nodes and ψ_i are the basis functions. These basis functions can have arbitrary order, with the minimum order being the order of the PDE being evaluated. These basis functions are linearly combined using undetermined coefficients a_i and b_i in Eq. 3.173 and 3.174. Substituting Eq. 3.173 and 3.174 in Eq. 3.172, followed by simplification and rearrangement produces a linear system of algebraic equations of the nature

$$\sum_{k=1}^{N} K_{i,k} a_k = F_i \tag{3.175}$$

for all i=1,2,...,N, which may be solved to obtain the undetermined coefficients a_i. Substituting these coefficients back into Eq. 3.173 and 3.174 will produce the final solution for ϕ. The square matrix $K_{i,k}$ is known as the stiffness matrix, while the column matrix (vector) F_i is known as the load vector. With the contributions from all elements, results in a large sparse matrix equation system that can be solved for the final output.

Chapter 4

Structural, Material, Illumination Model, and External Control Factor Optimization

4.1 Validation of the employed Semi-Analytical Model with the Experiments and Visual TCAD Software Simulatons

Fig.4.1 compares the Si front-illuminated OPFET characteristics obtained using the employed model with that given in experiments in [6] showing reasonable agreement. The discrepancy is attributed to the fact that the series resistance-dependence on drain voltage is not considered in the employed model. This is true for high current operated and high series resistance devices (due to low mobility of Si) as in the present case. Table4.1 gives the parameters employed in the experiments and validation. The source of optical illumination is white light laser diode modulated by a signal of frequency 2.5 MHz. Under another set of operating conditions with (v_{gs}=$-$10 V, V_{DS}=24 V, λ=850 nm, and P=5 mW), a responsivity of 0.24 A/W is obtained from the semi-analytical model as compared to 0.27 A/W from the experiments thus, validating the model. Fig.4.2 shows the validation of the present model with the experimental results given in [7] and with Visual TCAD software simulations, both of which show close resemblance. The illumination model employed in the experiments and for validation

is the opaque-gate model. The parameter values used in experiments and for validation are specified in Table4.2. The I-V characteristics under dark show a saturation drain voltage of around 1.32 V as opposed to a predicted value of 1.69 V due to the negative shift on account of the series resistance-induced voltage drop. The same is the case under illumination. Fig.4.3 shows the comparison of the present simulation results with another set of experimental results given in [8]. The illumination model used for validation is the opaque-gate OPFET, while the parameter used for comparison is the transconductance. Table4.2. lists the parameters used in validation. The graphs in Fig.4.3 show reasonable agreement. The discrepancy in the values of transconductances between the measured and calculated values is due to the presence of short channel effects in practical devices with gate lengths shorter than 2 μm. These effects cause a negative shift in the threshold voltage and consequently a suppression of the transconductance. The shift in threshold voltage hinders the gate control ability over the channel. With higher applied gate voltages, the depletion width reduces greatly, and consequently, the variation in depletion width with gate bias is a small fraction of the large channel area compressing the transconductance. Since the present work employs a semi-analytical model suitable for medium- and long-channel devices, the two-dimensional effects such as short channel effects are not apparent in the theoretical plots. In the simulated plots, the transconductance is significantly enhanced at larger gate voltages because there is no shift in the threshold voltage. At higher gate voltages, the zero threshold voltage-shift amplifies the depletion width sensitivity. The change in the depletion width is still a larger fraction of the total channel area. At zero gate bias voltage, the gate junction, forward biased by the developed photovoltage attracts a significant number of electrons away from the drain, lowering the transconductance. The above two effects are not apparent in practical devices due to the short channel effects. The threshold voltage of the device is obtained by extending the drain-to-source current graph to negative gate-to-source and is the voltage at which the drain current is zero as

depicted in Fig.4.4. The graphical value is matching with the predicted value of -2.154 V. Yet another set of experimental results [9] is compared to demonstrate the simulation results in this work Fig.4.5. The illumination model in both the cases is the front-illuminated OPFET, wherein the transparent surface gate is illuminated and not the spacings. In Fig. 4, the drain-to-source current is plotted as a function of the photon flux density. The measured and simulated values show close agreement. Refer to Table4.2 for the parameter values used in experiments and calculation. Figures 4.2, 4.3, and 4.5 are sufficient to demonstrate the responsivity and partly the other parameters since the responsivity only depends upon the photocurrent which is clearly understood from these graphs. To further demonstrate the validity of 3-dB bandwidth and f_T, the S_{21} parameter is compared at a range of frequencies from the experimental works [7, 8] with that obtained using our model showing close resemblance (Figs. 4.6 and 4.7). The S_{21} parameter incorporates all the individual parameters i.e. g_m, C_{gs}, and modulation frequency which are significant enough to validate the 3-dB bandwidth and f_T of the device.

There is no sufficient data available for comparing the experimental plots of switching time with the present simulations. However, the switching time from the present model is contrasted with that from the reference model [38] showing close agreement as presented in Table4.3. The parameters employed in calculation are given in Table4.4.

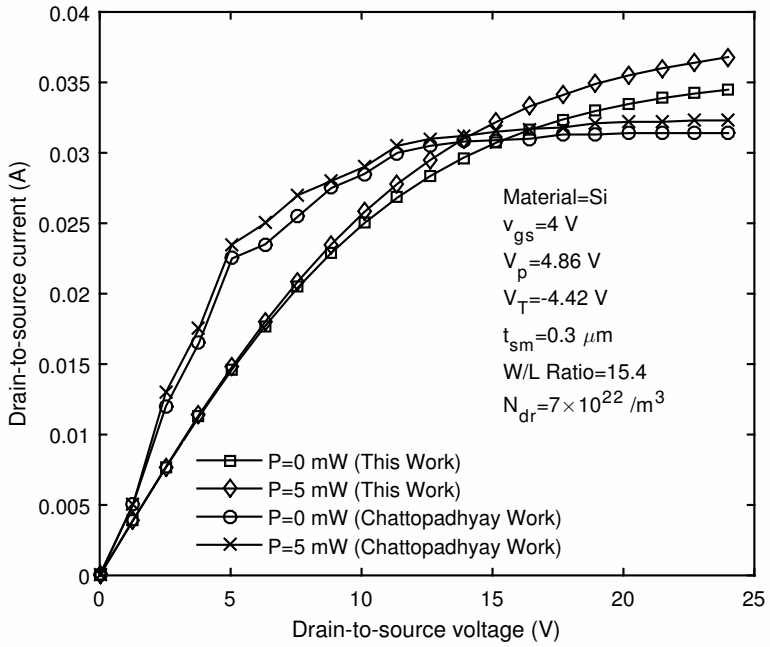

Figure 4.1: Validation of the present model results with the experiments in [6]

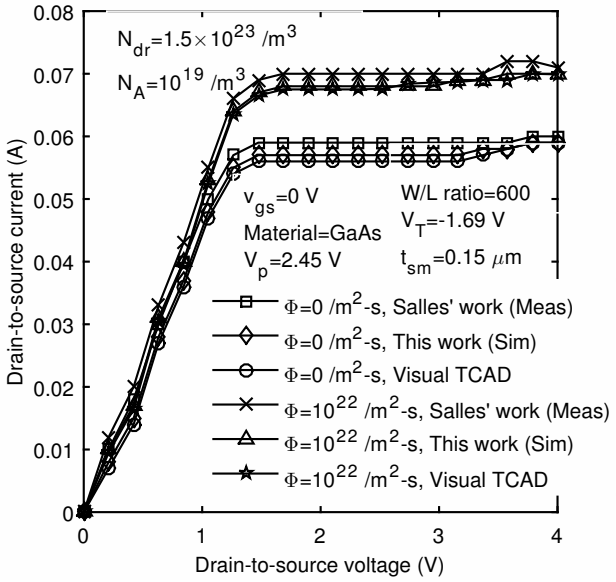

Figure 4.2: Comparison of the present model results with the experiments in [7] and Visual TCAD simulations

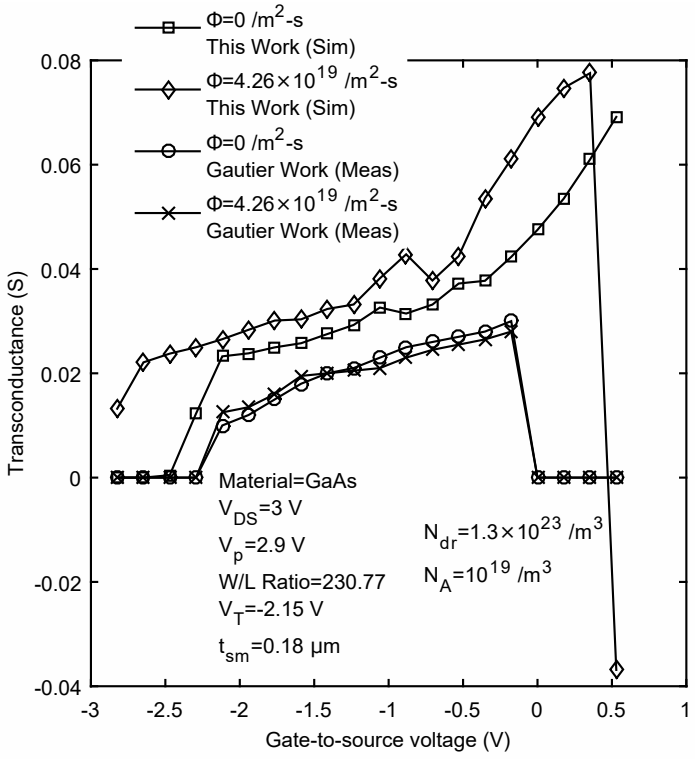

Figure 4.3: Comparison of the present simulation model results with the experiments in [8]

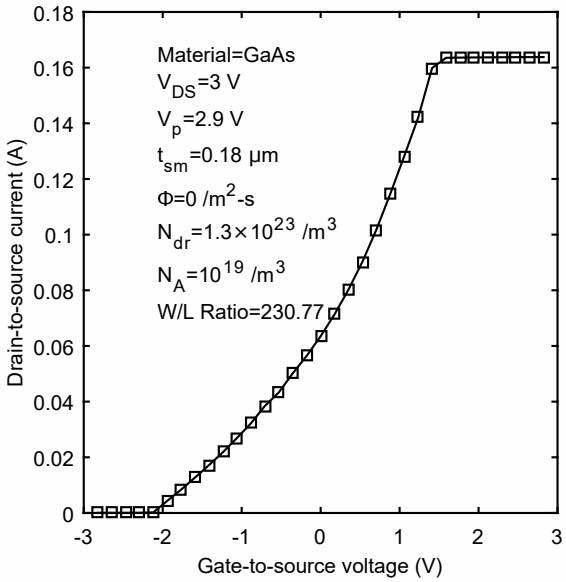

Figure 4.4: Threshold voltage detection of the device presented in [8]

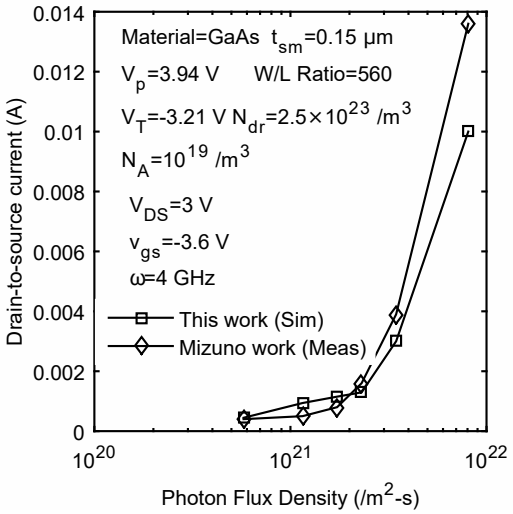

Figure 4.5: Comparison of the present model results with the experiments in [9]

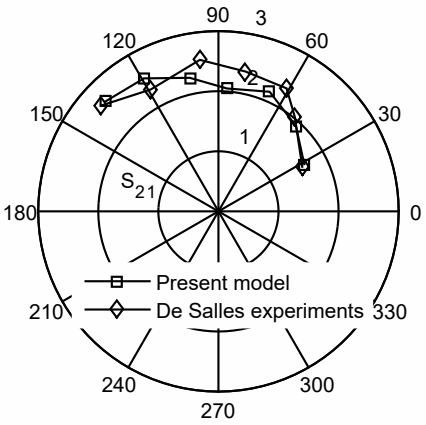

Figure 4.6: Comparison of the S_{21} parameter from [7] and the present model under illumination (10^{22} $/m^2$-s) in the frequency range 2 GHz to 8 GHz at zero gate to source voltage

Table 4.1: Parameters employed in Chattopadhyay experiments/validation

Parameter	Name	Value	Unit
μ	Low field electron mobility	(0.08)	(m^2/V.s)
V_{bi}	Gate built-in potential	(0.44)	(V)
v_{yn}	Saturated electron velocity	9.4×10^4	(m/s)
v_{yp}	Saturated hole velocity	6.3×10^4	(m/s)
τ_p	Lifetime of holes	$35 \times 10^{\breve{}6}$	(s)
τ_n	Lifetime of electrons	$35 \times 10^{\breve{}6}$	(s)
ϵ	Permittivity	$1.036 \times 10^{\breve{}10}$	(F/m)
L	Gate length	$13 \times 10^{\breve{}6}$	(m)
Z	Gate width	$200 \times 10^{\breve{}6}$	(m)
L_{gs}	Gate-to-source spacing	$4 \times 10^{\breve{}6}$	(m)
L_{gd}	Gate-to-drain spacing	$4 \times 10^{\breve{}6}$	(m)
t_{sm}	Active layer thickness	$0.3 \times 10^{\breve{}6}$	(m)
N_{dr}	Channel doping concentration	7×10^{22}	($/m^3$)

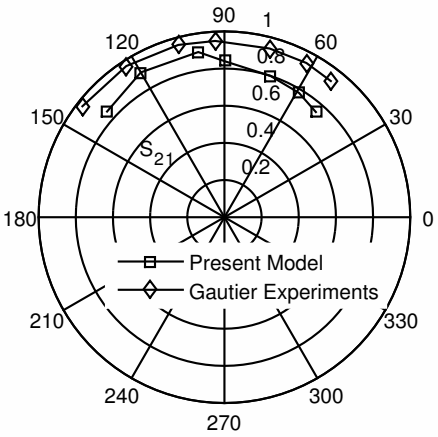

Figure 4.7: Comparison of the S_{21} parameter from [8] and the present model under illumination (2×10^{20} $/m^2$-s) in the frequency range 2 GHz to 8 GHz at -2 V gate to source voltage and 3.7 V drain to source voltage

The validations with Visual TCAD software are also provided in the UV region for Au-gated GaN, 6H-SiC, and ZnO front-illuminated OPFETs as shown in Figures. 4.8, 4.9, and 4.10 respectively showing close agreement. The parameters used in validation are provided in Table4.5. In the case of GaN OPFET, the high

Table 4.2: Parameters employed in De Salles, Gautier, Mizuno experiments/validation

Parameter	Name	Value (De Salles)	Value (Gautier)	Value (Mizuno)	Unit
μ	Low field electron mobility	(0.45)	(0.45)	(0.4)	(m^2/V.s)
V_{bi}	Gate built-in potential	(0.76)	(0.75)	(0.73)	(V)
v_{yn}	Saturated electron velocity	1.2×10^5	1.23×10^5	1.15×10^5	(m/s)
v_{yp}	Saturated hole velocity	0.7×10^5	0.73×10^5	0.65×10^5	(m/s)
τ_p	Lifetime of holes	$10^{\check{}9}$	$10^{\check{}8}$	$10^{\check{}8}$	(s)
τ_n	Lifetime of electrons	$10^{\check{}6}$	$10^{\check{}6}$	$10^{\check{}6}$	(s)
ϵ	Permittivity	$1.1 \times 10^{\check{}10}$	$1.16 \times 10^{\check{}10}$	$1.14 \times 10^{\check{}10}$	(F/m)
L	Gate length	$0.5 \times 10^{\check{}6}$	$1.3 \times 10^{\check{}6}$	$0.5 \times 10^{\check{}6}$	(m)
Z	Gate width	$300 \times 10^{\check{}6}$	$300 \times 10^{\check{}6}$	$280 \times 10^{\check{}6}$	(m)
L_{gs}	Gate-to-source spacing	$3.5 \times 10^{\check{}6}$	$1.85 \times 10^{\check{}6}$	$0.8 \times 10^{\check{}6}$	(m)
L_{gd}	Gate-to-drain spacing	$1.5 \times 10^{\check{}6}$	$2.5 \times 10^{\check{}6}$	$2.3 \times 10^{\check{}6}$	(m)
t_{sm}	Active layer thickness	$0.15 \times 10^{\check{}6}$	$0.18 \times 10^{\check{}6}$	$0.15 \times 10^{\check{}6}$	(m)
N_{dr}	Channel doping concentration	1.5×10^{23}	1.3×10^{23}	2.5×10^{23}	($/m^3$)
N_A	Substrate doping concentration	10^{19}	10^{19}	10^{19}	($/m^3$)
α	Absorption Coefficient @ 750, 870, 830 nm	1×10^6	2×10^5	9.5×10^5	($/$m)

Table 4.3: Comparison of Switching time in Si OPFET using the employed model with that in [38] at v_{gs}=0 V and V_{DS}=1.5 V

Photon Flux ($/m^2$-s)	Switching time (Present model)	Switching time (Reference model)
0	6.1×10^{-11} s	5.1×10^{-11} s
10^{17}	1.66×10^{-11} s	1×10^{-11} s

Table 4.4: Parameters employed in Chattopadhyay Si OPFET model [38]

Parameter	Name	Value	Unit
μ	Low field electron mobility	(0.12)	(m^2/V.s)
V_{bi}	Gate built-in potential	(0.40)	(V)
v_{yn}	Saturated electron velocity	1×10^5	(m/s)
v_{yp}	Saturated hole velocity	1×10^5	(m/s)
τ_p	Lifetime of holes	$85 \times 10^{\check{}6}$	(s)
τ_n	Lifetime of electrons	$85 \times 10^{\check{}6}$	(s)
ϵ	Permittivity	$1.036 \times 10^{\check{}10}$	(F/m)
L	Gate length	$1 \times 10^{\check{}6}$	(m)
Z	Gate width	$60 \times 10^{\check{}6}$	(m)
L_{gs}	Gate-to-source spacing	$0.8 \times 10^{\check{}6}$	(m)
L_{gd}	Gate-to-drain spacing	$0.8 \times 10^{\check{}6}$	(m)
t_{sm}	Active layer thickness	$0.3 \times 10^{\check{}6}$	(m)
N_{dr}	Channel doping concentration	1.7×10^{22}	($/m^3$)
α	Absorption Coefficient @ 850 nm	6.4×10^4	(/m)

series resistances due to the wide bandgap and low mobility as well as moderate doping concentration causes the difference in the graphical and calculated values of the drain-to-source saturation voltage (V_{DSAT}=0.25 V (under dark-graphical); V_{DSAT}=0.1876 V (under dark-calculated); V_{DSAT}=1.5 V (under illumination-graphical); V_{DSAT}=0.62 V (under illumination-calculated)). The same is the case with SiC OPFET. This is because the series resistance-dependence on drain voltage is not considered in the present model.

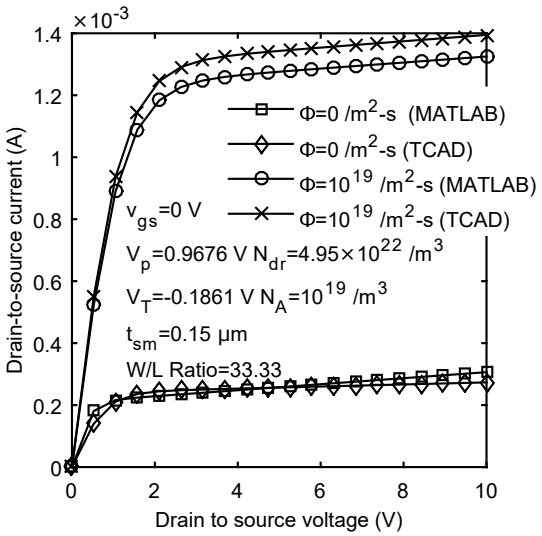

Figure 4.8: Comparison of the present model results with the simulations using Visual TCAD software (Au-GaN front-illuminated OPFET)

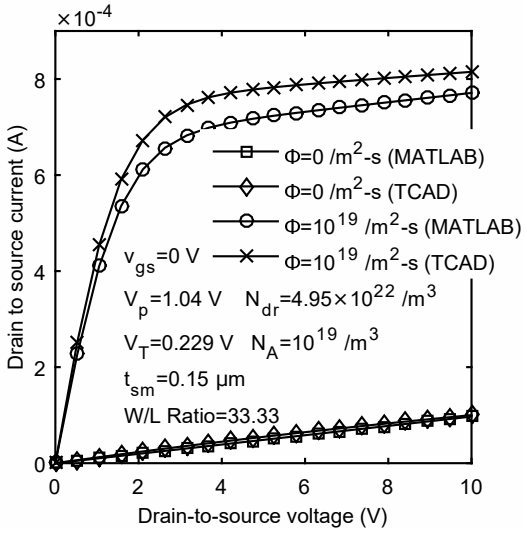

Figure 4.9: Comparison of the present model results with Visual TCAD (Au-SiC front-illuminated OPFET)

Table 4.5: Parameters employed in calculation for GaN, 6H-SiC, and ZnO OPFETs validation with Visual TCAD results

Parameter	Name	Value (GaN)	Value (ZnO)	Value (6H-SiC)	Unit
μ	Low field electron mobility	0.1	0.032	0.037	$(m^2/V.s)$
Φ_B	Schottky Barrier Height (Au-gate)	0.88	0.65	1.37	(eV)
v_y	Carrier velocity in the y direction (electrons/holes)	$2 \times 10^5/4 \times 10^4$	$2.8 \times 10^5/1.8 \times 10^5$	$2 \times 10^5/9 \times 10^4$	(m/s)
τ_p	Lifetime of holes	0.9×10^{-9}	1×10^{-6}	9.19×10^{-9}	(s)
τ_n	Lifetime of electrons	1.15×10^{-6}	1×10^{-6}	9.19×10^{-9}	(s)
ϵ	Permittivity	9.21×10^{-11}	7.97×10^{-11}	8.55×10^{-11}	(F/m)
α	Absorption Coefficient @ 350 nm	8×10^5	2.7×10^7	1.06×10^5	(/m)
Z	Channel Width	100×10^{-6}	100×10^{-6}	100×10^{-6}	(m)
L	Channel Length	3×10^{-6}	3×10^{-6}	3×10^{-6}	(m)
t_{sm}	Active-layer thickness	0.15×10^{-6}	0.15×10^{-6}	0.15×10^{-6}	(m)
d	Surface-to-substrate thickness	1×10^{-6}	1×10^{-6}	1×10^{-6}	(m)
N_{dr}	Ionized impurity concentration	4.95×10^{22}	4.95×10^{22}	4.95×10^{22}	$(/m^3)$

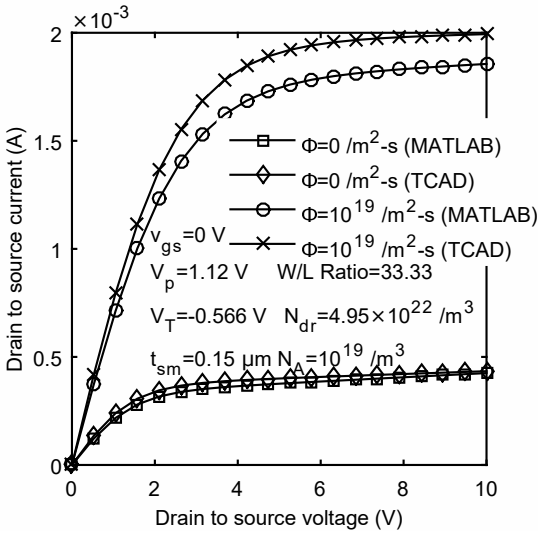

Figure 4.10: Comparison of the present model results with Visual TCAD (Au-ZnO front-illuminated OPFET)

Further, the modeled Schottky junction of OPFET under dark and illumination has been validated with experiments reported elsewhere [7] (Fig.4.11) and with Visual TCAD simulations (Fig.4.12).

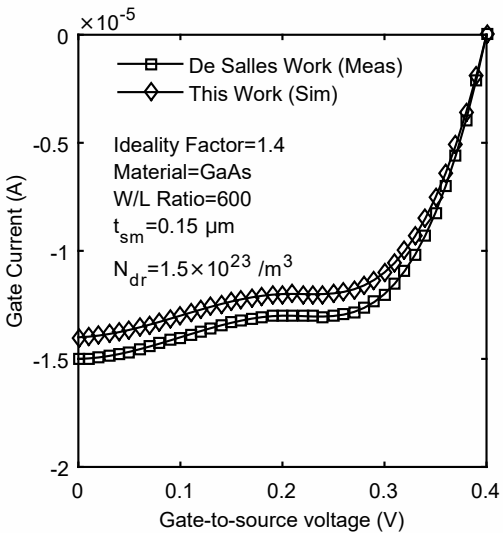

Figure 4.11: Validation of the Schottky junction model with the experiments [7] under 750 nm illumination at a flux density of $10^{22}/m^2$-s

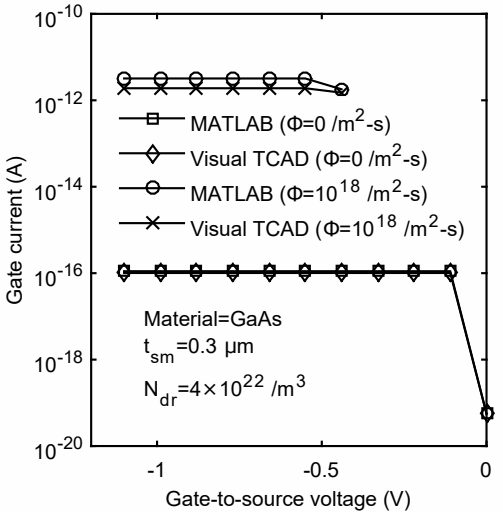

Figure 4.12: Verification of the Schottky junction model with commercially availabe Visual TACD software under reverse bias conditions with and without 600 nm illumination

The parameter values employed in experiments (DeSalles) and for validation are same as that given in Table4.2. For Visual TCAD software validation using Au-GaAs front-illuminated OPFET, the parameters used are specified in Table4.6.

Table 4.6: Parameters employed in Schottky junction model validation (Au-GaAs OPFET) with Visual TCAD software

Parameter	Name	Value	Ref.	Unit
α	Absorption Coefficient @ 600 nm	4×10^{6}	[32]	(/m)
ϵ	Permittivity	9.21×10^{-11}	[3]	(F/m)
L	Channel Length	4×10^{-6}	[33]	(m)
Z	Channel width	4×10^{-6}	[33]	(m)
t_{sm}	Active layer thickness	0.3×10^{-6}	[33]	(m)
N_{dr}	Ionized donor concentration	4×10^{22}		$(/m^3)$
v_y	Carrier velocity in the y direction	1.2×10^{5}	[33]	(m/s)
Φ_B	Schottky Barrier Height	0.865	[34]	(eV)
τ_p	Lifetime of holes	1×10^{-8}	[33]	(s)

4.2 Structural Optimization and Analysis of the GaAs Buried-gate Front-illuminated OPFET for Visible-Light Communication (VLC)

The optimization problem: Consistent with the scaling rules, the gate length and the active-layer thickness have a definite relation to each other. The gate length-doping concentration product is constant. The minimum and the maximum values of the active layer thickness have been defined for a given gate length. The maximum drain voltage that can be applied below the breakdown voltage is also stated.

Previous research did not establish whether there is a trade-off between bandwidth and f_T in OPFET as the gate length increases. The variation of the bandwidth with gate length has a complex dependence on various factors. These include the type of the gate and the semiconductor material used, the illumination model employed, the structural parameters utilized, the photon flux density used, and the values of series resistances. Cumulatively, these factors determine the relative contributions of the photovoltaic and the photoconductive effects and

hence the bandwidth. The bandwidth depends upon the magnitude and the relative variation of the photovoltaic and the photoconductive effects vis a vis the frequency. The degree of influence of the above listed factors on the transconductance and the gate-tosource capacitance of the device determines the dependence of f_T on gate length. The two photoeffects also have a significant bearing on the responsivity. The foregoing discussion delineates the parameters of the optimization problem. Although the above contributions affect the bandwidth and f_T-dependence on gate length, as a general rule, this work reveals for the first time that the 3-dB bandwidth has a direct relationship with gate length when the limiting factors such as series resistances and photoconductive effects are kept to their optimum values. Further, it is well established in literature that the f_T and responsivity decrease with the increase in gate length. Thus, a trade-off is established between bandwidth and f_T as well as between gain and bandwidth which calls for optimization.

The main aim of this work is to achieve simultaneous high-speed detection and amplification using GaAs buried-gate OPFET for OEIC-based VLC applications. The model has been studied by imposing a constraint on responsivity of greater than 2×10^5 A/W. The dimensions and the doping concentration have been appropriately varied to switch the photocontributions on and off. The value of the constraint has been adopted at the highest value reported for an APD in the visible region (Gaberl et al. 2014). The optimization is discussed under two conditions, namely, with and without constraints on the dark current.

Objective Function:

$Maximize(Bandwidth$ and $f_T) = f(structure) = f(L,Z,t_{sm},N_{dr})$

Subject to: Responsivity $> 2 \times 10^5$ A/W.

Where: $t_{sm(max)}=\frac{L}{\pi}$; $t_{sm(min)} = d_0 + 6L_D$; $LN_{dr} = 1.6 \times 10^{17}$;

L=(3 μm,. . . ,25 μm); Z=(100 μm,. . . ,1200 μm); t_{sm}=(0.26 μm,. . . ,7.8 μm);

The large values of gate lengths are considered for optimization to cover a

wide range of medium to long gate lengths on the basis that the 3-dB bandwidth increases with gate length as proposed in this work. Generally, devices with gate length shorter than 2 μm are short channel devices and vice versa for long channel devices. Short channel devices are known for their higher f_{Ts} but the bandwidth-dependence is not known. In this case too, the same bearing of bandwidth-dependence on gate length as that for long channel devices is expected and will be investigated in a future work. The scaling rules take into account the relationship between gate length, doping concentration, minimum and maximum active layer thickness, and the breakdown voltage at the chosen active layer thickness. There are no constraints on the gate width. Also, according to the authors' literature survey, there are no scaling rules in correlation with the reference (Golio 1988) which state the relation between the above parameters and the gate width. Thus, to cover a wide range of dimensions, the gate width is chosen between sufficiently low (100 μm) to sufficiently high (1200 μm) values. The simulations from medium gate lengths of 3 μm to 8 μm and long gate lengths of 8 μm to 25 μm are presented. The active layer thickness is chosen to satisfy the minimum and maximum values (0.26 μm to 7.8 μm) for each device. The structural optimization is carried out over the range of dimensions and doping concentrations as given in the objective function as well as below the breakdown voltage and only the most relevant eight sets of results are provided for analysis.

The performance metrics of the GaAs buried-gate OPFET have been evaluated using the MATLAB 2015a software. The device is biased in the saturation region of operation with the gate shorted to the source. There are no restrictions on the drain bias voltage except that it should be below the breakdown voltage. The gate to source voltage is set to a constant value of 0 V to avoid additional power supply and since the author intends to demonstrate clearly the fact the 3-dB bandwidth increases with gate length which can be understood only at a fixed gate-to-source voltage and photovoltage. The drain bias has no significant influence on the

dark current, bandwidth, and responsivity until it is biased in the pinch-off or saturation region of operation. The drain bias has a significant bearing on the unity-gain cut-off frequency. The amplification bandwidth (f_T) increases at high drain voltages since the gate-to-source capacitance reduces significantly although the transconductance remains almost constant. This decrease in capacitance is attributed to the complete depletion of most of the channel regions at high drain voltages, thus inducing insensitivity. The high f_{Ts} at larger drain voltages is the reason for high voltage operation. Since f_{Ts} tend to decrease with gate length, the bias voltages are scaled upwards. Generally, the avalanche photodiodes operate at high reverse bias voltages of about 24 V to 100 V [86, 87, 89]. Thus, the maximum bias voltage was limited to 50 V to keep it comparable to the photodiodes and to contrast the performance with that of the photodiodes while at the same time not significantly limiting the effective detection-cum-amplification bandwidth. The photon flux densities of 10^{16}, 10^{19}, and 10^{22} $/m^2$-s correspond to optical power densities of 0.33 μW$/cm^2$, 0.33 mW/cm^2, and 0.33 W/cm^2, respectively at an operating wavelength of 600 nm. Results of the structural optimization from the medium gate lengths (3 μm) to long gate lengths (25 μm) are listed in Table4.7 and 4.8 at the bandwidth frequency. The parameters employed in the calculation are presented in Table4.9.

In the figures to follow, **PV** stands for photovoltaic and **PC** for photoconductive. The first component of the total charge under illumination (see Eq.3.34) represents the PV charge, while the second and third components the photoconductivity. Figures 4.13, 4.14, and 4.15 depict respectively the variations of g_m, C_{gs}, and f_T with gate length at different photon flux densities. Figures 4.16, 4.17, 4.18, 4.19, 4.20, and 4.21, present the dependence of depletion width sensitivity, dark current/photocurrent, photogenerated charge, and bandwidth on gate length.

The device photocurrent gain accrues from two basic effects: the photovoltaic

Table 4.7: Results of structural optimization at the bandwidth frequency

Set No. and dimensions	Photon flux densities ($/m^2$-s)	Bias voltage (V) and Dark current (A)	Responsivity (A/W)	Bandwidth (Hz)	f_T (Hz)
1st set ($L = 3$ μm, $Z = 100$ μm, $t_{sm} = 0.27$ μm, $N_{dr} = 5.33 \times 10^{22}/m^3$)	0	10 V and **10.2 mA**	0 A/W	0 Hz	10.28 GHz
	10^{16}		3×10^9 **A/W**	**1.5 GHz**	**10.8 GHz**
	10^{19}		4.27×10^6 A/W	3.1 GHz	11.1 GHz
	10^{22}		1.4×10^4 A/W	1.6 MHz	16.2 GHz
2nd set ($L = 4$ μm, $Z = 150$ μm, $t_{sm} = 0.3$ μm, $N_{dr} = 4 \times 10^{22}/m^3$)	0	25 V and **13.1 mA**	0 A/W	0 Hz	10.68 GHz
	10^{16}		1.91×10^9 **A/W**	**1.625 GHz**	**10 GHz**
	10^{19}		2.69×10^6 **A/W**	**3.6 GHz**	**10.2 GHz**
	10^{22}		9.5×10^3 A/W	1.48 MHz	15.4 GHz
3rd set ($L = 5$ μm, $Z = 200$ μm, $t_{sm} = 0.4$ μm, $N_{dr} = 3.2 \times 10^{22}/m^3$)	0	30 V and 22.8 mA	0 A/W	0 Hz	8.4 GHz
	10^{16}		1.36×10^9 A/W	1.386 GHz	9.1 GHz
	10^{19}		1.9×10^6 A/W	3.326 GHz	9.2 GHz
	10^{22}		9.14×10^3 A/W	1.163 MHz	13.9 GHz
4th set ($L = 8$ μm, $Z = 350$ μm, $t_{sm} = 0.45$ μm, $N_{dr} = 2 \times 10^{22}/m^3$)	0	30 V and 23.7 mA	0 A/W	0 Hz	5.6 GHz
	10^{16}		6.15×10^8 A/W	1.625 GHz	5.3 GHz
	10^{19}		8.57×10^5 A/W	3.6 GHz	5.9 GHz
	10^{22}		4.57×10^3 A/W	1.1 MHz	7.5 GHz
5th set ($L = 15$ μm, $Z = 700$ μm, $t_{sm} = 0.6$ μm, $N_{dr} = 1.067 \times 10^{22}/m^3$)	0	40 V and 26.5 mA	0 A/W	0 Hz	3.26 GHz
	10^{16}		1.98×10^8 A/W	1.76 GHz	3 GHz
	10^{19}		2.73×10^5 A/W	3.6 GHz	3.3 GHz
	10^{22}		1.78×10^3 A/W	1.163 MHz	4.2 GHz
6th set ($L = 18$ μm, $Z = 850$ μm, $t_{sm} = 0.64$ μm, $N_{dr} = 8.9 \times 10^{21}/m^3$)	0	50 V and **29.6 mA**	0 A/W	0 Hz	2.81 GHz
	10^{16}		1.45×10^8 **A/W**	**1.9 GHz**	**2.4 GHz**
	10^{19}		1.98×10^5 A/W	4.57 GHz	2.6 GHz
	10^{22}		1.28×10^3 A/W	1.26 MHz	3.72 GHz

Table 4.8: Results of structural optimization at the bandwidth frequency (continued)

Set No. and dimensions	Photon flux densities ($/m^2$-s)	Bias voltage (V) and Dark current (A)	Responsivity (A/W)	Bandwidth (Hz)	f_T (Hz)
7th set ($L = 20$ μm, $Z = 950$ μm, $t_{sm} = 0.7$ μm, $N_{dr} = 8 \times 10^{21}/m^3$)	0	50 V and 34.6 mA	0 A/W	0 Hz	2.6 GHz
	10^{16}		1.22×10^8 A/W	1.9 GHz	2.2 GHz
	10^{19}		1.7×10^5 A/W	4.57 GHz	2.3 GHz
	10^{22}		1.16×10^3 A/W	1.26 MHz	2.9 GHz
8th set ($L = 25$ μm, $Z = 1200$ μm, $t_{sm} = 0.75$ μm, $N_{dr} = 6.4 \times 10^{21}/m^3$)	0	50 V and 33.3 mA	0 A/W	0 Hz	1.95 GHz
	10^{16}		8.1×10^7 A/W	2.063 GHz	1.85 GHz
	10^{19}		1.12×10^5 A/W	4.57 GHz	1.94 GHz
	10^{22}		0.72×10^3 A/W	1.48 MHz	2.6 GHz

Table 4.9: Parameters employed in calculation for structural optimization of GaAs Buried-gate OPFET for VLC

Parameter	Name	Value	Ref.	Unit
μ	Low field electron mobility	(0.5–0.64)	[10]	(m^2/V.s)
Φ_B	Schottky Barrier Height (Au-GaAs)	(0.86–0.9)	[171]	(eV)
v_{yn}	Saturated electron velocity	$\sim 1.2 \times 10^5$	[33]	(m/s)
v_{yp}	Saturated hole velocity	$\sim 0.9 \times 10^5$	[33]	(m/s)
τ_p	Lifetime of holes	10^{-8}	[33]	(s)
τ_n	Lifetime of electrons	10^{-6}	[33]	(s)
ϵ	Permittivity	1.14×10^{-10}	[10]	(F/m)
α	Absorption Coefficient @600 nm	4×10^6	[172]	(/m)

and photoconductive effects. In the depletion and neutral channel regions, the transport mechanisms are the drift and the diffusion respectively. The built-in electric field enables the photogenerated holes in the space charge region to cross the junction by inducing a drift and generating photovoltage. The photovoltaic gain arises from the fact that the device amplifies the photovoltage developed across the Schottky junction through transconductance. Photoconductivity arises from the drift of photogenerated electrons towards the drain under a positive drain-to-source voltage. The gain, expressed as the ratio of electron lifetime to transit time results from prolonged electron lifetimes and/or short transit times between source and drain. The photogenerated electron density in the neutral channel region reduces slightly owing to surface recombination.

At 3 μm gate length, the dark current is the lowest (10.2 mA) since the active layer thickness is low (0.27 μm) (Table4.7). Since the device is operated in the saturation region, the currents involved are large. The photovoltage developed is high ($\sim$0.52 V, $\sim$0.7 V, and $\sim$0.88 V) at the corresponding three flux densities of 10^{16}, 10^{19}, and 10^{22} $/m^2$-s owing to the buried-gate structure. In this structure, the additional factor of ($\alpha \times v_y \times \tau_{\omega p}$) in the equation for hole density (refer Eq.3.4) relative to the primary hole density induces the amplification effect. Due

to high photovoltage, responsivity is high ($> 10^9$ A/W, $> 10^6$ A/W, and $> 10^4$ A/W) with contributions from photoconductive effect especially at higher flux densities (10^{22} $/m^2$-s). The photoconductive contributions arise from the channel side illumination with improved absorption in the neutral channel region. The reduced depletion width due to the photovoltage boosts the photoconductive current. The photoconductive current arising from photogeneration in the neutral channel region is comparable to but significantly higher than that in the gate-depletion region. This fact is attributable to the relatively wider zero-bias effective channel thickness in comparison to the depletion region thickness. The bandwidth being inversely proportional to lifetime, and hole lifetime being of the order of nanoseconds, the bandwidth resulting from photovoltaic effect is large. On the other hand, the electrons with a lifetime of microseconds result in moderate photoconductive bandwidth. When the photovoltaic effect is the dominant mechanism, the bandwidth increases with the increase in the photovoltage. As such, the bandwidths achieved at the gate length of 3 μm at the corresponding three flux densities are 1.5 GHz, 3.1 GHz, and 1.6 MHz (Table4.7).

The transconductances are moderate (10.1 mS, 13 mS, and 16.5 mS) at the corresponding flux densities and are the lowest among all the sets (Fig.4.13). As the gate length increases, the doping concentration reduces (Golio 1988). In the absence of the series resistances, the change in depletion width with the gate-to-source voltage significantly increases with the decrease in doping concentration. However, in practical devices, such as OPFET, series resistances exist. At increasing gate lengths, the series resistances, source series resistance, in particular, limit the sensitivity of the depletion width to the applied gate-to-source voltage. Thus, the junction width sensitivity slightly rises at the lower gate lengths and saturates at the higher gate lengths as depicted in Fig.4.16. Larger currents saturate the sensitivity at higher gate lengths. Assisted by a decrease in the doping concentration, the saturation reduces the variation in the channel charge with the gate-to-source voltage. Although the junction width sensitivity

increases at the lower gate lengths, the channel charge experiences a periodic decrease in its value due to the reduction in doping concentration (Fig.4.17). But the gate width increases proportionally to the gate length. As a result, the drain-to-source saturation current which is the product of the electronic charge, the saturated electron velocity, the gate width, and the channel charge at the source end, proportionally increases with the gate length (Fig.4.17). Also, the elongation of gate length offers more longitudinal area for the channel charge. In spite of the periodic reduction in the doping concentration, as the gate length increases, the above-discussed factors raise the sensitivity of the drain-to-source current to gate-to-source voltage. Illumination enhances transconductances caused by the boosting of the photoconductive and photovoltaic effects (Fig.4.13).

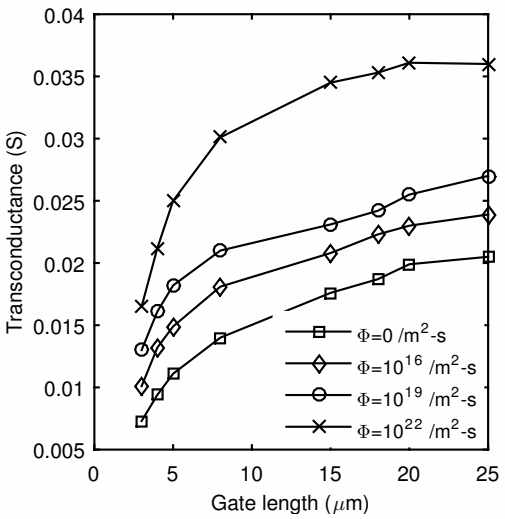

Figure 4.13: Transconductance versus gate length at different photon flux densities

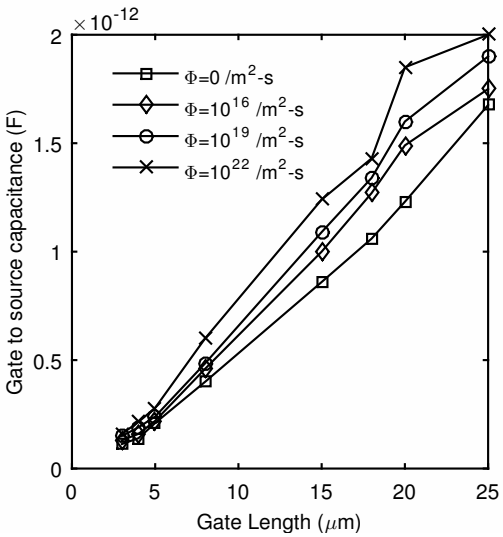

Figure 4.14: Gate-to-source capacitance versus gate length at different photon flux densities

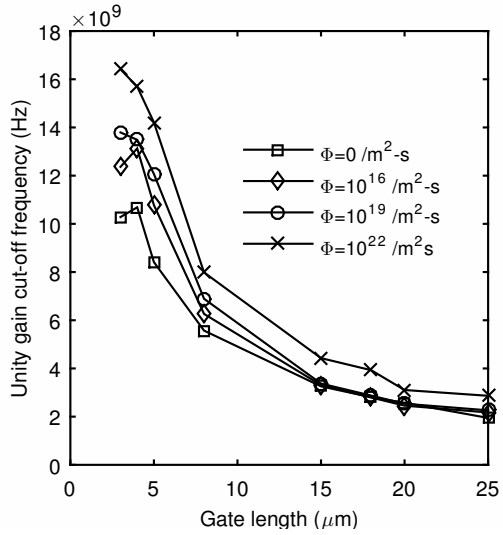

Figure 4.15: Unity-gain cut-off frequency versus gate length at different photon flux densities

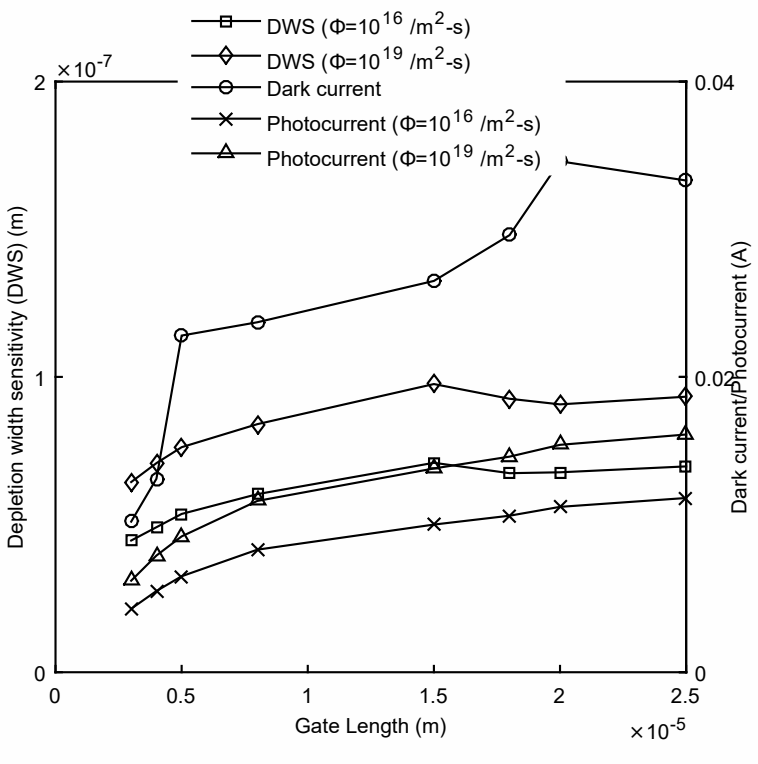

Figure 4.16: Depletion width sensitivity (DWS) (left) and dark/photocurrent (right) versus gate length at different flux densities

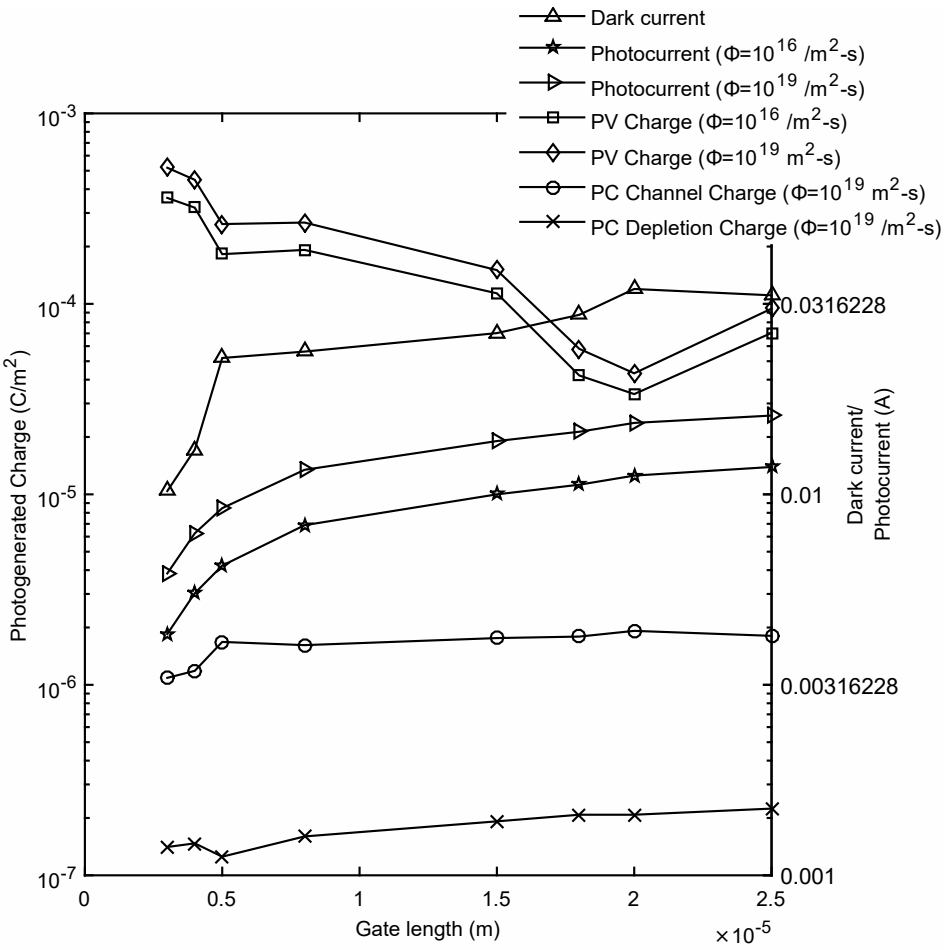

Figure 4.17: Photogenerated charge (left) and dark/photocurrent (right) as a function of gate length at different flux densities

For reasons stated above in connection with the discussion on transconductance, the gate-to-source capacitance is also the lowest at the gate length of 3 μm (0.13 pF, 0.15 pF, and 0.16 pF) (Fig.4.14). The only exception, however, is that the depletion charge replaces the drain-to-source current. Photovoltaic effect is the only factor responsible for the increase in capacitance with illumination (Fig.4.14). Capacitance is independent of the photoconductive effect as it is related only to space charge and independent of the channel charge. At the gate length of 3 μm, the f_T, which is the cumulative effect of moderate g_m and low C_{gs}, remains high (12.36 GHz, 13.79 GHz, and 16.41 GHz) (Fig.4.15). The f_T shows an increase with illumination since the rate of rise in transconductance with illumination is higher than that in the gate-to-source capacitance (compare Figs.4.13 and 4.14). Modulation of the input signal also modulates the device

parameters. At first, the parameters under consideration remain constant till the frequency attains to a certain level, beyond which they undergo a fall in values. Thus, at this gate length, the device can simultaneously detect and amplify the frequencies upto 1.5 GHz, 3.1 GHz, and 1.6 MHz with responsivities of 3×10^9 A/W, 4.27×10^6 A/W, and 1.4×10^4 A/W at the corresponding three flux densities.

When the gate length is increased from 3 μm to 4 μm, the dark current increases (13.1 mA) (Table4.7) whereas the photovoltage remains almost constant. The constant photovoltage results from a decrease in doping concentration, which widens the depletion region and enables photogeneration. Also, the moderate absorption coefficient of GaAs (4×10^6 /m) corresponding to an absorption depth of 0.25 μm is sufficient enough for photogeneration to take place in the depletion region. The photovoltage remains constant at all the gate lengths. The enhancement of the dark current is due to the higher device dimensions at the gate length of 4 μm. The higher gate length also boosts the photovoltaic and the photoconductive effects. The photocurrent generated due to photovoltage and the transconductance of the device are analogous to each other. Relative to the dark current, variation in the drain-to-source current with photovoltage generates photocurrent. On the other hand, transconductance represents the variation in the drain-to-source current with gate bias. Thus, the same reasons hold good for the increase in transconductance with gate length as well as the photovoltaic effect. Elongation of the gate length increases the active-layer thickness proportionally [154], besides increasing the gate width and the longitudinal area for the photoconductive charge. However, increasing the gate length prolongs the transit time of electrons between the source and the drain, but does not alter the lifetime. The prolonged transit time reduces the photoconductive gain. But this effect is not significant enough in comparison to the positive effect of the gate length on the photoconductive current. The electron mobility and the electron saturation velocity play but a minor role in the increase of photocurrent. The

enhancement in photovoltaic effect with the increase in depletion width sensitivity has a significant edge over that in the photoconductive effect resulting in increased bandwidth at the flux densities of 10^{16} and 10^{19} $/m^2$-s (1.625 GHz and 3.6 GHz) (see Figs.4.17 and 4.20 for correlation of PV and PC charge, photocurrent, and bandwidth). The series resistances and photoconductive effects play a minor role with lower currents involved and lesser area for photogeneration. For reasons stated earlier and because of availability of high optical power, at the flux density of 10^{22} $/m^2$-s, the increase in the photoconductive current supersedes the increase in photovoltaic effect. Hence there is a net reduction in bandwidth (1.48 MHz) (see Figs.4.19 and 4.21 for similar correlation as above). The transconductance is increased compared to that at 3 μm gate length (13.2 mS, 16.1 mS, and 21.2 mS) (Fig.4.13). The gate-to-source capacitance also increases (0.16 pF, 0.19 pF, and 0.215 pF) (Fig.4.14). However, the increase in the capacitance is more pronounced than the rise in the transconductance, causing a net decrease in the f_T value with this gate length (13.1 GHz, 13.35 GHz, and 15.7 GHz) (Fig.4.15).

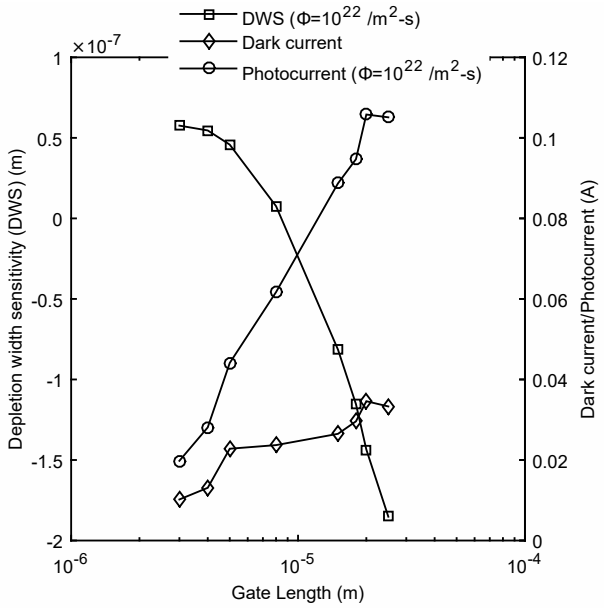

Figure 4.18: Depletion width sensitivity (DWS) (left) and dark/photocurrent (right) versus gate length at the flux density of 10^{22} $/m^2$-s

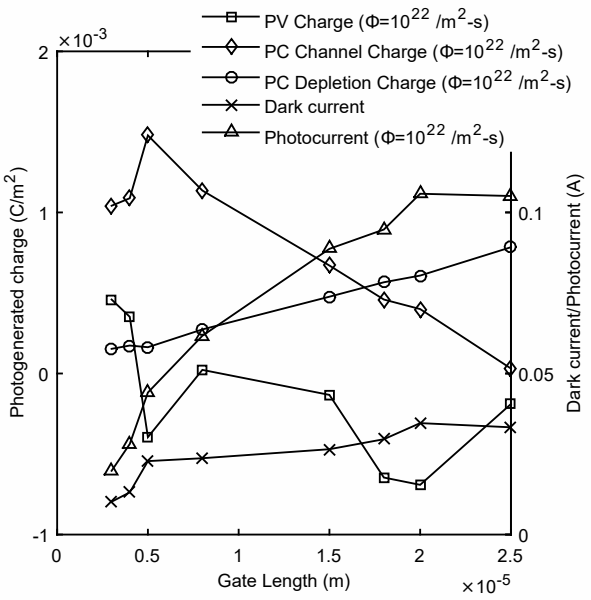

Figure 4.19: Variation of photogenerated charge (left) and dark/photocurrent (right) with gate length at the flux density of 10^{22} $/m^2$-s

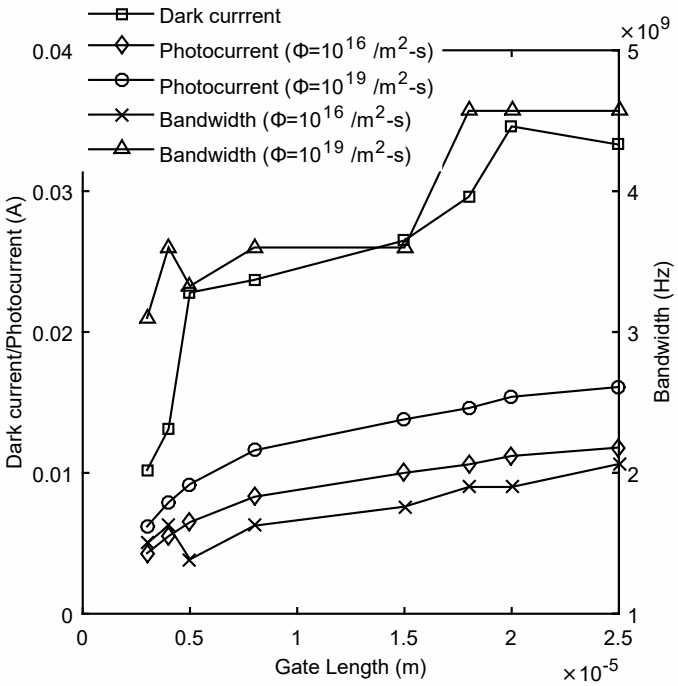

Figure 4.20: Dark/photocurrent (left) and 3-dB bandwidth (right) as a function of gate length at different flux densities

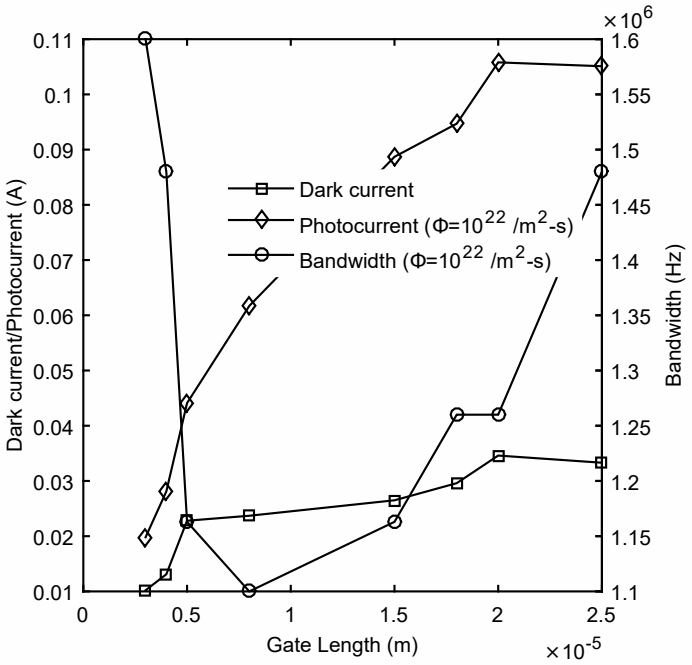

Figure 4.21: Dark/photocurrent (left) and 3-dB bandwidth (right) versus gate length at the flux density of 10^{22} $/m^2$-s

With total illumination of the device area, although the photocurrent intensifies with gate length, the total optical power applied to the device area ($Z \times L$) is considerably higher since the device area itself increases. Thus, the device generates lesser photocurrent per incident optical power with the elongation of the gate length signifying slightly reduced responsivity values (1.91×10^9 A/W, 2.69×10^6 A/W, and 9.5×10^3 A/W). The responsivities decrease further as the gate length increases. At the next higher gate length (5 μm), the active-layer thickness employed (0.4 μm) is much higher as compared to the first two sets. Hence the dark current is considerably larger (22.8 mA) (Table4.7). Owing to a large channel thickness, the photoconductive effects are significantly enhanced at all flux densities. However, the photovoltaic effect is still dominant at the lower intensities. At the flux densities of 10^{16} $/m^2$-s and 10^{19} $/m^2$-s, the high drain-to-source saturation current through the series resistance effect causes a significant reduction in the photovoltaic channel charge. In addition, insufficient gate width and length restrain production of significant photovoltaic effect. As a consequence of the above two factors, the bandwidth reduces (1.386 GHz, and

3.326 GHz) (refer Figs.4.17 and 4.20 for the correlation as stated previously along with the dark current). At the flux density of 10^{22} $/m^2$-s, the photoconductive effect is dominant, and hence the bandwidth decreases (1.163 MHz) (see Figs.4.19 and 4.21). The transconductance and the gate-to-source capacitance increase further (Figs.4.13 and 4.14) while the f_T continues to decrease (Fig.4.15).

With further increase in the gate length from 5 to 8 μm and so on till 25 μm, the dark current rises (Table4.7). At the lower intensities, the photovoltaic currents significantly increase owing to the employment of larger gate widths and lengths (see Fig.4.17). The photoconductive effects are also boosted. In fact, at larger intensities, as the gate length elongates, the photoconductive contribution from the gate-depletion region begins to increase since the higher currents involved increases the depletion width under illumination. In contrast, the contribution from the neutral channel region starts to decrease due to a decrease in the effective channel thickness (see Fig.4.19). At 8 μm gate length, there is an increase in the bandwidth (1.625 GHz and 3.6 GHz) owing to significant photovoltaic effect as compared to that at 5 μm gate length (refer Figs.4.17 and 4.20). At the higher gate length of 15 μm, the bandwidths are (1.76 GHz and 3.6 GHz). The increase in bandwidth at 10^{16} $/m^2$-s occurs from the enhancement of photovoltaic current with gate length and due to insignificant photoconductive effect at this intensity. At this juncture, remarkably, the photoconductive effect is fairly comparable to the photovoltaic effect at the flux density of 10^{19} $/m^2$-s (Fig.4.17). The bandwidth remains constant since the augmentation of photovoltaic effect exactly balances the boosting of the photoconductive effect. At 18 μm gate length, the depletion width sensitivity as well as both the photovoltaic and photoconductive effects increase considerably (Fig.4.17) due to the significantly higher gate width (850 μm) and length. But, the former supersedes the latter to give increased bandwidth (1.9 GHz and 4.57 GHz) (Fig.4.20). At longer gate lengths, there is almost saturation of the bandwidth. This is attributed to: the saturation of sensitivity of the depletion width to illumination (Fig.4.16); considerable reduc-

tion of photovoltaic charge causing significant saturation of photovoltaic current (Fig.4.17); and the significant boosting of photoconductive effect at these gate lengths (Fig.4.17). The photovoltaic and photoconductive effects exactly cancel each other out to maintain constant bandwidth. The phenomenon of saturation is evident from the near saturation of transconductance under the dark condition at higher gate lengths (Fig.4.13). Further, non-saturated transconductance under illumination emanates from the photovoltaic and photoconductive contributions.

At the higher flux density of 10^{22} $/m^2$-s under dc conditions, the devices with gate lengths from 15 to 25 μm experience a negative sensitivity, i.e. increase in depletion width with illumination (Fig.4.18). This can be ascribed to the very high photoconductive currents developed due to the high power levels involved and the reasons already explained. These currents introduce large voltage drops across the source series resistances, which are significantly higher than that under dark, giving negative sensitivity and producing zero photovoltaic currents (Fig.4.19). At high frequencies, the photoconductive current falls to lower values, the voltage drop developed is comparatively less, and significant photovoltaic effect exists. But since the dc current is only contributed by the photoconductive effect, with the elongation of the gate length, the boosting of this effect increases the bandwidth (Fig.4.18). The transconductance and the gate-to-source capacitance increase further (Figs.4.13 and 4.14) while the f_T continues to decrease (Fig.4.15). Overall, there is an increase in bandwidth at the lower intensities (10^{16} $/m^2$-s and 10^{19} $/m^2$-s). The increased bandwidth emanates from the fact that at a fixed gate-to-source voltage, the depletion width sensitivity due to the developed photovoltage is larger at lower doping concentrations (Fig.4.16). It further results in a gentler slope of the roll-off of the frequency response curve as the gate length increases. This fact broadens the frequency response and hence the bandwidth. This work addresses an important novel finding i.e. the 3-dB bandwidth is directly related to the depletion width sensitivity and hence, the

gate length at least at low to moderate intensities, when the limiting factors such as series resistances and photoconductive effects are kept to their minimum or optimum values. We demonstrate this relationship more specifically with the help of (Figs.4.22 and 4.23). Correlating Figs.4.22 and 4.23, it is observed that there is a one-to-one correspondence between depletion width sensitivity and bandwidth as the gate length increases. The intermediate and higher gate lengths have been purposefully excluded in these figures where the limiting factors play a significant role.

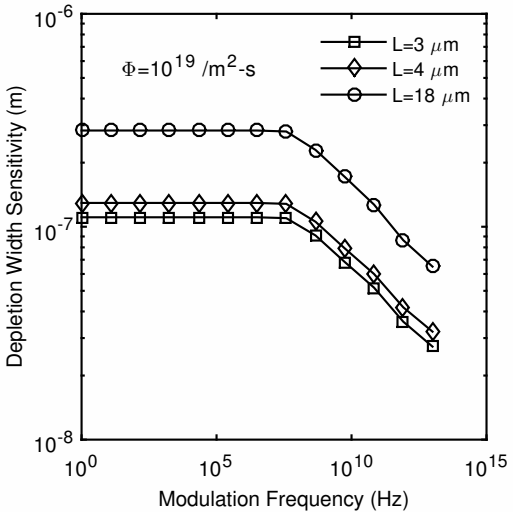

Figure 4.22: Depletion width sensitivity (DWS) versus modulation frequency at different gate lengths at the flux density of 10^{19} $/m^2$-s

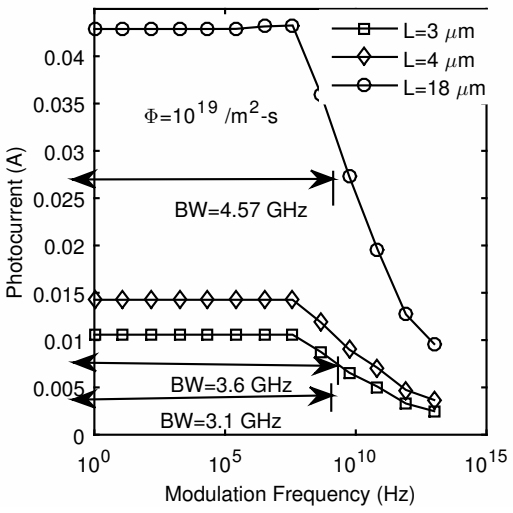

Figure 4.23: 3-dB bandwidth at different gate lengths at the flux density of of 10^{19} $/m^2$-s

In the present work, the illumination has a negligible effect on the minority

carrier lifetime since the photogenerated carrier density is negligible compared to the doping concentration.

The optimized values are indicated in bold in Table4.7. At a flux density of 10^{16} $/m^2$-s, the optimum value of gate length is 18 μm. At this gate length, the device exhibits a responsivity of 1.45×10^8 A/W or higher up to a detectable modulation frequency of 1.9 GHz (with simultaneous amplification) and a dark current of 29.6 mA (Table4.7). The optimum gate length value for a flux density of 10^{19} $/m^2$-s is 4 μm with the device responsivity of 2.69×10^6 A/W and above and a gain of greater than one till the detectable modulation frequency of 3.6 GHz and a dark current of 13.1 mA. On the other hand, for a flux density of 10^{22} $/m^2$-s, the constraint on responsivity is not satisfied. For lower dark currents, the optimum gate lengths are 3 μm and 4 μm. In the former case, at flux densities of 10^{16} $/m^2$-s and 10^{19} $/m^2$-s respectively, the device exhibits detection-cum-amplification bandwidths of 1.5 GHz and 3.1 GHz, responsivities of 3×10^9 A/W and 4.27×10^6 A/W or above and a dark current of 10.2 mA. In the latter case, the corresponding values are: responsivities of 1.91×10^9 A/W and 2.69×10^6 A/W or higher, bandwidths of 1.625 GHz and 3.6 GHz and a dark current of 13.1 mA (Table 4.7). Operation in the linear region can further reduce the dark current with little compromise in responsivity, bandwidth, but a significant reduction in f_T. The comparison of the present work with the reported results on photodiodes shows significant improvement (Table 4.10). The comparison also illustrates that the buried-gate OPFET has a low power detection efficiency as compared to detectors reported [86, 87, 89] which enables a larger transmission distance for communication. Further, the OPFET device has an higher f_T than that of the TIAs employed in [84, 87, 173]. The above results suggest that the device is capable of simultaneous detection and amplification at speeds greater than 1 Gb/s suiting the VLC applications. It can also provide a high sensitivity of greater than 10^6 A/W, which is much higher than the state-of-art p-i-n and avalanche photodiodes and is useful, especially in noisy environments.

Table 4.10: Performance comparison of the structurally optimized buried-gate front-illuminated OPFET with state-of-art photodetectors and amplifiers for VLC

Ref.	Detector type	Optical Power Density (W/cm^2)	Responsivity (A/W) @ Wavelength (nm)	Bandwidth (Detector) (Hz)	Amplifier Type and f_T (Hz)
[83]	PIN	NP	0.36 A/W @ 660 nm	1.35 GHz	TIA (25 GHz)
[91]	Photodiode (PD)	NP	0.21 A/W @ 660 nm	70 MHz	TIA (NP)
[173]	PD	NP	0.36 A/W @ 670 nm	60 MHz	TIA (4.5 GHz)
[84]	PIN	NP	0.52 A/W @ 660 nm	720 MHz	TIA (0.622 GHz)
[85]	PIN	NP	0.54 A/W @ 675 nm	995 MHz	TIA (NP)
[86]	APD	0.147 W/cm^2	27.9 A/W @ 670 nm	700 MHz	NP
[87]	APD	0.016 W/cm^2	30 A/W @ 670 nm	850 MHz	TIA (0.731 GHz)
[88]	APD	NP	0.28 A/W @ 450 nm	650 MHz	NP
[89]	APD	0.75 mW/cm^2	14.2 A/W @ 675 nm	960 MHz	TIA (NP)
[90]	APD	NP	2.61 A/W @ 450 nm	>90 MHz	TIA (NP)
This work	OPFET	0.33 mW/cm^2	2.69×10^6 A/W @ 600 nm	3.6 GHz	OPFET (10.2 GHz)

With further investigation, it is observed that the drain bias can be lowered for the first four sets of results substantially below the breakdown voltage to an optimum value without affecting the dark current, bandwidth, and responsivity, simultaneously lowering the fT but sufficient enough to maintain the same effective detection-cum-amplification bandwidth. At the last four set of dimensions, the drain voltage needs to be increased for maintaining the effective bandwidth. Thus, the optimum values of bias voltages for the corresponding eight sets are found to be 4.5 V, 3.7 V, 5.54 V, 7.14 V, 17.31 V, 19.23 V, 67.31 V, and 90 V. With the above results, the optimized device (lower dimensions) shows significant enhancement over that of PIN/PD detectors (Table 4.10) at comparable bias voltages whereas over that of APDs (Table 4.10) at much lesser voltages. The devices with higher dimensions show even better effective bandwidth performance at the cost of larger bias voltages.

4.3 Relatively New Aspects of Physics investigated from Structural Optimization

- At a fixed photovoltage, the change in the depletion width with gate-to-source voltage is larger at lower doping concentrations or in other words, at higher gate lengths.
- Although the depletion width sensitivity increases with gate length, the variation in the channel or the space charge decreases owing to the reduced doping concentration at higher gate lengths superseding the effect of depletion width sensitivity.
- The variation of the drain-to-source current increases as the gate length is increased due to the corresponding increase in the device dimensions.
- The photovoltage remains almost constant even though the gate length is increased.
- The transconductance and the gate-to-source capacitance rise with the elongation in gate length; however, the capacitance rise is more pronounced, resulting in the reduction in the unity-gain cut-off frequency with gate length.
- Responsivity decreases with the increase in the gate length.
- At a fixed doping concentration, the depletion width sensitivity to variation in the gateto- source voltage is larger at higher photovoltages as a result of which the transconductance and the gate-to-source capacitance rise with the increase in optical power.
- At a fixed gate-to-source voltage, the depletion width sensitivity to the developed photovoltage is larger at lower doping concentrations or in other words, at longer gate lengths.

- Bandwidth on the whole, at the lower flux densities (10^{16} $/m^2$-s and 10^{19} $/m^2$-s) increases with the gate length. More specifically, the slope of the roll-off of the frequency response curve becomes gentler as the gate length is elongated. At these flux densities, the photoconductive effect plays a minor role, only affecting the net bandwidth at long gate lengths.

- As the gate length increases, both the photovoltaic and the photoconductive effects are boosted. When the two effects are comparable, they tune the net bandwidth to lower values to a certain extent depending upon the contribution from the photoconductive effect.

- At the flux density of 10^{22} $/m^2$-s, the photoconductive effect is significantly high, relegating the bandwidth to much lower values as compared to that at lower intensities. As the gate length increases to 15 μm and above, the photoconductive contribution from the depletion region begins to increase while that from the neutral channel region begins to decrease.

- At the flux density of 10^{19} $/m^2$-s, the bandwidth saturates above 18 μm gate length.

- Above 15 μm gate length, at the flux density of 10^{22} $/m^2$-s, under dc conditions, the device exhibits negative sensitivity, i.e. it exhibits increase in the depletion width with illumination.

The factors limiting the process of optimization are the series resistances and the photoconductive effect.

4.4 Structural and Material Optimization of the GaAs Back-illuminated OPFET for Visible-Light Communication

High gain-bandwidth product and visible/UV contrast photodetectors are vital in Visible Light Communication (VLC) and Ultraviolet (UV) reflectance imaging

Table 4.11: Parameters employed in calculation for structural and material optimization of back-illuminated OPFET for VLC

Parameter	Name	Value (ITO-Si)	Value (Au-InP)	Value (ITO-GaAs)	Unit
μ	Low field electron mobility	($\sim$0.09)	($\sim$0.43)	($\sim$0.5)	(m^2/V.s)
Φ_B	Schottky Barrier Height	($\sim$0.71)	($\sim$0.8)	($\sim$0.98)	(eV)
v_{y1}	Saturated electron velocity	$\sim 9.4 \times 10^4$	$\sim 7.6 \times 10^4$	$\sim 1.2 \times 10^5$	(m/s)
v_y	Saturated hole velocity	$\sim 6.3 \times 10^4$	$\sim 5.6 \times 10^4$	$\sim 9 \times 10^4$	(m/s)
τ_p	Lifetime of holes	75×10^{-6}	0.3×10^{-6}	1×10^{-8}	(s)
τ_n	Lifetime of electrons	75×10^{-6}	0.3×10^{-6}	1×10^{-6}	(s)
ϵ	Permittivity	1.04×10^{-10}	1.11×10^{-10}	1.14×10^{-10}	(F/m)
α	Absorption Coefficient @600 nm	7.5×10^5	1×10^7	4×10^6	(/m)
α	Absorption Coefficient @350 nm	1×10^7	7.6×10^7	8×10^7	(/m)

applications respectively. Material and structural optimization is adopted to perceive such photodetectors with back-illuminated Optical Field Effect Transistor (OPFET).

The wavelengths used are 600 nm for the visible light and 350 nm for the UV radiation. The photon flux densities of 10^{16}, 10^{19}, and 10^{22} $/m^2$-s used in these simulations correspond to optical power densities of 0.33 μW/cm^2, 0.33 mW/cm^2, and 0.33 W/cm^2, respectively at 600 nm and 0.57 μW/cm^2, 0.57 mW/cm^2, and 0.57 W/cm^2 respectively at 350 nm. The structural optimization is performed over a wide range of medium gate lengths from 3 μm to 5 μm. However, only the four most relevant sets are provided here for comparison. The design variables are chosen based on the scaling rules stated in [16]. The materials being employed are Si, GaAs, and InP for the back-illuminated OPFET device with the gate electrodes being Indium-Tin-Oxide (ITO) for Si and GaAs, and gold (Au) for InP. The parameters used for calculation are given in Table 4.11. The simulated optimization results are presented in Tables 4.12, 4.13, 4.14, and 4.15.

Table 4.12: Comparative Studies of Si, InP, and GaAs back-illuminated OPFET detectors (1st set)

(v_{gs}=0 V, V_{DS}=10 V, λ=600 nm (visible) and 350 nm (UV)

1st set (L=3 μm, Z=100 μm, t_{sm}=0.15 μm, $N_{dr}=5\times10^{22}/m^3$)

Photon Flux Density ($/m^2$-s)	Photo-voltage (V)	I_{ds}	Responsivity (A/W)	g_m (S)	C_{gs}	f_T (Hz)	BW (Hz)	Photovoltage (V)	I_{ds}	Responsivity (A/W)
	Visible							UV		
Si back-illuminated OPFET with ITO gate										
0	0	0.36 mA	– – ––	1.4 mS	0.0546 pF	4.08 GHz	– – ––	0	0.36 mA	– – ––
10^{16}	0.28 V	0.9 mA	5.3×10^{8}	2.4 mS	0.084 pF	4.53 GHz	0.16 MHz	0.31 V	1 mA	3.53×10^{8}
10^{19}	0.46 V	1.7 mA	1.32×10^{6}	3.9 mS	0.105 pF	5.89 GHz	0.136 MHz	0.49 V	7.9 mA	4.33×10^{6}
10^{22}	0.606 V	15.6 mA	1.49×10^{4}	29.1 mS	0.0076 pF	606.7 GHz	0.57 MHz	0.61 V	16.1 mA	9×10^{3}
InP back-illuminated OPFET with Au gate										
0	0	0.27 mA	– – ––	2.3 mS	0.034 pF	10.7 GHz	– – ––	0	0.27 mA	– – ––
10^{16}	0.297 V	1.3 mA	9.97×10^{8}	4.3 mS	0.0695 pF	9.74 GHz	67.35 MHz	0.094 V	0.54 mA	1.53×10^{8}
10^{19}	0.476 V	2.2 mA	1.9×10^{6}	5.6 mS	0.092 pF	9.65 GHz	0.26 GHz	0.27 V	1.2 mA	5.2×10^{5}
10^{22}	0.65 V	27.8 mA	2.7×10^{4}	6.7 mS	0.016 pF	65.4 GHz	3.84 MHz	0.44 V	30.1 mA	1.71×10^{4}
GaAs back-illuminated OPFET with ITO gate										
0	0	97.1 μA	– – ––	0 mS	0 pF	0 GHz	– – ––	0	97.1 μA	– – ––
10^{16}	0.41 V	1.4 mA	1.24×10^{9}	5.5 mS	0.064 pF	13.7 GHz	1.5 GHz	0.19 V	0.37 mA	1.57×10^{8}
10^{19}	0.58 V	2.5 mA	2.4×10^{6}	7.5 mS	0.086 pF	13.8 GHz	6.3 GHz	0.37 V	1.2 mA	6.4×10^{5}
10^{22}	0.76 V	54.9 mA	5.37×10^{4}	67.2 mS	0.018 pF	596 GHz	1.1 MHz	0.55 V	44.9 mA	2.56×10^{4}

4.4.1 Series resistance and photovoltage analysis in Si, InP, and GaAs OPFETs

Beginning the discussion with the Si back-illuminated OPFET, this device exhibits the largest series resistances among all the material devices with similar dimensions in the visible range. The low electron mobility ($\sim$0.09 cm^2/(V.s)) in Si substantially reduces the current in the gate to source and gate to drain spacings. This raises the series resistance value to compensate for the fall with the increment in the depletion width through the voltage drop across the series resistance. Other materials, GaAs and InP exhibit lower and almost equal series resistances attributed to the higher mobility of GaAs ($\sim$0.5 cm^2/(V.s)) and InP ($\sim$0.43 cm^2/(V.s)). The series resistances play an important role in limiting the photocurrent. The series resistances decrease with illumination.

The photovoltage generated is almost the same in both Si and InP devices ($\sim$0.27 V, $\sim$0.46 V, and $\sim$0.61 V) in the visible range considering most of the sets. This can be explained as follows: InP possesses a high absorption coefficient of 1×10^7 /m corresponding to an absorption depth of 0.1 μm. Hence, the hole density experiences a considerable exponential decrease with distance upon crossing the Schottky junction. On the other hand, the moderate absorption coefficient of 7.5×10^5 /m in Si results in a large absorption depth (1.33 μm), thus, causing a lesser degradation of hole density. Further, the lower magnitude of absorption coefficient (7.5×10^5 /m), higher hole lifetime (75 μs), higher saturated hole velocity ($\sim$ 6.3×10^4 m/s), and lower barrier height ($\sim$0.71 eV) in the Si OPFET partly compensate the higher absorption coefficient (1×10^7 /m), lower hole lifetime (0.3 μs), lower saturated velocity ($\sim$ 5.6×10^4 m/s), and the larger barrier height ($\sim$0.8 eV) in the InP device. As a cumulative effect of the above described factors, the photovoltages saturate to same values in both the devices. On the other hand, the photovoltage generated in GaAs OPFET is enhanced

(∼0.398 V, ∼0.576 V, and ∼0.755 V). This is due to the moderate absorption coefficient of GaAs in the visible region (4×10^6 /m), the higher saturated hole velocity ($\sim 9 \times 10^4$ m/s), and the significantly higher Schottky barrier height of the ITO-GaAs junction (∼0.98 eV) superseding the effect of lower hole lifetime (10^{-8} s).

At the lowest gate length under consideration of 3 μm and the highest doping concentration of 5×10^{22} $/m^3$ (gate length-doping concentration product is constant from scaling rules [16]) with an active layer thickness of 0.15 μm, the OPFET devices exhibit the lowest dark and photocurrents among all the sets as described in the earlier sections.

4.4.2 Analysis of Si OPFET at 3 μm gate length and 0.15 μm channel thickness

The drain-to-source currents obtained using Si OPFET are (0.36 mA, 0.9 mA, 1.7 mA, and 15.6 mA). The large series resistances owing to the small active layer thickness (0.15 μm) and significantly high barrier height (∼0.71 eV) limit the said currents. At the flux density of 10^{16} $/m^2$-s, the photovoltaic effect is significant (0.28 V) whereas the photoconductive effect is negligible as compared to the photovoltaic effect (due to the lower power level) resulting in a current of 0.9 mA. As the flux density is increased to 10^{19} $/m^2$-s, the photoconductive effect also contributes in addition to the photovoltaic effect (0.46 V) owing to the higher power level and the long electron lifetime (75 μs). Most of the photoconductive contribution emanates from the depletion region since the major portion of the channel is depleted owing to high barrier height, small channel thickness, and the large series resistance which incurs significant voltage drop across it. This results in a quite high current of 1.7 mA. At the flux density of 10^{22} $/m^2$-s, the current is significantly enhanced (15.6 mA) owing to the boosting of the photoconductive effect. There is no photovoltaic contribution; instead the device shows negative sensitivity i.e. increase in depletion width with illumination. As such,

the responsivities attained are (5.3×10^8 A/W, 1.32×10^6 A/W, and 1.49×10^4 A/W) which are significantly high owing to the above discussed phenomena and the low dark current. The 3-dB bandwidths exhibited by this device are (0.16 MHz, 0.136 MHz, and 0.57 MHz). These megahertz range bandwidths are due to the long electron and the hole lifetimes (75 μs) upon which the bandwidth is inversely related through the modulation of carrier lifetime with frequency. At the lowest flux density, the bandwidth is 0.16 MHz due to the contribution from the photovoltaic effect alone. At the higher flux density, the bandwidth falls to 0.136 MHz due to both photovoltaic and photoconductive effects adding to the response. This can be explained by the fact that when the identical frequency responses of two independent comparable effects are added, the net frequency response exhibits reduced bandwidth as compared to the individual ones. As the flux density is increased further, the bandwidth rises to 0.57 MHz. This is attributed to the sole and substantially high contribution from the photoconductive charge as compared to the previous responses. The transconductances (1.4 mS, 2.4 mS, 3.9 mS, and 29.1 mS) and gate-to-source capacitances (0.0546 pF, 0.084 pF, 0.105 pF, and 0.0076 pF) obtained are the lowest among all the sets and increase with optical power as discussed in the earlier sections. However, at the highest flux density, the saturation component of current is insensitive to gate to source voltage, channel being completely depleted, but the transconductance is high due to the sensitivity of the conductance component of current evaluated at zero zero drain-to-source voltage. There is a significant drop in the gate to source capacitance at this flux density due to the de-ionization of the space charge ions in the depletion region. As such, the unity-gain cut-off frequencies attained are (4.08 GHz, 4.53 GHz, 5.89 GHz, and 606.7 GHz). Under UV illumination of 350 nm, the photovoltage is slightly enhanced (0.31 V, 0.49 V, and 0.61 V) as compared to that under visible light since Si possesses a larger absorption coefficient of 1×10^7 /m at the UV wavelength. The smaller active layer thickness (0.15 μm) enables significant number of holes to cross the junction before the gener-

ated carriers experience degradation due to the dependence on the distance. The series resistances experienced by the device are almost the same due to the slight difference between the photovoltages. The drain-to-source current is almost the same at the lower intensity (1 mA) whereas there is a considerable boosting of the current at the higher intensities. This is attributed to the large absorption coefficient of Si under UV light which augments the photoconductive charge in the depletion region. The currents so obtained are 7.9 mA and 16.1 mA. The lesser enhancement of current at the flux density of 10^{22} $/m^2$-s is due to the limitation of the drain-to-source conductance by the series resistances, and the large saturation current limiting the factor η defined in the theory section, restricting the total drain-to-source current. As such, the responsivities attained are (3.53×10^8 A/W, 4.33×10^6 A/W, and 9×10^3 A/W). The visible/UV rejection or the contrast ratios are very low (1.5, 0.3, and 1.65).

4.4.3 Analysis of InP OPFET at 3 μm gate length and 0.15 μm channel thickness

In the InP OPFET, the photovoltage is slightly enhanced (0.297 V, 0.476 V, and 0.65 V) as compared to the Si OPFET due to the small active layer thickness which eliminates the degradation of the generated carriers with distance as would occur in other cases. The series resistances are significantly lower than the Si OPFET but comparatively higher than that at higher gate length devices. The InP OPFET exhibits slightly larger photovoltage-induced currents (1.3 mA, and 2.2 mA) and higher transconductances (4.3 mS and 5.6 mS) than the Si OPFET at the lower intensities emanating from the lower series resistances, higher mobility, slightly larger photovoltages, and lower dark current in the InP device. At the flux density of 10^{22} $/m^2$-s, the photoconductive charge from the depletion region alone contributes significantly with the channel totally depleted. The InP detector generates a current of 27.8 mA as opposed to 15.6 mA in the Si OPFET. This can be explained by the larger absorption coefficient of InP producing substantial

amount of carriers in the depletion region along with the lower series resistances which do not limit the conductance as in the case of Si OPFET. However, the transconductance is significantly lower at this intensity in InP OPFET (6.7 mS) due to the lower electron saturated velocity in InP and the larger insensitive saturation current in Si OPFET enabling greater modulation of the drain to source current with gate bias through sensitivity of the much lower conductance component. The 3-dB bandwidths achieved are (67.35 MHz, 0.26 GHz, and 3.84 MHz). These bandwidths are higher than that in Si OPFET owing to the shorter hole and electron lifetimes (0.3 μs) in InP as compared to 75 μs in Si. The boosting of the photovoltage as the intensity is increased from 10^{16} to 10^{19} $/m^2$-s also boosts the bandwidth from 67.35 MHz to 0.26 GHz. At the flux density is raised to 10^{22} $/m^2$-s, the bandwidth drops to 3.84 MHz due to the following: Under dc conditions or at lower frequencies, the photoconductive effect is significantly high and is the sole contributor. However, as the frequency is increased, the photoconductive contribution starts decreasing due to the dependence of the electron lifetime on frequency. This reduces the voltage drop across the series resistance thus, widening the effective channel width and increasing the photovoltaic contribution. Hence, at the juncture of the 3-dB point, both the effects effectively contribute causing the drop in the bandwidth. The responsivities attained are (9.97×10^8 A/W, 1.9×10^6 A/W, and 2.710^4 A/W) which are higher than that in the Si device due to larger photocurrents. The gate-to-source capacitances attained in the InP device are (0.034 pF, 0.0695 pF, 0.092 pF, and 0.016 pF). These values are lower than that of Si device. This is explained by the fact that at a constant or slightly varying photovoltage and a fixed doping concentration, the depletion width sensitivity to the applied gate-to-source voltage is larger for the lower barrier height (and dielectric constant) device i.e. Si OPFET. The unity-gain cut-off frequencies thus obtained are (10.76 GHz, 9.74 GHz, 9.65 GHz, and 65.4 GHz). Under UV illumination, the photovoltages developed are substantially lower (0.0943 V, 0.27 V, and 0.44 V) than that in the visible region owing

to the very high absorption coefficient of InP in the UV region (7.6×10^7 /m) corresponding to an absorption depth (0.013 μm)). The drain-to-source currents obtained are (0.272 mA, 0.54 mA, 1.2 mA, and 30.1 mA). Due to the lesser photovoltages, the currents obtained are lower in the UV region upto the intensity of 10^{19} $/m^2$-ss. At the flux density of 10^{22} $/m^2$-s, the current is higher (30.1 mA) owing to the substantially high contribution from the photoconductive effect in the depletion region emanating from the larger absorption coefficient of InP in the UV region. The responsivities obtained are (1.53×10^8 A/W, 5.2×10^5 A/W, and 1.71×10^4 A/W) based on the above photocurrents. The visible/UV contrast ratios obtained are (6.516, 3.65, and 1.58).

4.4.4 Analysis of GaAs OPFET at 3 μm gate length and 0.15 μm channel thickness

This device develops photovoltages of (0.41 V, 0.58 V, and 0.76 V) which are substantially higher than the Si and the InP devices. Under dark, the channel is totally depleted on account of a large Schottky barrier height of ITO-GaAs junction (0.98 eV). Thus, the current from the device channel ceases to exist but there is a small current flowing in the device due to the presence of the shunt resistance. The higher photovoltages ought to have produced larger photovoltaic charge responses as compared to the other detectors (InP OPFET). However, since the channel is deeply depleted (beyond the active-layer thickness), the developed photovoltages do not open the channel wide enough (also limited by the series resistances) as opposed to the InP device. The InP device is partially depleted under dark and the generated photovoltages (0.297 V, 0.476 V, and 0.65 V) are able to significantly reduce the depletion width thus yielding greater photovoltaic charges than the GaAs device. In spite of this, the drain-to-source currents (97.1 μA, 1.4 mA, 2.5 mA, and 54.9 mA) and the transconductances (0, 5.5 mS, 7.5 mS, and 67.2 mS) achieved in GaAs OPFET under illumination are higher than the InP device. This is attributed to the higher electron saturated

velocity (1.2×10^5 m/s) of GaAs as compared to InP (7.6×10^4 m/s) and the lower dark current. At the flux density of 10^{22} $/m^2$-s, the photocurrent as well as the transconductance are considerably enhanced due to the substantially high contribution from the photoconductive effect in the depletion region as a result of moderate absorption coefficient of GaAs and one order of magnitude higher lifetime (1 μs). The gate-to-source capacitances under illumination (0.064 pF, 0.086 pF, and 0.018 pF), on the whole, are lower than the other devices due to the earlier stated fact that the sensitivity of depletion width to the change in the gate-to-source voltage is higher with devices bearing lower barrier height and lower dielectric constant when other factors are almost constant. As such, the f_T values attained are (13.68 GHz, 13.79 GHz, and 596.5 GHz). The 3-dB bandwidths exhibited by the device are (1.5 GHz, 6.3 GHz, and 1.1 MHz) which are considerably higher than the other two detectors at the lower intensities owing to the significant photovoltaic effect and lower hole lifetime (10^{-8} s) with the photovoltage increasing with the optical power. However, at the higher intensity, the bandwidth falls due to the significant sole contribution from the photoconductive effect with a large electron lifetime of 1 μs. The responsivities obtained are (1.24×10^9 A/W, 2.4×10^6 A/W, and 5.37×10^4 A/W) which are larger than the other two devices due to larger photocurrents. Under UV light, the response falls significantly (1.57×10^8 A/W, 6.4×10^5 A/W, and 2.56×10^4 A/W), due to the lower photovoltages (0.19 V, 0.37 V, and 0.55 V) emanating from the larger absorption coefficient of GaAs (8×10^7 /m) which enables lesser hole density to traverse the Schottky junction. In this case, the significantly high generation takes place only at or near the absorption surface. The photoconductive charge contribution at the high intensity of 10^{22} $/m^2$-s is comparable to that in the visible region since the absorption coefficients and absorption depths in the visible and UV regions compensate each other. The currents obtained are as (97.1 μA, 0.37 mA, 1.2 mA, and 44.9 mA). The contrast ratios obtained are (7.9, 3.75, and 2.1).

Table 4.13: Comparative Studies of Si, InP, and GaAs back-illuminated OPFET detectors (2nd set)

(v_{gs}=0 V, V_{DS}=10 V, λ=600 nm (visible) and 350 nm (UV)

2nd set (L=3 μm, Z=100 μm, t_{sm}=0.27 μm, $N_{dr}=5\times10^{22}/m^3$)

Photon Flux Density ($/m^2$-s)	Photo-voltage (V)	I_{ds}	Responsivity (A/W)	g_m (S)	C_{gs}	f_T (Hz)	BW (Hz)	Photovoltage (V)	I_{ds}	Responsivity (A/W)
	Visible							UV		
Si back-illuminated OPFET with ITO gate										
0	0	4.8 mA	– – – –	3.7 mS	0.1 pF	5.72 GHz	– – – –	0	4.8 mA	– – – –
10^{16}	0.28 V	5.8 mA	9.35×10^8	4.3 mS	0.12 pF	5.57 GHz	0.66 MHz	0.28 V	5.9 mA	6.43×10^8
10^{19}	0.46 V	7.3 mA	2.43×10^6	5.5 mS	0.14 pF	6.39 GHz	84.16 kHz	0.46 V	9.9 mA	2.94×10^6
10^{22}	0.606 V	28.3 mA	2.3×10^4	27.1 mS	0.0078 pF	554.3 GHz	0.57 MHz	0.59 V	28.1 mA	1.33×10^3
InP back-illuminated OPFET with Au gate										
0	0	5.9 mA	– – – –	4.5 mS	0.098 pF	7.23 GHz	– – – –	0	5.9 mA	– – – –
10^{16}	0.266 V	7.3 mA	1.34×10^9	5.3 mS	0.11 pF	7.6 GHz	32.9 MHz	0.1 mV	5.9 mA	0.0764
10^{19}	0.44 V	8.2 mA	2.2×10^6	4.9 mS	0.13 pF	5.9 GHz	0.39 GHz	42.1 mV	6.1 mA	1.02×10^5
10^{22}	0.62 V	16.8 mA	1.064×10^4	7.6 mS	0.034 pF	35.7 GHz	4.15 MHz	0.21 V	6.9 mA	5.4×10^2
GaAs back-illuminated OPFET with ITO gate										
0	0	7.5 mA	– – – –	6.7 mS	0.088 pF	12.1 GHz	– – – –	0	7.5 mA	– – – –
10^{16}	0.39 V	10.1 mA	2.55×10^9	7.6 mS	0.11 pF	10.9 GHz	12.87 GHz	2.6 mV	7.5 mA	48.9
10^{19}	0.57 V	11.7 mA	4.1×10^6	8.6 mS	0.13 pF	10.8 GHz	16.34 GHz	0.12 V	8.2 mA	4×10^5
10^{22}	0.75 V	88.1 mA	7.9×10^4	38.5 mS	0.018 pF	342 GHz	0.72 MHz	0.3 V	9.5 mA	1.15×10^3

4.4.5 Comparative Analysis of Si, InP, and GaAs OPFETs at 3 μm gate length and 0.27 μm channel thickness

As the active layer thickness is widened to 0.27 μm, keeping the gate length constant at 3 μm, the series resistances are significantly reduced owing to the wider thickness. However, they are still higher in the Si device as compared to the other two devices. The photovoltage remains almost the same in the Si and the GaAs OPFETs whereas it is slightly decreased in the InP OPFET explained by the possession of moderate absorption coefficient by Si and GaAs which enables significantly high hole density to cross the Schottky junction even if the channel thickness is increased. On the other hand, the high absorption coefficient of InP results in lesser hole density to traverse the junction when the channel is widened. With the increase in active-layer thickness, the drain-to-source currents and the photocurrents are substantially enhanced due to the increment in the conducting charge as well as the reduction in the series resistances, however, with some exceptions at higher intensity of 10^{22} $/m^2$-s. At this flux density, in InP OPFET, due to the low series resistance, and the moderate Schottky barrier height, the increase in the channel thickness leads to the partial depletion of the channel. Hence, both the neutral channel and depletion regions contribute to the photoconductive effect significantly. However, owing to the large absorption coefficient or small absorption depth of InP, the contribution from the depletion region is lesser as compared to that at the lower active-layer thickness. But, it is still larger than the neutral channel contribution attributed to the factor in the denominator of the electron density equation in the depletion region which is absent in the equation for electron density in the neutral channel region. This results in one order higher density in the case of depletion region considering the same thicknesses for their contribution (by inspection of the two equations). At this intensity, the photovoltaic effect also contributes to the response, due to partial depletion of the channel and the device does not exhibit negative sensi-

tivity. However, in overall, the response falls as compared to that at the lower channel thickness resulting in a lower current of 16.8 mA. In the other two detectors, these phenomena do not occur as the series resistance is sufficiently large in Si OPFET and the barrier height is considerably high in the GaAs OPFET thus maintaining complete depletion of the channel thickness at this flux density. Further, due to the moderate absorption coefficient of Si and GaAs (absorption depth is large), the photoconductive effect from the whole of the depletion region contributes significantly, thus, boosting the photocurrent. The devices exhibit negative sensitivity as usual at this intensity, thus, eliminating the photovoltaic response. The transconductances, in overall, are boosted as the channel thickness is increased owing to the larger currents involved and the lesser limitation of the depletion width sensitivity due to the lower series resistances. One anomalous behavior is observed at the flux density of 10^{19} $/m^2$-s in the InP OPFET, wherein the transconductance falls to 4.9 mS from its previous value of 5.6 mS at the lower active layer thickness and is also lower than its value (5.3 mS) at the flux density of 10^{16} $/m^2$-s. The reason behind this is still under our own investigation. The gate-to-source capacitance values increase with the increase in the channel thickness owing to the fact that at the lower channel thickness, with the applied drain-to-source voltage of 10 V, significant channel area is depleted as compared to that with the higher channel thickness. Thus, the change in the space charge with the change in the gate-to-source voltage is greater in the structure possessing larger channel thickness leading to the enhancement of the gate-to-source capacitance. As such, with the obtained tranconductance and capacitance values, the Si OPFET experiences an overall rise in f_T whereas the InP and the GaAs devices perceive a drop in the f_T with the widening of the channel thickness. With the enhanced photocurrents, on the whole, all the detectors show increased responsivities with the increment in the channel thickness. The 3-dB bandwidths obtained using Si device jare as (0.66 MHz, 84.16 kHz, and 0.57 MHz) as compared to its previous values at the lower channel thickness

(0.16 MHz, 0.136 MHz, and 0.57 MHz). The boosting of the bandwidth at the lower flux density is owing to the increase in the photovoltaic effect whereas the fall at the flux density of 10^{19} $/m^2$-s is due to the rise in the photovoltaic effect but simultaneous augmentation of the photoconductive effect due to widening of the channel thickness, thus, causing the drop. The reason for the constant bandwidth at the intensity of 10^{22} $/m^2$-s is still under our own study. The frequency responses of the InP device are (32.9 MHz, 0.39 GHz, and 4.156 MHz) at the higher active layer thickness as opposed to (67.35 MHz, 0.26 GHz, and 3.84 MHz) at the lower channel thickness. At the intensity of 10^{19} $/m^2$-s, the rise in the bandwidth is due to the increase in the photovoltaic effect. The slight increase in the bandwidth at the flux density of 10^{22} $/m^2$-s can be discussed as follows: At the lower channel thickness, at dc or lower frequencies, the photoconductive effect alone contributes but as stated earlier at the juncture of the 3-dB point, both the photovoltaic and the photoconductive effects are equally contributing. This results in a bandwidth of 3.84 MHz. On the contrary, at the higher channel thickness, under dc or lower frequencies, both the effects contribute significantly but the photoconductive charge is higher. As the frequency increases, the photovoltaic charge starts incrementing whereas the photoconductive charge starts decreasing. Thus, at the juncture of the 3-dB point, the photovoltaic charge has rose to significantly high value but the photoconductive charge has decreased significantly. Hence, the non-equally contributing charges results in a wider bandwidth (4.156 MHz).The reason behind the drop in the bandwidth at the optical intensity of 10^{16} $/m^2$-s is still being investigated (shows anomalous behavior being contrary to the increase in the photovoltaic effect). On the other hand, the bandwidths attained using GaAs OPFET are (12.87 GHz, 16.34 GHz, and 0.72 MHz) as compared to that at the lower channel thickness (1.5 GHz, 6.3 GHz, and 1.1 MHz). At the lower flux densities, the enhancement of the photovoltaic effect results in the rise in the bandwidth whereas at the higher intensity, the device shows anomalous behavior being contrary to the increase in the photoconductive

effect alone. The UV responses of the Si OPFET device (4.8 mA, 5.9 mA, 9.9 mA, and 28.1 mA) are almost the same as that in the visible region except at the flux density of 10^{19} $/m^2$-s (higher in the UV region) due to similar photovoltages and photoconductivity on account of the absorption coefficient of Si at the UV wavelength (1×10^7 /m) being sufficient enough to create substantial photogeneration. Due to the almost same photovoltages as that in the visible region, the series resistances almost remain unaltered. The responsivities and contrast ratios attained are (6.43×10^8 A/W, 2.94×10^6 A/W, and 1.33×10^4 A/W) and (1.45, 0.826, and 1.73) respectively signifying that the Si detector can function well in both the visible and UV regions. In the InP OPFET, there is significant degradation of photovoltage (0.105 mV, 42.1 mV, and 0.2107 V) and photocondcutive response at the UV wavelength owing to the very large absorption coefficient of InP (7.6×10^7 /m) and the higher channel thickness (0.27 μm). Due to the low photovoltages, the series resistances are higher. The currents involved are (5.9 mA, 5.9 mA, 6.1 mA, and 6.9 mA) leading to responsivities of (0.0764 A/W, 1.02×10^5 A/W, and 5.4×10^2 A/W). The contrast ratios thus obtained are (1.75×10^{10}, 22 and 19.7). This shows that the InP device with the structure under consideration can detect visible light with high responsivity under background UV radiation with rejection ratio of 1.75×10^{10} at the intensity of 10^{16} $/m^2$-s. At the higher intensities, the ratios are not high but can suffice in certain instances of applications. In the GaAs OPFET, similar situation occurs under UV illumination since the absorption coefficient of GaAs (8×10^7 /m) is identical to that of InP (7.6×10^7 /m) signifying small absorption depth. With this, the photovoltages produced are (2.6 mV, 0.12 V, and 0.3 V), the currents induced are (7.5 mA, 7.5 mA, 8.2 mA, and 9.5 mA) and the responsivities registered are (48.88 A/W, 4×10^5 A/W, and 1.15×10^3 A/W) rejecting UV wavelength with the factors of (5.21×10^7, 10.25, and 68.7).Thus, the rejection ratio is inferior to the InP OPFET at the lower intensities and vice versa at the higher intensity.

Table 4.14: Comparative Studies of Si, InP, and GaAs back-illuminated OPFET detectors (3rd set)

(v_{gs}=0 V, V_{DS}=25 V, λ=600 nm (visible) and 350 nm (UV)

3rd set (L=4 μm, Z=150 μm, t_{sm}=0.3 μm, $N_{dr}=4\times10^{22}/m^3$)

Si back-illuminated OPFET with ITO gate										
	Visible							UV		
Photon Flux Density ($/m^2$-s)	Photo-voltage (V)	I_{ds}	Responsivity (A/W)	g_m (S)	C_{gs}	f_T (Hz)	BW (Hz)	Photovoltage (V)	I_{ds}	Responsivity (A/W)
0	0	6.4 mA	– – – –	4.6 mS	0.12 pF	6 GHz	– – – –	0	6.4 mA	– – – –
10^{16}	0.286 V	7.7 mA	6×10^8	5.7 mS	0.145 pF	6.2 GHz	0.72 MHz	0.28 V	7.7 mA	3.5×10^8
10^{19}	0.46 V	10.3 mA	1.87×10^6	7.4 mS	0.16 pF	7.3 GHz	44.5 kHz	0.46 V	14.6 mA	2.34×10^6
10^{22}	0.607 V	91.6 mA	4.17×10^4	84.7 mS	0.011 pF	1.25 THz	0.41 MHz	0.58 V	90.2 mA	2.4×10^4
InP back-illuminated OPFET with Au gate										
0	0	7.9 mA	– – – –	5.7 mS	0.116 pF	7.73 GHz	– – – –	0	7.9 mA	– – – –
10^{16}	0.26 V	9.4 mA	7.4×10^8	7 mS	0.13 pF	8.4 GHz	92.6 MHz	Very less	7.9 mA	0
10^{19}	0.44 V	10.9 mA	1.47×10^6	7.9 mS	0.15 pF	8.2 GHz	0.36 GHz	10.7 mV	7.9 mA	0
10^{22}	0.61 V	24.2 mA	7.97×10^3	18.2 mS	0.044 pF	65.6 GHz	3.84 MHz	0.15 V	8.9 mA	279.1
GaAs back-illuminated OPFET with ITO gate										
0	0	9.4 mA	– – – –	8.3 mS	0.106 pF	12.3 GHz	– – – –	0	9.4 mA	– – – –
10^{16}	0.398 V	13 mA	1.75×10^9	9.4 mS	0.13 pF	11.4 GHz	4.57 GHz	0.3 mV	9.4 mA	0
10^{19}	0.576 V	14.6 mA	2.6×10^6	10.9 mS	0.15 pF	11.5 GHz	42.4 GHz	66.2 mV	10 mA	1.62×10^5
10^{22}	0.755 V	180.5 mA	8.39×10^4	28.9 mS	0.027 pF	171 GHz	0.615 MHz	0.24 V	11.5 mA	6.1×10^2

4.4.6 Comparative Analysis of Si, InP, and GaAs OPFETs at 4 μm gate length and 0.3 μm channel thickness

When the gate length is elongated from 3 μm to 4 μm with a proportionate increase in the active layer thickness from 0.27 μm to 0.3 μm and a corresponding increment in gate width from 100 μm to 150 μm, the doping concentration is reduced to from 5×10^{22} $/m^3$ to 4×10^{22} $/m^3$ considering constant gate length-doping concentration product from scaling rules [16]. These changes in the structural parameters have a significant change in the device parameters as discussed in the previous sections. At first, the series resistances are reduced due to the larger channel thickness. Secondly, the photovoltages remain almost unaltered owing to the materials' absorption depths which are sufficient enough to cause the hole density crossing the junction to experience very less carrier decay with distance. The drain to source currents are enhanced as also the photocurrents superseding the lower doping induced charge. The transconductances and gate to source capacitances are boosted. The photoconductive effects are also augmented. The resposivities decrease. However, in the case of Si and GaAs OPFETs, at the intensity of 10^{22} $/m^2$-s the responsivity increases due to large photoconductive effects. The bandwidths exhibited by the devices are: In Si OPFET, with the elongation of the gate length, the bandwidths attained are (0.72 MHz, 44.5 kHz, and 0.41 MHz) as opposed to (0.66 MHz, 84.16 kHz, and 0.57 MHz) at the lower gate length. The slight rise in the bandwidth at the intensity of 10^{16} $/m^2$-s is attributed to the fact that the depletion width sensitivity increases at lower doping concentration. The fall in the bandwidth at the flux density of 10^{19} $/m^2$-s in spite of the roll-off slope of the photovoltaic effect being gentler is owing to the increase in the photoconductive contribution due to larger channel thickness. The reason behind the drop in the bandwidth at the intensity of 10^{22} $/m^2$-s is still under study. On the other hand, in the InP OPFET, the bandwidths obtained are (92.6 MHz, 0.36 GHz, and 3.84 MHz) as compared to (32.9 MHz,

0.39 GHz, and 4.156 MHz) at the lower gate length. The same principles apply for the attained bandwidths at the flux densities of 10^{16} and 10^{19} $/m^2$-s, however, the slight fall in the bandwidth at the intensity of 10^{19} $/m^2$-s is due to the limitation by the series resistance. Whereas at the flux density of 10^{22} $/m^2$-s, there is slight drop in bandwidth. The 3-dB bandwidths attained with the GaAs OPFET device are (4.57 GHz, 42.4 GHz, and 0.615 MHz) as compared to (12.87 GHz, 16.34 GHz, and 0.72 MHz) at the lower gate length. The reduction in the bandwidth at the lower intensity is contrary to the fact of gentler roll-off slope of photovoltaic charge frequency response (reason behind it is under study) whereas it is in line with the said fact at the intensity of 10^{19} $/m^2$-s. The slight drop in the bandwidth at the flux density of 10^{22} $/m^2$-s is contrary to the increment in photoconductive response with gate length and is under investigation. Under UV illumination, in the Si OPFET, the photovoltages are almost the same as that in the visible region for reasons described at the lower gate length. The responsivities obtained are (3.5×10^8 A/W, 2.34×10^6 A/W, and 2.4×10^4 A/W) with the visible/UV contrast ratios as (1.71, 0.8, and 1.74). This shows again that at this gate length, the Si device can detect both the visible and UV wavelengths with high sensitivities. The InP OPFET can reject very well the UV radiation and detect visible light with the rejection ratios as (Very High, Very High, and 28.556) at this gate length ascribed to the significant degradation of photovoltages at the lower intensities and considerable response at the higher intensity owing to the higher optical power level. On the other hand, the GaAs OPFET exhibits rejection ratios of (Very High, 16.05, and 137.54). This can be explained as follows: Although the absorption coefficient of GaAs is almost the same as that of InP, the photovoltages generated in GaAs are slightly higher than that in InP owing to the larger barrier height. Hence, the GaAs device produces zero response (due to very low photovoltage) at the lower intensity whereas substantial responses (due to reasonable photovoltages and photoconductivity) at the higher intensities which account for the obtained ratios.

Table 4.15: Comparative Studies of Si, InP, and GaAs back-illuminated OPFET detectors (4th set)

(v_{gs}=0 V, V_{DS}=30 V, λ=600 nm (visible) and 350 nm (UV)

4th set (L=5 μm, Z=200 μm, t_{sm}=0.4 μm, N_{dr}=$3.2 \times 10^{22}/m^3$)

Si back-illuminated OPFET with ITO gate										
	Visible							UV		
Photon Flux Density ($/m^2$-s)	Photo-voltage (V)	I_{ds}	Responsivity (A/W)	g_m (S)	C_{gs}	f_T (Hz)	BW (Hz)	Photovoltage (V)	I_{ds}	Responsivity (A/W)
0	0	11.9 mA	– – – –	7 mS	0.18 pF	6 GHz	– – – –	0	11.9 mA	– – – –
10^{16}	0.289 V	13.8 mA	5.54×10^8	8.1 mS	0.216 pF	6 GHz	0.72 MHz	0.26 V	13.4 mA	2.55×10^8
10^{19}	0.47 V	17.5 mA	1.63×10^6	7.6 mS	0.23 pF	5.2 GHz	30 kHz	0.449 V	18.6 mA	1.14×10^6
10^{22}	0.61 V	150.2 mA	4.07×10^4	100 mS	0.013 pF	1.42 THz	0.42 MHz	0.56 V	143.7 mA	2.26×10^4
InP back-illuminated OPFET with Au gate										
0	0	13.8 mA	– – – –	6.2 mS	0.178 pF	5.5 GHz	– – – –	0	13.8 mA	– – – –
10^{16}	0.24 V	15.5 mA	5.1×10^8	7 mS	0.197 pF	5.6 GHz	62.2 MHz	Very less	13.8 mA	0
10^{19}	0.42 V	17 mA	9.3×10^5	7.6 mS	0.22 pF	5.5 GHz	0.33 GHz	Very less	13.8 mA	0
10^{22}	0.596 V	25.7 mA	3.5×10^3	0 mS	0.106 pF	0.65 mHz	6.2 MHz	6 mV	13.8 mA	0
GaAs back-illuminated OPFET with ITO gate										
0	0	17.5 mA	– – – –	7.9 mS	0.16 pF	7.6 GHz	– – – –	0	17.5 mA	– – – –
10^{16}	0.39 V	21.5 mA	1.18×10^9	12.7 mS	0.2 pF	10.1 GHz	19.1 GHz	Very less	17.5 mA	0
10^{19}	0.57 V	24.2 mA	2×10^6	10.6 mS	0.22 pF	7.65 GHz	19.1 GHz	0.13 mV	17.5 mA	0
10^{22}	0.75 V	275.4 mA	7.59×10^4	30 mS	0.036 pF	133 GHz	0.615 MHz	0.046 V	274.8 mA	4.42×10^4

4.4.7 Comparative Analysis of Si, InP, and GaAs OPFETs at 5 μm gate length and 0.4 μm channel thickness

As the gate is elongated from 4 μm to 5 μm, with a corresponding increase in the active layer thickness from 0.3 μm to 0.4 μm, and the gate width from 150 μm to 200 μm, the doping concentration is reduced to 3.2×10^{22} $/m^3$. This tends to increase the depletion width sensitivity but is significantly limited by the voltage drop across the series resistances since the large channel thickness induces high conducting charge under dark which considerably raises the dark current. The series resistances are substantially lowered due to large active layer thickness. The photovoltaic currents, transconductances, and the photovoltaic bandwidth tend to increase with the elongation of gate length as discussed earlier, but exhibit reduced or constant values at certain instances due to the series resistance limiting effects. The gate to source capacitances and photoconductive effects are enhanced. The responsivities attained at this gate length are (5.54×10^8 A/W, 1.63×10^6 A/W, and 4.07×10^4 A/W) which are lower than that at the previous gate length as the device uses more illuminated area for achieving the said photoresponse. In the UV region, the Si OPFET device generates slightly lower photovoltages due to the large channel thickness. The responsivities achieved are (2.55×10^8 A/W, 1.14×10^6 A/W, and 2.26×10^4 A/W). As such, the contrast ratios obtained are (2.17, 1.43, and 1.8). In the InP OPFET, the currents are further enhanced at the lower intensities whereas at the higher intensity, the photocurrent drops owing to the limited sensitivity caused by the presence of large dark current. This large dark current, in addition to the photocurrent creates large voltage drop across the series resistance. Thus, with a finite channel width due to moderate barrier height of Au-InP junction and the high absorption coefficient of InP, the photoconductive effect contributes non-significantly as compared to the lower gate length. In this case, the contributions are divided between the neutral channel region and the depletion region, with depletion region still the

major contributor. Hence, both the photovoltaic and photoconductive effects fall at this flux density at this gate length causing a drop in the photocurrent. The bandwidths drop at the lower flux densities (62.2 MHz, and 0.33 GHz) owing to the series resistance limiting effects. At the higher flux density, the bandwidth is raised (6.2 MHz). This can be discussed as follows: Under dc or lower frequencies, both the effects contribute significantly but here the photovoltaic effect contribution has increased and the photoconductive contribution has decreased (still photoconductive charge is higher). But as the frequency increases, the photovoltaic charge starts incrementing whereas the photoconductive charge starts decreasing. Thus, at the juncture of the 3-dB point, the photovoltaic charge has rose to significantly high value but the photoconductive charge has decreased significantly. Hence, the non-equally contributing charges results in a wider bandwidth (6.2 MHz). The responsivities attained are (5.1×10^8 A/W, 9.3×10^5 A/W, and 3.5×10^3 A/W) which account for the generated photocurrents and the optical power used under visible light. Under UV illumination, the photovoltages are severely degraded and the photoconductive responses are negligible owing to the very large absorption coefficient of InP and the larger active layer thickness which produce zero responsivities. Thus, the visible/UV contrast ratios are very high. This shows that the InP OPFET with a gate length of 5 μm is a high sensitivity detector with a very high contrast between visible and UV wavelengths but at the expense of a larger dark current. On the other hand, the GaAs OPFET device exhibits the same photovoltages as that with other gate lengths owing to the moderate absorption coefficient of GaAs even if the channel thickness is increased to 0.4 μm. The responsivities achieved are (1.18×10^9 A/W, 2×10^6 A/W, and 7.59×10^4 A/W) which account for the generated photocurrents utilizing larger illuminated areas. Under UV light, the photovoltages are significantly degraded. owing to the very large absorption coefficient of GaAs and wider channel thickness (0.4 μm). This produces zero photoresponses at the lower flux densities but at the higher flux density since the optical power level is high and on account of

the very high absorption coefficient of GaAs, the photoconductive effect from the depletion region is large. This is because the photovoltage is very low and the high photoconductive current develops significant voltage drop across the series resistance thus, making the channel totally depleted and producing high response (4.42×10^4 A/W). Hence, the visible/UV rejection ratios attained are (Very High, Very High, and 1.72). Thus, the GaAs OPFET is comparable to the InP OPFET at the lower intensities in terms of contrast ratio whereas it is inferior to the InP OPFET at the higher intensity.

4.5 Material and Illumination Model Optimization of the OPFET for Visible-Light Communication

Through material and illumination model optimization, the performance of Optical Field Effect Transistor (OPFET)-based detector-cum-amplifier in Visible Light Communication (VLC) applications has been enhanced. This work studied Si, InP, and GaAs materials and the buried-gate front-illuminated and generalized OPFET models.

4.5.1 Simulation set up and representation of results

The gate-to-source voltage has been set to 0 V while varying the drain-to-source voltage from 0 to 25 V. The operating wavelength is 600 nm. The device dimensions of 4 μm gate length, 150 μm gate width, 0.3 μm active layer thickness, and doping concentration of 4×10^{22} $/m^3$ used in this work satisfy the scaling rules [20] and are amongst the sets of optimum dimensions investigated in our work [8]. The specific device parameters have been obtained for the condition when the device is biased in the deep saturation region (25 V) for larger amplification bandwidth. At high drain voltages, even at constant transconductance, the amplification bandwidth (f_T) increases due to the reduction in the gate-to-source capacitance. Complete depletion of most of the channel regions induces insensi-

tivity suppressing the capacitance.

Table4.16 and 4.17 presents the performance metrics of the Si, InP, and the GaAs OPFETs. The material parameters used in calculation are the same as that given in previous section in Table4.11. Table4.18 and 4.19 represents the performance metrics of the detectors at bias voltages suitable for Signal-to-Noise ratio calculations.

4.5.2 Series resistance

The lower electron mobility in Si (0.09 m^2/(V.s)) as compared to InP (0.43 m^2/(V.s)) and GaAs (0.5 m^2/(V.s)) reduces the current flow in the spacings. As a result, the series resistance rises to compensate the fall in current. The series resistances, therefore in Si OPFET (Buried-gate (86.7 Ω, 53.5 Ω); generalized (192.9 Ω, 308.15 Ω); back-illuminated (192.9 Ω, 308.15 Ω) (all values under dark condition)) are higher than the InP (Buried-gate (18.2 Ω, 22.2 Ωs); generalized (51.4 Ωs, 69.9 Ω); back-illuminated (51.4 Ω, 69.9 Ω)) and the GaAs OPFETs (Buried-gate (15.16 Ω, 21.7 Ω); generalized (47.4 Ω, 68.71 Ω); back-illuminated (47.4 Ω, 68.71 Ω)). On the other hand, with comparable mobilities, the InP and the GaAs devices exhibit similar series resistances. The values listed above are for dark condition. Resistances reduce under illumination due to the photovoltaic effect.

Compared to the surface gate devices, the buried-gate structures exhibit lower series source and drain resistances. On account of the lower series resistances, the dark current is higher in the buried-gate device. The buried gate prevents the formation of a free surface depletion region to a large extent. In contrast, the surface gate devices induce considerable depletion width in the spacings. These findings are line with the reported literature [21,22] and can be explained by the existence of the fringing electric field between gate and source/drain in surface

Table 4.16: Comparative Studies of Si, InP, and GaAs buried-gate OPFET detectors

(v_{gs}=0 V, V_{DS}=25 V, λ=600 nm)

(L=4 μm, Z=150 μm, t_{sm}=0.3 μm, $N_{dr}=4\times10^{22}/m^3$)

Photon Flux Density ($/m^2$-s)	Photo-voltage (V)	I_{ds}	Responsivity (A/W)	g_m (S)	C_{gs}	f_T @DC (BW) Frequency (Hz)	BW (Hz)
Si buried-gate OPFET with ITO gate							
0	0	8.6 mA	– – – –	5 mS	0.12 pF	6.6 GHz	– – – –
10^{16}	0.69 V	12.2 mA	1.77×10^9	5.3 mS	0.23 pF	3.6 (8.7) GHz	0.32 MHz
10^{19}	0.87 V	13 mA	2.1×10^6	5.8 mS	0.068 pF	13.5 (9.7) GHz	1.87 MHz
10^{22}	0.97 V	132.9 mA	6.1×10^4	0 mS	0 pF	0 (0) GHz	14.6 kHz
InP buried-gate OPFET with Au gate							
0	0	9.4 mA	– – – –	6.8 mS	0.114 pF	9.4 GHz	– – – –
10^{16}	0.6 V	14.2 mA	2.3×10^9	8.4 mS	0.197 pF	6.75 (7.7) GHz	62.2 MHz
10^{19}	0.8 V	16 mA	3.2×10^6	12 mS	0.31 pF	6.2 (12.2) GHz	0.13 GHz
10^{22}	0.97 V	27.2 mA	8.73×10^3	16.2 mS	0.0566 pF	45.5 (41) GHz	9.2 MHz
GaAs buried-gate OPFET with ITO gate							
0	0	11.9 mA	– – – –	8.9 mS	0.11 pF	13 GHz	– – – –
10^{16}	0.64 V	18.5 mA	3.24×10^9	11 mS	0.16 pF	11 (14) GHz	4.57 GHz
10^{19}	0.82 V	20.8 mA	4.4×10^6	15.7 mS	0.075 pF	33.2 (13.2) GHz	10.1 GHz
10^{22}	0.99 V	41.3 mA	1.44×10^4	24.6 mS	0.15 pF	26 (14.7) GHz	1.87 MHz

Table 4.17: Comparative Studies of Si, InP, and GaAs generalized OPFET detectors

(v_{gs}=0 V, V_{DS}=25 V, λ=600 nm)

(L=4 μm, Z=150 μm, t_{sm}=0.3 μm, $N_{dr}=4\times10^{22}/m^3$)

Photon Flux Density ($/m^2$-s)	Photo-voltage (V)	I_{ds}	Responsivity (A/W)	g_m (S)	C_{gs}	f_T @DC (BW) Frequency (Hz)	BW (Hz)
Si generalized OPFET with ITO gate							
0	0	6.1 mA	– – – –	4.3 mS	0.12 pF	5.66 GHz	– – – –
10^{16}	1.91 V	16 mA	4.21×10^{9}	4.7 mS	0.078 pF	9.6 (7.07) GHz	0.72 MHz
10^{19}	2.45 V	19.1 mA	5.5×10^{6}	5.6 mS	0.088 pF	10.2 (9.2) GHz	1.1 MHz
10^{22}	2.77 V	125.7 mA	5.1×10^{4}	0.67 mS	0 pF	0 (0) GHz	48.2 kHz
InP generalized OPFET with Au gate							
0	0	7.7 mA	– – – –	5.7 mS	0.11 pF	7.85 GHz	– – – –
10^{16}	1.71 V	22.1 mA	6.15×10^{9}	0 S	0.099 pF	0 (16.14) GHz	0.19 GHz
10^{19}	2.25	V 22.1 mA	6.2×10^{6}	0 S	0.082 pF	0 (15.8) GHz	4.95 GHz
10^{22}	2.76 V	38.9 mA	1.33×10^{4}	17.7 pS	0.053 pF	52.9 (52.9) Hz	9.97 MHz
GaAs generalized OPFET with ITO gate							
0	0	9.4 mA	– – – –	8.3 mS	0.11 pF	12.1 GHz	– – – –
10^{16}	1.76 V	33.5 mA	1.03×10^{10}	9.7 mS	0.075 pF	20.4 (27.5) GHz	1 GHz
10^{19}	2.3 V	33.5 mA	1×10^{7}	0 S	0.098 pF	0 (22.2) GHz	68.4 GHz
10^{22}	2.8 V	70.7 mA	2.61×10^{4}	16.7 nS	0.053 pF	49.7 (49.7) kHz	1.6 MHz

Table 4.18: Performance metrics of Si, InP, and GaAs OPFET detectors for Signal-to-Noise Ratio calculations (v_{gs}=−1 V, V_{DS}=1.9 V, λ=600 nm) (L=4 μm, Z=150 μm, t_{sm}=0.3 μm, $N_{dr}=4\times10^{22}/m^3$)

	Si Back-illuminated OPFET		Si buried-gate OPFET	
Photon Flux Density ($/m^2$-s)	f_T @DC Frequency (Hz)	BW (Hz)	f_T @DC Frequency (Hz)	BW (Hz)
0	1.5 GHz	– – ––	1.29 GHz	– – ––
10^{16}	1.35 GHz	0.22 MHz	1.53 GHz	0.57 MHz
10^{19}	1.1 GHz	0.277 MHz	2.01 GHz	1.1 MHz
10^{22}	12.2 GHz	5.7 MHz	3.52 GHz	56.5 kHz
	InP Back-illuminated OPFET		InP buried-gate OPFET	
0	3.2 GHz	– – ––	3.63 GHz	– – ––
10^{16}	2.97 GHz	53.05 MHz	2.8 GHz	0.12 GHz
10^{19}	2.88 GHz	0.36 GHz	3.67 GHz	0.33 GHz
10^{22}	1.65 GHz	8.5 MHz	7.1 GHz	8.5 MHz
	GaAs Back-illuminated OPFET		GaAs buried-gate OPFET	
0	4.42 GHz	– – ––	5.56 GHz	– – ––
10^{16}	4.2 GHz	46 GHz	4.24 GHz	3.3 GHz
10^{19}	4.4 GHz	208.5 GHz	3.9 GHz	10.1 GHz
10^{22}	7.71 GHz	22.1 MHz	8.22 GHz	1.87 MHz

Table 4.19: Performance metrics of Si, InP, and GaAs OPFET detectors for Signal-to-Noise Ratio calculations (continued)
(v_{gs}=−3 V, V_{DS}=1.05 V, λ=600 nm)
(L=4 μm, Z=150 μm, t_{sm}=0.3 μm, $N_{dr}=4\times10^{22}/m^3$)

GaAs generalized OPFET		
Photon Flux Density ($/m^2$-s)	f_T @DC Frequency (Hz)	BW (Hz)
0	0 GHz	− − −−
10^{16}	3.67 GHz	0.11 GHz
10^{19}	3.1 GHz	0.5 GHz
10^{22}	2.44 GHz	57.4 MHz

gate devices, which enhances the depletion width, and hence the series resistances.

4.5.3 Photovoltage

The buried-gate and generalized models develop higher photovoltages than the back-illuminated OPFETs. The higher photovoltages are attributed to the additional factor of $(\alpha \times v_y \times \tau_{\omega p})$ in Eq.3.4 for hole density in buried-gate front-illuminated and generalized OPFETs which is absent in Eq.3.15 for hole density in back-illuminated devices. In addition, the high absorption coefficients and depths (1.33 μm, 0.1 μm, and 0.25 μm) in Si, InP, and GaAs materials along with the other pertinent factors generate a significantly large number of holes in the depletion region. The additional contribution from the sidewalls of the gate depletion region raises the photovoltages in the generalized model above the buried-gate model.

The InP and GaAs devices feature similar photovoltages in the front-illuminated models. In InP, the high absorption coefficient (1×10^7 /m), and moderate barrier height (0.8 eV) neutralize the shorter hole lifetime (0.3 μs) and low saturated hole velocity (5.6×10^4 m/ s). Similarly in GaAs, the moderate absorption coefficient (4×10^6 /m) and the short hole lifetime (10 ns) counterbalance the high saturated velocity (9×10^4 m/s) and the barrier height (0.98 eV). In the case of Si OPFET, at lower intensities, the slightly larger photovoltages are brought about by the long hole lifetime (75 μs). On the other hand, at higher intensity, the minority carrier lifetime under illumination [3] falls yielding constant photovoltages. For reasons explained in [8], the Si and InP devices in back-illuminated OPFET show identical photovoltages, but the GaAs device registers slightly larger photovoltages.

4.5.4 Drain-to-source current and frequency response

The drain-to-source currents are greatly sensitive to illumination. Depending upon the presence or otherwise of series resistances, the current given by Eq.3.37 is determined by the charge in the effective undepleted channel area at the source end of the device [16,17]. Two quantities constitute the total drain-to-source current: the saturation current and the drain-to-source conductance evaluated at $V_{DS} = 0$ V. Refer to the Theory Section of Chapter 3 for the factors determining the current components. Under dark and photovoltaic conditions, the conducting channel charge is higher in the InP OPFET due to the lower barrier height of Au-InP junction (0.8 eV) unlike the ITO-GaAs junction (0.98 eV). Compared to other material models, the higher series resistances in the Si OPFET models set the channel charge to lower values. Despite higher charge, the InP devices generate moderate currents because of lower mobility (0.43 m^2/(V.s)) and saturation velocity (7.6×10^4 m/s). In the GaAs detector, the high electron saturation velocity (1.165×10^5 m/s) and mobility (0.5 m^2/(V.s)) produce larger currents. Whereas, in the Si OPFET, lower charge and reduced mobility (0.09 m^2/(V.s)) produces lower currents. At the flux density of 10^{22} /m^2-s, due to the large photoconductive contribution, the Si, GaAs, and InP OPFETs generate large currents. The generated currents are in the decreasing order of magnitude on account of the long electron lifetime (75 μs) in Si as opposed to GaAs (1 μs) and InP (0.3 μs). In the generalized OPFET model, the currents involved are higher due to the large photovoltages developed.

Series resistances being equal in surface gate devices, the back-illuminated and generalized models produce the same dark current. However, owing to the higher series resistances that they have, surface gate devices generate lower dark current than the buried gate devices. In the back-illuminated model, at lower intensities, the low photovoltages increase the series resistances and reduce the photocur-

rents and drain-to-source currents. Eqs.3.29 and 3.31 make it apparent that under dc conditions, the magnitude of electron density in the depletion region is one order higher than the front-illuminated models. Factors $(1 + \alpha \times v_y \times \tau_{\omega n})$ and $(1 - \alpha \times v_y \times \tau_{\omega n})$ in Eqs.3.29 and 3.31 have the same significance as in [15]. High electron density brings about large saturation current in Si OPFET at higher intensity through negative sensitivity. Total current, however, is limited to an inferior value than in the other two models due to the reduced conductance on account of lower photovoltages. In the InP back-illuminated OPFET, the modest photoconductive charge arising from lower electron lifetime is insufficient to induce negative sensitivity. With low photovoltage, the InP OPFET generates nearly the same current as the buried-gate OPFET, whose photovoltaic charge compensates for the relatively low photoconductive contribution. The photovoltage-boosted photoconductive and photovoltaic charges push up current in the generalized InP model. GaAs back-illuminated OPFET records the highest current amongst all the devices and models since the large saturation current induced by negative sensitivity assisted by a high conductance enhances the total current. The high conductance in GaAs OPFET results from the higher photovoltage, as also from high electron mobility, and low series resistances.

Bears as it does an inverse proportion to the carrier lifetime, bandwidth is the highest under photovoltaic conditions in GaAs OPFET with a shorter hole lifetime (10 ns) as compared to InP (0.3 μs) and Si (75 μs). Boosted by optical power, the photovoltage elevates the device sensitivity and bandwidth. Influenced by large photovoltages, the generalized model overall shows a superior bandwidth performance to the buried-gate and back-illuminated OPFETs. Currents generated in the three generalized models are shown in Table 4.17. At the flux density of $10^{16}/m^2$-s, the photovoltage of 1.76 V reduces the depletion width at the source end to zero in the GaAs and InP devices. Increased optical power does not affect the effective channel thickness and maintains a constant photovoltaic charge. As

a consequence, at the intensity of 10^{19} $/m^2$-s, the GaAs generalized model bandwidth increases to 68.4 GHz in comparison to the back-illuminated OPFET (42.4 GHz) and the buried-gate model (10.1 GHz). The same is the case with the InP OPFET. The result is the outcome of the very high photovoltage in the generalized model (2.3 V), which reduces the depletion width at the source end below the zero point. Though both the photovoltage and photocurrent experience roll-off with frequency, the photocurrent starts roll-off at a higher frequency. Initially, when the photovoltage drops with frequency, the depletion width is still zero maintaining constant current. With further increase in frequency, the depletion width returns to its finite value and begins to increase. Thus, the current shows rolloff at a wider point than that under normal circumstances. This phenomenon, combined with the influence of the high photovoltage results in enhanced bandwidth. At the intensity of 10^{16} $/m^2$-s, as opposed to the back-illuminated device (4.57 GHz) and buried-gate OPFET (4.57 GHz), the drop in the bandwidth in GaAs generalized OPFET (1 GHz) arises from a large current enhancing the series resistance effects. In the generalized model, the gate depletion region and its sidewalls contribute identical frequency responses to lower the bandwidth. On the other hand, in the Si generalized OPFET device, the non-equal photocurrents at lower intensities (16 mA, 19.1 mA, and 125.7 mA) are due to the non-zero depletion width at the source end maintained by the large series resistances. Thus, the effect of bandwidth enhancement observed in the InP and GaAs OPFETs at the intensity of 10^{19} $/m^2$-s is not registered in the Si device.

An important feature of the back-illuminated OPFET under photovoltaic conditions is the differential roll-off rate of the frequency response curve. It varies as $(\alpha \times \Phi \times \tau_{\omega p})$ in contrast to the buried-gate and generalized models which vary as $(\alpha^2 \times \Phi \times v_y \times \tau_{\omega p}^2)$ (see Eq.3.4 and 3.15). In the generalized model, two more similar contributions from the sidewalls of the gate depletion region add to this primary roll-off rate. The fact that the squared lifetime term pro-

duces steeper slope than the non-squared, the frequency response curve is wider for back-illuminated OPFET. In the buried-gate model, at lower intensity, the larger photovoltaic effect on the bandwidth assisted by the lower series resistances dominates the roll-off rate. However, when the intensity increases, the effect of roll-off rate is felt more than the magnitude of the photovoltage. With some exceptions, the above features are evident from the values of 3-dB bandwidths as shown in Tables 4.14, 4.16, and 4.17. At the intensity of 10^{19} $/m^2$-s, the Si back-illuminated OPFET exhibits lower bandwidth than the other two models. As explained earlier, the reduction in bandwidth is caused by a boost in the photoconductive charge at this intensity also, with comparable contributions from the photovoltaic effects. When two comparable effects with equal carrier lifetimes add in terms of frequency responses, the resulting net bandwidth is lower than the individual bandwidths. Another exception occurs at the flux density of 10^{16} $/m^2$-s in the GaAs back-illuminated OPFET. The bandwidth remains constant as that of the buried-gate OPFET (4.57 GHz), but increases as compared to the generalized OPFET (1 GHz). This phenomenon is explainable by the fact that when the hole lifetime is very short, as in the case of GaAs, the roll-off rate dominates the photovoltage. Also, the photovoltage in the GaAs back-illuminated OPFET is enhanced as compared to the other material detectors [8]. These two factors hold the bandwidth at constant values in the GaAs back-illuminated and buried-gate OPFETs. For reasons stated earlier, the bandwidth in the generalized model drops. Even more exceptions occur at the intensity of 10^{19} $/m^2$-s, at which the GaAs and InP generalized models exhibit enhanced bandwidths.

The illumination level of 10^{19} $/m^2$-s used in this work (2250 lx) is higher than the minimum illuminance standard of 200 lx specified in ISO/CIE 8995.1 for indoor work places with continuous work. It is also lower than the safety limit specified in ISO 8995-1: 2002. However, the background light ($\sim$400 lx) photocurrent is comparable to the photocurrent at the illumination level of 10^{19}

$/m^2$-s. Also, the illuminance level of 10^{16} $/m^2$-s (2.3 lx) is lower than the minimum illuminance standard. Thus, the devices can be used under dark or very low background lighting conditions. Alternatively, the same high frequency modulated optical source can be used for lighting the room as well as for VLC communication (at 10^{19} $/m^2$-s). To increase the illuminance, the number of optical sources can be increased without exceeding the safety limits.

High background lighting conditions, on the other hand, require optical sources of high brightness. This work, therefore, has also considered OPFET devices under optical flux density of 10^{22} $/m^2$-s. At this flux density, against the generalized model (48.2 kHz) and the back-illuminated OPFET (0.41 MHz), Si buried-gate OPFET exhibits a bandwidth of 14.6 kHz. In the Si back-illuminated OPFET, with large photoconductive effect, as the frequency increases, the photoconductive contribution reduces while the photovoltaic effect increases. At or near the 3-dB point, the contribution is still dominated by the photoconductive effect since the photovoltage is low. With unequal contributions from the photoconductive and photovoltaic effects, the bandwidth level is high. In the Si buried-gate OPFET, as compared to the back-illuminated OPFET, the inferior photoconductivity modulated by the higher photovoltage results in comparable contributions and a reduction in bandwidth. On the other hand, in the Si generalized model, there is a high photoconductive contribution from the semi-insulting substrate in addition to the gate depletion region. Despite the high photovoltage, its less pronounced effect than that of the photoconductive effect, shifts the bandwidth to lie between those of the buried-gate and back-illuminated models. In the case of the InP back-illuminated OPFET, the bandwidth is 2.6 MHz in contrast with the buried-gate model (9.2 MHz) and the generalized model (9.97 MHz). The only dominant mechanism of photocurrent in the InP back-illuminated model is the photoconductive contribution from the depletion region with a bandwidth of 2.6 MHz. In the buried-gate OPFET, under dc conditions, the photoconduc-

tive effect from the neutral channel region and the photovoltaic effect contribute comparably. As the frequency increases, the photoconductive contribution decreases with a concomitant reduction in the series resistance effect. The photovoltage also reduces with frequency. But due to the lower series resistance effect and with the large photovoltage effectively cancelling the barrier height, the photovoltaic charge is maintained at a constant level upto a wide frequency range. The combined effect of the two contributions results in a broadening of the bandwidth. In the generalized model, similar criteria hold good, resulting in a bandwidth comparable to the buried-gate model. In the GaAs buried-gate and the generalized OPFETs, various regions contribute with similar magnitudes of charges. Hence, almost the same bandwidths are observed. But, the back-illuminated model exhibits reduced bandwidth due to the higher magnitude of photoconductive charge.

4.5.5 Transconductance, gate-to-source capacitance, and unity-gain cut-off frequency (f_T)

The dc transconductances of GaAs buried-gate OPFET devices are higher than those of the InP and Si devices. With analogous photovoltages and series resistances in the InP and GaAs devices, the transconductance would have been higher in the InP device. This derives from the fact that at fixed doping concentration and constant photovoltage, the depletion width sensitivity to the applied gate bias is larger in the device with lower barrier height, i.e. InP OPFET. But, the factors mentioned earlier for the enhancement of the drain-to-source current account for the attained transconductances. The higher series resistances and other factors stated earlier for Si OPFET limit the sensitivity to the applied gate bias, causing a fall in the transconductances. The transconductance bears a direct proportion to the optical power since at a fixed doping concentration, the depletion width sensitivity to the gate to source voltage is higher at larger photovoltages. At the higher flux density, the channel of Si OPFET, depleted by

a large photoconductive effect reduces the transconductance to zero. The gate to source capacitances attained in the GaAs detector in contrast with InP detector and Si detector are as shown in Table 4.16. The tabulated values follow the same rationale as of the transconductance, but with a difference that the space charge in the gate depletion region and its sidewalls replace the drain-to-source current. Photovoltages in the Si OPFET are either equal or marginally higher. Capacitance of the device is independent of saturation velocity and electron mobility, but dependent on Schottky barrier height and dielectric constant. For any device with lower barrier height and dielectric constant which is true for Si OPFET, with the photovoltage held constant, the depletion width sensitivity to applied gate-to-source voltage is larger for a given doping concentration. This relation reflects in higher capacitance values in Si OPFET followed by the InP and GaAs detectors. At higher intensities, however, an anomalous behaviour marked by arbitrary values and capacitance drops are observed. The drops in capacitances are caused by (i) the effective cancellation of the depletion width by the developed photovoltage or (ii) by the de-ionization of the space charge ions by the photoconductive electrons. GaAs OPFET has the highest unity-gain cut-off frequencies brought about by larger transconductances followed by the InP and Si OPFETs.

The dc transconductances of the generalized GaAs OPFET is reduced at the lower intensity and severely degraded at the higher optical power levels. The large currents in the GaAs generalized model besides the depletion width values nearing zero and the higher series resistances in surface-gate devices limit the sensitivity at the lower intensity. At higher intensities, the depletion width is beyond the zero point at the source end. Thus, any variation in the gate-to-source voltage is of no consequence. Similar results hold good for the InP OPFET. In the Si OPFET, there is no significant degradation of the transconductance since the depletion width is finite. The gate-to-source capacitances are unaffected but

decrease slightly with optical power at lower intensities, but drop significantly at higher intensity. The values are typically smaller than in the buried-gate device. The large photovoltages reduce the depletion width to zero in some of the channel regions. Additionally, with increased optical power, the depletion width reduces to zero in several other regions, causing a fall in capacitance. At the higher intensity, the drop in capacitance is attributed to the de-ionization process as discussed earlier.

The Si back-illuminated OPFET exhibits comparable dc transconductances to those in buried-gate OPFET at lower intensities. This phenomenon occurs in spite of the fact that at a fixed doping concentration and other constant parameters, the depletion width sensitivity to the applied gate to source voltage is larger in the device with higher photovoltages, such as the buried-gate OPFET. Also, in the buried-gate device, in spite of larger currents, the lower series resistances induce voltage drops of smaller magnitude. The comparable transconductances of Si back-illuminated OPFET are explainable by the negligible sensitivity of channel conductance to the applied bias at the source end of the device in the buried-gate OPFET. This fact occurs due to the effective cancellation of the barrier height by the induced photovoltage, although the magnitudes of conductance and saturation current are higher. In the back-illuminated model, the photovoltages are small, thus showing variation in conductance with applied bias. At the higher intensity, the transconductance rises to 72.6 mS as compared to 0 mS in the buried-gate OPFET. In the latter case, the saturation current and conductance are alike insensitive to applied bias due respectively to negative sensitivity and zero depletion width. On the contrary, in the back-illuminated OPFET, the large saturation current and the sensitive conductance results in high transconductance in spite of the insensitive saturation current. The depletion width sensitivity reduced by the lower photovoltage brings down the capacitance at the lower intensity. The lower photovoltages in back-illuminated OPFET rule out

the effective cancellation of the depletion width by the photovoltage. At higher intensities, therefore, the back-illuminated device capacitances exceed those in the buried-gate OPFET. At lower intensities, the dc transconductances are higher in the buried-gate OPFET models than in the back-illuminated models of the InP and GaAs materials. These findings are explained by the larger photovoltages, lower series resistances, and by the fact that the photovoltages do not effectively cancel the barrier height in the buried-gate OPFETs. The analysis and the findings apply commonly to the capacitances and transconductances. At the higher intensity, the transconductance in the InP back-illuminated OPFET is enhanced as compared to the buried-gate model since both the conductance and the saturation components of current are sensitive to the applied bias in the former case. The latter case displays insensitivity of the conductance parameter. For GaAs OPFET, the insensitive, large saturation current and sensitive conductance in the former case balance out the sensitive, modest saturation current and insensitive conductance in the latter case. The corresponding transconductance, therefore, in the GaAs OPFETs remains the same in both cases. At higher intensity, the capacitance in the InP back-illuminated OPFET is comparable to the buried-gate model. The magnitude of the deionization process in the back-illuminated model, and similar effect of the effective cancellation of barrier height in the buried-gate OPFET explains the finding. Contrarily, the de-ionization process ensures that the capacitance of the GaAs back-illuminated model is less than that of the buried-gate model. The de-ionization process is absent in GaAs buried-gate OPFET as the magnitude of photoconductive charge is small. The back-illuminated model undergoes no effective cancellation of the depletion width by the photovoltage. It occurs to a smaller extent in the buried-gate model. The larger photovoltage in the buried-gate model thus enhances the capacitance. The similar transconductances observed in the Si generalized and back-illuminated models at the lower intensities are attributable to the same reasons as for buried-gate OPFET.

At the bandwidth frequency i.e. under ac conditions, the unity-gain cut-off frequency remains constant, or decreases, or increases as compared to the dc values depending upon the relative contributions of the transconductance and the gate-to-source capacitance. The unity-gain cut-off frequency is severely degraded in the InP and GaAs generalized OPFETs under dc conditions. But, operation at the bandwidth frequency registers high f_T values (Table 4.17) due to the restoration of the depletion width to its finite value through the photovoltage roll-off.

4.5.6 Responsivity

All the material models display high reponsivities. GaAs device with its large photovoltaic and photoconductive effects attains to the highest responsivities among the models, followed by the InP and Si devices. The buried-gate and generalized Si OPFETs at the flux density of $10^{22}/m^2$-s are an exception to this finding. The generalized model exhibits larger responsivities than the other two models in all the three material systems, whereas the back-illuminated OPFET shows the least responsivities.

4.5.7 Operating at lower drain voltages

The lowering of drain voltage significantly improves the 3 dB bandwidth performance in Si OPFET. At the lower intensities, the reduction in operating currents with the consequent reduction of series resistance and improvement of sensitivity explains the finding. At the higher flux density, the minimized series resistance effect greatly reduces the photoconductive current. It also induces substantial photovoltaic effect at the 3 dB point, improving the bandwidth. Conversely, the reduced transconductance and increased gate-to- source capacitance lower the unity-gain cut-off frequency at lower drain voltages. Causes for the decrease in transconductance are still being investigated by the authors. The reasons behind

the fall in capacitance have been stated earlier. The detection-cum-amplification bandwidth is large at lower voltages with some decrease in responsivity. The dark current is considerably reduced. Specifically, among all the Si OPFET models, the Si back-illuminated OPFET exhibits the highest 3 dB-cum-amplification bandwidth of 38.2 MHz at a flux density of 10^{16} $/m^2$-s and a bias of 2.48 V. The generalized OPFET, on the other hand, shows the largest bandwidths of 73 MHz and 2.79 MHz respectively, at the flux densities of 10^{19} $/m^2$-s and 10^{22} $/m^2$-s at the same bias voltage. The detection-cumamplification bandwidth performance is superior at higher voltages in the GaAs and InP buried-gate and back-illuminated OPFET models at lower intensities. This is because the 3 dB bandwidth is almost unaffected with the change in bias due to relatively lesser series resistance effect. The amplification bandwidth is larger at higher voltages as discussed earlier. The same is the case with the InP generalized OPFET. In the GaAs generalized OPFET, the 3 dB bandwidth improves at lower voltages, but at the cost of considerably reduced amplification bandwidth. Remarkably, in Si OPFET, there is a substantial enhancement of 3 dB bandwidth at the flux density of 10^{22} $/m^2$-s for the reasons stated earlier. At this intensity, the InP generalized OPFET exhibits the highest combined bandwidth of 22 MHz at a bias of 2.48 V.

4.5.8 Signal-to-Noise Ratio

Referring to Tables 4.18 and 4.19, the performance metrics are calculated at the bias voltages appropriate or valid for Signal-to-Noise ratio computations as given in the theoretical model presented in [174]. At these voltages, i.e. at the gate bias of -1 V and a drain bias of 1.9 V, the GaAs back-illuminated OPFET exhibits ultra-high bandwidths of 46 GHz and 208.5 GHz at the intensities of 10^{16} $/m^2$-s and 10^{19} $/m^2$-s respectively. With the GaAs OPFET possessing comparatively lesser series resistances, these findings are explained by the lower bias-driven suppression of the dark current and the drain-to-source currents under illumination,

thus reducing considerably the series resistance effects.

Fig.4.24 depicts the computed Signal-to-Noise ratios in the various detectors as a function of modulation frequency. The ratios exceed 10^{10} in all the cases which is equivalent to 200 dB suited for very noisy applications. The high ratios are attributable to the large photovoltages which not only boost the gain through the transconductance, but also reduce the diffusion noise current sources. The shot noise current sources are reduced too since the gate leakage current is maintained at its minimum level through the counter effect of the forward photovoltage over the reverse flowing drift-diffusion currents. In addition, the thermal noise is suppressed due to the presence of large bias, input resistances and high drain-to-source resistance. The Signal-to-Noise Ratio decreases at higher frequencies due to the roll-off of the photovoltage with frequency.

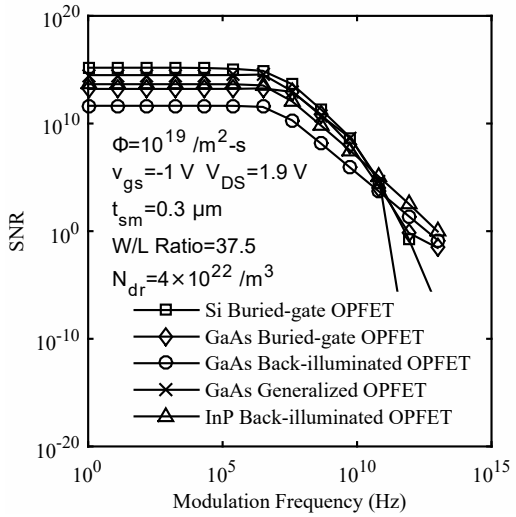

Figure 4.24: Signal-to-Noise Ratios in the various detectors as a function of modulation frequency

4.5.9 Applications

The GaAs OPFET is suitable for high data rate VLC applications such as Light-Fidelity Networks (Li-Fi) and other communication applications with data rate of 100 Gbits/s and higher. The InP device can serve in moderate bandwidth applications such as in hospitals and health-care, under-water communication,

defence, security etc. The Si OPFET device can operate in low data rate applications such as general positioning, vehicle and transportation, smart lighting etc.

Table 4.20 provides comparison of the GaAs OPFET performance with the state-of-art Si and GaAs detectors and amplifiers in OEIC receivers. The 3-dB bandwidth and responsivity of the OPFET device are superior to the reported devices. Responsivities of the latter detectors are sufficient for short-distance communications. For long haul communications, the very high responsivity of OPFET gives it an edge over the reported devices. In high data rate VLC applications, even with lower 3-dB and detection-cum-amplification bandwidths in some cases, the OPFET devices have higher gain-bandwidth product. An additional advantage is that a single device acts as a detector-cum-amplifier as compared to other OEIC receivers, which employ distinct detectors and amplifiers.

4.6 Material and Illumination Model Optimization of the OPFET for Ultraviolet High Dynamic Range Imaging and Communication

The ultraviolet (UV) photoresponses of Wurtzite GaN, ZnO, and 6H-SiC-based Optical Field Effect Transistor (OPFET) detectors are estimated considering the generalized model, the front-illuminated model, buried-gate front- and back-illumination models for high resolution imaging and UV communication applications. The gate materials considered for the proposed study are gold (Au) and Indium-Tin-Oxide (ITO) for GaN, Au for SiC, and Au and silver dioxide (AgO_2) for ZnO.

The gate-source voltage is set to 0 V and the drain-to-source voltage to 10 V (saturation region). The wavelength of operation is 350 nm. This UV wavelength falls in the range of UV Type A radiation (315 - 400 nm) which is least harmful

Table 4.20: Comparison of the GaAs OPFET with the state-of-art Si and GaAs-based detectors and amplifiers in OEIC receivers

Device	Wave-length (nm)	Applied Bias (V)	Responsivity (A/W)	3-dB Bandwidth (Hz)	f_T/TIA Bandwidth (Hz)	Ref.
GaAs Buried-gate OPFET	600 nm	Gate bias (0 V) Drain bias (25 V)	4.4×10^6 A/W	10.1 GHz	13.2 GHz (f_T)	This Work
GaAs Generalized model of OPFET	600 nm	Gate bias (0 V) Drain bias (25 V)	1×10^7 A/W	68.4 GHz	22.2 GHz (f_T)	This Work
GaAs Back-illuminated OPFET	600 nm	Gate bias (0 V) Drain bias (25 V)	2.6×10^6 A/W	42.4 GHz	11.1 GHz (f_T)	This Work
Spatially modulated Si PN PD	850 nm	−14.2 V	0.029 A/W	6.9 GHz	TIA (7.1 GHz)	[175]
Si APD	670 nm	−65 V	30 A/W	0.85 GHz	TIA (0.731 GHz)	[87]
Si PIN Finger PD	660 nm	−17 V	0.43 A/W	3 GHz	TIA (NP)	[42]
GaAs/AlGaAs PIN/HBT	690 nm	−3 V	0.224 A/W	35 GHz	60 GHz (f_T)	[39]
GaAs/AlGaAs/AlAs MSM/MODFET	850 nm	NP	0.6 A/W	9 GHz	70 GHz (f_T) TIA (14 GHz)	[40]
GaAs MSM-MESFET	850 nm	−5 V	0.2 A/W	8 GHz	15 GHz (f_T)	[41]

to the humans and accounts for 95% of the sun's radiation reaching the earth's surface. However, there is some risk of damage caused by this type of radiation, hence, preventive measures need to be taken. The other UV ranges (Type B (280 - 315 nm)) and Type C (100 - 280 nm) are significantly damaging and hence, should be avoided. The photon flux densities used in the simulations (10^{16}, 10^{19}, and 10^{22} $/m^2$-s) correspond to optical power densities of 0.575 μW/cm^2, 0.575 mW/cm^2, and 0.575 W/cm^2 respectively. The performance evaluation of the GaN, SiC, and ZnO-based illumination OPFET models considered in this work is provided in Tables 4.21, 4.22, 4.23, and 4.24. Refer to Table 4.5 for the parameters employed in calculation.

The basic detector parameters such as the photovoltage, drain-to-source current, responsivity, switching time, sensitivity, detectivity, unity-gain cut-off frequency (f_T), and Linear and Dynamic Range (LDR) are evaluated. The generalized and the front-illumination models exhibit a significant improvement in the linear dynamic range over the GaN buried-gate OPFET illumination models due to higher dark current in the buried-gate models. The generalized model is superior to the front-illuminated model in terms of the dynamic range. The buried-gate GaN OPFET models show faster responses and higher bandwidths however, with some exceptions. The responsivities are considerably high and comparable in all the devices with the generalized OPFET showing better response than the front-illuminated OPFET at the lower intensities, and vice versa at the higher intensity. The detectivities are substantially high in all the cases due to high responsivity values. The SiC OPFET considering the generalized model exhibits the highest 3-dB bandwidths of 11.88 GHz, 36.2 GHz, and 364 GHz and the highest detection- cum-amplification bandwidths of 4.62 GHz, 8.71 GHz, and 5.71 GHz at the optical power densities of 0.575 μW/cm^2, 0.575 mW/cm^2s, and 0.575 W/cm^2 respectively. The LDR obtained is also the highest (73 dB). The lowest response times are attained in the AgO_2-ZnO generalized OPFET model

(48 ps, 39 ps, and 9 ps). The ZnO OPFET is perceived as a high optical power detector from its large sensitivity and responsivity ascribed to the high absorption coefficient of ZnO (2.7×10^7 /m), its long electron lifetime (1 μs), and high electron saturated velocity (2.8×10^5 m/s) which assist in enhancing the photoconductivity at the high optical intensity of 0.575 W/cm^2. In overall, the ZnO OPFET exhibits high responsivity, moderate to high LDR values ranging from 24 dB to 69 dB, modest f_T values and 3-dB bandwidths ranging between low MHz to low GHz frequencies. Whereas the GaN OPFET is observed to show high responsivities, bandwidths in the sub-megahertz to high gigahertz ranges, modest to high cut-off frequencies and LDR in the 24 dB to 65 dB range. Employing ITO gate in the GaN generalized OPFET model and AgO_2 gate in the ZnO generalized model of OPFET (both possessing large barrier heights) improves the performance of these devices over that using conventional Au gates.

4.7 Strutural and Material Optimization of the Buried-gate Front-illuminated OPFET for Ultraviolet (UV) Communication

Buried-gate front-illuminated OPFET is structurally and materially optimized to enhance its performances for use as Ultraviolet (UV) photodetectors in UV communication, high noise, high speed, high gain, and high power applications. This work considers the effects of four relevant sets of structural dimensions ranging from 3 μm to 5 μm gate lengths and three distinct semiconductor materials (GaN, 6H-SiC, and ZnO) in analyzing the optimization of OPFETs. The optimum gate length and active layer thickness are found to be 3 μm and 0.27 μm respectively. The simulation results reveal that on the whole, the GaN OPFET with Indium-Tin-Oxide (ITO) gate exhibits reasonably high 3 dB bandwidth (20.7 GHz, 30.88 GHz), fast switching (69.6 ps, 64.2ps), and high amplification bandwidth (8.2 GHz, 7.8 GHz) at the optical power densities of 0.575 μW/cm^2

Table 4.21: Performance comparison of GaN, SiC, and ZnO OPFET illumination models

Photon Flux Density ($/m^2$-s)	Photovoltage (V)	Responsivity (A/W)	Photocurrent Gain	EQE (%)	Sensitivity (%)	Switching time (s)	Bandwidth (Hz)	Detectivity ($\mathrm{cm}Hz^{1/2}W^{-1}$)	f_T (Hz)
GaN buried-gate front illuminated OPFET with Au gate									
0	0	–	–	–	–	67 ps	–	–	7.37 GHz
10^{16}	0.346 V	1.1×10^{9}	2×10^{10}	3.8×10^{11}	15.06	53.6 ps	10.1 GHz	7.73×10^{16}	6.1 GHz
10^{19}	0.525 V	1.6×10^{6}	3.1×10^{7}	5.8×10^{8}	7.13	48 ps	33.4 GHz	1.17×10^{14}	5.8 GHz
10^{22}	0.7 V	3.69×10^{3}	6.92×10^{4}	1.31×10^{6}	20.85	34 ps	4.87 MHz	2.6×10^{11}	11.8 GHz
GaN buried-gate back-illuminated OPFET with Au gate									
0	0	–	–	–	–	67 ps	–	–	7.37 GHz
10^{16}	0.2 V	5.6×10^{8}	1.06×10^{10}	2×10^{11}	8.7	60 ps	16.34 GHz	3.95×10^{16}	7.25 GHz
10^{19}	0.38 V	1.2×10^{6}	2.2×10^{7}	4.2×10^{8}	8.63	54 ps	28.5 GHz	8.2×10^{13}	7.1 GHz
10^{22}	0.56 V	1.57×10^{4}	2.94×10^{5}	5.56×10^{6}	67.1	4 ps	0.846 MHz	9.97×10^{11}	16.2 GHz
GaN front illuminated OPFET with Au gate									
0	0	–	–	–	–	1.25 ns	–	–	5.2 GHz
10^{16}	0.2696 V	2.9×10^{8}	1.916×10^{9}	1.0×10^{11}	62.31	0.45 ns	5.8 GHz	6.57×10^{16}	6.2 GHz
10^{19}	0.4483 V	5.8×10^{5}	3.9×10^{6}	2.1×10^{8}	38.66	0.268 ns	12.87 GHz	1.17×10^{14}	6.7 GHz
10^{22}	0.6271 V	4.42×10^{3}	2.9×10^{4}	1.57×10^{6}	83.5	38 ps	0.78 MHz	7.55×10^{11}	4.95 GHz

Table 4.22: Performance comparison of GaN, SiC, and ZnO OPFET illumination models (continued)

Photon Flux Density ($/m^2$-s)	Photovoltage (V)	Responsivity (A/W)	Photocurrent Gain	*EQE* (%)	Sensitivity (%)	Switching time (s)	Bandwidth (Hz)	Detectivity ($\mathrm{cm}Hz^{1/2}W^{-1}$)	f_T (Hz)
GaN generalized model of OPFET with Au gate									
0	0	–	–	–	–	1.25 ns	–	–	5.2 GHz
10^{16}	0.65 V	5.25×10^8	6.94×10^9	3.7×10^{11}	85.7	0.16 ns	2.836 GHz	9.145×10^{16}	7.6 GHz
10^{19}	1.2 V	1.29×10^6	1.71×10^7	9.2×10^8	55.67	58 ps	10.97 GHz	1.78×10^{14}	7.76 GHz
10^{22}	1.724 V	2.91×10^3	3.85×10^4	2.07×10^6	53.94	22 ps	3.27 MHz	3.9×10^{11}	74.4 MHz
GaN generalized model of OPFET with ITO gate									
0	0	–	–	–	–	1.91 ns	–	–	5.4 GHz
10^{16}	0.91 V	1.66×10^9	1.2×10^{10}	5.9×10^{11}	94	91 ps	2.836 GHz	2.4×10^{17}	6.9 GHz
10^{19}	1.44 V	2.71×10^6	2×10^7	9.6×10^8	37.4	49 ps	19.15 GHz	3.77×10^{14}	8.8 GHz
10^{22}	1.98 V	5.33×10^3	3.87×10^4	1.89×10^6	48	21 ps	0.45 GHz	7.23×10^{11}	86 MHz
SiC generalized model of OPFET with Au gate									
0	0	–	–	–	–	4 ns	–	–	0 GHz
10^{16}	2.22 V	1.56×10^9	6.21×10^{10}	5.5×10^{11}	96.8	79 ps	11.88 GHz	3.4×10^{17}	4.6 GHz
10^{19}	2.76 V	2×10^6	7.8×10^7	6.9×10^8	19.7	57 ps	36.2 GHz	4.2×10^{14}	8.7 GHz
10^{22}	3.3 V	2.35×10^3	9.35×10^4	8.3×10^5	16.3	43 ps	364 GHz	5×10^{11}	5.7 GHz

Table 4.23: Performance comparison of GaN, SiC, and ZnO OPFET illumination models (continued)

Photon Flux Density ($/m^2$-s)	Photovoltage (V)	Responsivity (A/W)	Photocurrent Gain	EQE (%)	Sensitivity (%)	Switching time (s)	Bandwidth (Hz)	Detectivity ($\mathrm{cm}Hz^{1/2}W^{-1}$)	f_T (Hz)
SiC front-illuminated model of OPFET with Au gate									
0	0	–	–	–	–	4 ns	–	–	0 GHz
10^{16}	0.79 V	2.39×10^8	8.64×10^9	8.5×10^{10}	81.12	700 ps	1.62 GHz	7.75×10^{16}	2.8 GHz
10^{19}	0.97 V	3.9×10^5	1.4×10^7	1.37×10^8	33.3	400 ps	3.1 GHz	1.13×10^{14}	3.2 GHz
10^{22}	1.15 V	6.05×10^2	2.19×10^4	2.15×10^5	33.2	288 ps	2.42 GHz	1.59×10^{11}	4.2 GHz
ZnO generalized model of OPFET with Au gate									
0	0	–	–	–	–	837 ps	–	–	2.7 GHz
10^{16}	1.61 V	1.38×10^9	5.52×10^9	4.9×10^{11}	85.9	77.3 ps	38.6 MHz	3.12×10^{17}	5.4 GHz
10^{19}	2.15 V	1.8×10^6	7×10^6	6.2×10^8	19.2	56.7 ps	0.13 GHz	3.9×10^{14}	7 GHz
10^{22}	2.67 V	4×10^3	1.6×10^4	1.4×10^6	52.9	7.8 ps	3.84 MHz	7.74×10^{11}	0.5 GHz
ZnO front illuminated model of OPFET with Au gate									
0	0	–	–	–	–	837 ps	–	–	2.72 GHz
10^{16}	0.58 V	6.47×10^8	2.35×10^9	2.3×10^{11}	72.2	197 ps	7.85 MHz	1.65×10^{17}	3.2 GHz
10^{19}	0.76 V	8.4×10^5	3.1×10^6	3×10^8	17.97	150 ps	49 MHz	2×10^{14}	3.3 GHz
10^{22}	0.93 V	4.24×10^3	1.54×10^4	1.5×10^6	75.64	11 ps	3.84 MHz	8.35×10^{11}	7.86 GHz

Table 4.24: Performance comparison of GaN, SiC, and ZnO OPFET illumination models (continued)

ZnO generalized model of OPFET with AgO_2 gate									
Photon Flux Density ($/m^2$-s)	Photovoltage (V)	Responsivity (A/W)	Photocurrent Gain	EQE (%)	Sensitivity (%)	Switching time (s)	Bandwidth (Hz)	Detectivity ($\mathrm{cm}Hz^{1/2}W^{-1}$)	f_T (Hz)
0	0	–	–	–	–	2.73 ns	–	–	2.46 GHz
10^{16}	2.96 V	2.1×10^9	8.4×10^9	7.5×10^{11}	96.6	48 ps	0.625 GHz	4.75×10^{17}	5.8 GHz
10^{19}	3.5 V	2.4×10^6	9.4×10^6	8.4×10^8	10.5	39 ps	4.2 GHz	5.3×10^{14}	5.8 GHz
10^{22}	4.01 V	3.98×10^3	1.59×10^4	1.4×10^6	40	9 ps	6.2 MHz	7.9×10^{11}	28.3 MHz

and 0.575 mW/cm^2s. The other parameters show reasonably high values. The ZnO OPFET with silver oxide (AgO_2) gate is an established highly sensitive and high speed detector with responsivities (1.69×10^9 A/W, 2×10^6 A/W, 9.2×10^3 A/W), *EQEs* (6×10^{11}%, 7.2×10^8%, 3.26×10^6%), response times (58 ps, 57.6 ps, 20.6 ps), and detectivities (2×10^{17} Jones, 2.5×10^{14} Jones, 1.1×10^{12} Jones) at the intensities of 0.575 μW/cm^2, 0.575 mW/cm^2, and 0.575 W/cm^2 respectively. However, the photocurrent gain is much inferior to the SiC OPFET. The 3-dB bandwidth at the lower intensities is in the gigahertz or sub-gigahertz range. The f_{Ts} are inferior to the other devices. Over the range of applied optical power densities of 0.575 μW/cm^2, 0.575 mW/cm^2, 0.575 W/cm^2, and 57.5 W/cm^2, the SiC OPFET with gold (Au) gate exhibits much higher photocurrent gain (1.02×10^{11}, 1.2×10^8, 1.45×10^5, and 1.69×10^3) as well as larger 3-dB bandwidth (20.7 GHz, 33.4 GHz, 500 GHz, and 151.7 GHz) as compared to the GaN and the ZnO OPFET detectors.

The parameter values at the optimum dimensions are depicted in Table 4.25. The gate bias is 0 V, whereas the drain bias is 25 V. The operating wavelength is 350 nm. The photon flux densities used in the simulations (10^{16}, 10^{19}, 10^{22}, and 10^{24} /m^2-s) correspond to optical power densities of 0.575 μW/cm^2, 0.575 mW/cm^2, 0.575 W/cm^2, and 57.5 W/cm^2 respectively. The parameters used in calculation are to be referred from Table 4.5.

4.8 Reliability and the Effect of Elevated Temperatures on the Characteristics of 6H-SiC Buried-gate Front-illuminated OPFET for UV Applications

In the backdrop of the established characteristics of SiC OPFET as a high gain and high bandwidth device, the study further investigates the effect of elevated temperature on the device parameters. These harsh environments are typical of

Table 4.25: Comparative Studies of GaN, ZnO, and 6H-SiC buried-gate front-illuminated OPFET detectors (L=3 μm, Z=100 μm, t_{sm}=0.27 μm, N_{dr}=5 $\times$ 10^{22} $/m^3$)

Photon Flux Density ($/m^2$-s)	Photovoltage (V)	Responsivity (A/W)	Photocurrent Gain	EQE (%)	Sensitivity (%)	Switching time (s)	Bandwidth (Hz)	Detectivity ($\mathrm{cm}Hz^{1/2}W^{-1}$)	f_T (Hz)
GaN buried-gate OPFET with ITO gate									
0									
10^{16}	0.44	9.3×10^8	3.3×10^{11}	3.78×10^9		69.6 ps	20.7 GHz	1.2×10^{17}	
10^{19}	0.62	1.24×10^6	4.4×10^8	5×10^6		64.2 ps	30.88 GHz	1.6×10^{14}	
10^{22}		5.8×10^3	2×10^6	2.35×10^4		22.2 ps	1.36 MHz	7.5×10^{11}	
ZnO buried-gate OPFET with AgO_2 gate									
0									
10^{16}	1.03	1.69×10^9	6×10^{11}	6.16×10^9		58 ps	0.13 GHz	2×10^{17}	8.5 GHz
10^{19}	1.2	2×10^6	7.2×10^8	7.4×10^6		57.6 ps	1.2 GHz	2.5×10^{14}	7.7 GHz
10^{22}	1.36	9.2×10^3	3.26×10^6	3.35×10^4		20.6 ps	0.846 MHz	1.1×10^{12}	3.2 GHz
SiC buried-gate OPFET with Au gate									
0	0	–	–	–	–	0.19 ns	–	–	5.96 GHz
10^{16}	0.79 V	7.92×10^8	1.02×10^{11}	2.8×10^{11}	28.64	0.13 ns	20.7 GHz	1.57×10^{17}	4.56 GHz
10^{19}	0.97 V	9.5×10^5	1.2×10^8	3.4×10^8	5.53	0.12 ns	33.4 GHz	1.9×10^{14}	2.87 GHz
10^{22}	1.15 V	1.12×10^3	1.45×10^5	4×10^5	5.55	0.11 ns	500 GHz	2.23×10^{11}	3.8 GHz

industrial applications. At 300 K, i.e. at room temperature, apart from high gain and bandwidth, reasonably large values for the other parameters are obtained, except the low sensitivities and long switching times. The effect is studied at temperatures of 300 K, 400 K, 500 K, and 600 K.

Figure 4.25 shows the influence of temperature on the photocurrent gain at different radiation flux densities. It depicts the immense immunity of the SiC detector gain to the elevated temperatures at all intensities. The responsivities and the EQEs follow the photocurrent gain. Temperature effect on the other distinct parameters i.e. the switching time and the detectivity is shown respectively in Figures 4.26 and 4.27. Both switching time and detectivity exhibit quite stable responses. At higher flux densities and temperatures, the switching time improves significantly. The above results show that the device is capable of delivering reasonably high gain, fast response, and good detectivity even at higher temperatures up to 325 degrees Celsius. On the downside, there is a significant reduction in the 3-dB bandwidth from up to hundredths of gigahertz at 300 K to lower values at elevated temperatures. At 400 K, the bandwidth is in gigahertz or sub-gigahertz whereas at 500 K and 600 K respectively, it is in megahertz and kilohertz. This is attributed to the emptying out of recombination centres at such high temperatures which were otherwise responsible for the short lifetime at 300 K. The transconductances, the gate-to-source capacitances, and the unity-gain cut-off frequencies also show reasonable stability.

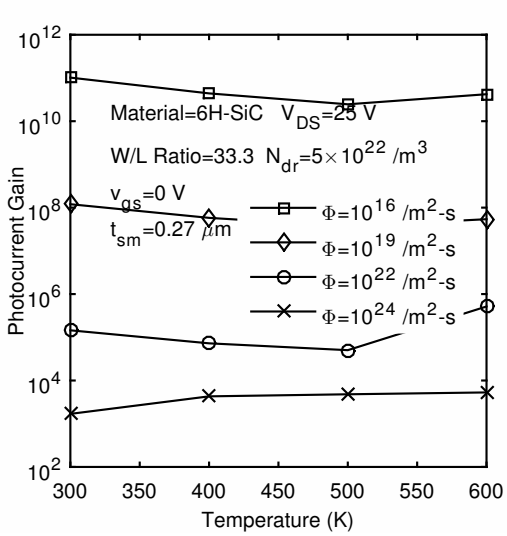

Figure 4.25: Photocurrent gain as a function of temperature in 6H-SiC OPFET at different radiation flux densities

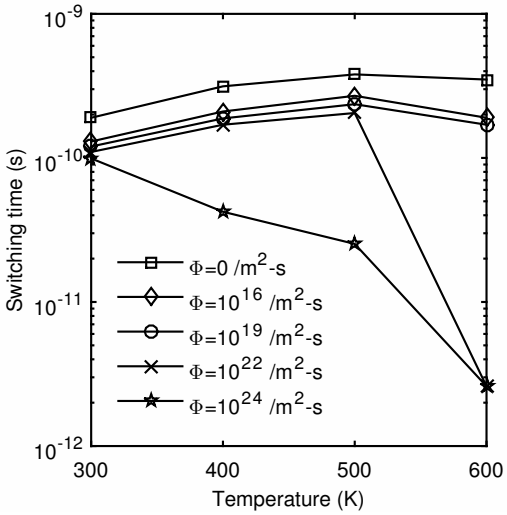

Figure 4.26: Temperature-dependent switching response in 6H-SiC OPFET at different radiation flux densities

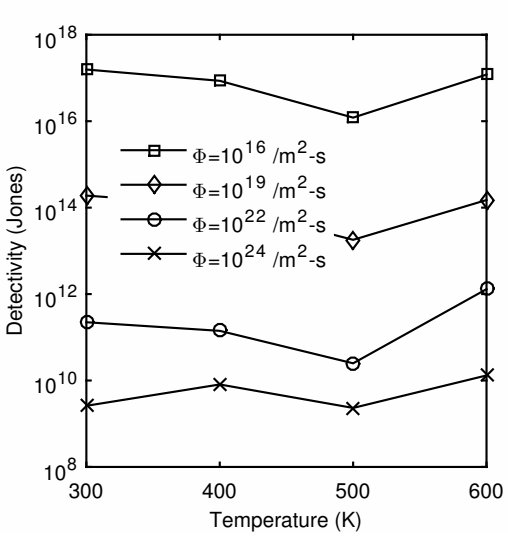

Figure 4.27: Detectivity in 6H-SiC OPFET at elevated temperatures at different radiation flux densities

4.8.1 Effect of Temperature on Device Parameters

With temperature elevation, the photovoltage remains constant or slightly rises (0.81 V, 1.046 V, 601 1.28 V, and 1.42 V) at 400 K. It remains almost unaltered (0.68 V, 0.976 V, 1.27 V, and 1.43 V) at 500 K, before increasing significantly (1.37 V, 1.726 V, 1.88 V, 1.89 V) at 600 K. The above phenomenon is explainable as follows: At 400 K, the photogenerated hole density is orders of magnitude higher than at 300 K because of the higher absorption coefficient, and the longer hole lifetime, although the hole saturation velocity is lower. Table 4.26 presents the temperature-dependent values of the parameters. Simultaneously, the reverse saturation current density across the Schottky junction is considerably raised from ($\sim 6 \times 10^{-13}$ A/m^2) at 300 K to ($\sim 6 \times 10^{-7}$ A/m^2) at 400 K. The photovoltage is directly proportional to the temperature. Its relationship with saturation current is one of inversely logarithmic while that with saturation velocity and hole density is directly logarithmic. The photovoltage thus undergoes compensating effects from the various parameters and results in either constant or slightly raised photovoltages at 400 K. As the temperature rises to 500 K, with the other compensating factors, the photovoltages remain constant. The value of the are greatly enhanced as the temperature is raised to 600 K by the consid-

erably increased hole lifetime. The reverse saturation current density at 600 K is 0.8241 A/m^2. Photovoltages saturate at larger intensities due to the effect of illumination on the minority carrier lifetime [1].

The series resistances increase considerably with temperature ($\sim$Rs=488 Ω, 890 Ω, 1.12×10^3 Ω, and 9.4×10^2 Ω) on account of the degradation of mobility with temperature. One more factor affecting the series resistances is the difference between the gate and p-n junction built-in voltage. While the gate junction voltage is constant at $\sim$1.27 V, even upon increasing the temperature, the p-n junction voltage drops significantly with temperature. The drop in voltage occurs because the intrinsic carrier concentration rises at elevated temperatures. The difference is higher at 400 K, drops to a minimum at 500 K, and then again rises to some reasonable value at 600 K. Thus the voltage-drops across the spacing follow the difference in the two built-in voltages. The attained mobilities and the voltage drops determine the series resistances. The drain-to-source currents and the photocurrents undergo reduction at 400 K and 500 K except at the flux density of 10^{24} /m^2-s on account of the slightly higher photovoltages but significantly raised series resistances, lower mobilities, and reduced electron saturation velocities. At this intensity, there is a significant improvement in the response resulting from the larger absorption coefficients and the longer electron lifetimes.

The responsivities, the photocurrent gains, and the *EQEs* follow the photocurrents generated. Response times increase, transconductances fall, whereas capacitances remain at nearly the same level at lower flux densities; the unity-gain cut-off frequencies decrease, and detectivities reduce. The 3-dB bandwidths periodically decrease at the lower intensities but are comparable at higher intensity.

Table 4.26: Temperature-dependence of 6H-SiC parameters

Parameter	Name	Temperature (300 K)	400 K	500 K	600 K	Unit
μ	Low field electron mobility	(∼0.037)	(∼0.020)	(∼0.016)	(∼0.009)	(m^2/V.s)
Φ_B	Schottky Barrier Height (Au)	(∼1.37)	(∼1.37)	(∼1.37)	(∼1.37)	(eV)
v_{yn}	Saturated electron velocity	$\sim 2 \times 10^5$	$\sim 1.5 \times 10^5$	$\sim 1.3 \times 10^5$	$\sim 1.1 \times 10^5$	(m/s)
v_{yp}	Saturated hole velocity	$\sim 9 \times 10^4$	$\sim 7.7 \times 10^4$	$\sim 6.9 \times 10^4$	$\sim 6.3 \times 10^4$	(m/s)
τ_p	Lifetime of holes	9.19×10^{-9}	2.25×10^{-7}	3.1×10^{-9}	9.3×10^{-4}	(s)
τ_n	Lifetime of electrons	9.19×10^{-9}	2.25×10^{-7}	3.1×10^{-9}	9.3×10^{-4}	(s)
ϵ	Permittivity	8.5×10^{-11}	8.5×10^{-11}	8.5×10^{-11}	8.5×10^{-11}	(F/m)
α	Absorption Coefficient @ 350 nm	1.06×10^5	1.45×10^5	1.7×10^5	2.4×10^5	(/m)

The scenario is quite different at 600 K. There is an improvement in the photoresponse over that at 400 K and 500 K. The response is comparable at lower intensities to that at 300 K, whereas it increases at higher intensities. This improved response comes at the cost of much reduced bandwidth in the kHz range at the lower intensities. At higher intensity, the bandwidth is raised to MHz range owing to the effect of illumination on the minority carrier lifetime. The same hole/electron lifetime responsible for bandwidth reduction conversely leads to the high photoresponse through the gain.

The above results show that the device response is stable at elevated temperatures and can operate at frequencies ranging from kilohertz to gigahertz.

4.8.2 Reliability of the SiC OPFET at Elevated Temperatures

One of the primary factors responsible for the device failure is the electromigration at the gate Schottky contact [176]. The Mean-Time-to-Failure ($MTTF$) is governed by well known Arrhenius equation:

$$MTTF = AJ^{-n}e^{\frac{E_A}{k_B T}} \tag{4.1}$$

where A is the proportionality constant, J is the current density, n is a constant, E_A is the activation energy. At zero gate and drain bias, and under dark condition, the activation energy is the same as the Schottky barrier height [10], i.e. 1.37 eV and the current density is the reverse saturation current density. At elevated temperatures, the Schottky barrier height remains constant [177], whereas the current density increases significantly. Assuming A and n to be unity, the $MTTF$ as a function of temperature is plotted in Figure 4.28.

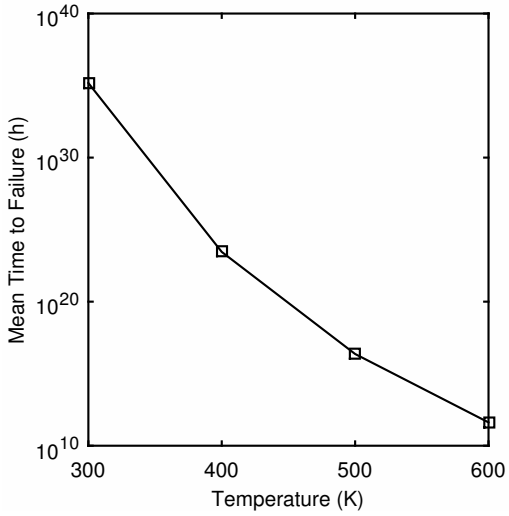

Figure 4.28: $MTTF$ in 6H-SiC OPFET at elevated temperatures under dark condition at zero gate and drain bias

The graph in Figure 4.28 shows that the Mean Time to Failure is far above par values even at elevated temperatures, thus showing its reliable operation under dark and zero bias conditions. These long failure times arise mainly from the large activation energy of 1.37 eV apart from the comparatively lesser contributions from the saturation current density. Under illumination and positive drain-to-source bias in the deep saturation region, which are the conditions of normal operation of this device as a photodetector, the activation energy either increases further or maintains its original value, but never deteriorates. The developed photovoltage acting as a forward bias tends to decrease the activation energy. Voltage drops across the source series resistance and the channel, compensate or overcompensate the loss of activation energy. The Schottky junction

thus functions in reverse bias.

The drift and the diffusion phenomena in the Schottky diode greatly increase the reverse photocurrents as the optical power increases. As the depletion width is at its maximum, it remains unaffected with temperature changes. The only remaining effect of temperature changes on drift current, therefore, comes from the absorption coefficient. On the contrary, the diffusion photocurrent is affected by temperature through the absorption coefficient, the hole diffusion length, the depletion width and the intrinsic carrier concentration. But the diffusion photocurrent ceases to exist due to almost complete depletion of the channel. At lower flux densities and higher temperatures, the contribution still comes from the reverse saturation current density.

Thus fuelled by the drift currents and the reverse saturation current, the diode net current density significantly rises with optical power as well as with temperature. Considering these factors and the least value of the activation energy (1.37 eV), the $MTTF$ is plotted as a function of temperature in Figure 4.29 under different illumination conditions at zero gate bias and 25 V drain bias. As is apparent from Figure 4.29, the $MTTF$ reduces both with the optical power and temperature. The highest value lies at the temperature of 300 K at the flux density of 10^{16} $/m^2$-s (2.1×10^{27} h), whereas the lowest value is at 600 K under the flux density of 10^{24} $/m^2$-s (3.1×10^{7} h), which is 695 still very high.

The above-observed results show the suitability of the device and its high reliability in elevated temperature environments under normal operating bias voltages and radiation flux densities.

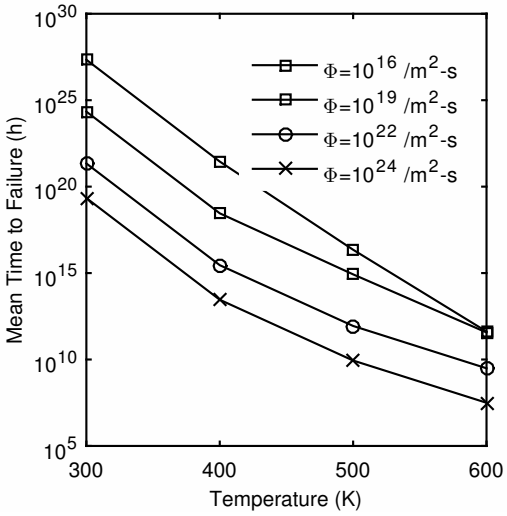

Figure 4.29: *MTTF* in 6H-SiC OPFET at elevated temperatures under different illumination conditions at zero gate bias and 25 V drain bias

4.9 Switching Performance and Frequency Response of GaAs OPFET Models

The switching and frequency responses of the buried-gate front-illuminated, and the generalized models with ITO gate are examined for VLC applications such as traffic lighting and compared with that using Au gate.

The gate bias is set to 0 V whereas the drain bias is variable. The device is studied under deep saturation region of operation for higher sensitivity and larger amplification bandwidth. The optical radiation has a wavelength of 600 nm. The radiation flux densities of 10^{12}, 10^{15}, 10^{18}, 10^{21}, and 10^{24} $/m^2$-s employed in the simulations are equivalent to power densities of 33 pW/cm^2, 33 nW/cm^2, 33 μW/cm^2, 33 mW/cm^2, and 33 W/cm^2 respectively. Structural optimization of the switching and frequency responses of the buried-gate model is carried out over a wide range of dimensions with gate length from 3 μm to 8 μm; the structural parameters being chosen from the scaling rules [38]. The analysis considers only the 4 most relevant sets. Refer to Table 4.27 and 4.28 for the frequency response comparison of the OPFET models. Parameters used in the

calculation are specified in Table 4.9.

At first, the photo-induced voltages developed in the studied illuminated models are compared. As seen from Figure 4.30, the devices with ITO gates exhibit enhanced photovoltages over that of the Au gates. This enhancement is attributed to the larger Schottky barrier of the ITO-GaAs junction (0.98 eV) as compared to that of Au (0.865 eV), which decreases the reverse saturation current density and boosts the photovoltage.

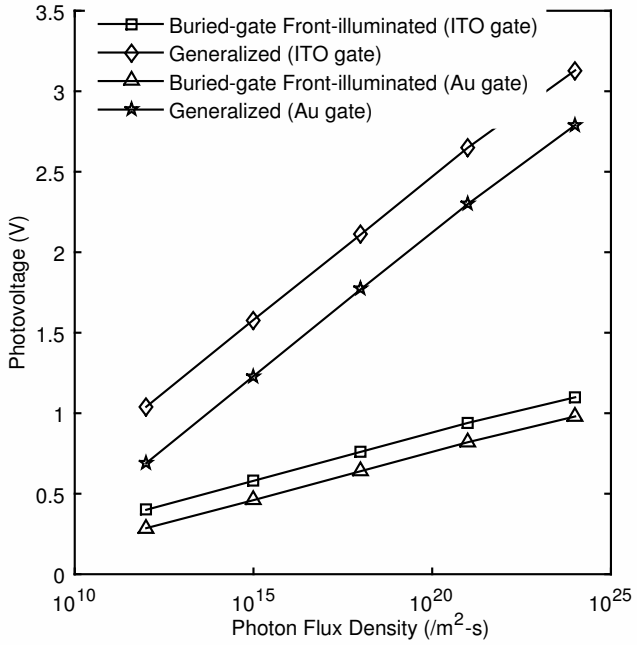

Figure 4.30: Photovoltage versus radiation flux density in the buried-gate and generalized models (with Au and ITO gates)

For switching applications, an important parameter, the switching time is defined as the ratio of the total gate depletion space charge and the sidewalls charge to the total drain current and is the average of the rise and fall times of the pulse response. The effect of structural parameters and the optical power on the switching time in buried-gate OPFET model with ITO gate is demonstrated in Figure 4.31. The figure shows that with the increase in gate length, i.e. with the corresponding increase in dimensions and a decrease in the doping density from scaling rules [154], the response time considerably increases. As can be seen from Figure 4.32, the space charge increases with gate length, so also the drain-to-

Table 4.27: Comparative Studies of GaAs OPFET detectors

GaAs buried-gate OPFET with Au (ITO) gate (v_{gs} = 0 V, V_{DS} = 10 V, λ= 600 nm (visible)) 1st Set (L=3 μm, Z=100 μm, t_{sm}=0.27 μm, N_{dr}=5 × 10^{22} /m^3)					GaAs buried-gate OPFET with Au (ITO) gate (v_{gs} = 0 V, V_{DS} = 16.4 V, λ= 600 nm (visible)) 2nd Set (L=4 μm, Z=150 μm, t_{sm}=0.3 μm, N_{dr}=4 × 10^{22} /m^3)				
Photon Flux Density (/m^2-s)	g_m (mS)	C_{gs} (pF)	f_T (GHz) @ Bandwidth Frequency	Bandwidth (GHz)	Photon Flux Density (/m^2-s)	g_m (mS)	C_{gs} (pF)	f_T (GHz) @ Bandwidth Frequency	Bandwidth (GHz)
0	7.6 (7)	0.095 (0.088)	12.7 (12.6)	–	0	9.7 (8.9)	0.135 (0.13)	11.5 (11)	–
10^{12}	7.4 (7.4)	0.11 (0.11)	10.5 (10.4)	0.45 (0.86)	10^{12}	9.4 (9.4)	0.16 (0.16)	9.4 (9.4)	0.42 (0.86)
10^{15}	8.4 (8.4)	0.13 (0.13)	10.6 (10.5)	1.1 (1.76)	10^{15}	10.6 (10.6)	0.18 (0.18)	9.4 (10.7)	1.1 (1.76)
10^{18}	9.4 (9.4)	0.16 (0.16)	10.2 (10.2)	2.23 (3.3)	10^{18}	12 (12)	0.23 (0.23)	9.2 (11.5)	2.23 (3.9)
10^{21}	14.3 (14.3)	0.24 (0.24)	18.4 (20.4)	1.1 (1.62)	10^{21}	14.8 (14.8)	0.24 (0.24)	60 (52)	0.53 (0.86)
10^{24}	0 (0)	0 (0)	–	2.58 (3.84) MHz	10^{24}	0 (0)	0 (0)	–	1.87 (2.03) MHz

GaAs buried-gate OPFET with Au (ITO) gate (v_{gs} = 0 V, V_{DS} = 20 V, λ= 600 nm (visible)) 3rd Set (L=5 μm, Z=200 μm, t_{sm}=0.4 μm, N_{dr}=3.2 × 10^{22} /m^3)					GaAs buried-gate OPFET with Au (ITO) gate (v_{gs} = 0 V, V_{DS} = 20 V, λ= 600 nm (visible)) 4th Set (L=8 μm, Z=350 μm, t_{sm}=0.45 μm, N_{dr}=2 × 10^{22} /m^3)				
Photon Flux Density (/m^2-s)	g_m (mS)	C_{gs} (pF)	f_T (GHz) @ Bandwidth Frequency	Bandwidth (GHz)	Photon Flux Density (/m^2-s)	g_m (mS)	C_{gs} (pF)	f_T (GHz) @ Bandwidth Frequency	Bandwidth (GHz)
0	10 (12.7)	0.2 (0.195)	7.68 (10.4)	–	0	13.9 (13.1)	0.43 (0.38)	5.12 (5.5)	–
10^{12}	11.6 (11.6)	0.236 (0.236)	8.1 (8.86)	0.58 (1.2)	10^{12}	16.7 (16.7)	0.5 (0.46)	4.45 (4.42)	0.33 (0.625)
10^{15}	12.7 (12.7)	0.265 (0.265)	10.4 (10.4)	1.5 (2.836)	10^{15}	18.3 (18.3)	0.6 (0.54)	4.95 (4.72)	1.62 (2.42)
10^{18}	13.9 (13.9)	0.33 (0.33)	10.2 (10.2)	3.9 (6.3)	10^{18}	15.2 (15.2)	0.7 (0.7)	5.43 (5.5)	2.62 (4.57)
10^{21}	16.6 (16.6)	0.5 (0.5)	8.3 (13.9)	0.067 (0.16)	10^{21}	19.3 (19.3)	1.2 (1.2)	4.86 (4.73)	0.033 (0.057)
10^{24}	0 (0)	0 (0)	–	2.58 (2.8) MHz	10^{24}	0 (0)	0 (0)	–	6.2 (6.2) MHz

Table 4.28: Comparative Studies of GaAs OPFET detectors

GaAs generalized OPFET with Au (ITO) gate (v_{gs} = 0 V, V_{DS} = 16.4 V, λ= 600 nm (visible)) 2nd Set (L=4 μm, Z=150 μm, t_{sm}=0.3 μm, N_{dr}=4 × 10^{22} $/m^3$)				
Photon Flux Density ($/m^2$-s)	g_m (mS)	C_{gs} (pF)	f_T (GHz) @ Bandwidth Frequency	Bandwidth (GHz)
0	8.1 (7.4)	0.135 (0.13)	9.02 (9.2)	–
10^{12}	13.9 (16.7)	0.26 (0.188)	10.3 (10.1)	0.24 (0.455)
10^{15}	20.5 (14.3)	0.14 (0.126)	14.4 (21.4)	0.58 (0.625)
10^{18}	37 (32) pS	0.11 (0.11)	17.4 (21.2)	4.57 (39.4)
10^{21}	0.1 (0.1) nS	0.1 (0.074)	21.2 (17.4)	140.1 (394.1)
10^{24}	0 (0)	0 (0)	–	5.7 (5.7) MHz

source current (Figure 4.33), but the rate of increase of the space charge is higher than that of the current (compare Figures 4.32 and 4.33) resulting in the increase in the switching time. The space charge enhancement with the gate length is due to the increase of the longitudinal, lateral, and transverse domains of the device superseding the effect of lower doping-induced charge. With the elongation of the gate length, the depletion width increases due to decrease in the doping concentration, which also enhances the space charge. The increase in dimensions augments the drain current too, with the gate length acting as both enhancement and limiting factor. This boost of current is assisted by the fact at a constant photovoltage, the junction width sensitivity to applied illumination is larger at lower doping concentration. The above effects surpass the effect of lower doping induced charge. It can be seen from Figure 4.32 that the space charge remains constant with applied optical power except at the highest flux density of 10^{24} $/m^2$-s. This phenomenon occurs due to the deep saturation region of operation causing depletion of most of the channel area and due to the de-ionization process at the higher intensity.

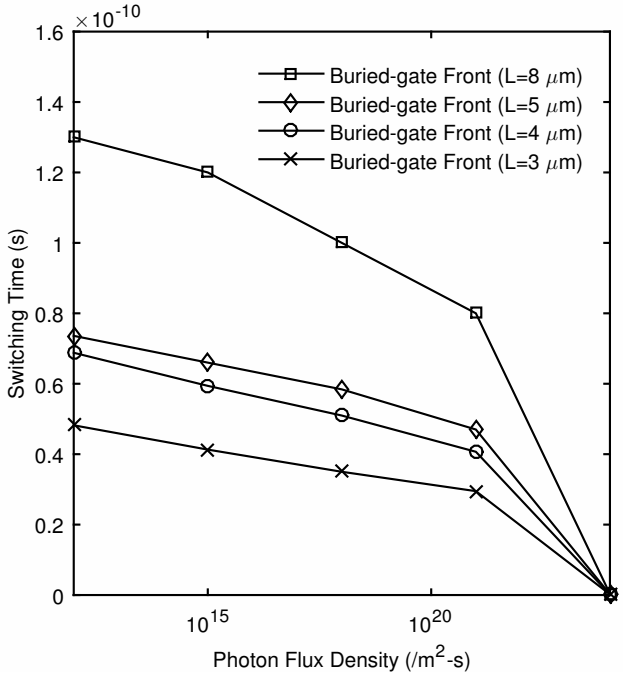

Figure 4.31: Switching time versus radiation flux density in the buried-gate model with ITO gate at different gate lengths

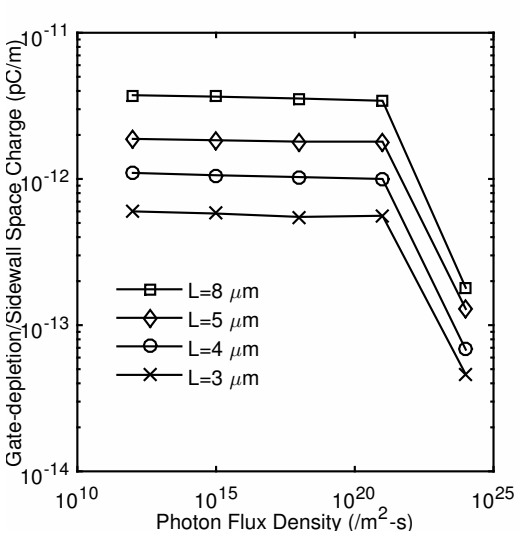

Figure 4.32: Space charge variation with photon flux density in the ITO-gated buried-gate OPFET (front-illumination) at various gate lengths

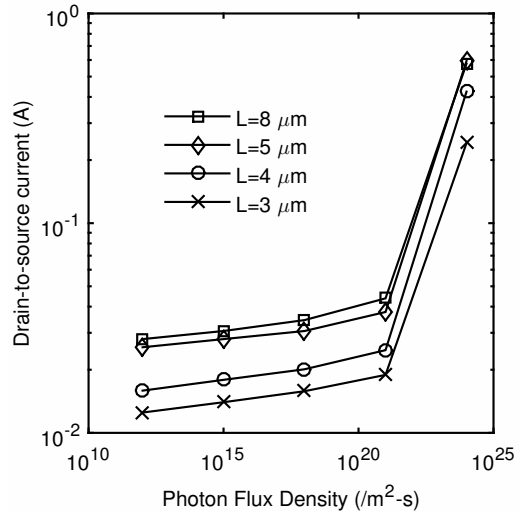

Figure 4.33: Drain current versus radiation flux density in the buried-gate front-illuminated model with ITO gate at various gate lengths

In contrast, the drain current increases with illumination. This is due to the fact that the current as opposed to space charge depends upon the channel charge and not on the depletion charge. By raising the applied optical power, the photovoltage is significantly boosted which decreases the junction width at or near the source end of the device and increases the channel current. The series resistance limits the current to some extent. At the highest intensity, there is a significant boost in current, which is accounted by the large photoconductivity in the junction region of the device. This effect incurs considerably high voltage

drop across the series resistance, thus totally depleting the channel and inducing negative sensitivity. Although almost constant space charge is maintained, the significant increase of the drain current with illumination results in the decrease in the switching time as the optical power is increased (Figure 4.31).

The comparison of response time of both the illumination models with ITO and Au gates as a function of photon flux density for a 4 μm device is presented in Figure 4.34. The switching response, on the whole, remains unaltered for both ITO and Au gates with respect to both the illumination models, however, with some exceptions. The devices with ITO gate experience decrease in the dark current compared to that with Au gate due to larger barrier height of ITO-GaAs junction, which enhances the depletion width. As discussed earlier, the photovoltages generated in the ITO-gated devices are higher, resulting in larger photocurrents. In most of the cases, these are not sufficient enough to produce larger drain-to-source currents. Co-incidentally, the ITO-gated detectors exhibit the same drain-to-source currents as for the Au-gated detectors except at the highest flux density. At this flux density, the magnitude of the current depends upon the relative values of the saturation and conductance components of current. The saturation component is affected by the large photoconductive effect, whereas the conductance is affected by both the large photovoltaic and the photoconductive effects. The same drain currents and unaltered space charges result in equal switching times in both the ITO and Au-gated devices upto the flux density of 10^{21} $/m^2$-s. The exception to this is with the generalized OPFET wherein the response time decreases significantly upto the intensity of 10^{15} $/m^2$-s when ITO gate is employed. The decrease in switching time results from the very large photovoltaic effect in the generalized model, which causes a significant increase in the drain current along with a reduction in the space charge (see Figure 4.35). After that, the switching time matches that with Au gate. This is because the drain current no longer further increases with optical power since

the photovoltage at the previous flux density had rendered the junction width to zero. Thus, increasing the optical power does not induce any more sensitivity, and there is a saturation of current at the intensity of 10^{18} $/m^2$-s. The increase in the current at the flux density of 10^{21} $/m^2$-s is due to the significant contribution from the photoconductivity in the neutral channel region. The photovoltaic effect remains saturated at this intensity. Unlike in other model wherein the space charge remains constant with optical power at the lower intensities (see Figure 4.32), the space charge in the generalized model exhibits a negative slope with optical power (see Figure 4.35). This is again due to the very high photovoltaic effect, which causes a significant portion of the depletion width to be reduced. In the other model, the space charge remains constant, but the drain current increases substantially with optical power. In contrast, in the generalized OPFET, the space charge undergoes reduction, whereas the current increases at a slower rate. These effects in the two sets of models compensate each other maintaining a similar slope for the switching time with the applied optical power in both the models. The consequence of the reduced space charges and the higher currents at the lower intensities in the generalized model is the lowest switching times among both the models.

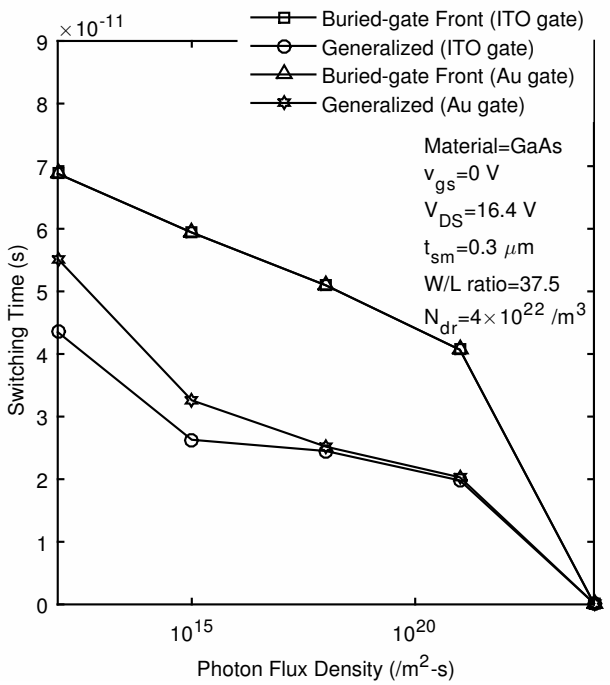

Figure 4.34: Switching time versus radiation flux density in the buried-gate and generalized models (with Au and ITO gates) for a 4 μm device

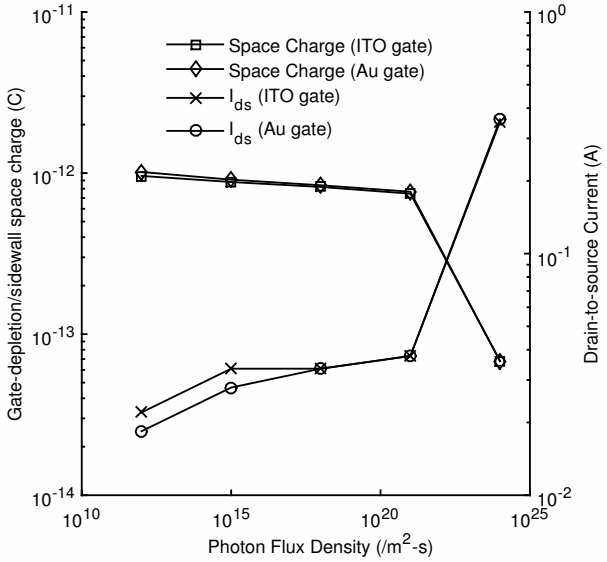

Figure 4.35: Gate-depletion and sidewall space charge (left) and drain-to-source current (right) versus radiation flux density in the generalized model (with Au and ITO gates) for a 4 μ device

In contrast to the switching time which remains in overall, almost constant in both the ITO and Au-gated devices, the 3-dB bandwidth in the ITO-gated detectors is enhanced as compared to that with Au gate (refer Table 4.27 and 4.28). This is attributed to the fact that unlike the response time, which depends upon the drain current, the bandwidth is obtained from the photocurrent response.

Since the photocurrent is larger with the devices employing ITO gate due to the higher photovoltages, the bandwidth is enhanced. It has been estimated that the bandwidth at the lower intensities shows more than 32% increase over that of Au gate with an average of 50%. At the highest intensity, the corresponding figures are 8% and 11% respectively. The structural dimensions and doping concentrations profoundly affects the bandwidth of the device as seen in Table 4.27 for the buried-gate OPFET. Ideally, when all the limiting factors such as series resistances, dark current, and in some cases the photoconductive effect are kept to their minimum or optimum values, the 3-dB bandwidth increases with the gate length. In other words, it increases with the decrease in the doping concentration as discussed in the earlier sections. This is not fully achieved in the present case due to the limiting factors discussed above are not at their optimum or minimum values. At the flux densities of 10^{12}, 10^{15}, and 10^{18} $/m^2$-s, only the photovoltaic effect prevails, whereas at the intensities of 10^{21} and 10^{24}-s, both the photoconductive and the photovoltaic effects contribute.

At the second group of flux densities (10^{21} and 10^{24}-s) in the case of buried-gate device with ITO gate and front-illumination, the scenario is slightly different from the discussions in the earlier sections where the power level was 10^{22} $/m^2$ as the gate length is elongated to higher values. At the gate length of 3 μm, 3-dB bandwidths of (1.625 GHz, and 3.84 MHz) are observed. The moderately high bandwidth of 1.625 GHz at the flux density of 10^{21} $/m^2$-s is due to still dominant contribution of the photovoltaic charge resulting from the higher doping concentration. This bandwidth is lower than that at the intensity of 10^{18} $/m^2$-s since at the current flux density, the photoconductive effects from the depletion and the channel regions also contribute partially. The bandwidth significantly falls to 3.84 MHz at the intensity of 10^{24} $/m^2$-s due to the sole contribution from the photoconductivity in the totally depleted channel region. With the elongation of gate length to 4 μm and so on till 8 μm, the bandwidths periodically fall to lower

values at the intensity of 10^{21} $/m^2$-s. This is because the photovoltaic charge decreases, whereas the photoconductive charge is either boosted or remains constant with gate length. At the higher intensity, there is at first, a fall in the bandwidth at the gate length of 4 μm (2.03 MHz) attributed to not sufficient enhancement of the photoconductive charge from the gate depletion region as the gate length is increased. At 5 μm gate length, the bandwidth is 2.8 MHz since the photoconductive charge is significantly enhanced surpassing the bandwidth at the 4 μm gate length. The negative photovoltaic charge emanating from the higher optical power level significantly boosting the photoconductive charge at this gate length reduces the bandwidth to some extent. In the 8 μ gate length device, the bandwidth rises to 6.2 MHz since the photoconductive depletion contribution is significantly high with low negative photovoltaic charge emanating from lower doping concentration. In the buried-gate front-illuminated device employing Au gate, the bandwidths follow the similar dependence upon the gate length as that in the ITO-gated device but in overall with the bandwidths showing reduced values. This is due to the lower photovoltaic charges from the lesser photovoltages which add to the constant photoconductive charges at the intensity of 10^{21} $/m^2$-s. The Au gate has a lower barrier height than the ITO gate. This produces larger negative photovoltaic charges at the higher intensity, which compensate the constant photoconductive charges slightly more than that with ITO gate leading to a fall in the bandwidth.

In the generalized model with ITO gate, the bandwidths observed at the corresponding five flux densities under consideration are (0.455 GHz, 0.625 GHz, 39.2 GHz, 394.1 GHz, and 5.71 MHz). As shown in Figure 4.35, the drain-to- source currents involved in this case are higher because of large photovoltages. Thus, at the intensities of 10^{12} and 10^{15} $/m^2$-s, the comparatively lower photovoltaic effects and larger currents inducing considerably high voltage drops across the series resistance substantially limit the bandwidths to sub-gigahertz values. At the

next higher intensity of 10^{18} $/m^2$-s, there is a significant boost in the bandwidth since the very high photovoltage reduces the depletion width beyond the zero point. Thus, even if the frequency is increased above the roll-off point of the photovoltage, the photocurrent remains constant until the frequency brings the photovoltage to a level which is low enough to maintain finite depletion width. This occurs at a much farther point than that under normal circumstances enhancing the bandwidth. At the intensity of 10^{21} $/m^2$-s, the still higher photovoltage further reduces the depletion width deeply beyond the zero point. Thus, the point of rolloff shifts further to the right producing even higher bandwidth. Note that the photoconductive effect from the channel region is comparable to the photovoltaic effect at this intensity, limiting the bandwidth to some extent. At the highest intensity of 10^{24} $/m^2$-s, there is a significant drop in the bandwidth (5.71 MHz) due to the sole photoconductive contributions from the totally depleted channel and substrate regions. The similar conditions exist in the generalized model with Au gate, but the bandwidth values are comparatively lower emanating from the lower photovoltaic effects and constant photoconductive effects.

The parameter unity-gain cut-off frequency (f_T) shapes the amplification response of the device and depends upon the parameters viz. the transconductance and the gate-to-source capacitance. Employing Au gate registers same transconductances and capacitances as that with ITO gate under illumination in buried-gate OPFET (Table 4.27). Under dark, these parameters are higher with Au gate attributed to the fact that at a fixed doping concentration and a constant photovoltage, the junction width sensitivity to applied gate bias is larger in the device with lower barrier height, i.e. the Au gate device in the present case. Under illumination, the above fact and the higher photovoltages in the ITO-gated device exactly balance each other to maintain constant transconductances and capacitances. It has been observed that the unity-gain cut-off frequencies calculated at the bandwidth frequency are either constant or higher than that at dc

frequencies. This is because both the transconductance and capacitance decrease with the increase in the modulation frequency but the rate of decrease of the capacitance is either constant or higher than that of the transconductance.

In the generalized OPFET model with ITO gate, the transconductances at the lower intensities are higher than that in the buried-gate front-illuminated OPFET due to significantly large photovoltaic effects (Table 4.27 and 4.28). But at the higher intensities, the transconductances are severely degraded due to the reduced the depletion width beyond the zero point by the photovoltages. Thus, the change in the gate bias has no effect on the effective channel width and hence, on the current. The gate-to- source capacitances are comparable to that in the buried-gate device at the lower intensities since the effect of high photovoltages on the capacitance is compensated by the significant decrease of the depletion width by the photovoltage. This effect significantly drops the capacitance value. The capacitance is further reduced at the higher intensities due to the de-ionization process. Thus, there is a significant boost in the unity-gain cut-off frequency at the lower intensities but is severely degraded at the higher flux densities. The degraded cut-off frequencies are restored to their high values when the device is operated at bandwidth frequencies. Analogous phenomena occur for the Au-gated device.

All the devices showed high responsivities in the range 10^{13} A/W to 10^{3} A/W with a periodic decrease as the flux density was varied between 10^{12} $/m^2$-s to 10^{24} $/m^2$-s. The ITO-gated devices showed superior responsivities than Au-gated devices.

Among both the illumination models, the generalized model with ITO gate exhibits larger detection-cum-amplification bandwidths of 21.2 GHz and 17.4 GHz

respectively at the intensities of 10^{18} and 10^{21} $/m^2$-s at the gate length of 4 μm. The switching times are also lower ranging from 43.5 ps to 0.193 ps. The photoresponse is significantly higher or comparable to the buried- gate model spanning from $5.05 \times 10^{13} - 1.456 \times 10^{3}$ A/ W, thus proving to be a high-performance detector. The optimum 3-dB as well as detection-cum-amplification bandwidths for the buried-gate front-illuminated device are 2.836 GHz and 6.3 GHz at the gate length of 5 μm at the intensities of 10^{15} and 10^{18} $/m^2$-s respectively. The response times span from 73.6 ps to 0.22 ps. The devices show great potential for VLC applications such as traffic lighting.

4.10 Reliability of GaAs OPFET Illumination Models under Visible-Illumination

The reliability of the front-illuminated, buried-gate front-illuminated, and generalized models with Au gate is analyzed at the gate length of 4 μm. At zero gate and drain bias, and under dark, the activation energy is the same as barrier height [10] which is 0.865 eV and the current density is the reverse saturation current density (2.06×10^{-5} A/m^2). At room temperature, referring to Eq. 4.1, assuming A and n to be unity, the above values correspond to a Mean-Time-to- Failure ($MTTF$) of 1.3×10^{19} hours which is a very large value. When the device is illuminated, with zero gate bias and 16.4 V drain bias, the activation energy tends to decrease significantly by the forward photovoltage developed in all the devices. But due to the substantial voltage drop across the source series resistance as also the voltage drop across the channel with the device biased in the deep saturation region, this reduction is nullified. Specifically, most of the regions of the gate-semiconductor contact are experiencing large barrier in the form of reverse bias. As a result, the activation energy never deteriorates if not enhanced. In the regions of gate-semiconductor contact close to the source end

of the channel wherein the barrier experiences considerable reduction through photovoltaic effect, the current densities are larger and flow in the forward direction. In contrast, small current densities flow in the regions farther from the source end emanating from the reverse drift-diffusion currents. Since the total current is an integration of the individual current densities through the contact area under consideration, the total current is dominated by the photovoltaic current itself. Considering the above facts and the least value of activation energy, the *MTTF* under the operating conditions stated earlier and at different radiation flux densities are plotted in Figure 4.36 for all the three models. The current densities exhibited by the models are depicted in Figure 4.37. It can be seen from the above figures that the current densities and the *MTTFs* of the buriedgate and the front-illuminated models are almost the same due to similar photovoltages. They exhibit large *MTTFs* since the current densities involved are of lesser magnitude. In contrast, in the generalized model, on account of the very high photovoltages, the current densities are greatly boosted which correspondingly decrease the *MTTFs*. The current densities and the *MTTFs* saturate at higher intensities due to the effect of series resistance. The significant reduction of barrier at the source end of the channel along with increase in current density would have caused electro-migration. But since the larger portion of the contact is under high reverse bias, the flux created by the forward current densities is overcompensated. On the whole, all the devices show substantially high *MTTFs* and thus, reliable operation.

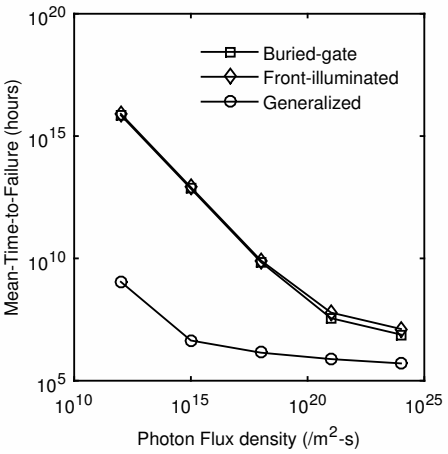

Figure 4.36: Mean-Time-to-Failure ($MTTF$) versus photon flux density in the GaAs OPFET illumination models

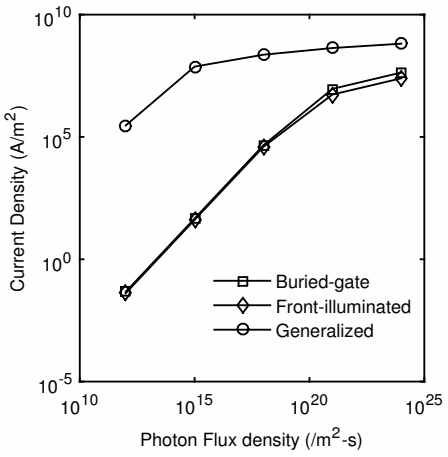

Figure 4.37: Current densities at the gate junction versus photon flux density in the GaAs OPFET illumination models

Chapter 5

Optimization of Schottky Junction in OPFET

5.1 Comparative Analysis of Graphene-GaN/GaAs and Au-GaN/GaAs Schottky Junctions in OPFET for UV Photodetector Applications

A comparative study of the photovoltaic, forward, and reverse characteristics of graphene and Au-gated GaN/GaAs Schottky junctions in OPFET for Ultraviolet (UV) photodetector applications is presented.

Refer to Tables 5.1 and 5.2 for various parameters of the 4 devices calculated under 350 nm UV illumination. Tables 5.3 and 5.4 give the various parameters used in calculation.

The flux densities shown correspond to optical power densities of 57.5 pW/cm^2, 57.5 nW/cm^2, 57.5 μW/cm^2, 57.5 mW/cm^2, and 57.5 W/cm^2 respectively. Graphene-GaN and Au-GaN Schottky junctions, under photovoltaic conditions exhibit almost the same maximum photoresponse of about 36 A/W, a photocurrent gain of about 1.17×10^3 and external quantum efficiency of 131.09×10^2%, which is highest among all the 4 devices. This is because, at 0 V bias, the depletion width is nonzero, hence a forward photovoltage is developed across the junction which

Table 5.1: Performance characteristics comparison of Schottky devices under UV illumination and photovoltaic conditions

Graphene-GaN Schottky junction					
	Φ=10^{12} $/m^2$-s	10^{15}	10^{18}	10^{21}	10^{24}
Photovoltage (V)	1.06×10^{-5}	0.0089	0.156	0.334	0.513
Responsivity (A/W)	36.9	36.8	35.3	32.83	5.81
Photocurrent Gain	1.17×10^3	1.17×10^3	1.12×10^3	1.04×10^3	184.72
External Quantum Efficiency (%)	131.08×10^2	130.77×10^2	125.28×10^2	116.51×10^2	20.62×10^2
Au-GaN Schottky junction					
	Φ=10^{12} $/m^2$-s	10^{15}	10^{18}	10^{21}	10^{24}
Photovoltage (V)	0.0092	0.156	0.335	0.514	0.693
Responsivity (A/W)	36.45	36.45	36.45	36.01	5.57
Photocurrent Gain	1.16×10^3	1.16×10^3	1.16×10^3	1.14×10^3	177.14
External Quantum Efficiency (%)	129.37×10^2	129.38×10^2	129.39×10^2	127.81×10^2	19.77×10^2
Graphene-GaAs Schottky junction					
	Φ=10^{12} $/m^2$-s	10^{15}	10^{18}	10^{21}	10^{24}
Photovoltage (V)	1.66×10^{-5}	0.013	0.167	0.346	0.525
Responsivity (A/W)	0.335	0.333	0.305	0.269	0.203
Photocurrent Gain	1.2	1.2	1.1	0.97	0.73
External Quantum Efficiency (%)	120	118.2	108.3	95.5	72.2
Au-GaAs Schottky junction					
	Φ=10^{12} $/m^2$-s	10^{15}	10^{18}	10^{21}	10^{24}
Photovoltage (V)	2.7×10^{-4}	0.063	0.24	0.42	0.6
Responsivity (A/W)	0.178	0.177	0.177	0.177	0.157
Photocurrent Gain	0.64	0.64	0.64	0.64	0.64
External Quantum Efficiency (%)	63.1	63	63	63	55.7

Table 5.2: Performance characteristics comparison of Schottky devices under UV illumination and reverse-bias conditions

Graphene-GaN Schottky junction					
	Φ=10^{12} /m^2-s	10^{15}	10^{18}	10^{21}	10^{24}
Photovoltage (V)	8.3×10^{-6}	0.0072	0.15	0.33	0.507
Responsivity (A/W)	0	0	0.075	0.075	0.075
Photocurrent Gain	0	0	2.3	2.4	2.4
External Quantum Efficiency (%)	0	0	25.75	26.72	26.72

Au-GaN Schottky junction					
	Φ=10^{12} /m^2-s	10^{15}	10^{18}	10^{21}	10^{24}
Photovoltage (V)	0.0091	0.156	0.335	0.514	0.692
Responsivity (A/W)	0.075	0.075	0.075	0.075	0.075
Photocurrent Gain	2.4	2.4	2.4	2.4	2.4
External Quantum Efficiency (%)	26.7	26.7	26.7	26.7	26.7

Graphene-GaAs Schottky junction					
	Φ=10^{12} /m^2-s	10^{15}	10^{18}	10^{21}	10^{24}
Photovoltage (V)	9.44×10^{-6}	0.008	0.15	0.33	0.51
Responsivity (A/W)	0.276	0.276	0.278	0.278	0.278
Photocurrent Gain	0.99	0.99	1	1	1
External Quantum Efficiency (%)	98.03	98.14	98.73	98.74	98.74

Au-GaAs Schottky junction					
	Φ=10^{12} /m^2-s	10^{15}	10^{18}	10^{21}	10^{24}
Photovoltage (V)	2.62×10^{-4}	0.062	0.24	0.42	0.596
Responsivity (A/W)	0.278	0.278	0.278	0.278	0.278
Photocurrent Gain	1	1	1	1	1
External Quantum Efficiency (%)	98.74	98.74	98.74	98.74	98.74

Table 5.3: Various parameters used in the calculation for GaN-based Schottky junction photodetector performance under UV illumination

Parameter	Name	Value	Ref.	Unit
α	Absorption Coefficient @ 350 nm	8×10^5	[178]	(/m)
ϵ	Permittivity	9.21×10^{-11}	[10]	(F/m)
L	Channel Length	3×10^{-6}	[33]	(m)
Z	Channel width	100×10^{-6}	[33]	(m)
t_{sm}	Active layer thickness	0.15×10^{-6}	[33]	(m)
N_{dr}	Ionized donor concentration	4.95×10^{22}		$(/m^3)$
v_y	Carrier velocity in the y direction	2×10^5	[179]	(m/s)
Φ_B	Schottky Barrier Height (Graphene-GaN)	0.7	[180]	(eV)
Φ_B	Schottky Barrier Height (Au-GaN)	0.88	[181]	(eV)
V_F	Fermi velocity in graphene	1.1×10^6	[180]	(m/s)
n_0	Graphene extrinsic residual doping density	5×10^{16}	[180]	$(/m^2)$
τ_p	Lifetime of holes	0.9×10^{-9}	[182]	(s)

Table 5.4: Various parameters used in the calculation for GaAs-based Schottky junction photodetector performance under UV illumination

Parameter	Name	Value	Ref.	Unit
α	Absorption Coefficient @ 350 nm	8×10^{7}	[172]	(/m)
ϵ	Permittivity	1.1×10^{-10}	[10]	(F/m)
L	Channel Length	3×10^{-6}	[33]	(m)
Z	Channel width	100×10^{-6}	[33]	(m)
t_{sm}	Active layer thickness	0.15×10^{-6}	[33]	(m)
N_{dr}	Ionized donor concentration	4.95×10^{22}		$(/m^3)$
v_y	Carrier velocity in the y direction	1.2×10^{5}	[33]	(m/s)
Φ_B	Schottky Barrier Height (Graphene-GaAs)	0.78	[180]	(eV)
Φ_B	Schottky Barrier Height (Au-GaAs)	0.86	[171]	(eV)
V_F	Fermi velocity in graphene	1.1×10^{6}	[180]	(m/s)
n_0	Graphene extrinsic residual doping density	5×10^{16}	[180]	$(/m^2)$
τ_p	Lifetime of holes	1×10^{-8}	[33]	(s)

causes a forward current to flow in a direction opposite to that of photocurrent arising from drift and diffusion of photogenerated carriers. The photocurrent arising from drift and diffusion of photogenerated carriers is negligible compared to that arising from the developed forward photovoltage. The Schottky barrier height of graphene-GaN junction is 0.7 eV whereas that of Au-GaN junction is 0.88 eV. Hence the depletion width under dark condition of graphene-GaN junction is less compared to Au-GaN junction. Hence more photovoltage is developed across the Au-GaN junction compared to that of graphene-GaN junction, due to more area available for photogeneration (holes) which drift and cross the junction developing photovoltage. Another reason for more photovoltage in Au-GaN junction is low reverse saturation current density of Au-GaN junction due to high Schottky barrier height of the junction (0.88 eV); since photovoltage is inversely proportional to reverse saturation current density. However, still the responses of graphene-GaN and Au-GaN junction are almost the same. This is because the reverse saturation current density of graphene-GaN junction is higher compared to Au-GaN junction owing to the lower Schottky barrier height of the former than the latter. This increases the thermionic emission current at a given photovoltage. The fall of the response at higher intensities is due to the saturation of current at higher photovoltages because of the series resistance. In addition to the series resistance, the fall in response in graphene-GaN junction is due to the decrease in Fermi level of graphene with forward photovoltages, increasing the Schottky barrier height, due to removal of electrons from graphene. Thus series resistance and the increased barrier height cause a deviation from linearity in response.

When graphene-GaN and graphene-GaAs Schottky junctions are compared under 0 V bias conditions, graphene- GaN junction exhibits far better response than graphene-GaAs junction although the forward photovoltages developed across the junction in both the cases are comparable. This is because the reverse satu-

ration current density of graphene- GaN junction is higher compared to that of graphene-GaAs junction owing to the lower Schottky barrier height of graphene-GaN junction (0.7 eV) as compared to graphene- GaAs junction (0.78 eV); also, due to higher effective mass of GaN (0.27) as compared to GaAs (0.063). This makes the current arising from forward photovoltage in graphene-GaN junction higher than that of graphene-GaAs junction. The photocurrent arising from drift as well as diffusion components is negligible compared to that arising from developed photovoltage in case of graphene-GaN junction. Hence there is no degradation of forward current. However, in case of graphene-GaAs junction, the drift component of photocurrent is comparable to that arising from forward photovoltage mainly due to the higher absorption coefficient of GaAs compared to GaN. Hence, there is degradation of forward current to some extent. This is the second reason of lowered photoresponse in graphene-GaAs junction. The fall of response at higher flux densities is due to the contribution of series resistance and voltage dependent barrier height as discussed earlier.

When graphene-GaN and Au-GaN Schottky junctions are compared in the reverse bias conditions, graphene-GaN junction has zero photoresponse at lower flux densities, and Au-GaN has positive moderate response. This is because, in graphene-GaN junction, graphene Fermi level is bias-dependent unlike in other metal-semiconductor junctions where the Fermi level of metal stays constant due to a high density of states at the Fermi level. (Note: graphene-GaN junction has large dark current. Thus, a small reduction in response may be significant to reduce the net response to zero). The photovoltage increase with illumination has no effect on the exponential term appearing in the thermionic emission equation, since the device is conducting at its reverse saturation current density at the applied reverse voltage and the induced photovoltage. However, due to the reason described earlier, the reverse saturation current density goes on decreasing with increased illumination. At the applied illumination, the drift and diffusion com-

ponents exist. Since there is a decrease in response due to the voltage-dependent barrier height with increased illumination and there is an increase in response due to the drift and diffusion components, the net response is the addition of the two. But, at lower flux densities, the drift and diffusion components are negligible compared to the voltage-dependent barrier height-induced reduced response. Thus, the graphene-GaN junction shows zero response at these intensities. At higher intensities, the voltage-dependent barrier height-induced response is negligible or slightly comparable to the drift and diffusion components. Thus, the device net response is moderate positive response at these intensities. In case of Au-GaN junction, it shows moderate positive response at all intensities because the drift-diffusion components-induced increased response is present whereas there is no voltage-dependent barrier height-induced reduced response due to the absence of bias-dependent Fermi level in Au metal. The photovoltage increase with illumination has no effect on the exponential term appearing in the thermionic emission equation, since the device is conducting at its reverse saturation current density at the applied reverse voltage and the induced photovoltage. The zero bias barrier heights of graphene-GaN and Au-GaN junctions are different being 0.7 eV and 0.88 eV respectively. Hence the zero bias depletion width is larger in Au-GaN junction than graphene-GaN junction. However, at the reverse bias applied along with the induced photovoltages, the depletion width is same in both cases and is maximum. Hence the difference in zero bias depletion widths in the two junctions does not have any effect on the drift and diffusion components, since the area is the same, the material is same. Thus, the absorption coefficient and other parameters are same. Hence, the drift and diffusion components are same in both cases at all intensities.

When graphene-GaN and graphene-GaAs junctions are compared in the reverse bias conditions, the graphene-GaN junction shows the response as shown in Table 5.2 due to the reasons discussed earlier. However, graphene-GaAs junction

has positive moderate response at all intensities. This is because, the dark current of graphene-GaAs junction is much low due to the higher barrier height (0.78 eV) and lower effective mass (0.063). Thus, a decrease in response due to the barrier height increase as illumination increases may not be significant to lower the net response. There is little reduction in response due to the photovoltage induced barrier height increase as illumination increases. However, the drift component of graphene-GaAs junction is high due to the large absorption coefficient of GaAs. The decrease in response is negligible compared to the increase in response due to the drift component. Hence the device shows a positive moderate response at all intensities. The photovoltages developed in both junctions are comparable. They don't affect the exponential term in the thermionic emission equation because the device is conducting at its reverse saturation current density at the applied reverse bias and the induced photovoltage. The dark zero bias depletion width of graphene-GaN junction is lower than that of the graphene-GaAs junction due to the lower zero bias barrier height of graphene-GaN junction (0.7 eV) as compared to graphene-GaAs junction (0.78 eV) and lower dielectric constant of GaN (10.4) as compared to GaAs (12.9). However, at the applied reverse bias and the induced photovoltages at all intensities, the depletion width is same in both cases and is maximum. Hence, the difference in characteristics of both the junctions is due to the reasons described earlier. The maximum response of graphene-GaAs junction is higher than that of graphene-GaN junction because the drift component of graphene-GaAs junction is higher than that of the drift-diffusion components of graphene-GaN junction owing to the larger absorption coefficient of GaAs. The maximum response is obtained at the intensities where there is negligible degradation of response due to the voltage-dependent barrier height. However, the maximum gain of graphene-GaN junction is higher than that of graphene-GaAs junction because graphene-GaN junction generates more photocurrent for a given primary photocurrent, than the graphene-GaAs junction.

When Au-GaAs junction is compared with other junctions in 0 V bias conditions, Au-GaAs junction exhibits moderately low response. This is because, the reverse saturation current density of Au-GaAs junction is low due to the higher Schottky barrier height of the junction (0.86 eV) and low effective mass of GaAs (0.063). This reduces the photovoltage-induced thermionic emission current at the illumination applied. The photovoltage induced is large but less than that of Au-GaN junction. The high photovoltage is due to the large photogeneration area owing to the high Schottky barrier height of Au-GaAs junction (0.86 eV) and high dielectric constant of GaAs (12.9). Also, due to the high Schottky barrier height of the junction and low effective mass of GaAs, the reverse saturation current density is low. Since the photovoltage is inversely proportional to reverse saturation current density, it helps in increasing the photovoltage. The high photovoltage assists in increasing the response but other factors reduce the response of the junction to low response. Because of the large absorption coefficient of GaAs, the drift component of Au-GaAs junction is high. This reduces the photovoltage-induced dark current to certain extent. This is another reason for reduced response of Au-GaAs junction. The reduced response at high intensities is due to the contribution of series resistance as described earlier. The Au metal Fermi level is bias-independent, hence its contribution is absent.

When Au-GaAs junction is compared to other junctions in the reverse bias conditions, the Au-GaAs junction exhibits moderate response higher than Au-GaN and graphene-GaN junctions, but almost equivalent to graphene-GaAs junction. It shows constant response of 0.2782 A/W at all intensities. Due to the absence of voltage-dependent barrier height in Au-GaAs junction, there is no reduction of response i.e. there is no negative response. There is only a positive response i.e. from the drift component of Au-GaAs junction. The drift component of Au-GaAs junction is high because of the large absorption coefficient of GaAs. This increases the response. The photovoltage induced is high due to the reasons

described earlier. However, it does not affect the thermionic emission current, since the barrier height is voltage-independent and the device is conducting at its reverse saturation current density at the applied reverse bias and the induced photovoltage. The depletion width of the junction at the applied reverse bias voltage and the induced photovoltage is maximum and same as that of other junctions. Hence maximum response is drawn with respect to area as in other junctions.

Under forward bias, the photodetectors have zero response. This can be explained as follows: Under this condition, the depletion width reduces to zero eliminating the possibility of photogeneration in the depletion region, thus, causing zero response at this bias condition.

5.2 Visible Range Characterization of Au/Graphene-GaAs Schottky Junctions in OPFET

The visible range characteristics of Au-GaAs Schottky junction and graphene-GaAs Schottky junction in MESFET are discussed and analysed under zero bias, forward bias and reverse bias conditions and compared those with the UV characteristics.

The parameter values used in computation are given in Table 5.4. In addition to these, the absorption coefficients at 450 nm and 650 nm respectively are 9×10^6 /m and 3.5×10^6 /m. The detector parameters (photocurrent gain and the external quantum efficiency (EQE)) of Au-GaAs Schottky junction and graphene-GaAs Schottky junction at 450 and 650nm illumination under photovoltaic conditions are presented in Table 5.5.

The device parameters are calculated at different photon flux densities. The dark currents in the Schottky devices are negligible compared to the photocur-

Table 5.5: Schottky junction detector parameters under zero bias conditions in the visible region

Au-GaAs Schottky junction (λ= 450 nm)					
	Φ=10^{12} /m^2-s	10^{15}	10^{18}	10^{21}	10^{24}
Photocurrent Gain	3.81×10^3	3.81×10^3	3.81×10^3	3.53×10^3	153.47
External Quantum Efficiency (%)	2.79×10^5	2.79×10^5	2.79×10^5	2.58×10^5	1.12×10^4
Au-GaAs Schottky junction (λ= 650 nm)					
	Φ=10^{12} /m^2-s	10^{15}	10^{18}	10^{21}	10^{24}
Photocurrent Gain	6.1×10^3	6.1×10^3	6.1×10^3	5.7×10^3	270.31
External Quantum Efficiency (%)	2.46×10^5	2.46×10^5	2.46×10^5	2.3×10^5	1.1×10^4
Graphene-GaAs Schottky junction (λ= 450 nm)					
	Φ=10^{12} /m^2-s	10^{15}	10^{18}	10^{21}	10^{24}
Photocurrent Gain	4.08×10^3	3.88×10^3	3.64×10^3	3.15×10^3	156.52
External Quantum Efficiency (%)	2.98×10^5	2.84×10^5	2.66×10^5	2.3×10^5	1.14×10^4
Au-GaAs Schottky junction (λ= 650 nm)					
	Φ=10^{12} /m^2-s	10^{15}	10^{18}	10^{21}	10^{24}
Photocurrent Gain	6.25×10^3	5.96×10^3	5.59×10^3	4.88×10^3	271.7
External Quantum Efficiency (%)	2.52×10^5	2.4×10^5	2.25×10^5	1.97×10^5	1.1×10^4

rents generated under both zero bias and reverse bias conditions in UV as well as visible regions. The dark current at zero bias is of the order of 10^{-20} A whereas the dark current in reverse bias ranges from 10^{-13} to 10^{-16} A. Low dark current improves the signal-to-noise ratio [183] and the device performance [184]. It allows the functioning of detectors with standard CMOS readout circuits [184]. It also enables very low and very high temperature operation [185]. Au- GaAs Schottky junction and graphene-GaAs junction develop far greater photovoltage in the visible region than that in the UV region under both photovoltaic and reverse bias conditions (Figure 5.1). This is because the absorption coefficient of GaAs in the UV region is high in contrast to its moderate absorption coefficient in the visible region. In the UV region, on account of high absorption coefficient of GaAs, high light absorption takes place within a small depth fromthe surface generating electron–hole pairs there exponentially decaying with distance from the surface. Due to a large volume density of carriers, bulk recombination time is short. Hence, significant recombination occurs in this case, which reduces the density of carriers. On the other hand, in the visible region, owing to moderate absorption coefficient of GaAs, absorption is moderate upto a large depth from the surface. Since the volume density of carriers generated is moderate, recombination is insignificant. As a total contribution from the carriers occupying a larger volume in the visible region case as compared to contribution from the carriers occupying a smaller volume in the UV region case, photovoltage developed in the visible region is far more than that in the UV region.However, the reverse saturation current density in Au-GaAs junction is less compared to that in graphene- GaAs junction owing to lower Schottky barrier height of Au-GaAs junction as compared to that of graphene- GaAs junction. Photovoltage is inversely proportional to reverse saturation current density and hence the simulated difference between photovoltages in Au-GaAs junction and graphene-GaAs junction. There is no significant difference between photovoltages in photovoltaic and reverse bias conditions because of the following: In the Au-GaAs junction, since

the channel is totally depleted at zero bias due to high dielectric permittivity of GaAs and high barrier height of Au-GaAs junction, the zero bias and the reverse bias depletion widths under dark condition are the same. On the other hand, in graphene-GaAs junction, in the dark condition, the channel is partially depleted at zero bias, but the deeply generated carriers in reverse bias have insignificant effect on the photovoltage. The above reasons are applicable in the case of visible region. In the UV region, since the carriers are generated within a small depth from the surface, the width of the depletion region under dark condition at zero bias and reverse bias doesn't come into picture and the photovoltages are same in photovoltaic and reverse bias conditions in both junctions.

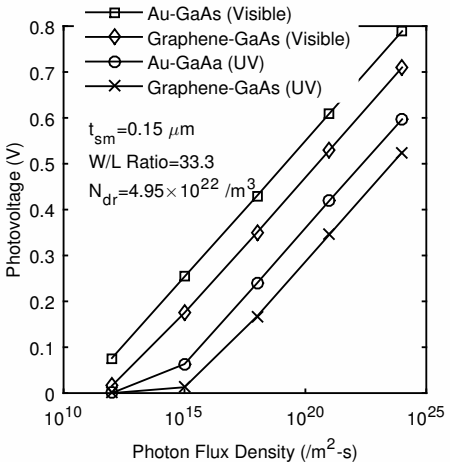

Figure 5.1: Photovoltage versus flux density in various Schottky junctions under visible and UV illumination

Under photovoltaic conditions, the high photovoltage developed in the visible region induces large forward thermionic emission current in opposition to negligible drift-diffusion photocurrent. This results in a high responsivity, of the order of 10^3 A/W (maximum), in both junctions (Figure 5.2). The photovoltage produced at λ= 450nm is slightly more than that at λ= 650nm owing to higher absorption coefficient of GaAs at 450nm than that at 650 nm. This generates more photocurrent at 450nm than that at 650 nm. Still the responsivity is greater at 650nm as compared to that at 450 nm. This signifies that the junctions pro-

duce more photocurrent for a given optical power falling on the device at 650nm than that at 450 nm. However, the *EQE* obtained is higher at 450 nm as compared to that at 650 nm since it depends only upon the photocurrent generated and the number of incident photons and is independent explicitly of the photon energy and the power level falling on the device. The junctions induce more photocurrent at 450nm than that at 650nm for a given photon flux and hence, the result. The maximum *EQE* attained is of the order of 10^5%. The gain at 650 nm is higher than that at 450 nm. This is because the junctions induce more photocurrent at 650nm for a given primary photocurrent than that at 450 nm. Owing to higher absorption coefficient of GaAs at 450nm as compared to that at 650 nm, the primary photocurrent at 450 nm is higher as compared to that at 650 nm. The maximum gain obtained is of the order of 10^3. This eliminates the need for external amplifying stages for the detectors.

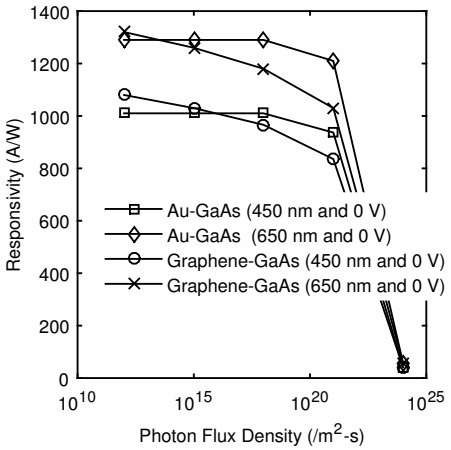

Figure 5.2: Responsivity versus flux density in Schottky junctions in the visible region under photovoltaic conditions

The photovoltaic response of Au-GaAs junction and graphene-GaAs junction in the UV region is inferior to that in the visible region (Figure 5.3) due to much lower photovoltage developed in the UV region as compared to that in the visible region (Figure 5.1). This produces lower photovoltage-induced forward thermionic emission current in opposition to comparable drift photocurrent. Since the drift-current is comparable to the forward thermionic emission current,

there is degradation of the response to some extent. Thus, the responsivity is of the order of 10^{-1} in both junctions. The drift-current is high in the UV region owing to the large absorption coefficient of GaAs which generates large amount of carriers. The drift photocurrent is the current arising from the drifting of photogenerated carriers (due to built-in electric field in the space charge region) prior to recombination. Thus, this current is independent of the recombination phenomenon. The diffusion photocurrent is absent in both junctions in the UV region since the carriers are generated only upto a small depth from the surface. The drift-diffusion photocurrent is moderate in the visible region owing to the moderate absorption coefficient of GaAs.

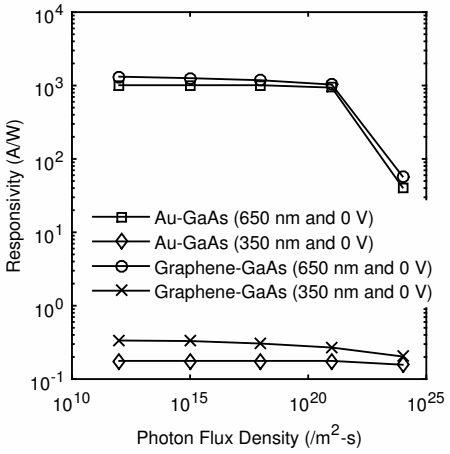

Figure 5.3: Responsivity in the UV and the visible regions in Schottky junctions under photovoltaic conditions

Although there is significant difference between photovoltages in the two junctions (the photovoltage in Au-GaAs junction is greater than that in graphene-GaAs junction), the responsivity, the gain, and the EQE recorded are comparable in the visible region (Figure 5.2, Table 5.5). Under photovoltaic conditions, this is attributed to the high reverse saturation current density in graphene-GaAs junction as compared to that in Au-GaAs junction – the same reason which made the difference in photovoltages which raises the thermionic emission current. The fall in response in Au-GaAs junction at higher flux densities is due to the con-

tribution of series resistance. At higher flux densities, the photovoltage induced is high resulting in high current. Thus, the voltage drop across the series resistance is significant causing saturation of current and hence, the fall in response. The fall in response in graphene-GaAs junction is owing to both the contribution of series resistance and the voltage-dependent barrier height of the junction. In graphene-semiconductor contacts, with applied reverse bias, there is an addition of electrons to graphene, the Fermi level shifts upwards, and the Schottky barrier height is reduced. With forward bias, there is removal of electrons from graphene, the Fermi level shifts downwards, and the Schottky barrier height is increased. With illumination, photovoltage is induced. This photovoltage acts as a forward bias and increases the barrier height of the junction, thus, reducing the reverse saturation current density and hence, the thermionic emission current. This phenomenon contributes to the fall in response. Under zero bias conditions, with UV illumination, the responsivity, gain and *EQE* in graphene-GaAs junction are higher than that in Au-GaAs junction (Figure 5.3, Table 5.5) even though the photovoltage is significantly more in Au-GaAs junction. This is because the difference between photovoltages in the two junctions is overcompensated by the higher reverse saturation current density in graphene-GaAs junction as compared to that in Au-GaAs junction. The high drift-current is the same in both junctions, the carriers being generated within a small depth from the surface. Thus, the degradation in response due to the drift-current is equal in both cases. The maximum responsivity, maximum *EQE* and maximum gain in graphene-GaAs junction are 0.3356 A/W, 119.9%, and 1.2061 whereas in case of Au-GaAs junction are 0.1777 A/W, 63.09%, and 0.6389 respectively. Thus, graphene-GaAs device shows some amplification whereas Au-GaAs device does not. The fall in response in graphene-GaAs junction is due to the contribution of series resistance and voltage-dependent barrier height. In Au-GaAs junction, only factor involved in the fall in response is the series resistance.

Under reverse bias conditions, moderate responses are obtained in both UV and visible regions (Figure 5.4). The only contributing factor towards positive photoresponse is the drift photocurrent. Diffusion photocurrent ceases to exist since the channel is totally depleted at the applied reverse bias and the generated photovoltage. The drift current is high in the case of UV region owing to the high absorption coefficient of GaAs whereas it is moderate in visible region due to the moderate absorption coefficient of GaAs. The exponential term in the thermionic emission equation does not induce negative responses due to the developed photovoltage because the device is conducting at its reverse saturation current density at the applied reverse bias and the induced photovoltage. However, negative responses are recorded in only graphene-GaAs junction, barrier height being voltage-dependent. The produced photovoltage acts as a forward bias and increases the barrier height, thus reducing the reverse saturation current density, and hence the thermionic emission current. This induces negative response and its effect is felt only at lower flux densities wherein this response is greater than or is comparable to the drift current- induced positive response, hence showing zero or reduced response at these intensities. At higher flux densities, drift-current completely dominates and maximum response is attained at these intensities.

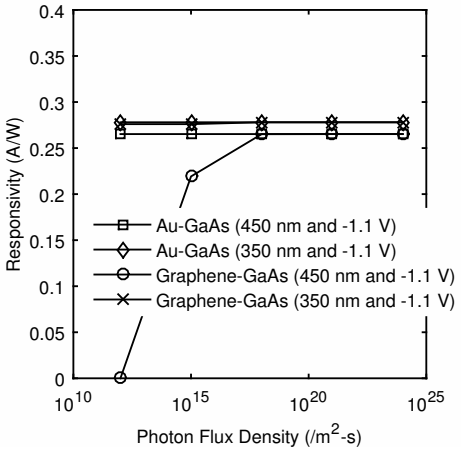

Figure 5.4: Responsivity in the UV and the visible regions in Schottky junctions under applied reverse bias

The reverse biased maximum response of Au-GaAs junction and graphene-GaAs junction vz. responsivity (Figure 5.4), gain (1), and *EQE* (73.14% @450 nm, 40.33% @650 nm, and 98.74% @350 nm) is the same in both UV and visible regions. This is because the channel being totally depleted, the drift photocurrent is equal in both junctions. Full device area has been utilized for photogeneration. Hence, optimum value of drift-current is obtained. Unity maximum photocurrent gain is attained in both junctions in UV and visible regions, drift-current (the only contributing factor) being at its optimum, thus equalling the primary photocurrent value. Unity gain indicates that external amplifying stages will be required for the detectors. The maximum responsivity and maximum *EQE* in the visible region are more at 450nm (0.2652 A/W and 73.14%) than that at 650nm (0.2117 A/W and 40.33%). This is because the drift-current is higher at 450nm compared to that at 650nm owing to the higher absorption coefficient of GaAs at 450 nm. The graphene-GaAs devices exhibit reduced responses at the lower intensities (10^{12} and 10^{15} $/m^2$ s) in the visible region, responsivity (Figure 5.4), (Gain (0, 0.82), and *EQE* (0%, 60.4%)) at 450nm and (Gain (0, 0.69) and *EQE* (0%, 27.9%)) at 650 nm. This is attributed to the voltage-dependent barrier height in graphene whose effect is felt at the lower flux densities since the photovoltage is low and drift-currents are also lower.

The UV maximum responsivity (Figure 5.4), and maximum *EQE* (0.2782 A/W and 98.74%) are greater than that in the visible region under applied reverse bias, drift current being higher in the UV region due to larger absorption coefficient of GaAs.

The potential profile of the investigated Au-GaAs MESFET device obtained using Visual TCAD software at a reverse gate-to-source bias voltage of -0.9V and zero drain-to-source voltage is shown in Figure 5.5. The profile clearly depicts that the potential is negatively high at regions near the gate where the reverse

bias is applied and falls at the regions farther from the gate.

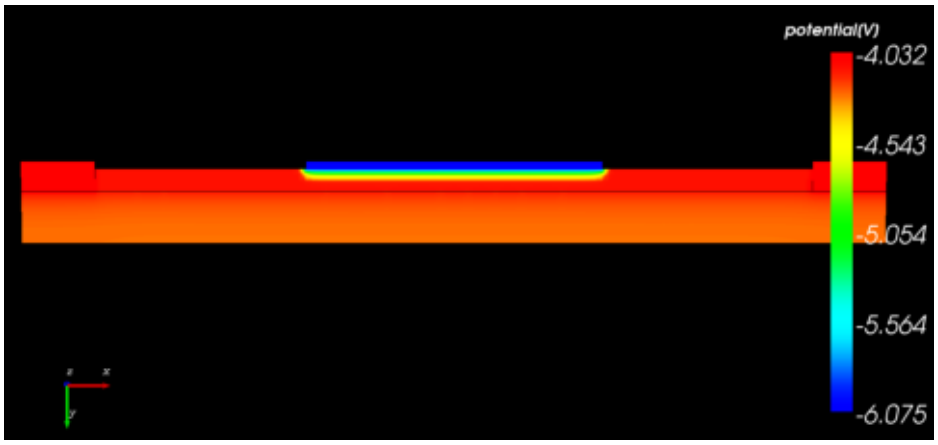

Figure 5.5: Potential profile of Au-GaAs MESFET device

Under forward bias conditions, the devices exhibit zero photoresponse. This is attributed to the following: At the applied voltage, the depletion width reduces to zero. This eliminates the possibility of photogeneration in the depletion region and the subsequent development of photovoltage. Hence the result.

The devices show good UV/visible contrast of the order of 10^{-4} (maximum) which is highly suitable for detecting under background radiation. Also, the devices can function as dual-band operating photodetectors (i.e. UV and visible) since the responses attained are significant in both cases. Further, the device can be switched between diode mode (Schottky junction) and transistor mode (MESFET) by suitably changing the bias conditions thus, operating as a dual-mode device.

The performance comparison of the investigated detectors with that reported in the literature is depicted in Table 5.6, 5.7, and 5.8. The present work shows comparable or enhanced performance than the reported literature.

Table 5.6: Performance comparison of various detectors operating in UV/visible regions with the present work on Schottky junctions

Sr. No.	Device	Wavelength (nm)	Applied Bias (V)	Responsivity (A/W)	External Quantum Efficiency (%)	Reference
1.	Graphene-GaAs Schottky junction in MESFET	UV @ 350 nm	$0/-1.1$	0.33/0.278	119.1/98.74	This work
2.	Graphene-GaAs Schottky junction in MESFET	Visible @ 450 nm Visible @ 650 nm	$0/-1.1$ $0/-1.1$	$1.08 \times 10^3/0.265$ $1.32 \times 10^3/0.212$	$2.98 \times 10^5/73.14$ $2.52 \times 10^5/40.33$	This work
3.	Au-GaAs Schottky junction in MESFET	UV @ 350 nm	$0/-1.1$	0.177/0.278	63.1/98.74	This work
4.	Au-GaAs Schottky junction in MESFET	Visible @ 450 nm Visible @ 650 nm	$0/-1.1$ $0/-1.1$	$1.01 \times 10^3/0.265$ $1.29 \times 10^3/0.212$	$2.79 \times 10^5/73.14$ $2.46 \times 10^5/40.33$	This work
5.	Graphene-GaN Schottky junction in MESFET	UV @ 350 nm	$0/-1.1$	36.9/0.0753	$1.31 \times 10^4/25.75$	This work
6.	Au-GaN Schottky junction in MESFET	UV @ 350 nm	$0/-1.1$	36.45/0.0753	$1.29 \times 10^4/26.7$	This work
7.	ZnO/Si heterojunction diode	UV/Visible	–	0.28/0.36	90/93	[186]
8.	Au/Ni-ZnSe Schottky diode	Visible @ 460 nm	–	0.1	27	[187]

Table 5.7: Performance comparison of various detectors operating in UV/visible regions with the present work on Schottky junctions (continued)

Sr. No.	Device	Wavelength (nm)	Applied Bias (V)	Responsivity (A/W)	External Quantum Efficiency (%)	Reference
9.	Au-GaN Schottky diode	UV @ 364 nm	–	53×10^{-3}	18.1	[187]
10.	Au/n-Si Schottky photodiode	Visible @ 550 nm	0	0.2081	47	[188]
11.	DNA-CTMA/GaN photodiode	UV/Visible	Positive or zero/Negative	$1.8 \times 10^{-3}/4.3 \times 10^{-6}$	–	[189]
12.	PtSi/n-Si Schottky diode	Visible from 560–700 nm	−5	–	70	[189]
13.	PtSi/p-Si Schottky diode	Visible @ 550 nm	–	0.3143	71	[189]
14.	$Cu_2ZnSn(S,Se)_4$ (CZTS)-based photodetector	Visible @ 532 nm	5	15×10^{-3}	3.5	[190]
15.	2D organic-inorganic hybrid thin films	UV @ 365 nm	−9	4	1361.5	[191]
16.	2D organic-inorganic hybrid thin films	Visible @ 532 nm	−9	0.7	163.47	[191]

Table 5.8: Performance comparison of various detectors operating in UV/visible regions with the present work on Schottky junctions (continued)

Sr. No.	Device	Wavelength (nm)	Applied Bias (V)	Responsivity (A/W)	External Quantum Efficiency (%)	Reference
17.	Reduced graphene oxide gel	Visible @ 465 nm	0.1	0.73	195	[192]
18.	Individual WS_2 nanotubes	Visible @ 633 nm	0.5	3.14	615	[193]
19.	CdTe single nanoribbon-based	Visible @ 400 nm	10	7.8×10^2	2.4×10^5	[194]
20.	High quality In_2Se_3 nanowire arrays	Visible @ 500 nm	3	89	22,000	[195]
21.	ITO-GaP Schottky photodiode	UV @ 375 nm Visible @ 435 nm	–	0.1992 0.28	66 80	[196]
22.	Organic small molecule photodetector	UV @ 250 nm Visible @ 446 nm	−3	0.3421 0.2154	170 60	[197]
23.	ZnO/Cu_2O nanowire electrolyte heterojunctions	UV @ 370 nm Visible @ 400 nm	0	0.0193 0.0082	6.48 2.55	[198]
24.	Si pyramidal microplasma	Visible @ 625 nm	–	950±250	1.89×10^5 @ 950 A/W 2.38×10^5 @ 1200 A/W 1.39×10^5 @ 700 A/W	[199]
25.	Ir-InGaN Schottky photodiode	Visible @ 410 nm	0	0.032	10	[200]
26.	Au-Ti/PbS Schottky photodiode	Visible−1600 nm	−3	0.667	53.3	[201]

5.3 Bias-dependent Dual Mode Buried-gate GaAs/GaN OPFET for VLC/UV Communication

5.3.1 Dual mode GaAs OPFET for Visible-Light Communication

A dual-mode buried-gate GaAs OPFET for Visible-Light Communication (VLC) is proposed which can be switched to high background light immunity applications or to applications in which the same optical source is used for lighting as well as communication by simply changing the biasing conditions. The device can be operated either in the diode mode wherein the Schottky junction can act as photodetector at zero gate and drain bias or in the transistor mode whereby the OPFET itself functions as photodetector at positive drain bias and zero gate bias. The individual detectors are studied at a wide range of optical power densities. The detector parameters such as responsivity, bandwidth, unity-gain cut-off frequency, and dark current are calculated.

The operating wavelength is 600 nm. Table 5.9 depicts the comparative study of the Schottky junction photodiode and the OPFET detector in terms of responsivity, bandwidth, unity-gain cut-off frequency (f_T), and dark current for a gate length of 25 μm and at different radiation flux densities. Refer to Table 4.9 for the parameters employed in calculation.

The advantage of the Schottky junction over the OPFET is the low dark current and the ability to function in the self-powered mode i.e. zero-bias operation. Further, it exhibits larger bandwidth at the higher flux densities as shown in Table 5.9. The responsivities are significantly high owing to the considerable photovoltage generated but comparatively lower than that in the OPFET. In other words, both the devices show tremendous gain, thus, avoiding the need for additional amplification. The frequency range in which the Schottky photodiode can amplify signals is determined from the plot of photocurrent gain versus fre-

Table 5.9: Performance comparison of the Schottky photodiode and the OPFET detector under visible illumination

Schottky junction (I_{dark}=10^{-19} A)			
Photon Flux Density ($/m^2$-s)	Responsivity (A/W)	Detection Bandwidth (Hz)	Amplification Bandwidth (Hz)
10^{16}	1.265×10^6	62.2 MHz	3 GHz
10^{19}	4.5×10^5	79 MHz	3.5 GHz
10^{22}	308.9	0.22 GHz	5.2 GHz
10^{24}	44.98	0.86 GHz	7 GHz
OPFET (I_{dark}=33 mA)			
Photon Flux Density ($/m^2$-s)	Responsivity (A/W)	Detection Bandwidth (Hz)	Amplification Bandwidth (Hz)
10^{16}	8.1×10^7	2.06 GHz	1.54 GHz
10^{19}	1.12×10^5	4.57 GHz	1.67 GHz
10^{22}	720	1.48 MHz	2.3 GHz
10^{24}	81.21	7.85 MHz	0 GHz

quency and is given by the frequency at which the gain is unity. In the case of the OPFET, the frequencies upto which the device exhibits amplification is given by the parameter, f_T. Since the OPFET device is operated with a very long gate length of 25 μm, the f_T is considerably decreased (Table 5.9). This relation of f_T with gate length is well established in theory. Thus, operating at longer gate lengths limits the detection-cum-amplification bandwidth of the OPFET device. However, this adversely increases the detection bandwidth of the Schottky junction at the higher intensities owing to the significant effect of the illumination on the minority carrier lifetime.

The basis of the investigation of the bandwidth enhancement in the Schottky photodiode at higher flux densities is that the photoconductive contribution is considerably less in photovoltaic mode. The photoconductive effect can greatly reduce the overall bandwidth due to the slow diffusion and the fast drift components adding negatively to the photovoltaic current. In addition, the diffusion current follows the combined net dependence of the depletion width and the hole lifetime on the frequency whereas the drift current only depends upon the depletion width. When the optical illumination is modulated with a small signal of frequency, ω, the lifetime of electrons and holes is also modulated. The fast drift of the photogenerated holes across the junction by the built-in electric field in the depletion region and the short lifetime of holes (10 ns) greatly increase the photovoltaic bandwidth, bandwidth being inversely proportional to the carrier lifetime. Further, the change in the lifetime of the minority carriers (holes) under illumination also plays a significant role in the augmentation of the bandwidth due to the insignificant photoconductive effect. The hole lifetime decreases with illumination when the excess carrier density is comparable to or greater than the doping density. In the present work, this occurs at the flux density of 10^{22} $/m^2$-s and significantly at the flux density of 10^{24} $/m^2$-s. However, at the lower intensities, the bandwidth is moderate since the excess carrier density is negligible

compared to the doping density.

On the other hand, in the OPFET device, the device is operated in photovoltaic-cum-photoconductive mode wherein the photovoltaic current contributes significantly at the lower flux densities owing to the high photovoltage being developed attributed to the buried-gate structure and the moderate absorption coefficient of GaAs at 600 nm (4×10^6 /m). This photovoltage is amplified through the transconductance of the device and results in a high bandwidth (in the gigahertz range). As the flux density is increased, since the photoconductive effect starts contributing considerably, the response is positively high, and owing to its sole contribution, the bandwidth falls in the megahertz range. The effect of illumination on the lifetime of the minority carriers does not affect the bandwidth.

The non-saturation of the photocurrent at higher flux densities evident in the Schottky photodiode and the OPFET detector is depicted in Figure 5.6. This phenomenon is of vital importance in the photodiode as being proposed to be used in high background light immunity applications. The effect of illumination on the lifetime of the minority carriers is portrayed in Figure 5.7.

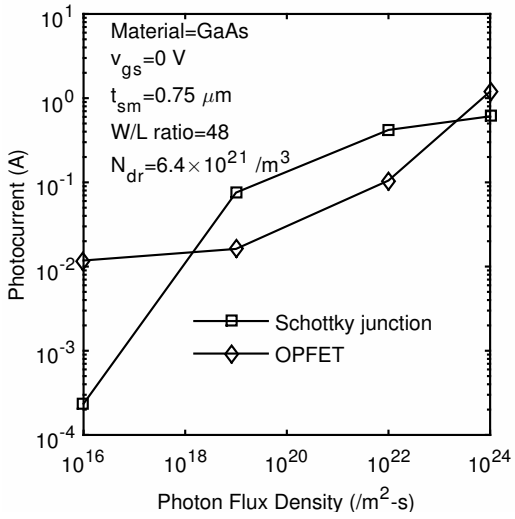

Figure 5.6: Photocurrent as a function of photon flux density in Schottky photodiode and the OPFET

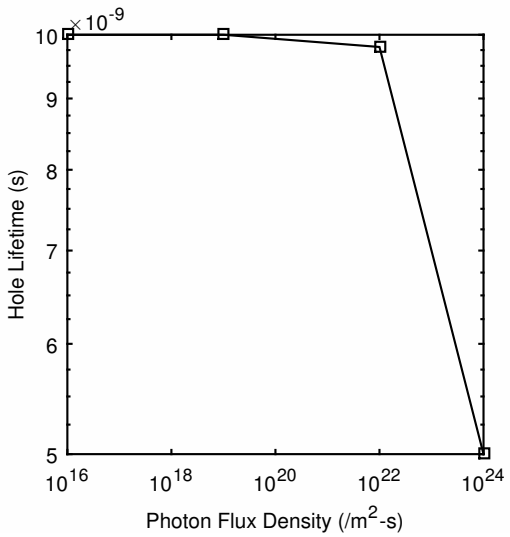

Figure 5.7: Illumination-dependent lifetime of minority carriers

The photodiode can simultaneously detect and amplify modulation frequencies upto 0.22 GHz and 0.86 GHz at the flux densities of 10^{22} and 10^{24} $/m^2$-s respectively whereas the OPFET device shows detection-cum-amplification upto 1.54 GHz and 1.67 GHz at the flux densities of 10^{16} and 10^{19} $/m^2$-s respectively.

5.3.2 Dual mode GaN OPFET for Ultraviolet Communication

The same principle of the dual-mode OPFET presented in the previous subsection is reproduced at UV wavelengths using GaN-based OPFET. The diode mode (Schottky junction mode) caters to high background light immunity applications whereas the transistor mode (OPFET mode) serves in applications in which the same optical source is used for imaging/treatment as well as communication. The operating wavelength is 350 nm. Table 5.10 summarizes estimated performance metrics of the Schottky junction photodiode and the OPFET detector. The material properties of GaN at the employed doping concentration are moderate absorption coefficient (8×10^5 /m) [178], low minority carrier lifetime (1 ns) [182], high saturation electron velocity (2.3×10^5 m/s) [179], high majority carrier lifetime (1.25 μs) [202], low saturation hole velocity (4.3×10^4 m/s) [203], moderate mobility (0.1 m^2/V.s) [204], high Schottky barrier height with Au metal (0.95 eV) [205], and high effective electron mass (0.27) [10].

Table 5.10: Performance comparison of the Schottky photodiode and the OPFET detector under Ultraviolet illumination

Schottky junction (I_{dark}=1.4 × 10^{-19} A)			
Photon Flux Density (/m^2-s)	Responsivity (A/W)	Detection Bandwidth (Hz)	Amplification Bandwidth (Hz)
10^{16}	291.4	0.73 GHz	68.13 GHz
10^{19}	289.8	0.73 GHz	68.13 GHz
10^{22}	74.1	1 GHz	68.13 GHz
10^{24}	2.47	2.2 GHz	63.2 GHz
OPFET (I_{dark}=14.9 mA)			
Photon Flux Density (/m^2-s)	Responsivity (A/W)	Detection Bandwidth (Hz)	Amplification Bandwidth (Hz)
10^{16}	1.05×10^7	24.3 GHz	0.38 GHz
10^{19}	1.9×10^4	16.3 GHz	0.61 GHz
10^{22}	565.3	0.615 MHz	1.29 GHz
10^{24}	9.45	57.4 MHz	2.23 GHz

Figure 5.8 shows the forward gate characteristics of the MESFET under different illumination conditions. The drain to source current voltage characteristics of the OPFET detector at different radiation flux densities are depicted in Figure 5.9.

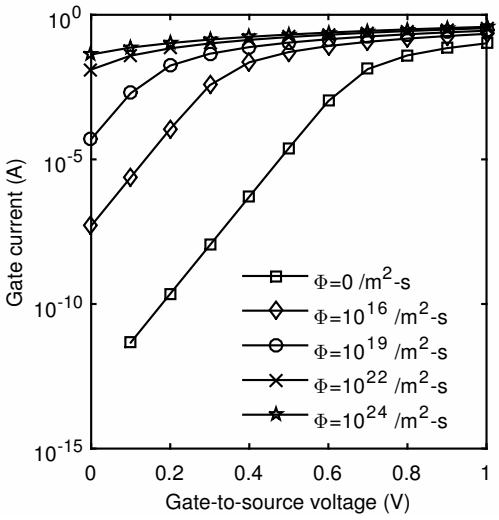

Figure 5.8: Gate current versus gate source voltage in OPFET at various flux densities.

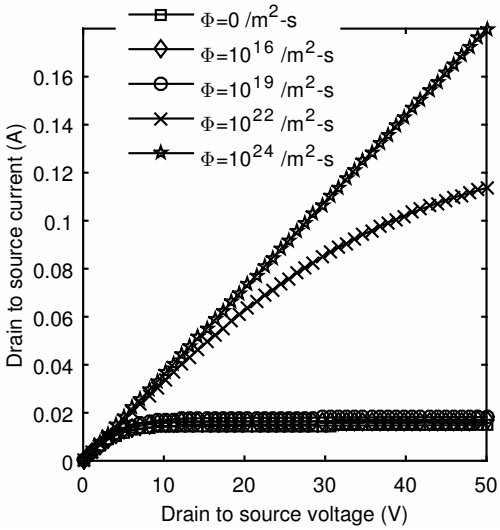

Figure 5.9: Drain-to-source current-voltage characteristics of the OPFET detector at different flux densities

The photovoltage perceived in the GaN buried-gate OPFET is considerable in the UV region (0.34 V, 0.52 V, 0.697 V, and 0.81 V), on account of the moderate absorption coefficient and high barrier height with Au, but is substantially lesser than that generated with GaAs buried-gate OPFET in the visible range (0.53 V, 0.71 V, 0.88 V, and 0.99 V) [24] owing to the higher absorption coefficient of GaAs

(4×10^6 /m) along with longer lifetime of holes (10 ns), and higher saturation hole velocity (1.085×10^5 m/s). The substantial photovoltage developed in the GaN OPFET device results in high responsivities in both the diode mode and the OPFET mode detectors. However, the difference in responsivities between the diode and transistor mode devices (transistor mode superior) in GaN OPFET is significantly higher than that in the GaAs OPFET owing to the substantial difference in the photovoltages (higher in the visible region). Thus, for a particular flux density, due to the exponential dependence of the thermionic emission current on the forward voltage, the effect of the higher photovoltage in the GaAs OPFET is felt more severely in terms of higher Schottky diode responsivities comparable to the OPFET device responsivities. On the other hand, in GaN OPFET, the lower photovoltage renders the Schotttky diode photoresponse to lower levels than the OPFET detector response. Owing to the absence of exponential dependence on the photovoltage of the OPFET mode device current (the OPFET device current exhibits dependence on photovoltage as understood from the modeling laid down in the referred works earlier −−−−−−−− the photovoltage is amplified through the transconductance of the device), the OPFET mode device is less sensitive to the difference in photovoltages in the UV and visible regions (as compared to the Schottky mode device) resulting in comparable responsivities in both the ranges.

Although the low hole lifetime is one of the contributing factors for reducing the photovoltage in GaN OPFET devices, this parameter inversely increases the photovoltaic bandwidth of the device since bandwidth is inversely proportional to the lifetime. This factor thus, establishes the trade-off between the efficiency and the bandwidth. Hence, the photovoltaic bandwidth is in the multi-gigahertz range (tens or twenties of gigahertz) in GaN OPFET mode device as opposed to in the gigahertz range in GaAs OPFET mode device and in the sub-gigahertz or gigahertz range in the GaN diode mode device in contrast to sixties or eighties of megahertz or sub-gigahertz range in the GaAs diode mode device (Tables 5.9 and

5.10). This clearly depicts the bandwidth enhancement in GaN-based devices.

The same principles apply as discussed in the previous subsection in the case of GaAs OPFET in regard to larger 3-dB bandwidths exhibited by Schottky junction at higher intensities and vice versa by OPFET at lower intensities.

As can been observed from Figure 5.8, the forward Schottky diode characteristics at different optical power levels notify that the device exhibits highest sensitivity at zero bias since it is at this bias condition that the photovoltage generated is maximum as compared to increased forward voltages where the photovoltage drops due to the reduction in the depletion width. The graph also shows that the characteristics saturate at high forward voltages due to the contribution of the source series resistance wherein the high currents involved produce significant voltage drop across the series resistance thus limiting the current. Further, the point of saturation shifts to lower levels of the forward applied voltage as the flux density increases. This is because, as the optical power increases, the photovoltage generated rises which is superimposed on the applied forward bias voltage thus, creating saturation at lower effective bias voltages.

Figure 5.9 depicts the saturation behavior of the OPFET device at low intensities at higher drain voltages and deviation from saturation at higher intensities. This is due to the photovoltaic effect being the mechanism at the lower intensities and the photoconductive effect dominance at the higher intensities. The large difference between the phototovoltaic and the photoconductive currents is owing to the significant enhancement of the photoconductive effect at high power levels.

The photodiode can simultaneously detect and amplify modulation frequencies up to 1 GHz and 2.2 GHz at the flux densities of 10^{22} and 10^{24} $/m^2$-s respec-

tively whereas the OPFET device shows detection-cum-amplification up to 0.38 GHz and 0.61 GHz at the flux densities of 10^{16} and 10^{19} $/m^2$-s respectively. The detection only bandwidths for the OPFET detector were 24.3 GHz and 16.3 GHz respectively.

The typical applications of the diode mode would be under-water communication in the presence of high background sunlight. The transistor mode would be employed in Li-Fi (Light-Fidelity) networks while the same optical source would be used for biomedical imaging or treatment applications.

Chapter 6

OPFET for 5G Applications

6.1 Graphene/Au-gated GaAs Front-illuminated OPFET Photodetector and Oscillator for 5G Applications

With the advancement of technology, the RF communication bandwidth is switching towards 5G and 6G communications. To relieve the congestion of traffic imposed on RF communication, operating in the optical domain or integrating RF and optical communication is imperative. The core components in this scenario are the oscillators as transmitters and photodetectors as receivers. These devices should be capable of high-speed and high-gain operation simultaneously. In this regard, the potential of graphene/Au-gated GaAs front-illuminated OPFET (Optical Field Effect Transistor) as oscillator and detector towards 5G applications is explored.

The device is studied at an operating wavelength of 600 nm. The drain bias is varied between 1.3 V to 25 V. The gate bias is set to 0 V. The device dimensions are suitably chosen from scaling rules [154]: 4 μm gate length, 150 μm gate width, 0.3 μm active layer thickness, and doping concentration of 4×10^{22} $/m^3$. The surface to substrate thickness is 1 μm [33]. The parameters utilised for calculation are to be referred from Table 4.9. The Schottky barrier heights of Au and graphene with GaAs are 0.865 eV and 0.795 eV respectively. Table 6.1

Table 6.1: Characteristics of Graphene-GaAs front-illuminated OPFET

Photon Flux Density ($/m^2$-s)	DC Responsivity (A/W)	3-dB Bandwidth (Hz)	DC Transconductance (S)	DC Gate-to-source capacitance (F)	Unity-gain cut-off frequency (Hz) @ DC/BW freq
10^{16}	2.29×10^9	1 GHz	12.3 mS	0.367 pF	5.33/5.5 GHz
10^{19}	3.3×10^6	2.234 GHz	14.3 mS	0.51 pF	4.46/5.33 GHz
10^{22}	1.37×10^4	1.48 MHz	21.3 mS	0.28 pF	9.42/8.25 GHz

presents the estimated performance metrics of the graphene-gated GaAs OPFET photodetector at a drain-to-source bias of 3.94 V.

The graphene-gated GaAs front-illuminated OPFET exhibits photovoltages of (0.45 V, 0.63 V, and 0.81 V) at the corresponding flux densities of (10^{16}, 10^{19}, and 10^{22} $/m^2$-s) as opposed to (0.52 V, 0.7 V, and 0.88 V) in the Au-gated device. The high photovoltages arise from the extra amplification factor of ($\alpha v_y \tau_{\omega p}$) in the equation for hole density over the primary hole density and the decreasing denominator term (1-$\alpha v_y \tau_{\omega p}$) by one order magnitude. Additionally, since the device is illuminated from the surface side, at the optical wavelength of 600 nm, the moderate absorption coefficient of 4×10^6 /m corresponding to an absorption depth of 0.25 μm is sufficient enough to create a significant number of photocarriers in the gate depletion region. The contrasting photovoltages in the graphene- and Au-gated devices are attributed to the higher barrier height in the Au-gated device (0.865 eV) as opposed to graphene-gated OPFET (0.795 eV). This higher barrier height decreases the reverse saturation current density across the Schottky junction, thus, boosting the photovoltage. Due to the high photovoltages in both cases, large photovoltaic currents are generated. The dark current is higher in the graphene-gated device (12 mA) in contrast with Au-gated OPFET (11.3 mA) due to larger depletion width in the Au-gated device arising from the higher barrier height with analogous series resistances in both cases. The drain currents under illumination are equal in both cases (16.7 mA, 18.8 mA, and 39.9

mA). It is known that when the barrier height apparent to the carriers is lower, the sensitivity of the depletion width to applied photovoltage is more than compared to the higher barrier height device. In the present case, since the device with graphene gate possesses a lower barrier height with a larger dark current, whereas the photovoltages are higher in the Au-gated device, the compensation mechanisms induced by these opposite effects result in equal currents. However, the photocurrents generated by the Au-gated device are higher due to the lower dark current. These larger photocurrents produce wider 3-dB bandwidths in the Au-gated device (1.62 GHz and 3.1 GHz) as compared to (1 GHz and 2.23 GHz) in the graphene-gated device at the lower intensities. At the higher intensity, the photoconductive effects from the gate junction region, the neutral channel region, and the substrate depletion region also contribute significantly with almost equal contributions in both cases. The equal contributions emanate from the compensation mechanism discussed earlier, which maintains equal depletion widths in both cases, thus, extracting similar photoconductive charges. The minority hole carrier lifetime being of the order of nanoseconds produces 3-dB bandwidths in the GHz range under photovoltaic conditions. The photoconductive lifetime being of the order of microseconds results in MHz range bandwidths (1.6 MHz in the Au-gated device and 1.477 MHz in the graphene-gated OPFET) at the higher intensity. The higher photocurrents also produce higher responsivities in the Au-gated OPFET (2.6×10^9 A/W, 3.7×10^6 A/W, and 1.39×10^4 A/W).

The dc transconductances and gate-to-source capacitances exhibit almost equal values in both the graphene-gated and Au-gated devices. The equal values arise from the compensation phenomena stated earlier. The transconductances increase with optical power (Figure 6.1) due to the increase in photovoltages and the additional contribution from the photoconductivity at the higher intensity. The capacitances show a similar behaviour except at the higher intensity due to the effective de-ionization of the space charge ions by the photogenerated electrons

in the junction region since the photogenerated electron density is comparable to the depletion charge density at this power level (Figure 6.2). The moderately high transconductances and moderate capacitances result in moderate unity-gain cut-off frequencies in both cases.

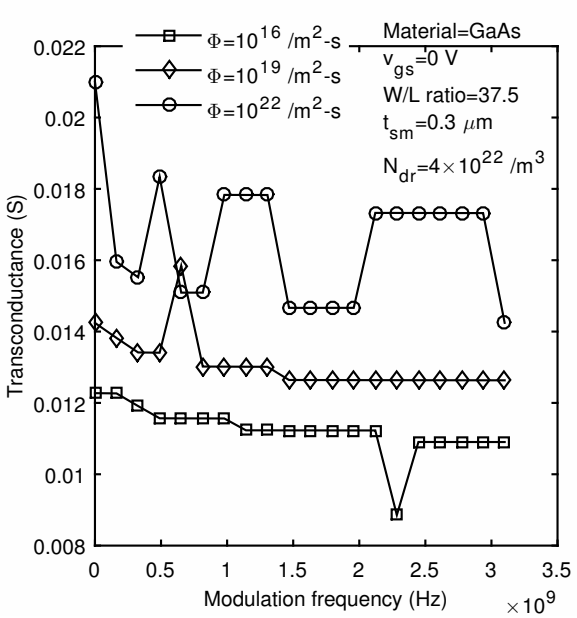

Figure 6.1: Transconductance versus modulation frequency at different optical flux densities

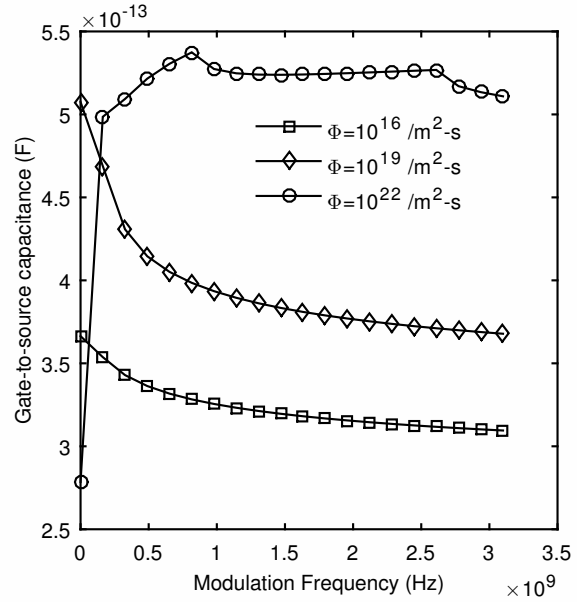

Figure 6.2: Gate-to-source capacitance versus modulation frequency at different optical flux densities

The oscillation performance of the graphene-gated OPFET is shown in Table 6.2 at a drain-to-source bias of 3.94 V after the stability factor (K-factor)

for oscillation and other oscillation conditions at the ports have been satisfied. The Au-gated device also shows the same performance since the oscillation parameters are dependent upon the transconductance, gate-to-source, gate-to-drain, and drain-tosource capacitances, the drain-to-source resistance, and the drain-to-source saturation current, which are estimated to be equal in both the devices. This is attributed to the reasons discussed above. The device exhibits resonance at a source resistance of 270 Ω, source inductance of 8 nH, load resistance of 27 Ω, and load inductance of 17 nH. At the flux density of 10^{16} $/m^2$-s, the OPFET device resonates over a narrow band of frequencies ranging from 1.47 GHz to 1.8 GHz. This is possible when the oscillation conditions are satisfied at a band of frequencies instead of a single frequency. This can be improved by optimisation. As the flux density increases to 10^{19} $/m^2$-s, the oscillation frequency reduces to 1.63 GHz with respect to the highest frequency (1.8 GHz) at the previous flux density. This observation is in line with previous studies [14, 35, 37]. Since the oscillation frequency is dependent only upon the intrinsic capacitances and is independent of the transconductance and the intrinsic resistances [37], the increase in optical power boosts the capacitances (Figures 6.2 and 6.3) and reduces the resonant frequency. At the higher flux density of 10^{22} $/m^2$-s, there is an increase in the oscillation frequency to 1.8 GHz. Although the dc gate-to-source capacitance undergoes a fall in its value, at the frequency of oscillation, the capacitance increases (Figure 6.2). This is ascribed to the significant reduction in the deionization process at high frequencies due to the modulation of electron lifetime with frequency. Additionally, the high photovoltage, although modulated with frequency, is sufficient enough to open many of the depleted regions, thus registering sensitivity. Also, there is a significant boost in the gate-to-drain capacitance at the higher intensity (Figure 6.3). Even though the capacitances increase, the oscillation frequency increases. The reason behind this is still being investigated by the authors.

Table 6.2: Oscillation parameters of graphene-GaAs OPFET

Photon Flux Density ($/m^2$-s)	Source Impedance (ohms)	Load Impedance (ohms)	Oscillation Frequency (Hz)	Gain (S_{21} dB)	Phase (S_{21} degrees)
10^{16}	270 Ω/8 nH	27 Ω/17 nH	(1.47, 1.63, 1.8 GHz)	4.1 dB	144.3°
10^{19}	270 Ω/8 nH	27 Ω/17 nH	1.63 GHz	4.5 dB	137.12°
10^{22}	270 Ω/8 nH	27 Ω/17 nH	1.8 GHz	3.94 dB	115.95°

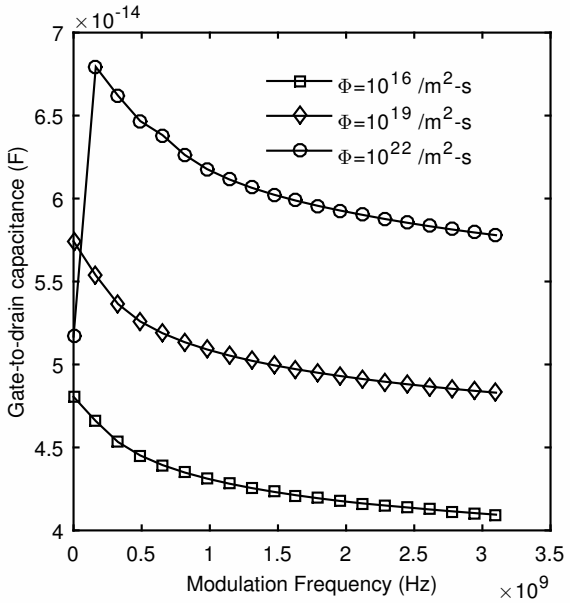

Figure 6.3: Gate-to-drain capacitance as a function of modulation frequency at various photon flux densities

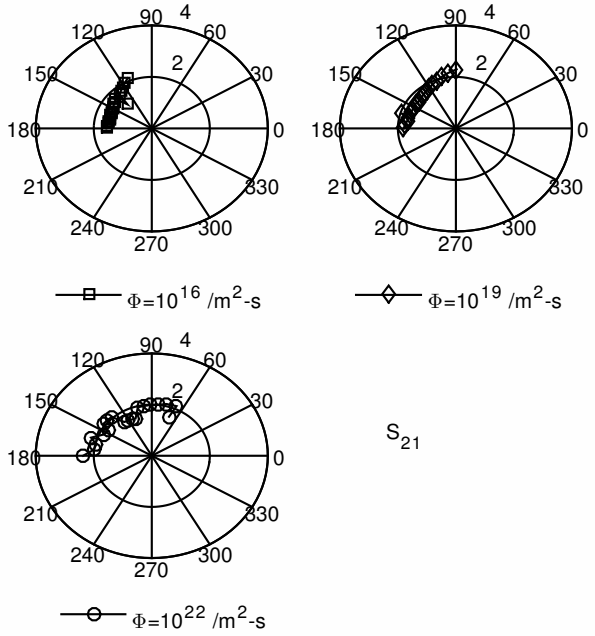

Figure 6.4: Polar plots of S_{21} at different flux densities

The oscillator gain initially increases from 4.1 dB to 4.5 dB as the flux density is varied from 10^{16} to 10^{19} $/m^2$-s and then reduces to 3.94 dB at the flux density of 10^{22} $/m^2$-s. The gain, which is directly proportional to transconductance and inversely related to capacitance, exhibits an initial increase due to the significant boost of the transconductance with optical power while the capacitance increases at a slower rate (compare Figures 6.1, 6.2, and 6.3). At the higher flux density, the gain falls since the transconductance increases at a slower rate than the capacitances at the oscillation frequency. The significant boost of capacitances is due to the reasons stated earlier. It is further observed that the oscillator phase reduces when the optical power increases. Thus, the oscillation frequency, gain, and phase can be suitably tuned with optical power. Figure 6.4 presents the simulated polar plots of the device at different radiation flux densities indicating that the gain and phase of the FET can be controlled to a larger extent when the optical power increases. This can have a significant bearing on the oscillator design when performing optimisation. The performance metrics estimated here are in line or close to the basic industrial standards for IoT (Internet of Things), i.e. IEEE802.15.4 based on Zigbee Technology operating in there frequency bands

(868MHz in Europe, 915MHz in the USA, and 2.4 GHz globally) [206, 207]. These standards are further divided into standards such as WirelessHART (2007) and ISA100.11a (2009) for employment in ultra-high reliability and ultra-low power industrial harsh environments. The performance also suits for two of the three frequency bands (183–683 MHz, 1640–2140 MHz, and 2200–2700 MHz) studied in [208] for indoor industrial applications. Further optimisation of the investigated devices will ensure complete compatibility with these standards.

The device performance metrics, together with the ability of the graphene and GaAs materials to resist harsh environments such as high temperatures suggest that this device will prove useful in sub-6 GHz harsh environment 5G applications viz. handheld 5G devices and industrial Internet of Things (IoT)-enabled systems in smart cities, automotive, space, and aeronautics applications.

6.2 Configurable OPFET-based Photodetector for 5G Smart Antenna Applications

The optical control of phased array smart antennas is possible with the help of lasers, modulators and photodetectors. Among these components, the photodetectors play a major role since these are the ones which directly control the voltages to be applied to the phased arrays. Photodetectors convert the intensity-modulated continuous-wave optical signal into microwave signal which is directly fed into the antenna. Depending upon the relative amplitudes and phases of the photodetector output current, the main beam will be directed in a specific direction and the nulls will be set to other directions.

Since the OPFET possesses high gain-bandwidth product, this work investigates and analyzes the extent to which the gain, phase, and bandwidth, of the GaAs OPFET-based photodetector can be varied by varying the drain bias, gate

bias, optical power, modulation frequency, as well as by choosing different illumination models and different structural dimensions. From these investigations, the optimum (Signal-to-Noise+Interference Ratio) in the desired direction can be derived. This work involving adaptive signal processing and the complete implementation of the optical phased array antenna system will be considered for future work.

The wavelength of optical source is considered to be 600 nm. The drain bias is varied between 0 to 10 V whereas gate bias is set between -2 V to 0 V. The radiation flux densities of 10^{15}, 10^{17}, 10^{19}, 10^{21}, and 10^{23} $/m^2$-s used in the simulations correspond to the optical power densities of 0.033 μW/cm^2, 3.3 μW/cm^2, 0.33 mW/cm^2, 33 mW/cm^2, and 3.3 W/cm^2 respectively. The gate material is assumed to be transparent ITO (Indium- Tin-Oxide). The parameters utilized in calculations are listed earlier in Table 4.11. The device dimensions chosen for structural optimization are obtained from scaling rules [29]. Only the four most relevant sets are shown for comparison. The source/load impedances being considered are (300 Ω+$j2\pi\omega$(19.7 nH))/(300 Ω+$j2\pi\omega$(73 nH)).

At first, the 3-dB bandwidth performance of the OPFET detector with respect to the different illumination models as well as the different dimensions is estimated, as this parameter will decide the maximum frequency of operation of the individual antenna elements. The bandwidth performance is tabulated in Table 6.3. Referring to Table 6.3 with the listed performance metrics, the earlier discussions and analysis of the 3-dB bandwidth performance with respect to various illumination models, different dimensions, and different optical input power levels are verified. It is also observed that the bandwidth is high at the lower intensities in all the cases (greater than 1 GHz) suitable for 5 G applications. There is no excessive dark current even with the device pos-sessing the highest dimensions since the drain bias voltage is in the lower range (less than

Table 6.3: Bandwidth Performance of GaAs OPFET illumination models

Bandwidth (Hz) at the Gate Length (L=4 μm), Gate Width (Z=150 μm), Active-Layer Thickness (t_{sm}=0.3 μm), and Doping Concentration (N_{dr}=4 × 10^{22} /m^3), V_{DS}∼0.42 V and v_{gs}∼−1 V				
Photon Flux Density (/m^2-s)	Surface-Gate Front-Illuminated	Buried-Gate Front-Illuminated	Surface-Gate Back-Illuminated	Buried-Gate Back-Illuminated
10^{15}	3.1 GHz	2.62 GHz	4.57 GHz	6.81 GHz
10^{17}	5.8 GHz	8.64 GHz	17.7 GHz	39.2 GHz
10^{19}	12.87 GHz	13.9 GHz	53.9 GHz	129.3 GHz
10^{21}	3.1 GHz	3.326 GHz	45.2 MHz	2.031 MHz
10^{23}	13.71 MHz	5.71 MHz	4.156 MHz	23.93 MHz

Bandwidth (Hz) of buried-gate front-illuminated OPFET at V_{DS}∼0.42 V and v_{gs}∼−1 V				
Photon Flux Density (/m^2-s)	(L=3 μm, Z=100 μm, t_{sm}=0.27 μm, N_{dr}=5.33 × 10^{22} /m^3)	(L=4 μm, Z=150 μm, t_{sm}=0.3 μm, N_{dr}=4 × 10^{22} /m^3)	(L=5 μm, Z=200 μm, t_{sm}=0.4 μm, N_{dr}=3.2 × 10^{22} /m^3)	(L=8 μm, Z=350 μm, t_{sm}=0.45 μm, N_{dr}=2 × 10^{22} /m^3)
10^{15}	3.6 GHz	2.62 GHz	3.326 GHz	4.22 GHz
10^{17}	7.98 GHz	8.64 GHz	5.8 GHz	8.64 GHz
10^{19}	11.88 GHz	13.9 GHz	11.88 GHz	17.7 GHz
10^{21}	3.326 GHz	3.326 GHz	0.62 GHz	0.53 GHz
10^{23}	4.5 MHz	5.71 MHz	5.71 MHz	7.25 MHz

4 V). The transconductances and gate-to-source capacitances are also boosted with the increase in dimensions. But, the slope of transconductance increase is lower than that of the capacitance resulting in decreased gain and phase. Thus, there is a trade-off between bandwidth and gain-phase relationship, which can be optimized by properly choosing the dimensions.

Now, the extent of the gain and phase variation with respect to the control parameters such as the drain bias, gate bias, modulating frequency, and optical power, the choice of illumination model, as well as the device dimensions is discussed. Figure 6.5a and 6.5b respectively show the simulated gain and phase of the different illumination models as a function of drain bias at a gate to source

voltage of -1 V, a modulation frequency of 1 GHz, and an optical flux density of 10^{15} $/m^2$-s. The entire analysis can be carried out based on the relative contributions of the transconductances and the gate-to-source, gate-to-drain, and drain-to-source ca-pacitances under the influence of the various control parameters since these parameters dominate the contributions to the intrinsic Y-parameters. The analysis will also be assisted by the contribution from the photovoltaic effect. The gain increases with drain bias in all the cases and eventually saturate at the higher drain voltages. This is ascribed to the fact that at lower drain voltages, as the voltage increases, the transconductance increases due to the boosting of the drain to source current whereas all the capacitances decrease due to the increase in the depletion width. Since the transconductance is directly related to the real part of the Y_{21} and hence the S_{21} parameter whereas the reduction in capacitances suppresses the imaginary parts of Y-parameters, and hence boosts the imaginary part of S_{21} parameter, the gain increases. The saturation of the gain at higher voltages is due to the saturation of transconductance following the saturation of the drain-to-source current. The differences observed in the gains of different illumination models are owing to the differences in photovoltages which affect both the transconductances and the capacitances along with the differences in series resistances between surface- gated and buried-gate devices. At a considerable drain bias of 0.6 V, the surface gate front-illuminated OPFET shows the least gain due to the high photovoltage which although boosts the transconductance, also simultaneously boosts the capacitances, and along with the contribution from the higher series resistances. The next lowest gain is exhibited by the surface-gate back-illuminated OPFET on account of its low photovoltage which suppresses the transconductance along with series resistance effects. The buried-gate front-illuminated device shows higher gain due to the high photovoltage and lower series resistances. The highest gain is exhibited by the buried-gate back-illuminated OPFET on account of the lower photovoltage which suppresses the capacitances and also due to lesser series resistances.

Though there is variation in gain amongst these illumination models at this drain voltage of 0.6 V, for practical purposes it can be considered as constant and as such at low drain voltages, the device functions as a constant gain detector. At higher drain voltages, there is significant variation in gain since the capacitances are suppressed to a large extent, which means the gain is highly amplified by the combination of high transconductances and suppressed capacitances. At these voltages, the device behaves as a variable gain detector. Also, the gain can be varied between -15 dB to $+14$ dB by varying the drain bias from 0.2 V to 3.8 V.

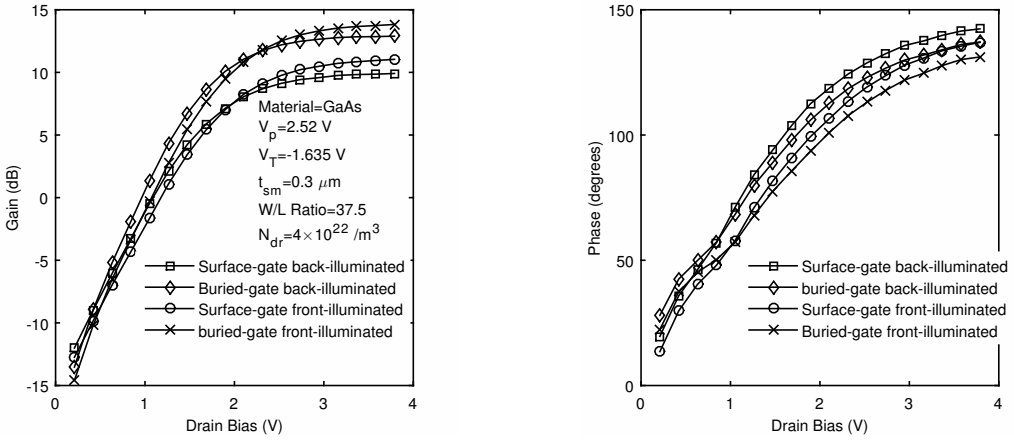

(a) (b)

Figure 6.5: Gain (a) and phase (b) versus drain bias for different illumination models at a gate voltage of -1 V, modulation frequency of 1 GHz, and flux density of 10^{15} $/m^2$-s.

On the other hand, the phase also shows significant increase as the drain bias increases. This can be explained by the fact that with the increase in voltage, the transconductance is enhanced while the capacitances decrease. This increases the real part of S_{21} parameter so also the imaginary part, but the rate of rise of imaginary part is higher than that of the real part, increasing the phase. The back-illuminated devices show higher phases than the front-illuminated OPFETs on account of the lower transconductances and suppressed capacitances. There is around 5 degree variation in phase with the change in the illumination model at a particular drain bias so that the total variation is around 15-20 degrees. The

phase can be varied between 20 degrees to 142 degrees with a change in bias from 0.2 V to 3.8 V.

Figure 6.6a and 6.6b respectively are the gain and phase plots obtained at the same set of control parameters as that in Figure 6.5a and 6.5b but at a higher modulation frequency of ∼5 GHz. The consequence of higher modulation frequency is the significant reduction in the transconductance due to roll-off of photovoltage with frequency. Also, the higher frequency increases the imaginary components of the Y-parameters although the capacitances decrease with the modulation of photovoltage with frequency. Thus, both the real and imaginary parts of the S_{21} parameter are reduced resulting in degraded gain. The gain also reduces through the transconductance delay component at high frequencies. The phase also shifts towards negative directions mainly because of the significant boost of the imaginary components of Yparameters along with the transconductance delay. It is observed that at high frequencies, both the gain and phase can be controlled to a larger extent with the change in illumination model. The increase in gain and phase with drain bias remained almost the same as that with low frequencies.

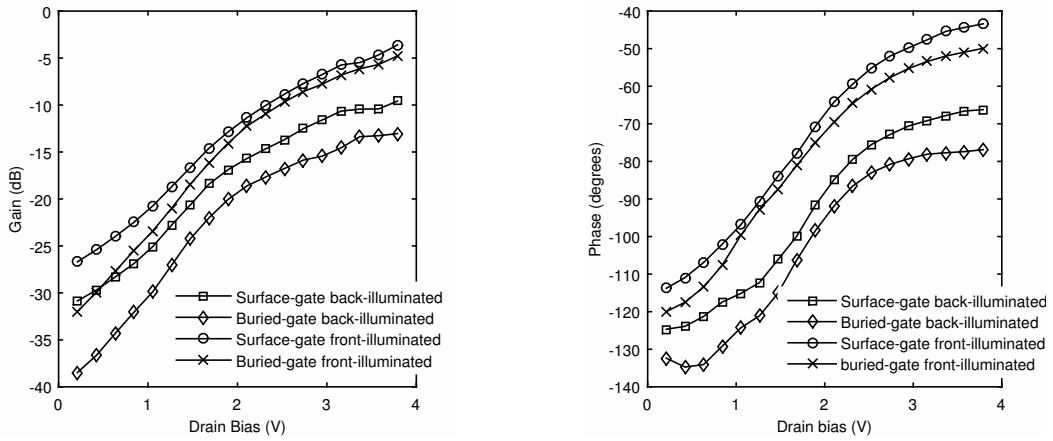

(a) (b)

Figure 6.6: Gain (a) and phase (b) versus drain bias for different illumination models at a gate voltage of −1 V, modulation frequency of ∼5 GHz, and flux density of 10^{15} $/m^2$-s.

Figure 6.7a and 6.7b represent the gain and phase responses versus drain bias of the buried-gate front-illuminated OPFETs with different dimensions at a gate voltage of -1 V, modulation frequency of 1 GHz, and flux density of 10^{15} $/m^2$-s. It can be seen from the above plots that the gain reduces with the increase in dimensions at the lower drain biases and tends to increase at higher voltages. This can be explained by the fact that at the lower voltages, both the transconductances and capacitances increase with dimensions (depletion width sensitivity being larger at lower doping concentrations), but the rate of increase of capacitances is higher than that of the transconductances. At larger voltages, the gain tends to increase attributed to the significant boost of transconductances and suppression of capacitances. The phase reduces with the increase in dimensions. At the lower voltages, this is ascribed to same reason as that for the gain response. At higher voltages, the boost of transconductances is higher than that of the suppression of capacitances, thus reducing the phase. It is also observed that the gain and phase can be controlled to a large extent by varying the dimensions. The phase range that can be controlled with the increase in dimensions is (52 to 150 degrees) and (20 to 130 degrees) for gate lengths of 3 μm and 4 μm respectively as the drain bias is varied between 0.2 to 3.8 V, (0 to 97 degrees) for gate length of 5 μm with drain bias variation from 0.2 to 5.1 V and (-25 to 70 degrees) for 8 μm gate length with change in bias from 0.2 to 6.5 V. This shows the versatility of the choice of dimensions on the phase responses; the dimensions should be carefully chosen along with the consideration of the dependence of 3-dB bandwidth and gain on gate length to give optimum results for a particular application.

Figure 6.8a and 6.8b show the gain and phase plots as a function of drain bias for buried-gate front-illuminated OPFET with a gate length of 8 μm at different gate voltages, modulation frequency of 1 GHz, and flux density of 10^{15} $/m^2$-s. The plots clearly show that the gain and phase can be controlled to a large extent with gate bias. The gain is lowered with the increase in gate voltages at the lower drain bias since both transconductance and capacitances

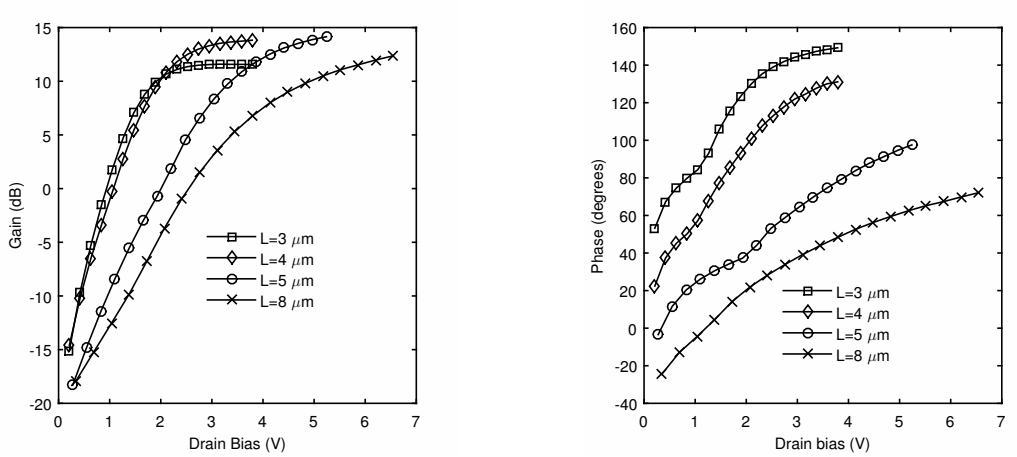

(a) (b)

Figure 6.7: Gain (a) and phase (b) versus drain bias for different dimensions of buried-gate front-illuminated OPFET at a gate voltage of -1 V, modulation frequency of 1 GHz, and flux density of 10^{15} $/m^2$-s.

increase with gate voltage, but the slope of increase of capacitances is larger than that of the transconductances. The transconductances are low at low drain biases due to the smaller magnitude of drain-to-source currents. Whereas, the capacitances being independent of drain-tosource currents, show large values. At higher drain bias, the gain increases with gate voltage due to the significant boost of transconductances and suppression of capacitances. The phase response shows a decrease with gate voltage at all drain biases due to the same reasons as mentioned above.

Figure 6.9a and 6.9b depict the gain and phase plots of the buried-gate front-illuminated OPFET with a gate length of 4 μm at different flux densities, modulation frequency of 1 GHz, and gate bias of -1 V. It is observed that the gain slightly reduces with the increase in optical power at the lower drain voltages since the rate of increase in capacitances is slightly larger than that of the transconductances. Almost equal gains are recorded at the higher drain voltages, the reason still being investigated. For practical purposes, the gain can be considered constant with optical power. The phase responses are shown to reduce by 5 degrees with a step increase in optical power with a total variation of 10 degrees due to the same reasons as mentioned above.

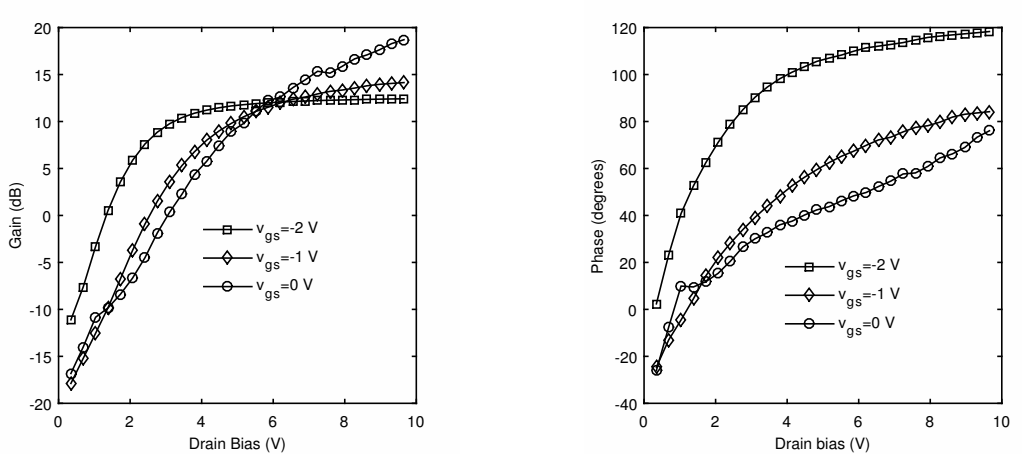

(a) (b)

Figure 6.8: Gain (a) and phase (b) versus drain bias for buried-gate front-illuminated OPFET with a gate length of 8 μm at different gate voltages, modulation frequency of 1 GHz, and flux density of 10^{15} $/m^2$-s.

In the plots represented in Figures 6.5 to 6.10, the x-y plots were used to depict individually the gain and phase responses since the comparative analysis using three or more values for control parameters were better represented using x-y plots. Polar plots on the other hand, give superior pictorial depiction, but when the number of values for control parameters is less as in the case of Figure 6.10a and 6.10b. Through these figures, we demonstrate that positive phase responses are also possible at high frequencies through optimization. Specifically, using higher value of gate voltage (0 V) and a source/load impedance value comparable to the frequency of operation would serve the purpose. Also, larger gains are achieved at higher drain voltages. The source/load impedances used for this purpose were $(300\ \Omega + j2\pi\omega(1\text{ nH}))$.

In all the above plots, the stability analysis has been done and it is found in overall that the device will produce unconditional stable response at the low to mid drain voltages. The unconditional stable response can be achieved at all drain voltages with further optimization. Nevertheless, the device produces conditional stable responses at the source and load impedances under consideration at all

drain voltages.

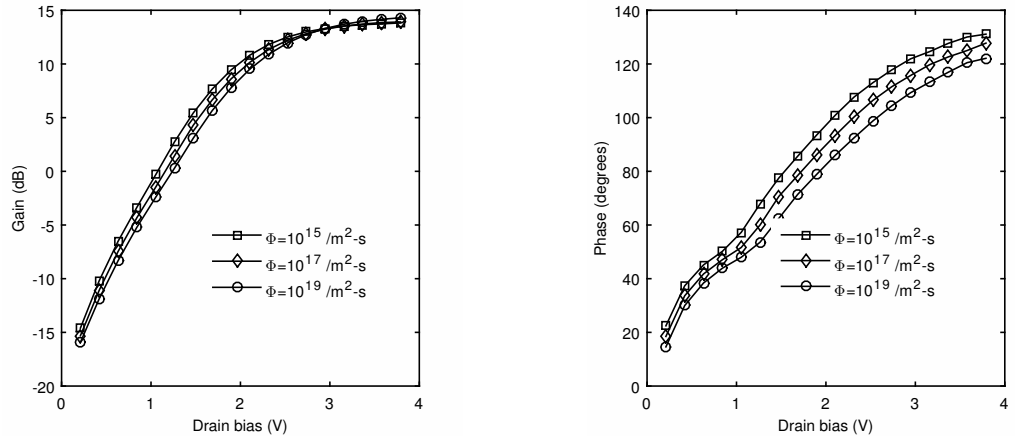

(a) (b)

Figure 6.9: Gain (a) and phase (b) versus drain bias for buried-gate front-illuminated OPFET with a gate length of 4 μm at different flux densities, modulation frequency of 1 GHz, and gate bias of -1 V.

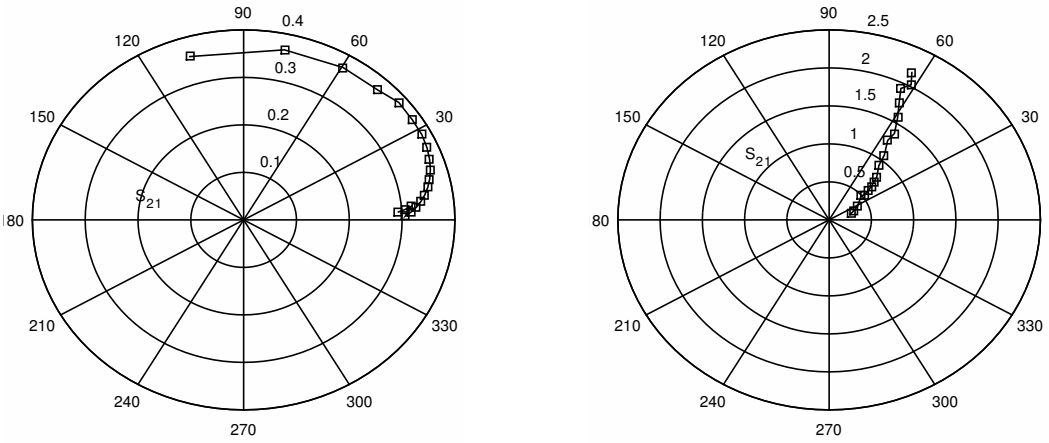

(a) (b)

Figure 6.10: Polar plots (a) as a function of frequency (1.7 GHz to 13.2 GHz) for buried-gate front-illuminated OPFET with a gate length of 4 μm at a gate bias of 0 V, a drain bias of 0.63 V, and an optical intensity of 10^{17} $/m^2$-s, and (b) as a function of drain bias (0.2 V to 3.8 V) at a frequency of $\sim$5 GHz with other control parameters maintained the same.

The frequency range of operation of these devices show that they will serve better purpose in 5G Internet of Things (IoT) or Optical Wireless Communication (OWC) based smart applications such as smart home, airport, train station and railway, smart shopping, plant and industry, smart healthcare, smart automobiles etc.

Chapter 7

OPFET under Solar Illumination

7.1 GaAs and Si OPFET Photodetectors for Solar Cell Applications

The potential of the GaAs and Si-based OPFET photodetectors for use in solar cell applications has been examined. The solar power spectrum with the air mass ($AM0$) suitable for satellite and space vehicle applications is provided as an input. The detectors parameters such as responsivity, External Quantum Efficiency (EQE), and switching time are calculated. The photocurrent and photovoltage generated as a function of wavelength are plotted and deeply analyzed. The comparative study of the Si and the GaAs OPFET detectors is presented. The analysis is based on the structural, material parameters, and the external factors applied. The gate materials utilized are Indium-Tin-Oxide (ITO) for Si and gold (Au) for GaAs. Two distinct illumination models: Buried-gate front-illuminated OPFET and the generalized model of OPFET are being considered for the study.

The drain bias is set to 3.45 V and the gate is shorted to the source (0V). A wavelength sweep of the input solar power spectrum considering air mass conditions ($AM0$) suitable for satellite and space vehicle applications is carried out. The power spectrum is shown in Figure 7.1. The corresponding average photon flux density is calculated to be 2×10^{21} $/m^2$-s. A sufficiently large gate length

of 4 μm, gate width of 150 μm, active layer thickness of 0.3 μm, and a doping concentration of 4×10^{22} $/m^3$ are being employed for the devices to deliver the necessary gain. The photovoltage and photocurrent as a function of wavelength for the two models and for the two materials (Si and GaAs) are plotted in Figures 7.2 to 7.5. The parameters employed in calculation are to be referred from Table 4.11. The Schottky barrier height of Au-GaAs junction is 0.865 eV.

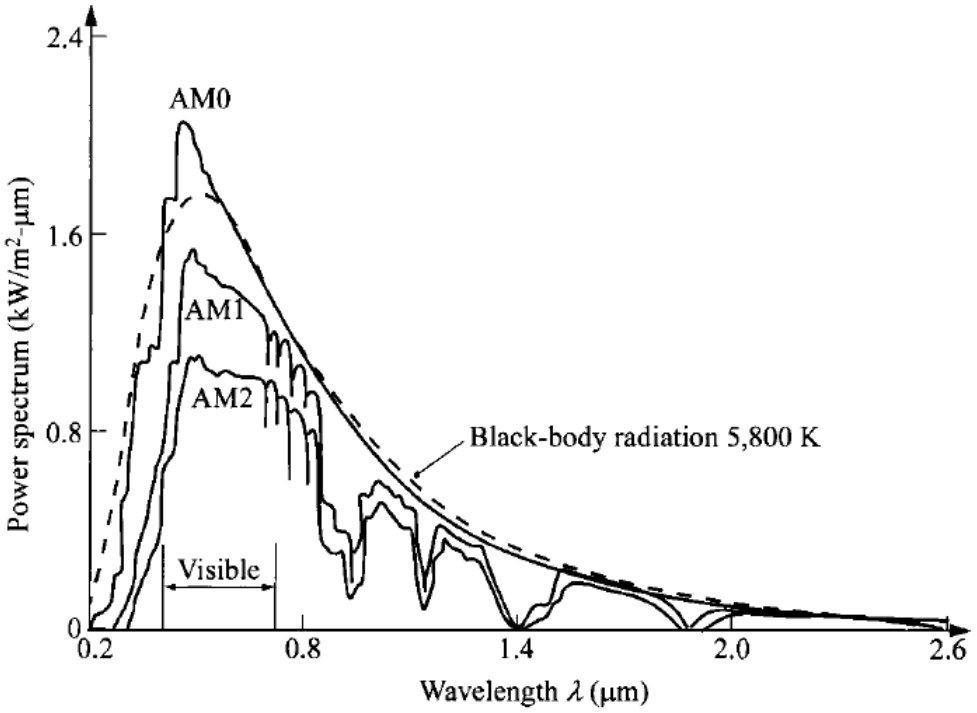

Figure 7.1: Solar power spectrum [10]

It is observed that the photovoltage spectra (Figure 7.2 and 7.3) are close replica of the input solar spectrum (Figure 7.1). Similarly, the photocurrent responses (Figure 7.4 and 7.5) are efficient reproduction of the input spectrum. This shows that the Si and GaAs devices have high potential of converting the solar energy into electricity as a combined function of the power (or the photon flux) and the wavelength of radiation. The average photocurrents generated in the Si and the GaAs generalized OPFET devices are 7.7 mA and 15 mA whereas in the buried-gate detectors are 6.2 mA and 5 mA respectively. These values are significantly high stating that these detectors are efficient converters of solar energy into electrical energy. The series resistances and the load resistances

can be optimized through various optimization procedures especially structural optimization to deliver maximum output power which can surpass the existing solar cells. These detectors when combined in series in the form of arrays can substantially generate large amount of electricity to power the satellites and the space vehicles.

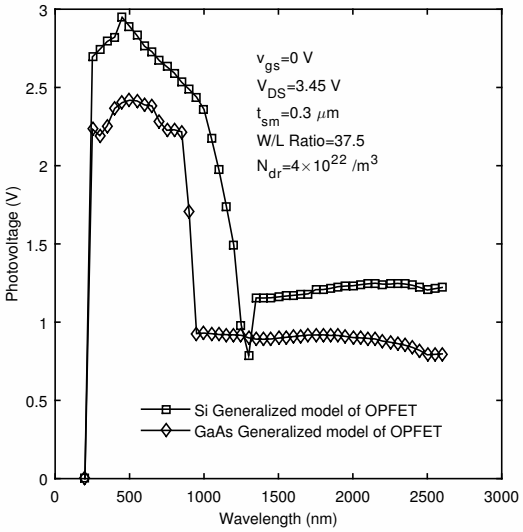

Figure 7.2: Photovoltage comparison of the Si and GaAs generalized OPFET models

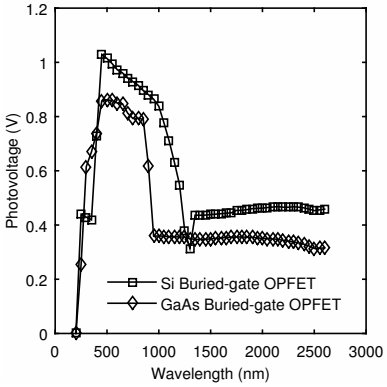

Figure 7.3: Photovoltage comparison of the Si and GaAs buried-gate OPFET models

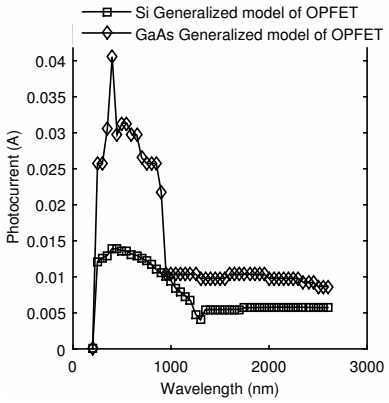

Figure 7.4: Photocurrent in Si and GaAs generalized OPFET models

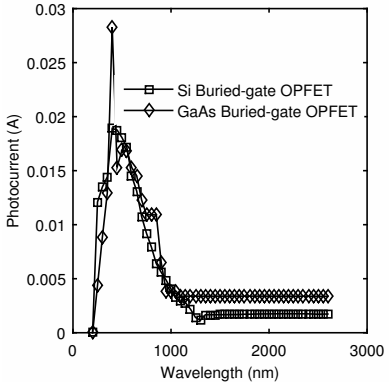

Figure 7.5: Photocurrent in Si and GaAs buried-gate OPFET models

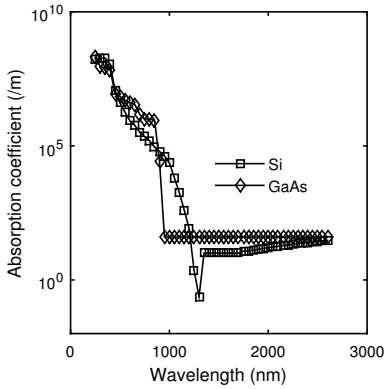

Figure 7.6: Absorption coefficient in Si and GaAs as a function of wavelength [12]

The photovoltages generated in the Si OPFET models are significantly larger than the GaAs devices mainly due to the fact that the hole lifetime in Si is considerably longer (75 μs) more than 3 orders of magnitude than that in GaAs (10 ns) (refer Figure 7.2 and 7.3). These higher photovoltages ought to have produced larger photocurrent responses in Si OPFET models. However, the fact is in the

case of generalized model, the GaAs OPFET greatly supersedes the Si OPFET in the whole of the spectrum (see Figure 7.4). This can be explained by the fact that in the Si OPFET, the electron mobility is much lower (0.09 m^2/V.s) as compared to that in GaAs OPFET (0.52 m^2/V.s), which draws very small current in Si OPFET in the spacings thus, considerably raising the series resistances. In GaAs OPFET, the series resistances are maintained to lower values (R_s ≈26 Ω and R_d ≈35 Ω) as compared to that in Si OPFET (R_s ≈117 Ω and R_d ≈85 Ω). On account of the lower series resistances in the GaAs OPFET, the limitation of the photovoltaic and the photoconductive currents due to the voltage drop across the series resistances is lesser in the GaAs device. Since in the wavelength region below 900 nm, the photovoltages generated in GaAs device are very high, the absorption coefficient is large (see Figure 7.6), the photon flux is high enough, and the electron lifetime is long (1 μs), large photovoltaic and photoconductive charges are perceived. These charges assisted by the higher mobility and higher saturation velocity in GaAs develop much larger photocurrents in the GaAs detector than that in the Si OPFET below 900 nm. In this region, in the Si OPFET, since the incident optical power is high, the absorption coefficient is large (Figure 7.6), the electron lifetime is much longer (75 μs), considerable photoconductive current is developed. This current develops large voltage drop across the series resistances owing to the high series resistances involved thus, increasing the depletion width with illumination and exhibiting negative sensitivity. The photovoltaic currents have no role to play in this wavelength region in the Si OPFET owing to negative sensitivity. The photoconductive contribution is from the gate depletion region at instances where the photon flux is high and eliminating the contribution from the neutral channel region due to the complete depletion of the channel. In this case, the saturation current increases without bounds since the contribution is from the gate depletion region which increases with illumination and the series resistances play an enhancing role instead of the limiting role. However, the much lower electron mobility in Si greatly suppresses the conductance

component resulting in lower current (Figure 7.4). As the wavelength is extended above 900 nm, the photovoltages significantly drop owing to the substantial fall in the absorption coefficient in both the Si and the GaAs devices (photovoltages still higher in the Si device). But due to the earlier mentioned factors of higher mobility, larger saturation velocity, and lower series resistances in GaAs OPFET, the photovoltaic currents are enhanced as compared to that in the Si OPFET. This produces larger photocurrent response in the GaAs device also at the wavelengths above 900 nm. The photoconductive currents are negligible in this region since the absorption coefficients have dropped considerably. On the other hand, in the buried-gate OPFET, the scenario is different (see Figure 7.5). The photovoltages generated are high but significantly lower than that in the generalized model owing to the additional contribution from the sidewalls of the gate depletion region in the generalized model. In the region below 900 nm, the photovoltaic current drops considerably in the GaAs OPFET due to the lower photovoltages whereas the photoconductive current is maintained at almost the same level. This is because in the GaAs generalized model of OPFET, the large photovoltages and the lower series resistances decrease the depletion width to zero thus, the photoconductive effect in the neutral channel region contributes at its potential. In the GaAs buried-gate OPFET, the illumination begins from the active layer side, hence, in this case too the photoconductive effect from the neutral channel region contributes substantially. Thus, in both the cases, the similar conditions exits resulting in almost equal photoconductive currents. But due to the lower photovoltaic currents in the buried-gate OPFET, the overall response drops significantly. In the Si buried-gate OPFET, the photovoltaic contribution is again eliminated due to the large photoconductive effect from the gate depletion region and high series resistances induce negative sensitivity. The photoconductive effect is almost sustained at the same level, since in both the cases the contribution is from the gate depletion region. Hence, in the region below 900 nm, due to similar conditions, the photocurrent response in the Si

buried-gate OPFET is in close resemblance to that in the generalized model of OPFET. Due to the above facts, the photocurrent responses below 900 nm in the Si and the GaAs buried-gate OPFETs are almost equal (Figure 7.5). However, above 900 nm, the considerable drop in the absorption coefficients eliminates the photoconductive contribution but significant photovoltaic effect still exits. The photovoltage is higher in the Si OPFET. But due to the factors mentioned earlier in the case of the generalized model, the photocurrent response is higher in the GaAs OPFET device.

The average responsivity in the wavelength range 200 nm-2600 nm for the Si and the GaAs generalized OPFET models is 4.54×10^4 A/W and 6.8×10^4 A/W respectively. The corresponding EQE values are $4.33 \times 10^6\%$ and $8.91 \times 10^6\%$. For the buried-gate OPFET models, the responsivity values in the Si and the GaAs OPFETs are 2.13×10^4 A/W and 3.1×10^4 A/W whereas the EQE values are $3.86 \times 10^6\%$ and $4.5 \times 10^6\%$ respectively. These high values show the potential of the devices as converters of solar energy into electrical energy. The response times which are vital for certain applications such as power beaming are observed to be in the range of nanoseconds to picoseconds depicting very fast response. The Si OPFET delivers significantly quick response (of the order of picoseconds) in the visible wavelength range (400 nm-700 nm) due to the large absorption coefficients, high photon flux, and substantially long electron lifetime, producing significantly high photoconductive effect in the gate depletion region greatly de-ionizing the space charge ions thus, reducing the switching times, switching time being the ratio of the space charge below the gate and its sidewalls to the drain-to-source current. In overall, the high photovoltages greatly reduce the space charge width along with the high drain to source currents considerably reduce the response times.

7.2 GaAs Front-illuminated OPFET for Solar Communication

Green energy technology using solar energy is gaining importance over the recent years due to its renewable nature. The present scenario reveals that the photovoltaic modules and the photodiodes used for communication under solar illumination have limited 3-dB bandwidth in the sub-megahertz range. Also, they require separate optical sources for modulation. In this research work, an OPFET (Optical Field Effect Transistor)-based photodetector is proposed which overcomes these limitations wherein modulated sunlight is used for communication. The proposed device with a GaAs surface-gate structure with front-illumination exhibits a 3-dB bandwidth of 1.386 GHz under air mass (*AM0*) solar illumination. The *AM0* spectrum is used for satellite, space vehicle, and space communication applications.

The parameters used in calculation are as follows: Gate length (4 μm), gate width (150 μm), active layer thickness (0.3 μm), and doping concentration (4×10^{22} $/m^3$) [154]; low field electron mobility (0.52 m^2/(V.s)) [10]; Schottky barrier height (gold (Au)- GaAs)(0.865 eV) [171]; saturation electron velocity ($\sim 1.2\times10^5$ m/s) [33]; saturation hole velocity in the y-direction ($\sim 0.9 \times 10^5$ m/s); electron lifetime (1 μs), hole lifetime (10 ns) [33]; permittivity (1.14×10^{-10} F/m) [10]; absorption coefficient [11]. The *AM0* solar spectrum is represented in Figure 7.7 [10], and the absorption spectrum of GaAs is depicted in Figure 7.8 [11].

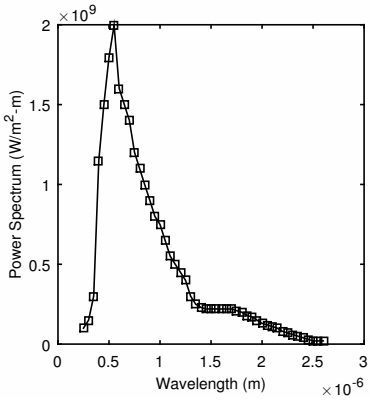

Figure 7.7: Air mass ($AM0$) solar spectrum [10]

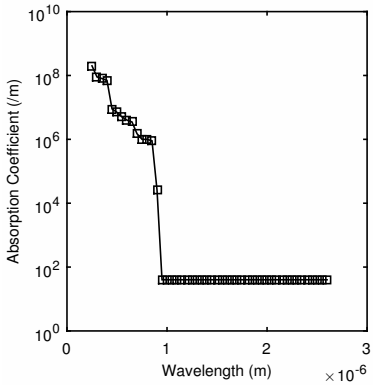

Figure 7.8: Absorption coefficient of GaAs versus wavelength [11]

It is observed from the above graphs that the power density as well as absorption coefficient, are significantly high at visible to near-infrared wavelengths (NIR) (400 nm to 900 nm). Therefore, mostly the device responses will be limited to these wavelengths. Figure 7.9 depicts the photovoltage-dependence on wavelength for the front-illuminated model at low (dc) and high frequencies. These plots clearly show the high response at visible-NIR wavelengths spanning from 400 nm to 900 nm. The observations are accounted by the high power density, moderately high value of absorption coefficient, and correspondingly a large enough absorption depth for substantial photogeneration to occur in the junction region with the carriers eventually crossing the Schottky junction. Apart from this, there are significant contributions at the Ultraviolet (UV) wavelengths of 250 nm to 350 nm. At these wavelengths, the absorption depth is very short due to very high absorption coefficients. Despite this fact, the photovoltage is significant at these

wavelengths since the generation of carriers begins from the metal-semiconductor contact side inside the depletion region. In contrast, at wavelengths higher than 900 nm, the absorption coefficient drops considerably resulting in reduced photovoltage. The lower photovoltages at higher frequencies are due to the fact with the modulation of the incident radiation, the lifetime of carriers is also modulated and decreases after certain frequency. The front-illuminated model exhibits high photovoltage due to the additional factor ($\alpha v_y \tau_{\omega p}$) in the numerator of the photo-induced hole density equation over the primary hole density which induces the amplification effect. One more aspect affecting the photovoltage is the factor ($\alpha v_y \tau_{\omega p}$) in the denominator term (1-$\alpha v_y \tau_{\omega p}$). The factor $\alpha v_y \tau_{\omega p}$ is to be treated as it is when $\alpha v_y \tau_{\omega p}<1$ and is to be substituted with the nearest fractional value to unity when $\alpha v_y \tau_{\omega p}>1$. This factor also contributes to high photovoltage. The high photovoltages result in large photovoltaic currents in the front-illuminated OPFET. In the discussion to follow, 'PV' stands for photovoltaic and 'PC' stands for photoconductive.

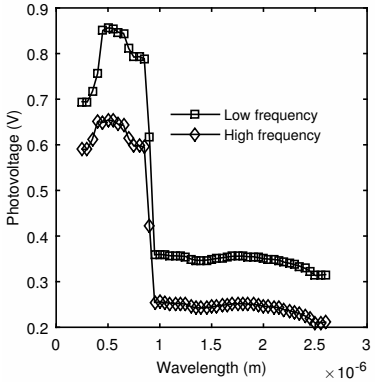

Figure 7.9: Photovoltage-wavelength spectrum of front-illuminated model at low (dc) and high frequencies

The solar spectrum has a range of wavelengths from 250 nm to 2600 nm. Thus, the solar response of the OPFET device is an integration of the responses at the individual wavelengths. The high average power density and the moderately high absorption coefficient greatly enhance the photoconductive charges and are com-

parable to the photovoltaic charges.

At the shorter wavelengths, the magnitude of photoconductivity is more in the neutral channel region and lesser in the depletion and substrate region along with lower photovoltaic effect. As the wavelength increases from 400 nm to 700 nm, the photoconductive contribution decreases and the photovoltaic contribution gradually increases accounting for the fall in series resistance effect. This is attributed to the wavelength-dependence of the absorption coefficient and absorption depth and to the value of diffusion length. The wavelength range 400 nm to 700 nm is purposely chosen since the response is the greatest at these wavelengths. At lower wavelengths, the absorption coefficient is larger than at higher wavelengths and vice versa for the absorption depth. Although the absorption begins from the metal contact side, the diffusion length is long enough along with high absorption coefficient to produce significantly high carrier density in the channel region at these wavelengths. These features are observed under dc conditions. As the frequency increases above dc levels, the photoconductive charges decrease significantly, and the photovoltaic charge dominates.

The transformation of the photo-induced charges into the photocurrent is depicted in Figure 7.10. As is apparent from this figure, at the majority of wavelengths, the photovoltaic effect has a greater impact, especially at higher frequencies resulting in a moderately high bandwidth of 1.386 GHz. The bandwidth would have been considerably more in the absence of photoconductive effect since the photoconductive lifetime is longer than the photovoltaic lifetime. This performance is critical of Li-Fi applications using modulated solar illumination. The present device will be useful as photodetector in future solar communication systems.

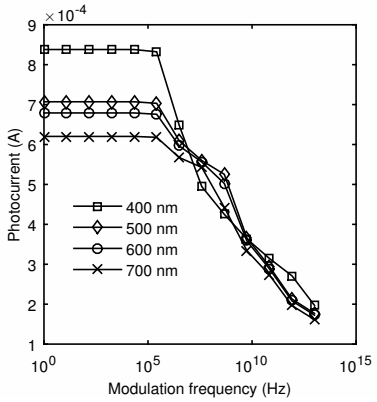

Figure 7.10: Photocurrent versus modulation frequency at different wavelengths

Chapter 8

Graphene-based OPFET and its Optimization

8.1 Feasibility Study of using Graphene as Semiconductor Material for OPFET

Graphene is an emerging material in the electronics industry due to its outstanding electrical, optical, mechanical, transport, structural, physical, chemical, and electronic properties. To name a few, it has ultra high carrier mobility (1,00,000 cm^2/(V.s)), high carrier saturation velocity (4×10^7 cm/s), ultrafast carrier dynamics, broadband absorption from Ultraviolet (UV) to Infrared (IR), high mechanical flexibility, robustness to harsh environments, high optical transmittance (97.7%), tunable Fermi level or bandgap, ambipolar nature, good chemical and physical stability. Despite these excellent properties, its use in practical devices is hindered by the high metal-graphene contact resistance, Fermi level pinning in metal-graphene contacts, absence of bandgap and low absorptance in monolayer graphene [140, 141, 142, 143]. The absence of bandgap in monolayer graphene results in low on/off ratios in digital logic devices affecting their high speed operation. On the other hand, high contact resistance in ohmic source and drain contacts in graphene FETs (Field Effect Transistors) resulting from low density of states at the Dirac point can cause fluctuations in the device parameters and

degrade the transconductance and unity-gain cut-off frequency. The low absorption in monolayer graphene (2.3%) leads to very low quantum efficiencies in photodetectors. Metal-graphene contacts based on physisorption metals such as Au (gold), Ag (silver), Cu (copper), Al (aluminium), Pt (platinum) tend to modulate the Fermi level by charge transfer depending upon the relative work functions of metal and graphene. They form a dipole layer and a voltage step at the inteface, thus pinning the Fermi level [140]. Fermi level pinning (FLP) prevents effective modulation of the carrier density in graphene by applied gate voltages. These issues have been handled in numerous ways in the past two decades. The issue of zero bandgap in monolayer graphene can be overcome by biasing bilayer graphene, constrainment of graphene in one dimension to produce graphene nanoribbons (GNRs) or quantum dots, or by chemically modifying graphene [153]. Contact resistance is dependent upon fabrication processes, device configuration and design, structure, type of metal, interface properties, contaminants, quality of contacts etc. [209]. Surface treatments, modifying fabrication processes, edge-contacts, introduction of defects in graphene surfaces, UV/ozone treatments, O_2 low power plasma treatments, rapid thermal annealing, increased surface bonding of metal and graphene, lowering barrier height, and increasing the doping density in graphene by biasing etc. are some of the methods used to lower the contact resistance in metal graphene contacts [144, 145, 146, 147, 148]. In fact, the contact resistance can be engineered to suit a particular application using one or more of these developed methods. Usually, the contact resistance required for high-performance transistors is less than or equal to 100 $\Omega - \mu$m as it impacts the device f_{max} for analog and radio frequency applications and the propagation delay of digital gates [210]. The contact resistance limit according to the International Technology Roadmap for Semiconductors (ITRS) is 80 $\Omega - \mu$m per contact. With graphene, the R_c values vary from 69 $\Omega - \mu$m to 10^9 $\Omega - \mu$m ascribed to the measurement conditions, fabrication procedures, and variations in graphene carrier density [211]. Some researchers have indicated that for radio

frequency devices and ultra-low power sensor applications, the desirable ohmic contact resistivities are in the range (0.2 to 1 $k\Omega - \mu m$) [212]. On the other hand, quantum efficiencies can be increased by utilizing graphene in transistor configuration, proliferation of hot carriers through Photo-thermoelectric effect (PTE), hot carrier-induced resistance change through biased Photo-bolometric effect (PBE), and by integrating graphene with other semiconductors or quantum dots [64, 150, 151, 152]. Finally, the Fermi level pinning in metal-graphene contacts can be reduced by Surface Charge Transfer Doping, construction of 2D/metal vdWs (Van-der Waals) contacts, or creating edge contacts [149]. The development of the above-discussed methods by various researchers to overcome the issues pertaining to graphene establishes the feasibility of the use of graphene as a semiconductor material for OPFET.

8.2 Analysis of Graphene OPFET for Photodetector, Amplifier, and Terahertz Modulator Applications and its Optimization

The graphene FET which is well known for its operation as photodetectors or terahertz modulators [150] can be made more electric field intensive or with more enhancement of electrostatic doping by simply modifying the structure to form a graphene MESFET (Metal-Semiconductor Field Effect Transistor). MESFET is also called OPFET (Optical Field Effect Transistor) when controlled optically. OPFET is known for its high gain-bandwidth product based on other semiconductors such as GaAs, GaN, SiC etc. The graphene MESFET is a special case of the graphene FET wherein the oxide/insulated layer capacitance between the gate and graphene in graphene FET is replaced by a dipole capacitance in graphene MESFET [162]. Since in this case, the equilibrium separation distance between the gate and graphene is of the order of angstroms, the dipole capacitance gets highly proliferated as compared to oxide/insulator cpapcitance. This results in a

large value of the dark carrier density in graphene MEFSET when the gate voltage is applied away from the Dirac point. This effect is undesirable under certain conditions since the photoconductive interband performance is highly affected with large dark carrier density. But the same is expected to be advantageous for the conditions when the device is used as a photovoltaic, photothermoelectic, or photobolometric detector wherein the high electric field encountered between large gate induced electrostatic doping and the doping induced in the uncovered part can create significant potential, temperature, conductivity, and resistance gradients thus enhancing the photoresponse. Further, the high frequency performance can be positively affected by this effect. Also, the high dark carrier density is greatly suited for the intra-band absorption characteristics for operating as a terahertz modulator [1]. On the other hand, incorporation of oxide between gate and channel in graphene FETs results in better power consumption, higher breakdown voltage, and low dark current. High K-dielectrics are advisable.

With the above viewpoints, in this work, the dark and photoconductive characteristics of graphene-based MESFET are modeled and comparatively analyzed with those of graphene FET for photodetector applications. The optical conductivities (inter-band and intra-band) of graphene FET and MESFET in the infrared and terahertz regions of spectrum are also distinguished. The high frequency amplification performance under dark and illumination is addressed. The effect of interface trap capacitance on these characteristics is analyzed.

Although significant research has been administered in standalone graphene-based transistor photodetectors [56, 213, 214, 215, 216, 217] in the UV, visible, terahertz and infrared ranges, the responsivity is limited to 980 A/W. This limits its use in practical high gain applications, although the communication bandwidths achievable using graphene FETs (Field Effect Transistors) span from tens of gigahertz to far gigahertz ranges. To overcome this issue, the photoconductive

characteristics are at first investigated at the optimum wavelength of operation i.e. the wavelength at which there is resonance effect induced by the optical phonon emission (6.3 μm) [1]. This ensured that the maximum photogeneration was obtained to give maximum output. Secondly, the device was biased close to the Dirac point to minimize the dark carrier density and prevent quenching of inter-band absorption, which led to a significant enhancement of photocurrent. Further, the device characteristics could be modulated by varying the device dimensions and considering different mobility samples. However, a trade-off is expected between the gain, bandwidth, unity-gain cut-off frequency, and dark current. This paper, adopts structural and mobility-based optimization to enhance the device gain-bandwidth performance without creating excessive dark current.

Graphene MESFET creates greater potential and conductivity gradients between gate-contacted and free space graphene than graphene FET. This is because the dipole capacitance between gate and graphene in the MESFET structure is higher than the oxide capacitance in the FET configuration. Thus, it is expected that the graphene MESFET would produce larger photovoltaic current than graphene FET because it relies on the strength of the built-in electric field at the junction of gate-covered and uncovered graphene when the illumination is allowed to fall within the junction and other factors kept constant. This fact led to the investigation of the factor by which the photovoltaic current in MESFET differs from that in the FET.

The Graphene-FET (GFET) and Graphene-MESFET (GMESFET) devices with drift-diffusion approach under dark and optical stimulation [1, 2] using MATLAB software have been simulated. The gold (Au) metal gate is considered to be optically transparent. The charge neutrality Dirac point is calculated to be 0.133 V. The gate is biased very close to the Dirac point (0.15 V) so that the

Table 8.1: Parameters used in calculation for Graphene FET/MESFET simulations

Parameter	Name	Value	Unit
μ	Low field electron mobility	(0.5-1.5)	(m^2/V.s)
Φ_m	Gate Work Function (Au)	(5.54)	(eV)
Φ_g	Graphene Work Function	(4.5)	(eV)
ϵ_{ox}	Oxide Dielectric Constant	(4)	—–
L	Gate length	(0.1-1)	(μm)
Z	Gate width	(1-100)	(μm)
d_{ox}	Oxide Thickness	(0.3)	(μm)
V_F	Fermi Velocity	(1×10^6)	(m/s)
C_{it}	Interface Trap Capacitance	(1×10^{-3})	(F/m^2)
d_{eq}	Equilibrium separation distance between Au and graphene	(0.331)	(nm)

dark current is suppressed. The drain bias is varied between 0 V to 1 V. The optical wavelength under consideration is 6.3 μm. The devices are studied under dark and radiation fields of 1 kV/m and 2 kV/m at room temperature of 300 K. The parameters used in calculation are presented in Table 8.1.

The photoconductive characteristics along with the dark current have been evaluated for both the devices as shown in Figure 8.1 and 8.2 for radiation fields of 1 kV/m and 2 kV/m respectively for the dimensions of gate length (1 μm), gate width (1 μm), and carrier mobility (0.5 m^2/(V.s)). The graphs clearly contrast the performance of both the devices. The dark current is in the lower regime for GMESFET as compared to that for GFET. Note that the devices are biased close to the Dirac point (0.15 V) for suppression of dark current. Hence, the Fermi levels and carrier densities are maintained relatively at the lowest level in both cases. Further, the dipole capacitance in GMESFET is much higher than that of the oxide capacitance in GFET, which implies that the diffusion component of current dominates the drift component which suppresses the dark current and vice versa for GFET. Although the devices are biased close to the Dirac point,

the large difference in the said capacitances leads to higher dark electron density in the GMESFET. Thus, under illumination the inter-band absorption is higher in GFET resulting in more photogenerated carriers producing larger photoconductive current. The graphs also depict that high sensitivities are attained in both devices. Another reason for this is that the operating wavelength of 6.3 μm corresponds to the optical phonon emission resonance, at which the photon and phonon absorption and emission processes are exactly balanced at higher quasi Fermi levels. The higher dark electron density in GMESFET induces significant Pauli blocking effects to limit the excitation of carriers and thus shows only 0.87 μA sensitivity. In contrast, in the case of graphene FET, due to the much lower oxide capacitance, the dark electron density is very low, and enhances the inter-band transitions resulting in photocurrent of 38.52 μA. The universal inter-band optical conductivity is estimated to be (60 μS). The optical conductivities in case of graphene MESFET and FET are calculated as 57.25 μS and 57.5 μS respectively at the radiation field of 1 kV/m due to similar net energy transfer rate induced by compensation of higher dark carrrier density and lower excited carrier density in GMESFET with the lower dark carrier density and larger photogenerated carrier density in GFET. At the radiation field of 2kV/m, the graphene MESFET now shows a larger sensitivity of 2.29 μA whereas the graphene FET delivers much higher current of a few milliamps. This shows the clear distinction of the two devices under inter-band conditions for photodetector applications. However, the inter-band conductivity is lesser in case of graphene FET (3.12 μS) but graphene MESFET still shows a significant conductivity (55.6 μS). This difference is due to the higher excitation Fermi level in case of graphene FET which reduces the energy transfer rate due to absorption of photons at steady state and hence the conductivity.

Figures 8.3 and 8.4 show the high frequency amplification performance characteristics of the devices (GMESFET and GFET respectively) under dark, 1

kV/m field, and 2 kV/m field when the interface trap capacitance is assumed to be 1 fF/μm^2. f_T is given by $(g_m/(2\pi \times W \times L \times C_G))$ where $(g_m = W/L \times \mu \times C_{CH} \times V_D)$, $(C_{CH} = C_Q/(1+(C_Q+C_{it})/C_{ox}))$, and $(C_G=(C_Q+C_{it})/(1+(C_Q+C_{it})/C_{ox}))$.Under dark condition and under radiation field of 1 kV/m, the graphene MESFET and graphene FET exhibit similar values and also least sensitivities to illumination attributed to the slight difference in Fermi levels, the devices being biased close to the Dirac point and the radiation field is not sufficient to create significantly large variation in Fermi levels, thus maintaining similar quantum capacitances and identical ratios of the channel and gate capacitances. The quantum capacitance is also fairly comparable to the interface trap capacitance, thus causing differences in gate and channel capacitances (gate capacitance is higher) and reducing the value of f_T. At the higher radiation field of 2 kV/m, as the quantum capacitance is much larger than the interface trap capacitance in GFET due to significant interband absorption, by inspection of the equations for channel capacitance and gate capacitance, we observe that these capacitances tend to the same value and cancel each other. Thus, the f_T is nearly independent of all the capacitances in this case and depends upon the structural dimensions, the carrier mobility, and the applied drain voltage. This leads to an f_T of $\sim$77.7 GHz in the case of graphene FET at a drain voltage of 1 V, close to the ideal value of 79.6 GHz which is obtained when the gate and channel capacitances are exactly equal. On the other hand, in GMESFET at the radiation field of 2 kV/m, the f_T is close to the values under dark and at 1 kV/m field on account of slight enhancement of Fermi level under illumination.

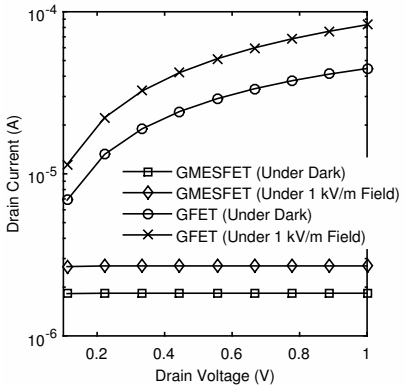

Figure 8.1: I-V Characteristics of the GFET and GMESFET devices under dark and illumination (1 kV/m field)

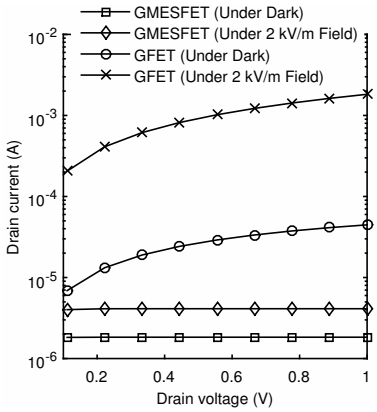

Figure 8.2: I-V Characteristics of the GFET and GMESFET devices under dark and illumination (2 kV/m field)

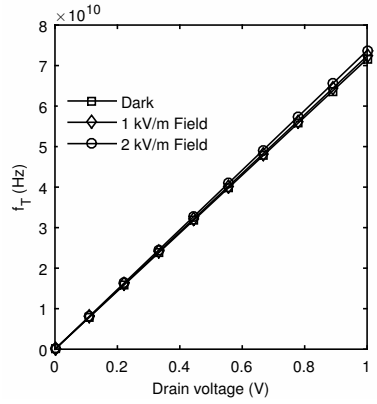

Figure 8.3: f_T of GMESFET under dark and illumination (1 kV/m and 2 kV/m fields)

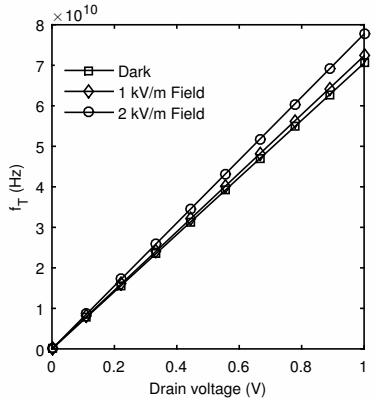

Figure 8.4: f_T of GFET under dark and illumination (1 kV/m and 2 kV/m fields)

The high frequency amplification characteristics are also studied when the interface trap capacitance is increased to 10 fF/μm^2 (see Figures 8.5 and 8.6). This caused the f_T to deteriorate to 37.3 GHz, 39.8 GHz, and 44.2 GHz under dark condition and radiation fields of 1 kV/m and 2 kV/m respectively at a 1 V drain voltage in the case of graphene MESFET since the trap capacitance is closer to the quantum capacitance greatly increasing the gate capacitance whereas the channel capacitance remains constant. On the other hand, in the case on graphene FET, the f_T under dark decreased (34.8 GHz) whereas under illumination, it decreased under 1 kV/m field (39.7 GHz) and decreased to a lesser extent under 2 kV/m field (64.2 GHz). Under dark and at 1 kV/m field, this is attributed to the enhancement of gate capacitance through the trap capacitance. When the radiation field is raised to 2 kV/m, since the quantum capacitance is enhanced and is dominant over the trap capacitance, there is lesser degradation of f_T. This shows that under illumination, the graphene FET has a greater tolerance or immunity towards the interface trap capacitance at certain radiation fields.

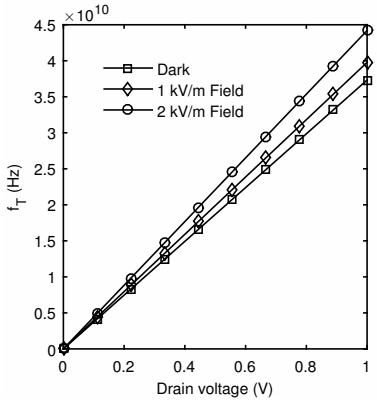

Figure 8.5: f_T of GMESFET under dark and illumination (1 kV/m and 2 kV/m fields) at interface trap capacitance of 10 fF/μm^2

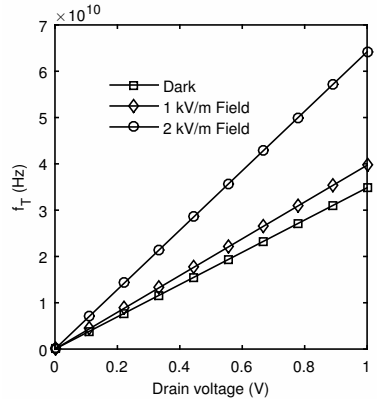

Figure 8.6: f_T of GFET under dark and illumination (1 kV/m and 2 kV/m fields) at interface trap capacitance of 10 fF/μm^2

Further, the RC-limited photoconductive bandwidth, amplification bandwidth (f_T), photoconductive responsivity, photovoltaic current, and the dark current have been calculated for both devices over a discrete set of dimensions and mobilities as depicted in Table 8.2 and 8.3 at a drain voltage of 1 V and radiation field of 1 kV/m. The RC-limited bandwidth is calculated at a matched load resistance (R_L) of 50 ohms and is given by $(1/(2\pi R_L C_G))$. Note that the gate capacitance depends upon the quantum capacitance, dipole/oxide capacitance, and the interface trap capacitance. In the present work, the interface trap capacitance is maintained constant. The quantum capacitance in both cases exhibit similar values due to the compensation effects of higher dark carrier density and lower photoconductive effect in GMESFET with the lower dark carrier density and higher photoconductive effect in GFET. Thus, the gate capacitance value is

decided by the dipole/oxide capacitance which is larger in the GMESFET thus increasing the gate capacitance. Thus, for similar dimensions and mobilities, the bandwidth is larger in GFET.

The unity-gain cut-off frequency (f_T) is maintained at the same level in both devices under the present operating conditions due to the reasons discussed earlier.

The responsivities are comparatively larger in the GFET devices due to larger photoconductive currents. The photovoltaic currents are comparable due to the compensation effects as discussed earlier for quantum capacitance which create similar built-in electric fields. The dark currents are much smaller in the case of GMESFET which is the major advantage of the device over GFET when biased close to the Dirac point.

Apart from the above observations, the other observations are that the optimum dimensions and mobility for GMESFET as detector-cum-amplifier with low dark currents are W=1 μm, L=0.5 μm, μ=0.5 m^2/(V.s) wherein it exhibits a detection-cum-amplification bandwidth of 289.6 GHz, a responsivity of 2.62×10^3 A/W, and a dark current of 3.67 μA. On the other hand, the GFET shows optimum bandwidth of 867.8 GHz, a responsivity of 3.48×10^5 A/W, and a dark current of 16.07 mA at the dimensions and mobility of W=60 μm, L=0.5 μm, μ=1.5 m^2/(V.s).

Table 8.4 depicts the intra-band optical conductivities of the devices at 300 K in the far infrared region (80 μm) where the interband conductivities are quenched. It is seen that the graphene MESFET shows both wide modulation of conductivity with small change in gate bias and also high magnitude of conduc-

Table 8.2: Structural and Mobility Optimization Results for GMESFET

Device Dimensions and Mobility	Bandwidth (Hz)	f_T (Hz)	Responsivity (A/W)	Photovoltaic Current (A)	Dark Current (A)
W=1 μm, L=1 μm, μ=0.5 m^2/(V.s)	319.3 GHz	72.4 GHz	654.3 A/W	0.11 nA	1.83 μA
W=10 μm, L=0.5 μm, μ=0.5 m^2/(V.s)	63.86 GHz	289.6 GHz	2.62×10^3 A/W	2.17 nA	36.67 μA
W=1 μm, L=0.5 μm, μ=0.5 m^2/(V.s)	**638.6 GHz**	**289.6 GHz**	2.62×10^3 **A/W**	**0.217 nA**	**3.67 μA**
W=1 μm, L=1 μm, μ=1 m^2/(V.s)	319.3 GHz	144.8 GHz	1.31×10^3 A/W	78.31 pA	3.67 μA
W=100 μm, L=0.5 μm, μ=1 m^2/(V.s)	6.386 GHz	579.3 GHz	5.13×10^3 A/W	15.6 nA	0.73 mA
W=40 μm, L=0.1 μm, μ=1 m^2/(V.s)	79.83 GHz	14.5 THz	1.31×10^5 A/W	31.3 nA	1.46 mA
W=40 μm, L=0.1 μm, μ=1.5 m^2/(V.s)	79.83 GHz	21.7 THz	1.96×10^5 A/W	11.1 nA	2.2 mA
W=60 μm, L=0.5 μm, μ=1.5 m^2/(V.s)	10.64 GHz	868.9 GHz	7.85×10^3 A/W	3.32 nA	0.66 mA
W=60 μm, L=0.1 μm, μ=1.5 m^2/(V.s)	53.2 GHz	21.7 THz	1.96×10^5 A/W	16.6 nA	3.3 mA

Table 8.3: Structural and Mobility Optimization Results for GFET

Device Dimensions and Mobility	Bandwidth (Hz)	f_T (Hz)	Responsivity (A/W)	Photovoltaic Current (A)	Dark Current (A)
W=1 μm, L=1 μm, μ=0.5 m^2/(V.s)	27.2 THz	72.3 GHz	2.9×10^4 A/W	0.11 nA	44.65 μA
W=10 μm, L=0.5 μm, μ=0.5 m^2/(V.s)	5.45 THz	289.3 GHz	1.16×10^5 A/W	2.22 nA	0.89 mA
W=1 μm, L=0.5 μm, μ=0.5 m^2/(V.s)	54.5 THz	289.3 GHz	1.16×10^5 A/W	0.22 nA	89.3 μA
W=1 μm, L=1 μm, μ=1 m^2/(V.s)	27.2 THz	144.6 GHz	5.8×10^4 A/W	84.8 pA	89.3 μA
W=100 μm, L=0.5 μm, μ=1 m^2/(V.s)	545.1 GHz	578.5 GHz	2.32×10^5 A/W	16.9 nA	17.86 mA
W=40 μm, L=0.1 μm, μ=1 m^2/(V.s)	6.81 THz	14.46 THz	5.8×10^6 A/W	33.9 nA	37.7 mA
W=40 μm, L=0.1 μm, μ=1.5 m^2/(V.s)	6.81 GHz	21.7 THz	8.7×10^6 A/W	15.3 nA	53.6 mA
W=60 μm, L=0.5 μm, μ=1.5 m^2/(V.s)	**908.5 GHz**	**867.8 GHz**	3.48×10^5 **A/W**	**4.6 nA**	**16.07 mA**
W=60 μm, L=0.1 μm, μ=1.5 m^2/(V.s)	4.54 THz	21.7 THz	8.7×10^6 A/W	22.97 nA	80.37 mA

Table 8.4: Intra-band conductivities of graphene devices

Gate Voltage (V)	Intra-band conductivity (μS) Graphene MESFET	Intra-band conductivity (μS) Graphene FET
0.4 V	76.22 μS	7.64 μS
0.45 V	92 μS	7.67 μS
0.5 V	109.34 μS	7.73 μS
0.55 V	127.2 μS	7.81 μS
0.6 V	146.5 μS	7.86 μS

tivity ($\sim$76-146 μS) suitable for both photodetector and terahertz modulation applications. In contrast, graphene FET exhibits slight variation of conductivity with gate bias so also lower magnitude of conductivity ($\sim$7.6-7.86 μS). This is because of the higher value of dipole capacitance in graphene MESFET which greatly improves the sensitivity to applied gate bias. Also, the large dark carrier density is favourable to intra-band absorption since large amount of free carriers are available for excitation to higher energy bands upon absorption of the incident photon energy. Although the amount of photogenerated carriers generated are lesser at this wavelength, a significant photoconductive responsivity is still registered in GFET.

To indicate the terahertz photovoltaic detection capability of the two devices, the devices were studied at an operating wavelength of 80 μm and at a gate bias of 0.6 V. Table 8.5 depicts the photovoltaic responsivities (as a function of dimensions in both devices). It can be observed that the responsivities, in overall, are more than one order magnitude higher in the GMESFET for the same set of dimensions and mobility. This show the higher strength of the built-in electric field created at the junction of gate-covered and uncovered graphene by the high gate voltage of 0.6 V. This all comes at the expense of much higher dark current ($\sim$750 mA). The significant boosting of the dark current is attributed to the

Table 8.5: Photovoltaic Performance Comparison of GFET and GMESFET at a gate bias of 0.6 V and a wavelength of 80 μm.

Device Dimensions and Mobility	Photovoltaic Current (A) GFET	Responsivity (A/W) GFET	Photovoltaic Current (A) GMESFET	Responsivity (A/W) GMESFET
W=1 μm, L=0.5 μm, μ=0.5 m^2/(V.s)	0.22 nA	0.33 A/W	0.474 nA	0.357 A/W
W=100 μm, L=0.5 μm, μ=1 m^2/(V.s)	23.5 nA	**0.35 A/W**	0.3 μA	**4.6 A/W**
W=60 μm, L=0.5 μm, μ=1.5 m^2/(V.s)	12.56 nA	**0.315 A/W**	0.326 μA	**8.19 A/W**

higher dark electron density and the enhancement of the Fermi level. Thus, the devices can be switched from photoconductive detection-cum-amplification mode at low bias levels and mid-infrared wavelengths to modulation-cum-photovoltaic detection mode at high biases and terahertz wavelengths.

Table 8.6 presents the performance comparison of the State-of-Art standalone graphene FET photodetectors with the present work. Although this is a theoretical work and most of the reported works are based on experiments, the much higher gain and bandwidth of the presently investigated GFET in the theoretical limit as compared to the reported work means that our device can still surpass the state-of-art photodetectors.

Table 8.6: Comparative Study of the State-of-Art GFET PDs with the present work

Device	Wavelength (m)	Responsivity (A/W)	Bandwidth (Hz)/Time Constant (s)	Ref
Mechanically exfoliated FLG or SLG	1.55 μm	$\sim$0.5 mA/W	40 GHz	[213]
Mechanically exfoliated BLG	300 nm-6 μm	$\sim$6.1 mA/W	16 GHz	[56]
Mechanically exfoliated BLG or SLG	1.3-17 μm	0.05 A/W	$\sim$18 GHz	[214]
3D Graphene FETs	UV-Visible	>1 A/W	>1 MHz	[215]
GFET	532 nm	980 A/W	$-------$	[216]
GFET	(0.1-10) THz	$-------$	<1 ns	[217]
GFET	6.3 μm	3.48×10^5 A/W	908.5 GHz/0.175 ps	This Work

Chapter 9

Finite Difference Simulations of the GaAs Front-Illuminated OPFET device

The Poisson's equation in the depletion region in the spacings between the gate and drain, and gate and source of front-illuminated OPFET is first solved numerically using FDM to give the currents in the spacings and hence the series resistances. For this purpose, the FDM approximation for the second order differential equation for the potential is substituted and solved for the unknown channel voltage for the assumed value of depletion width by applying proper boundary conditions. The calculated channel voltage is used to calculate the spacing current under illumination using the well known current equation. The estimated current is, in turn, used to obtain the depletion width from the voltage drop equation along the channel length wherein the channel is divided into strips of equal width. The process is repeated iteratively until the solutions converge. The same procedure is followed for the gate depletion region to give the channel voltage.

Similarly, the continuity equations in the channel, and depletion regions of the OPFET under illumination are converted into finite difference domain using backward-difference approximation for the depletion region equation and second order approximation for the channel equation. After applying the proper boundary conditions, the discretized equations so obtained form a system of sparse ma-

trix equations which are solved for the electron densities using MATLAB. Then the charges and the total drain current are obtained from the earlier calculated channel voltage and using the numerical Trapezoidal method. The results are presented below and compared with the presently used semi-analytical model-based results.

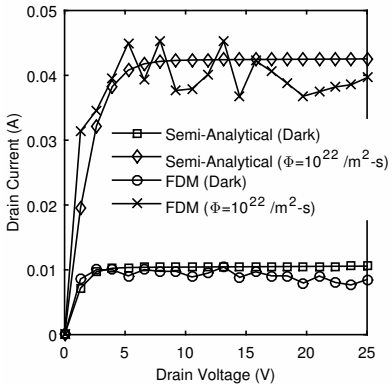

Figure 9.1: FDM versus Semi-Analytical model for GaAs front-illuminated OPFET at the flux density of $\Phi = 10^{22}\ /m^2$

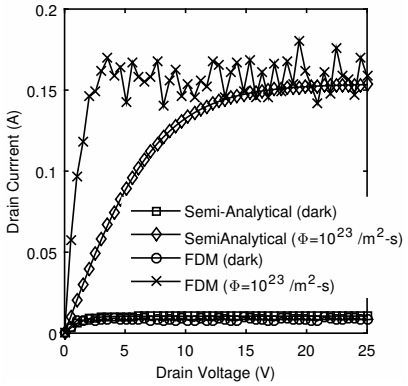

Figure 9.2: FDM versus Semi-Analytical model for GaAs front-illuminated OPFET at the flux density of $\Phi = 10^{23}\ /m^2$

The above figures, Figure 9.1 and 9.2, depict the comparison of the results obtained using Finite Difference Method and the presently employed semi-analytical method at two different flux densities showing close agreement. This shows the accuracy of the FDM method. It is also simple to learn and implement and computationally efficient. The slight oscillations in the graphs of FDM may be due to the inherent instability of the approximation method. The parameters used in calculation are the same as that for the 4 μm gate length, and 150 μm gate width

device as studied earlier for Au-gated GaAs OPFET under 600 nm illumination, at 0 V gate bias.

Chapter 10

Conclusion

This thesis presented extensive simulation results on the structural, material, and illumination model optimization of OPFET in the presence of various external control factors such as bias, optical power, wavelength, and modulation frequency. The applications targeted were detector-cum-amplifier in OEIC-based receiver for Visible Light Communication and Ultraviolet Communication, as well as other discrete applications. These discrete applications included UV reflectance imaging, Near-infrared imaging, high dynamic range or high resolution imaging, high speed switching, traffic lighting, automotive, solar-energy harvesting, and solar communication applications. Apart from these, the OPFET was studied for optically-driven 5G applications such as photodetector, oscillator, and detector-cum-amplifier. The extent to which the gain, phase, and bandwidth of the OPFET-based detector-cum-amplifier could be varied was evaluated for its possible use in configurable 5G smart antenna applications.The variation was carried out by manipulating the structural dimensions, illumination model, gate voltage, drain voltage, modulation frequency, and optical power. Further, this research established an important relationship that the 3-dB bandwidth is directly proportional to the gate length or inversely related to the doping concentration, subject to scaling rules atleast at medium to long gate lengths. This observation is based on the fact that the slope of the frequency response curve can be inversely correlated with the depletion width sensitivity to applied illumination, which in-

creases at lower doping concentration, provided that the limiting factors such as series resistance effects and photoconductive effect are kept to their minimum. At higher optical power levels, negative sensitivity was perceived in OPFET with certain material systems andd illumination models, wherein the depletion width increases with illumination. Under dc conditions, the only prevalent phenomenon in such cases is the photoconductive effect.

The study of Si, InP, and GaAs OPFET detectors for Visible Light Communication revealed that these detectors show potential for low, moderate, and high data rate VLC applications respectively. The InP and GaAs visible light detectors in the back-illuminated configuration exhibited good UV-visible contrast under background UV light, suitable for UV reflectance imaging, whereas Si-based devices detected both UV and visible light. The $In_{0.53}Ga_{0.47}As$ back-illuminated OPFET showed good infrared detection under background visible light, sufficing for Near-Infrared imaging applications.

When the generalized, buried-gate, and back-illuminated models were compared for Visible Light Communication, the GaAs generalized OPFET exhibited superior detection/amplification bandwidth performance (68.4 GHz/22.2 GHz) when biased at zero gate bias and 25 V drain bias under low background lighting conditions. When biased at -1 V gate bias and 1.9 V drian bias, the GaAs back-illuminated OPFET emerged as a high-speed detector (208.5 GHz bandwidth). All the models showed substantially high Signal-to-Noise Ratios exceeding 200 dB. Under high background lighting, the InP and GaAs generalized models produced better bandwidth responses (22.2 MHz and 57.4 MHz respectively) when biased at 0 V and -3 V gate voltages and low drain voltages. With the other parameters held constant, the lower barrier height and dielectric constant and larger photovoltages enhances the depletion width sensitivity to applied bias and hence the bandwidth. Under comparable conditions, the back-illuminated OPFET ex-

hibits gentler frequency response roll-off as compared to front-illuminated models. At lower intensities, the larger photovoltage values in the buried-gate model tends to dominate the roll-off rate in back-illuminated OPFET and vice versa occurs in the GaAs case where the minority carrier lifetime is short.

For Ultraviolet high dynamic range imaging and communication, the generalized and front-illuminated models exhibited a significant improvement in the Linear Dynamic Range (LDR) over the buried-gate OPFET models. The generalized model was superior to front-illuminated model in terms of dynamic range. The 6H-SiC generalized OPFET model exhibited the highest detection bandwidths ranging from tens of GHz to hundredths of GHz and also high combined detection-cum-amplification bandwidths in the sub-10 GHz range along with the highest LDR of 73 dB. The AgO_2-ZnO generalized model attained the lowest response times. The ZnO OPFET was perceived as a high optical power detector from its large sensitivity and responsivity. In overall, the ZnO OPFET exhibited moderate to high LDR values ranging from 24 dB to 69 dB, modest f_T values and 3-dB bandwidths ranging between low MHz to low GHz frequencies. On the other hand, the GaN OPFET produced bandwidths in the sub-megahertz to high gigahertz ranges, modest to high cut-off frequencies and LDR in the 24 dB to 65 dB range. All the devices showed considerably high responsivities ($>10^3$ A/W). Employing large barrier height gate materials such as ITO and AgO_2 in GaN and ZnO generalized models respectively, improved the performance over that of conventional Au gates.

The work on structural and material optimization of the buried-gate front-illuminated OPFET towards UV communication applications revealed that the optimum gate length and active layer thickness are 3 μm and 0.27 μm respectively. It is established that the GaN OPFET with ITO gate exhibits overall better performance with simultaneously larger 3-dB bandwidths (20.7 GHz, 30.88

GHz), f_{Ts} (8.2 GHz, 7.8 GHz), and lower response times (69.6 ps, 64.2ps) at the lower intensities and reasonably high values for other parameters. The ZnO OPFET with AgO_2 gate showed higher responsivities, *EQEs*, gains, detectivities, and lower response times except the photocurrent gain which was much inferior to the 6H-SiC OPFET. The 3-dB bandwidth at the lower intensities was in the gigahertz or sub-gigahertz range. The SiC OPFET with Au gate emerged as a very high gain-bandwidth product photodetector at all intensities with gains of (1.02×10^{11}, 1.2×10^{8}, 1.45×10^{5}, and 1.69×10^{3}) and 3-dB bandwidths of (20.7 GHz, 33.4 GHz, 500 GHz, and 151.7 GHz) sufficing for long haul communications. The other parameters showed reasonably high/low values. Further, the investigation of the effect of elevated temperatures viz. 400 K, 500 K, and 600 K on the SiC OPFET device stability showed significantly stable response in terms of gain, switching time, and detectivity. The examination of the reliability of the gate metallization contact of the Au-6H SiC OPFET revealed an estimated Mean-Time-to-Failure ($MTTF$) of around 3.14×10^{7} hours even at 600 K and high flux density of 10^{24} $/m^2$-s, thus showing reliable operation.

Considering traffic lighting applications, for Vehicle-to-Vehicle (V2V) and Vehicle-to-Infrastructure (V2I) communication and high speed switching, the GaAs buried-gate front-illuminated, and the generalized models with ITO gate showed significant improvement in the 3-dB bandwidth over that of Au gate but almost constant switching and amplification performance. The responsivity was enhanced with the employment of ITO gate. Thus, the gain-bandwidth product was boosted in the ITO-gated devices with reasonably fast response in the range of nanoseconds to picoseconds. The devices with reduced dimensions produced the least switching times. The investigation of the reliability of the gate metallization contact in the GaAs generalized, buried-gate front-illuminated, and surface-gate front-illuminated models revealed above par $MTTF$ values depicting reliable operation.

Further, an in depth comparative analysis of the graphene-GaN/GaAs and Au-GaN/GaAs Schottky junctions in OPFET under UV illumination at zero bias, forward and reverse bias conditions was carried out. The graphene-GaN and Au-GaN Schottky junctions showed high response under photovoltaic conditions whereas graphene-GaAs and Au-GaAs junctions showed better response in reverse bias conditions with zero response under forward bias. Also, the visible range characteristics of Au-GaAs Schottky junction and graphene-GaAs junction in OPFET under zero bias, forward bias and reverse bias conditions were obtained. High photovoltaic response and moderate reverse biased response were obtained in the visible region as compared to the moderate response under both photovoltaic and reverse bias conditions in the UV region. Zero forward bias response was recorded in both visible and UV regions. Due to high UV/visible contrast, the detectors can detect visible light under background UV radiation. In addition, the detectors can operate as dual-band photodetectors (i.e. UV and visible) owing to significant responses in both cases. The research explored dual-mode buried-gate GaAs/GaN OPFET based detector-cum-amplifier for suiting high background and low background lighting VLC/UV communication respectively. The device can be switched between diode mode (Schottky junction) and transistor mode (OPFET) by adjusting the biasing conditions. The Schottky photodiode showed superior bandwidth performance at the higher intensities, whereas OPFET produced better frequency response at the lower intensities. The transistor mode will suit to applications wherein the same optical source is used for lighting/imaging, treatment as well as VLC/UV communication.

Furthermore, the graphene- and Au-gated GaAs front-illuminated OPFETs were modeled as detector and oscillator towards optically-driven 5G applications. The study revealed that graphene- and Au-gated devices delivered the same amplification and oscillation performance, whereas the graphene-gated device showed inferior response with respect to bandwidth and responsivity. A

maximum oscillation frequency of 1.8 GHz and a minimum of 1.63 GHz were obtained, tuned with optical illumination. The gain could be varied between 3.94 dB to 4.5 dB, and the phase could be tuned between 115.95° to 144.3°, with a change in the flux density. As a detector, the device exhibited a maxomum 3-dB bandwidth of 2.234 GHz, a dc responsivity of 3.3×10^6 A/W, and an f_T of 5.33 GHZ. The devices will serve good purpose in sub-6 GHz 5G applications such as handheld 5G devices and industrial Internet of Things (IoT)-enabled systems in smart cities, automotive, space, and aeronautics applications.

For 5G phased array smart antenna applications, the GaAs OPFET device acts as almost constant gain variable phase detector withe the variation of optical power or by the choice of different illumination models, but the extent of variation is within 10 to 20 degrees. On the other hand, the device can be configured as a variable gain variable phase shift detector by varying the drain bias, gate bias, or by the choice of different dimensions, and the extent of variation is large. At higher frequencies, the gain is significantly reduced and phase is shifted to negative directions. The positive phase shifts at these frequencies were achieved by proper optimization. The buried-gate front-illuminated device with the longest gate length under consideration of 8 μm exhibited the highest bandwidths of 4.22 GHz, 8.64 GHz, and 17.7 GHz at the lower intensities. The gain and phase decreased with device dimensions as well as the gate voltages except the gain which tends to increase at higher drain voltages. The gain and phase significantly increased with the increase in the drain voltage whereas they decreased with optical power except at higher drain voltages where there is a slight increase in gain. The studied devices show potential for 5G Internet of Things (IoT) or Optical Wireless Communication (OWC) based smart applications such as smart home, airport, train station and railway, smart shopping, plant and industry, smart healthcare, smart automobiles etc.

In regard to solar cell applications, the solar energy harvesting capability of the Si and the GaAs generalized and the buried-gate front-illuminated OPFET models were explored. The devices efficiently reproduce the input solar power spectrum with high average photocurrents in the milliamperes to tens of milliamperes range, high responsivity of the order of 10^4 A/W, high EQE of the order of 10^6% and low switching times in the nanoseconds to picoseconds range. The GaAs generalized OPFET device has the highest conversion efficiency amongst all the devices. The GaAs front-illuminated OPFET device for solar-based communication was studied with a 3-dB bandwidth of 1.386 GHz under air mass ($AM0$) solar illumination suitable for satellite, space vehicle, and space communication applications.

This research also investigated the feasibility of the use of new material "graphene" as a channel material for the OPFET device. The investigation suggested that the graphene-OPFET can be functional if certain issues such as high metal-graphene contact resistance, and Fermi-level pinning at metal-graphene contacts can be handled using numerous techniques as provided by various researchers. Further, the dark and photoconductive characteristics of the graphene OPFET in the infrared region at 300K under 1 kV/m and 2 kV/m radiation fields near the charge neutrality point were evaluated andd contrasted with that of graphene FET. The dark current was lower for graphene OPFET than that for graphene FET, but with large dark electron density due to high dipole capacitance. The photocurrent was considerably higher in graphene FET due to larger inter-band absorption. The devices showed similar inter-band conductivities at 1 kV/m field, but lowered conductivity in graphene FET under 2 kV/m field. The amplification performance of the devices was studied under dark, 1 kV/m, and 2 kV/m fields, at an interface trap capacitance of 1 fF/μm^2, revealing similar response under dark and 1 kV/m field with least sensitivity to illumination. Whereas, under 2 kV/m field, the f_T increased to a certain extent in graphene FET close to its ideal value which is

capacitance-independent. When the interface trap capacitance was increased to 10 fF/μm^2, f_T, f_T deteriorated at all intensities in graphene OPFET, whereas graphene FET had lesser degradation of f_T at 2 kV/m field, showing its tolerance or immunity towards trap capacitance. The structural and mobility-based optimization of the graphene OPFET and FET devices at 1 kV/m field showed that for similar dimensions and mobilities, the RC limited bandwidth is larger in GFET. The f_T is maintained at the same level in both devices. The responsivities were larger in GFET, the photovoltaic currents were comparable , whereas dark currents were much smaller in graphene OPFET. Considering low dark currents, the graphene OPFET exhibited an optimum detection-cum-amplification bandwidth of 289.6 GHz, a responsivity of 2.62×10^3 A/W, and a dark current of 3.67 μA at gate width of 1 μm, gate length of 0.5 μm, and mobility of 0.5 m^2/(V.s). On the other hand, the GFET showed optimum bandwidth of 867.8 GHz, a responsivity of 3.48×10^5 A/W, and a dark current of 16.07 mA at gate width of 60 μm, gate length of 0.5 μm, and mobility of 1.5 m^2/(V.s). The graphene OPFET delivered better terahertz detection and modulation capability based upon its much higher intra-band conductivity, which could be tuned to a large extent with gate bias. The photovoltaic responsivities were larger in graphene OPFET at terahertz wavelengths (80 μm) and a gate bias of 0.6 V, for the same set of dimensions and mobility, but at the cost of much higher dark current. The devices can be switched from photoconductive detection-cum-amplification mode at low bias levels and mid infrared wavelengths to modulation-cum-photovoltaic detection mode at high bias levels at terahertz wavelengths.

Finally, the finite difference method was successfully applied to the OPFET device computational domain and the results were compared to that with the presently used semi-analytical method. The FDM approach was found to be simple to understand and use, highly accurate, and computationally efficient, and suited well to the rectangular geometry of the OPFET device.

Thus, this research extensively covered all aspects of optimization, came up with an alternative method for the modeling of OPFET device, as well as established the feasibility of the use of graphene for OPFET device and showed its potential for opto-electronic applications.

The simulation results were thoroughly analyzed based on photovoltaic, photoconductive, series resistance, and the scaling rules-induced effects, and the effects of depletion width sensitivity, barrier height, etc. The performance metrics were compared with the reported literature showing enhanced or comparable performance with boosted gain-bandwidth product. The simulation model was validated with experiments reported elsewhere as well as with Visual TCAD Software simulations.

Chapter 11

Extension of Research and Future Scope

This research work can be extended in the optimization domain. The OPFET device offers several distinct degrees of freedom which can be explored suitably through optimization techniques discussed to suit a particular application. The inherently high gain-bandwidth product and fast response times can be further optimized. It has been established that the 3-dB bandwidth increases with gate length as also the switching time. The f_T decreases with gate length so also the responsivity. Thus, a trade-off is established between 3-dB bandwidth and f_T, switching time, responsivity simultaneously, which can be minimized through structural optimization. The gate and semiconductor material have significant bearing on the detector characteristics and can be suitably chosen to suit a particular application. The material properties cannot be manipulated except to some extent by doping. The materials in the limelight of VLC are Si, GaAs, and InP with distinct electrical and optical properties. In the UV domain, the materials of interest are GaN, ZnO, and 6H-SiC.

The future scope of this work is the real time analysis of the sensitivity, bit rate and bit error rate (BER) of the VLC and Ultraviolet Communication (UVC) systems at large using the optimized detector obtained in this work, thus, demonstrating a practical scenario of the communication systems. The other components of the system models can be chosen from the state-of-art investigations.

Since the gain-bandwidth product of OPFET is higher than its photodiode and other counterparts, it can suffice for long haul communications. Hence, the transmission distance can be greatly increased. By optimizing the gain-bandwidth product, the transmission distance can also be maximized. This will induce high flexibility in the VLC and UVC applications.

The VLC and UVC systems using OPFET device can also be studied in the presence of interference sources such as ambient light from sunlight, fog, snow etc. Further, the integration of Wi-Fi with Li-Fi can enhance the system capabilities.

For solar cell applications, the series resistances and the load resistances, and the overall device response could be optimized using optimization procedures especially structural optimization to deliver maximum power output. The devices could function in arrays to generate large amount of electricity.

The present work investigated and analyzed the extent to which the gain, phase, and bandwidth, of the GaAs OPFET-based photodetector can be varied by varying the drain bias, gate bias, optical power, modulation frequency, as well as by choosing different illumination models and different structural dimensions for 5G smart antenna applications. From these investigations, the optimum (Signal-to-Noise+Interference Ratio) in the desired direction can be derived. This work involving adaptive signal processing and the complete implementation of the optical phase array antenna system will be considered for future work.

Further, the photoconductive, photovoltaic, photothermoelectric, and photobolometric characteristics of the graphene-based OPFET and FET devices could be thoroughly investigated. The devices could be studied under solar illumination.

References

[1] W Xu and HM Dong. *Photo-induced carrier density, optical conductance and transmittance in graphene in the presence of optic-phonon scattering.* INTECH Open Access Publisher, 2011.

[2] GI Zebrev. Graphene field effect transistors: Diffusion-drift theory in physics and applications of graphene-theory. *InTech, DOI*, 10:14211, 2011.

[3] Jacek Gosciniak and Jacob B Khurgin. Comparative analysis of room temperature plasmonic graphene hot electron bolometric photodetectors. *arXiv preprint arXiv:2008.11522*, 2020.

[4] Jacek Gosciniak and Jacob B Khurgin. On-chip ultrafast plasmonic graphene hot electron bolometric photodetector. *ACS omega*, 5(24):14711–14719, 2020.

[5] Justin CW Song, Mark S Rudner, Charles M Marcus, and Leonid S Levitov. Hot carrier transport and photocurrent response in graphene. *Nano letters*, 11(11):4688–4692, 2011.

[6] SN Chattopadhyay, CB Overton, S Vetter, M Azadeh, BH Olson, and N El Naga. Optically controlled silicon mesfet fabrication and characterizations for optical modulator/demodulator. *JSTS: Journal of Semiconductor Technology and Science*, 10(3):213–224, 2010.

[7] ALVARO AUGUSTO A De Salles. Optical control of gaas mesfet's. *IEEE Transactions on Microwave Theory and Techniques*, 31(10):812–820, 1983.

[8] JL Gautier, D Pasquet, and P Pouvil. Optical effects on the static and dynamic characteristics of a gaas mesfet (short paper). *IEEE transactions on microwave theory and techniques*, 33(9):819–822, 1985.

[9] Hideki Mizuno. Microwave characteristics of an optically controlled gaas mesfet. *IEEE Transactions on Microwave Theory and Techniques*, 31(7):596–600, 1983.

[10] SM Sze and KK Ng. Physics of semiconductor devices, 3wiley. *Hoboken New Jersey*, 2007.

[11] Levinshteĭ. Handbook series on semiconductor parameters, vol. 1: Si, ge, c (diamond), gaas, gap, gasb, inas, inp, insb.

[12] C Baack, G Elze, and G Walf. Gaas mesfet: A high-speed optical detector. *Electronics Letters*, 13(7):193, 1977.

[13] JC Gammel and JM Ballantyne. The opfet: A new high speed optical detector. In *1978 International Electron Devices Meeting*, pages 120–123. IEEE, 1978.

[14] HJ Sun, RJ Gutmann, and JM Borrego. Photoeffects in common-source and common-drain microwave gaas mesfet oscillators. *Solid-State Electronics*, 24(10):935–940, 1981.

[15] JR Forrest, FP Richards, and A Perichon. The microwave mesfet optical detector. In *1982 International Electron Devices Meeting*, pages 529–532. IEEE, 1982.

[16] HJ Sun, RJ Gutmann, and JM Borrego. Dc and pulse-light illuminated optical responses of microwave gaas-mesfet oscillators. *IEE Proceedings I (Solid-State and Electron Devices)*, 131(1):31–37, 1984.

[17] George J Papaionannou and John R Forrest. On the photoresponse of gaas

mesfet's: Backgating and deep traps effect. *IEEE transactions on electron devices*, 33(3):373–378, 1986.

[18] Rainee N Simons and Kul B Bhasin. Analysis of optically controlled microwave/millimeter-wave device structures. *IEEE transactions on microwave theory and techniques*, 34(12):1349–1355, 1986.

[19] ROBERTB Darling and JOHNP Uyemura. Optical gain and large-signal characteristics of illuminated gaas mesfet's. *IEEE journal of quantum electronics*, 23(7):1160–1171, 1987.

[20] ID Blanchflower and AJ Seeds. Optical control of frequency and phase of gaas mesfet oscillator. *Electronics Letters*, 25(5):359–360, 1989.

[21] B Lakshmi, K Chalapati, AK Srivastava, BM Arora, S Subramanian, and DK Sharma. Gallium arsenide photo-mesfet's. *IEEE transactions on electron devices*, 37(6):1533–1535, 1990.

[22] Sunita Mishra, VK Singh, and BB Pal. Effect of radiation and surface recombination on the characteristics of an ion-implanted gaas mesfet. *IEEE transactions on electron devices*, 37(1):2–10, 1990.

[23] P Chakrabarti, NL Shrestha, S Srivastava, and V Khemka. An improved model of ion-implanted gaas opfet. *IEEE transactions on electron devices*, 39(9):2050–2059, 1992.

[24] P Chakrabarti, SK Shrestha, A Srivastava, and D Saxena. Switching characteristics of an optically controlled gaas-mesfet. *IEEE transactions on microwave theory and techniques*, 42(3):365–375, 1994.

[25] BB Pal, SN Chattopadhyay, Sunita Mishra, S Singh, and RU Khan. Time dependent analysis of an ion-implanted gaas opfet. *IEEE transactions on electron devices*, 41(4):491–498, 1994.

[26] BB Pal and SN Chattopadhyay. Scaling rule for opfet. *IEEE Transactions on Electron Devices*, 43(2):368–369, 1996.

[27] P Chakrabarti, A Gupta, and NA Khan. An analytical model of gaas opfet. *Solid-State Electronics*, 39(10):1481–1490, 1996.

[28] Youssef Zebda and S Abu Helweh. Ac characteristics of optically controlled mesfet (opfet). *Journal of lightwave technology*, 15(7):1205–1212, 1997.

[29] Shubha Rani Saxena, RB Lohani, RU Khan, and BB Pal. Generalized dc model of gaas optical field effect transistor considering ion-implanted profile. *Optical Engineering*, 37(4):1343–1352, 1998.

[30] P Chakrabarti, M Madheswaran, A Gupta, and NA Khan. Numerical simulation of an ion-implanted gaas opfet. *IEEE transactions on Microwave Theory and Techniques*, 46(10):1360–1366, 1998.

[31] BB Pal, RU Khan, et al. Optically-controlled ion-implanted gaas mesfet characteristic with opaque gate. *IEEE Transactions on Electron Devices*, 45(1):78–84, 1998.

[32] S Bose, M Gupta, and RS Gupta. A threshold voltage model for short channel gaas opfet for optical communication systems. In *2000 Asia-Pacific Microwave Conference. Proceedings (Cat. No. 00TH8522)*, pages 1077–1080. IEEE, 2000.

[33] Nandita Saha Roy and BB Pal. Frequency-dependent opfet characteristics with improved absorption under back illumination. *Journal of lightwave technology*, 18(4):604, 2000.

[34] MK Verma and BB Pal. Analysis of buried gate mesfet under dark and illumination. *IEEE Transactions on Electron Devices*, 48(9):2138–2142, 2001.

[35] S Jit and BB Pal. New optoelectronic integrated device for optically controlled microwave oscillators. *IEE Proceedings-Optoelectronics*, 151(3):177–182, 2004.

[36] Neti VL Narasimha Murty and S Jit. Analytical modelling of photo-effects on the s-parameters of gaas mesfets. *Microwave and Optical Technology Letters*, 48(1):150–155, 2006.

[37] Satyabrata Jit and Neti VL Narasimha Murty. Analytical study of the photo-effects on common-source and common-drain microwave oscillators using high pinch-off n-gaas mesfets. *Microelectronics journal*, 37(5):452–458, 2006.

[38] SN Chattopadhyay, N Motoyama, A Rudra, A Sharma, S Sriram, CB Overton, and P Pandey. Optically controlled silicon mesfet modeling considering diffusion process. *JSTS: Journal of Semiconductor Technology and Science*, 7(3):196–208, 2007.

[39] KD Pedrotti, NH Sheng, RL Pierson, CW Farley, MJ Rosker, and MF Chang. Monolithic ultrahigh-speed gaas hbt optical integrated receivers. In *[1991] GaAs IC Symposium Technical Digest*, pages 205–208. IEEE, 1991.

[40] Andrew A Ketterson, J-W Seo, Minh H Tong, Kari L Nummila, James J Morikuni, K-Y Cheng, S-M Kang, and Ilesanmi Adesida. A modfet-based optoelectronic integrated circuit receiver for optical interconnects. *IEEE transactions on electron devices*, 40(8):1406–1416, 1993.

[41] Chian-Gauh Shih, Wei-Heng Chang, Jianshi Wang, Douglas W Barlage, Chih-Chong Teng, and Milton Feng. Design and fabrication of a 1 gb/s oeic receiver for fiber-optic data link applications. *Journal of Lightwave technology*, 14(6):1480–1487, 1996.

[42] Alexander Nemecek, Klaus Oberhauser, Gerald Zach, and Horst Zimmermann. Fast and efficient integrated silicon pin-finger photodetector from ultraviolet up to near infrared. In *IEEE International Conference on Group IV Photonics, 2005. 2nd*, pages 108–110. IEEE, 2005.

[43] Letian Dou, Yang Micheal Yang, Jingbi You, Ziruo Hong, Wei-Hsuan Chang, Gang Li, and Yang Yang. Solution-processed hybrid perovskite photodetectors with high detectivity. *Nature communications*, 5(1):1–6, 2014.

[44] Chun Hong Kang, Guangyu Liu, Changmin Lee, Omar Alkhazragi, Jonathan M Wagstaff, Kuang-Hui Li, Fatimah Alhawaj, Tien Khee Ng, James S Speck, Shuji Nakamura, et al. Semipolar () ingan/gan micro-photodetector for gigabit-per-second visible light communication. *Applied Physics Express*, 13(1):014001, 2019.

[45] Mike Marchywka, JF Hochedez, MW Geis, Dennis G Socker, D Moses, and RT Goldberg. Ultraviolet photoresponse characteristics of diamond diodes. *Applied optics*, 30(34):5011–5013, 1991.

[46] MM Anikin, AN Andreev, SN Pyatko, NS Savkina, AM Strelchuk, AL Syrkin, and VE Chelnokov. Uv photodetectors in $6h_sic$. *Sensors and Actuators A: Physical*, 33(1-2):91–93, 1992.

[47] RP Joshi, AN Dharamsi, and J McAdoo. Simulations for the high-speed response of gan metal-semiconductor-metal photodetectors. *Applied physics letters*, 64(26):3611–3613, 1994.

[48] Mira Misra, Theodore D Moustakas, Robert P Vaudo, Rajminder Singh, and Kanai S Shah. Photoconducting ultraviolet detectors based on gan films grown by electron cyclotron resonance molecular beam epitaxy. In *X-Ray and Ultraviolet Sensors and Applications*, volume 2519, pages 78–86. International Society for Optics and Photonics, 1995.

[49] JC Carrano, T Li, DL Brown, PA Grudowski, CJ Eiting, RD Dupuis, and JC Campbell. Very high-speed metal-semiconductor-metal ultraviolet photodetectors fabricated on gan. *Applied physics letters*, 73(17):2405–2407, 1998.

[50] W Yang, RD Vispute, S Choopun, RP Sharma, T Venkatesan, and H Shen. Ultraviolet photoconductive detector based on epitaxial mg 0.34 zn 0.66 o thin films. *Applied Physics Letters*, 78(18):2787–2789, 2001.

[51] N Biyikli, I Kimukin, T Kartaloglu, O Aytur, and Ekmel Ozbay. High-speed solar-blind algan-based metal–semiconductor–metal photodetectors. *physica status solidi (c)*, (7):2314–2317, 2003.

[52] M Mikulics, P Kordos, Dagmar Gregusova, R Adam, Martin Kocan, Shuai Wu, J Zhang, Roman Sobolewski, D Grutzmacher, and Michel Marso. Monolithic integration of ultrafast photodetector and mesfet in the gan material system. *IEEE photonics technology letters*, 23(17):1189–1191, 2011.

[53] Abdollah Pil-Ali and Mohammad Azim Karami. Through silicon via based metal-semiconductor-metal photodetector in cmos technology. *Optical and Quantum Electronics*, 48(1):1–9, 2016.

[54] Dali Shao, Weiguang Zhu, Xueqing Liu, Mingxin Li, Jie Chen, Yi-Yang Sun, Guoqing Xin, Jie Lian, and Shayla Sawyer. Ultrasensitive uv photodetector based on interfacial charge-controlled inorganic perovskite–polymer hybrid structure. *ACS Applied Materials & Interfaces*, 12(38):43106–43114, 2020.

[55] Nengjie Huo and Gerasimos Konstantatos. Recent progress and future prospects of 2d-based photodetectors. *Advanced Materials*, 30(51):1801164, 2018.

[56] Thomas Mueller, Fengnian Xia, and Phaedon Avouris. Graphene photodetectors for high-speed optical communications. *Nature photonics*, 4(5):297–301, 2010.

[57] Oriol Lopez-Sanchez, Dumitru Dumcenco, Edoardo Charbon, and Andras Kis. Avalanche photodiodes based on mos2/si heterojunctions. *arXiv preprint arXiv:1411.3232*, 2014.

[58] Oriol Lopez-Sanchez, Dominik Lembke, Metin Kayci, Aleksandra Radenovic, and Andras Kis. Ultrasensitive photodetectors based on monolayer mos 2. *Nature nanotechnology*, 8(7):497–501, 2013.

[59] Valeri N Kotov, Bruno Uchoa, Vitor M Pereira, F Guinea, and AH Castro Neto. Electron-electron interactions in graphene: Current status and perspectives. *Reviews of Modern Physics*, 84(3):1067, 2012.

[60] Jiwoong Park, YH Ahn, and Carlos Ruiz-Vargas. Imaging of photocurrent generation and collection in single-layer graphene. *Nano letters*, 9(5):1742–1746, 2009.

[61] Jun Yan, Mann Ho Kim, Jennifer A Elle, Andrei B Sushkov, Greg S Jenkins, Ho-ward M Milchberg, Michael S Fuhrer, and HD Drew. Dual-gated bilayer graphene hot-electron bolometer. *Nature nanotechnology*, 7(7):472–478, 2012.

[62] Liam Britnell, Ricardo Mendes Ribeiro, Axel Eckmann, Rashid Jalil, Branson D Belle, Artem Mishchenko, Y-J Kim, Roman V Gorbachev, Thanasis Georgiou, Sergei V Morozov, et al. Strong light-matter interactions in heterostructures of atomically thin films. *Science*, 340(6138):1311–1314, 2013.

[63] Dong-Ho Kang, Myung-Soo Kim, Jaewoo Shim, Jeaho Jeon, Hyung-Youl Park, Woo-Shik Jung, Hyun-Yong Yu, Chang-Hyun Pang, Sungjoo Lee, and Jin-Hong Park. High-performance transition metal dichalcogenide photodetectors enhanced by self-assembled monolayer doping. *Advanced Functional Materials*, 25(27):4219–4227, 2015.

[64] Gerasimos Konstantatos, Michela Badioli, Louis Gaudreau, Johann Osmond, Maria Bernechea, F Pelayo Garcia De Arquer, Fabio Gatti, and

Frank HL Koppens. Hybrid graphene–quantum dot phototransistors with ultrahigh gain. *Nature nanotechnology*, 7(6):363–368, 2012.

[65] Chun Ma, Yumeng Shi, Weijin Hu, Ming-Hui Chiu, Zhixiong Liu, Ashok Bera, Feng Li, Hong Wang, Lain-Jong Li, and Tom Wu. Heterostructured ws2/ch3nh3pbi3 photoconductors with suppressed dark current and enhanced photodetectivity. *Advanced Materials*, 28(19):3683–3689, 2016.

[66] Wenyi Wang, Andrey Klots, Dhiraj Prasai, Yuanmu Yang, Kirill I Bolotin, and Jason Valentine. Hot electron-based near-infrared photodetection using bilayer mos2. *Nano letters*, 15(11):7440–7444, 2015.

[67] Ivan Nikitskiy, Stijn Goossens, Dominik Kufer, Tania Lasanta, Gabriele Navickaite, Frank HL Koppens, and Gerasimos Konstantatos. Integrating an electrically active colloidal quantum dot photodiode with a graphene phototransistor. *Nature communications*, 7(1):1–8, 2016.

[68] W Knap, V Kachorovskii, Y Deng, S Rumyantsev, J-Q Lü, R Gaska, MS Shur, Grigory Simin, X Hu, M Asif Khan, et al. Nonresonant detection of terahertz radiation in field effect transistors. *Journal of Applied Physics*, 91(11):9346–9353, 2002.

[69] Dayong Zhang, Lin Gan, Yang Cao, Qing Wang, Limin Qi, and Xuefeng Guo. Understanding charge transfer at pbs-decorated graphene surfaces toward a tunable photosensor. *Advanced Materials*, 24(20):2715–2720, 2012.

[70] Shao-Yu Chen, Yi-Ying Lu, Fu-Yu Shih, Po-Hsun Ho, Yang-Fang Chen, Chun-Wei Chen, Yit-Tsong Chen, and Wei-Hua Wang. Biologically inspired graphene-chlorophyll phototransistors with high gain. *Carbon*, 63:23–29, 2013.

[71] Kallol Roy, Medini Padmanabhan, Srijit Goswami, T Phanindra Sai, Gopalakrishnan Ramalingam, Srinivasan Raghavan, and Arindam Ghosh.

Graphene–mos 2 hybrid structures for multifunctional photoresponsive memory devices. *Nature nanotechnology*, 8(11):826–830, 2013.

[72] Wenhao Guo, Shuigang Xu, Zefei Wu, Ning Wang, MMT Loy, and Shengwang Du. Oxygen-assisted charge transfer between zno quantum dots and graphene. *Small*, 9(18):3031–3036, 2013.

[73] Sandip Mazumder. *Numerical methods for partial differential equations: finite difference and finite volume methods*. Academic Press, 2015.

[74] George Fishman. *Monte Carlo: concepts, algorithms, and applications*. Springer Science & Business Media, 2013.

[75] Myrto Zeneli, Aris Nikolopoulos, Sotirios Karellas, and Nikolaos Nikolopoulos. Numerical methods for solid-liquid phase-change problems. In *Ultra-High Temperature Thermal Energy Storage, Transfer and Conversion*, pages 165–199. Elsevier, 2021.

[76] Edward Vigmond and Gernot Plank. Cardiac modeling. In Roger Narayan, editor, *Encyclopedia of Biomedical Engineering*, pages 1–20. Elsevier, Oxford, 2019.

[77] Jiri Blazek. Chapter 3 - principles of solution of the governing equations. In Jiri Blazek, editor, *Computational Fluid Dynamics: Principles and Applications (Third Edition)*, pages 29–72. Butterworth-Heinemann, Oxford, third edition edition, 2015.

[78] http://machinedesign.com/fea-and-simulation/what-s-difference-between-fem-fdm-and-fvm.

[79] Olek C Zienkiewicz, Robert L Taylor, and Jian Z Zhu. *The finite element method: its basis and fundamentals*. Elsevier, 2005.

[80] http://www.comsol.com.

[81] Ozgur Ergul, Ergin Dinc, and Ozgur B Akan. Communicate to illuminate: State-of-the-art and research challenges for visible light communications. *Physical Communication*, 17:72–85, 2015.

[82] Latif Ullah Khan. Visible light communication: Applications, architecture, standardization and research challenges. *Digital Communications and Networks*, 3(2):78–88, 2017.

[83] Robert Swoboda and Horst Zimmermann. 2.5 gbit/s silicon receiver oeic with large diameter photodiode. *Electronics Letters*, 40(8):505–507, 2004.

[84] Mohamed Atef, Robert Swoboda, and Horst Zimmermann. 1.25 gbit/s over 50 m step-index plastic optical fiber using a fully integrated optical receiver with an integrated equalizer. *Journal of lightwave technology*, 30(1):118–122, 2011.

[85] P Brandl and H Zimmermann. 3 gbit/s optical receiver ic with high sensitivity and large integrated pin photodiode. *Electronics letters*, 49(8):552–554, 2013.

[86] Wolfgang Gaberl, Kerstin Schneider-Hornstein, Reinhard Enne, and Bernhard Steindl. Avalanche photodiode with high responsivity in 0.35 μm cmos. *Optical Engineering*, 53(4):043105, 2014.

[87] Paul Brandl, Tomislav Jukić, Reinhard Enne, Kerstin Schneider-Hornstein, and Horst Zimmermann. Optical wireless apd receiver with high background-light immunity for increased communication distances. *IEEE Journal of Solid-State Circuits*, 51(7):1663–1673, 2016.

[88] X Li, Nikolaos Bamiedakis, Xuhan Guo, JJD McKendry, E Xie, R Ferreira, E Gu, MD Dawson, RV Penty, and IH White. Wireless visible light communications employing feed-forward pre-equalization and pam-4 modulation. *Journal of Lightwave Technology*, 34(8):2049–2055, 2016.

[89] Dinka Milovančev, Tomislav Jukić, Bernhard Steindl, Paul Brandl, and Horst Zimmermann. Optical wireless communication using a fully integrated 400 μm diameter apd receiver. *The Journal of Engineering*, 2017(8):506–511, 2017.

[90] Sujan Rajbhandari, Aravind VN Jalajakumari, Hyunchae Chun, Grahame Faulkner, Katherine Cameron, Robert Henderson, Dobroslav Tsonev, Harald Haas, Enyuan Xie, Jonathan JD McKendry, et al. A multigigabit per second integrated multiple-input multiple-output vlc demonstrator. *Journal of Lightwave Technology*, 35(20):4358–4365, 2017.

[91] Filip Tavernier and Michiel Steyaert. A high-speed pof receiver with 1 mm integrated photodiode in 180 nm cmos. In *36th European conference and exhibition on optical communication*, pages 1–3. IEEE, 2010.

[92] Osamu Wada, T Sakurai, and T Nakagami. Recent progress in optoelectric integrated circuits (oeic's). *IEEE journal of quantum electronics*, 22(6):805–821, 1986.

[93] Kadirvel Sindhubala and Baba Vijayalakshmi. Survey on noise sources and restrain techniques in visible-light communication. *Light & Engineering*, 24(2), 2016.

[94] P Chakrabarti and V Rajamani. A proposed oeic receiver using mesfet photodetector. *Journal of lightwave technology*, 17(4):659, 1999.

[95] Rajni Gautam, Manoj Saxena, RS Gupta, and Mridula Gupta. High sensitivity photodetector using si/ge/gaas metal semiconductor field effect transistor (mesfet). In *AIP Conference Proceedings*, volume 1391, pages 232–234. American Institute of Physics, 2011.

[96] Adarsh Singh, Anil Kumar, Mridula Gupta, and RS Gupta. Model for dc and rf characteristics of optically biased gan metal semiconductor field ef-

fect transistor for electronic/optoelectronic microwave applications. *Optical Engineering*, 41(11):2915–2922, 2002.

[97] Eva Monroy, Franck Omnès, and FJSS Calle. Wide-bandgap semiconductor ultraviolet photodetectors. *Semiconductor science and technology*, 18(4):R33, 2003.

[98] Dung-Sheng Tsai, Wei-Cheng Lien, Der-Hsien Lien, Kuan-Ming Chen, Meng-Lin Tsai, Debbie G Senesky, Yueh-Chung Yu, Albert P Pisano, and Jr-Hau He. Solar-blind photodetectors for harsh electronics. *Scientific reports*, 3(1):1–5, 2013.

[99] Zhengyuan Xu and Brian M Sadler. Ultraviolet communications: potential and state-of-the-art. *IEEE Communications Magazine*, 46(5):67–73, 2008.

[100] Renzhi Yuan and Jianshe Ma. Review of ultraviolet non-line-of-sight communication. *China Communications*, 13(6):63–75, 2016.

[101] John Son. Uv detectors: status and prospects. In *UV and Higher Energy Photonics: From Materials to Applications 2018*, volume 10727, page 107270F. International Society for Optics and Photonics, 2018.

[102] Xiaobin Sun, Zhenyu Zhang, Anas Chaaban, Tien Khee Ng, Chao Shen, Rui Chen, Jianchang Yan, Haiding Sun, Xiaohang Li, Junxi Wang, et al. 71-mbit/s ultraviolet-b led communication link based on 8-qam-ofdm modulation. *Optics express*, 25(19):23267–23274, 2017.

[103] Tian Lang. *Performance Analysis of Visible and Ultraviolet Light Communications*. University of California, Riverside, 2018.

[104] Brahim El Mansouri, WD van Driel, and GuoQi Zhang. Ultraviolet sensing in wbg: Sic. In *Sensor Systems Simulations*, pages 397–425. Springer, 2020.

[105] Paul Raymond Berger. Metal-semiconductor-metal photodetectors. In *Testing, Reliability, and Applications of Optoelectronic Devices*, volume 4285, pages 198–207. International Society for Optics and Photonics, 2001.

[106] BL Sharma. *Metal-semiconductor Schottky barrier junctions and their applications*. Springer Science & Business Media, 2013.

[107] Bill Mantovani. *Electronics in easy steps*. In Easy Steps Limited, 2019.

[108] Alain Richard Ndjiongue and Hendrik Christoffel Ferreira. An overview of outdoor visible light communications. *Transactions on Emerging Telecommunications Technologies*, 29(7):e3448, 2018.

[109] It Ee Lee, Moh Lim Sim, and Fabian Wai-Lee Kung. Performance enhancement of outdoor visible-light communication system using selective combining receiver. *IET optoelectronics*, 3(1):30–39, 2009.

[110] Isamu Takai, Tomohisa Harada, Michinori Andoh, Keita Yasutomi, Keiichiro Kagawa, and Shoji Kawahito. Optical vehicle-to-vehicle communication system using led transmitter and camera receiver. *IEEE photonics journal*, 6(5):1–14, 2014.

[111] Bassem Fahs, Matthew Romanowicz, and Mona M Hella. A gbps building-to-building vlc link using standard cmos avalanche photodiodes. *IEEE Photonics Journal*, 9(6):1–9, 2017.

[112] Moussa Ayyash, Hany Elgala, Abdallah Khreishah, Volker Jungnickel, Thomas Little, Sihua Shao, Michael Rahaim, Dominic Schulz, Jonas Hilt, and Ronald Freund. Coexistence of wifi and lifi toward 5g: concepts, opportunities, and challenges. *IEEE Communications Magazine*, 54(2):64–71, 2016.

[113] Zixiong Wang, Dobroslav Tsonev, Stefan Videv, and Harald Haas. On the design of a solar-panel receiver for optical wireless communications with

simultaneous energy harvesting. *IEEE Journal on Selected Areas in Communications*, 33(8):1612–1623, 2015.

[114] Gerardo Hernandez-Oregon, Mario E Rivero-Angeles, Juan C Chimal-Eguía, Arturo Campos-Fentanes, Jorge G Jimenez-Gallardo, Ulises O Estevez-Alva, Omar Juarez-Gonzalez, Pedro O Rosas-Calderon, Sergio Sandoval-Reyes, and Rolando Menchaca-Mendez. Performance analysis of v2v and v2i lifi communication systems in traffic lights. *Wireless Communications and Mobile Computing*, 2019, 2019.

[115] KD Pedrotti, RL Pierson, RB Nubling, CW Farley, EA Sovero, and MF Chang. Ultra-high speed pin/hbt monolithic oeic photoreceiver. *IEEE Transactions on Electron Devices*, 38(12):2713–2714, 1991.

[116] https://www.arrow.com/en/research-and events/articles/what-frequency-spectrum-will-5g-technology-useand- how-does-this-compare-to-4g.

[117] https://venturebeat.com/2019/03/15/fcc-opens- 95ghz-to-3thz-spectrum-for-6g-7g-or-whatever-is-next/.

[118] Mansoor Shafi, Andreas F Molisch, Peter J Smith, Thomas Haustein, Peiying Zhu, Prasan De Silva, Fredrik Tufvesson, Anass Benjebbour, and Gerhard Wunder. 5g: A tutorial overview of standards, trials, challenges, deployment, and practice. *IEEE journal on selected areas in communications*, 35(6):1201–1221, 2017.

[119] Di Zhang, Zhenyu Zhou, Shahid Mumtaz, Jonathan Rodriguez, and Takuro Sato. One integrated energy efficiency proposal for 5g iot communications. *IEEE Internet of Things Journal*, 3(6):1346–1354, 2016.

[120] Jeffrey G Andrews, Stefano Buzzi, Wan Choi, Stephen V Hanly, Angel Lozano, Anthony CK Soong, and Jianzhong Charlie Zhang. What will 5g be? *IEEE Journal on selected areas in communications*, 32(6):1065–1082, 2014.

[121] Mostafa Zaman Chowdhury, Md Tanvir Hossan, Amirul Islam, and Yeong Min Jang. A comparative survey of optical wireless technologies: Architectures and applications. *ieee Access*, 6:9819–9840, 2018.

[122] Emilio Calvanese Strinati, Sergio Barbarossa, Jose Luis Gonzalez-Jimenez, Dimitri Ktenas, Nicolas Cassiau, Luc Maret, and Cedric Dehos. 6g: The next frontier: From holographic messaging to artificial intelligence using subterahertz and visible light communication. *IEEE Vehicular Technology Magazine*, 14(3):42–50, 2019.

[123] James Eun and James A Cooper Jr. High temperature ohmic contact technology to n-type gaas. 1993.

[124] YA Kremenetskaya, SE Markov, and Yu V Melnyk. Structural optimization of optoelectronic components in millimeter-wave radio-transmitting modules. *Semiconductor Physics, Quantum Electronics & Optoelectronics*, 23(4):424–430, 2020.

[125] Ivan Aldaya, Gabriel Campuzano, Gerardo Castañón, and Alejandro Aragón-Zavala. A tutorial on optical feeding of millimeter-wave phased array antennas for communication applications. *International Journal of Antennas and Propagation*, 2015, 2015.

[126] Karel Van Acoleyen, Hendrik Rogier, and Roel Baets. Two-dimensional optical phased array antenna on silicon-on-insulator. *Optics express*, 18(13):13655–13660, 2010.

[127] Beatriz Ortega, Jose Mora, and Ruben Chulia. Optical beamformer for 2-d phased array antenna with subarray partitioning capability. *IEEE Photonics Journal*, 8(3):1–9, 2016.

[128] Raj K Jain and Geoffrey A Landis. Transient response of gallium arsenide and silicon solar cells under laser pulse. *Solid-State Electronics*, 42(11):1981–1983, 1998.

[129] KMA Saron and MR Hashim. Broad visible emission from gan nanowires grown on n-si (1 1 1) substrate by pvd for solar cell application. *Superlattices and Microstructures*, 56:55–63, 2013.

[130] Lingxian Meng, Yamin Zhang, Xiangjian Wan, Chenxi Li, Xin Zhang, Yanbo Wang, Xin Ke, Zuo Xiao, Liming Ding, Ruoxi Xia, et al. Organic and solution-processed tandem solar cells with 17.3% efficiency. *Science*, 361(6407):1094–1098, 2018.

[131] Nam Joong Jeon, Hyejin Na, Eui Hyuk Jung, Tae-Youl Yang, Yong Guk Lee, Geunjin Kim, Hee-Won Shin, Sang Il Seok, Jaemin Lee, and Jangwon Seo. A fluorene-terminated hole-transporting material for highly efficient and stable perovskite solar cells. *Nature Energy*, 3(8):682–689, 2018.

[132] Graham H Carey, Ahmed L Abdelhady, Zhijun Ning, Susanna M Thon, Osman M Bakr, and Edward H Sargent. Colloidal quantum dot solar cells. *Chemical reviews*, 115(23):12732–12763, 2015.

[133] Bilal Malik and Xun Zhang. Solar panel receiver system implementation for visible light communication. In *2015 IEEE International Conference on Electronics, Circuits, and Systems (ICECS)*, pages 502–503. IEEE, 2015.

[134] Nominoe Lorrière, Nathan Bétrancourt, Marcel Pasquinelli, Gilles Chabriel, Jean Barrère, Ludovic Escoubas, Jyh-Lih Wu, Veronica Bermudez, Carmen Maria Ruiz, and Jean-Jacques Simon. Photovoltaic solar cells for outdoor lifi communications. *Journal of Lightwave Technology*, 38(15):3822–3831, 2020.

[135] Shuyu Zhang, Dobroslav Tsonev, Stefan Videv, Sanjay Ghosh, Graham A Turnbull, Ifor DW Samuel, and Harald Haas. Organic solar cells as high-speed data detectors for visible light communication. *Optica*, 2(7):607–610, 2015.

[136] Meiwei Kong, Bin Sun, Rohail Sarwar, Jiannan Shen, Yifei Chen, Fengzhong Qu, Jun Han, Jiawang Chen, Huawei Qin, and Jing Xu. Underwater wireless optical communication using a lens-free solar panel receiver. *Optics Communications*, 426:94–98, 2018.

[137] Rens Bloom, Marco Zuniga, Qing Wang, and Domenico Giustiniano. Tweeting with sunlight: Encoding data on mobile objects. In *IEEE INFOCOM 2019-IEEE Conference on Computer Communications*, pages 1324–1332. IEEE, 2019.

[138] Haichao Guo, Tao Shan, Li Li, Li Zhang, Xiaojun Li, and Han Gao. A reliable sunlight communication system. *Chinese Optics Letters*, 17(12):120605, 2019.

[139] Gregory C Mooradian. Satellite mounted system for transferring information using modulated sunlight, February 25 1986. US Patent 4,573,214.

[140] Cheng Gong, Geunsik Lee, Bin Shan, Eric M Vogel, Robert M Wallace, and Kyeongjae Cho. First-principles study of metal–graphene interfaces. *Journal of Applied Physics*, 108(12):123711, 2010.

[141] Joshua A Robinson, Michael LaBella, Mike Zhu, Matt Hollander, Richard Kasarda, Zachary Hughes, Kathleen Trumbull, Randal Cavalero, and David Snyder. Contacting graphene. *Applied Physics Letters*, 98(5):053103, 2011.

[142] Inanc Meric, Melinda Y Han, Andrea F Young, Barbaros Ozyilmaz, Philip Kim, and Kenneth L Shepard. Current saturation in zero-bandgap, top-gated graphene field-effect transistors. *Nature nanotechnology*, 3(11):654–659, 2008.

[143] R Miloua, Z Kebbab, F Chiker, M Khadraoui, K Sahraoui, A Bouzidi, M Medles, C Mathieu, and N Benramdane. Peak, multi-peak and broadband absorption in graphene-based one-dimensional photonic crystal. *Optics Communications*, 330:135–139, 2014.

[144] Wei Li, Yiran Liang, Dangmin Yu, Lianmao Peng, Kurt P Pernstich, Tian Shen, AR Hight Walker, Guangjun Cheng, Christina A Hacker, Curt A Richter, et al. Ultraviolet/ozone treatment to reduce metal-graphene contact resistance. *Applied Physics Letters*, 102(18):183110, 2013.

[145] Yuehui Jia, Xin Gong, Pei Peng, Zidong Wang, Zhongzheng Tian, Liming Ren, Yunyi Fu, and Han Zhang. Toward high carrier mobility and low contact resistance: laser cleaning of pmma residues on graphene surfaces. *Nano-micro letters*, 8(4):336–346, 2016.

[146] Hyung-Youl Park, Woo-Shik Jung, Dong-Ho Kang, Jaeho Jeon, Gwangwe Yoo, Yongkook Park, Jinhee Lee, Yun Hee Jang, Jaeho Lee, Seongjun Park, et al. Extremely low contact resistance on graphene through n-type doping and edge contact design. *Advanced Materials*, 28(5):864–870, 2016.

[147] JS Moon, M Antcliffe, HC Seo, D Curtis, S Lin, A Schmitz, I Milosavljevic, AA Kiselev, RS Ross, DK Gaskill, et al. Ultra-low resistance ohmic contacts in graphene field effect transistors. *Applied Physics Letters*, 100(20):203512, 2012.

[148] He Ze-Zhao, Yang Ke-Wu, Yu Cui, Li Jia, Liu Qing-Bin, Lu Wei-Li, Feng Zhi-Hong, and Cai Shu-Jun. Improvement of metal-graphene ohmic contact resistance in bilayer epitaxial graphene devices. *Chinese Physics Letters*, 32(11):117204, 2015.

[149] Yue Zheng, Jing Gao, Cheng Han, and Wei Chen. Ohmic contact engineering for two-dimensional materials. *Cell Reports Physical Science*, page 100298, 2021.

[150] Jinhua Li, Liyong Niu, Zijian Zheng, and Feng Yan. Photosensitive graphene transistors. *Advanced Materials*, 26(31):5239–5273, 2014.

[151] Xinghan Cai, Andrei B Sushkov, Ryan J Suess, Mohammad M Jadidi, Gregory S Jenkins, Luke O Nyakiti, Rachael L Myers-Ward, Shanshan Li, Jun

Yan, D Kurt Gaskill, et al. Sensitive room-temperature terahertz detection via the photothermoelectric effect in graphene. *Nature nanotechnology*, 9(10):814–819, 2014.

[152] Yubing Wang, Weihong Yin, Qin Han, Xiaohong Yang, Han Ye, Qianqian Lv, and Dongdong Yin. Bolometric effect in a waveguide-integrated graphene photodetector. *Chinese Physics B*, 25(11):118103, 2016.

[153] Wenjing Zhang, Cheng-Te Lin, Keng-Ku Liu, Teddy Tite, Ching-Yuan Su, Chung-Huai Chang, Yi-Hsien Lee, Chih-Wei Chu, Kung-Hwa Wei, Jer-Lai Kuo, et al. Opening an electrical band gap of bilayer graphene with molecular doping. *ACS nano*, 5(9):7517–7524, 2011.

[154] J Michael Golio. Ultimate scaling limits for high-frequency gaas mesfets. *IEEE transactions on electron devices*, 35(7):839–848, 1988.

[155] Dean A Frickey. Conversions between s, z, y, h, abcd, and t parameters which are valid for complex source and load impedances. *IEEE Transactions on microwave theory and techniques*, 42(2):205–211, 1994.

[156] Robert W Jackson. Rollett proviso in the stability of linear microwave circuits—a tutorial. *IEEE Transactions on Microwave Theory and Techniques*, 54(3):993–1000, 2006.

[157] George D Vendelin, Anthony M Pavio, Ulrich L Rohde, and Matthias Rudolph. *Microwave circuit design using linear and nonlinear techniques*. John Wiley & Sons, 2021.

[158] Claire Berger, Zhimin Song, Xuebin Li, Xiaosong Wu, Nate Brown, Cécile Naud, Didier Mayou, Tianbo Li, Joanna Hass, Alexei N Marchenkov, et al. Electronic confinement and coherence in patterned epitaxial graphene. *Science*, 312(5777):1191–1196, 2006.

[159] Abdeladim Guermoune, Tarun Chari, Filip Popescu, Shadi S Sabri, Jonathan Guillemette, Helgi S Skulason, Thomas Szkopek, and Mohamed Siaj. Chemical vapor deposition synthesis of graphene on copper with methanol, ethanol, and propanol precursors. *Carbon*, 49(13):4204–4210, 2011.

[160] Yanwu Zhu, Meryl D Stoller, Weiwei Cai, Aruna Velamakanni, Richard D Piner, David Chen, and Rodney S Ruoff. Exfoliation of graphite oxide in propylene carbonate and thermal reduction of the resulting graphene oxide platelets. *ACS nano*, 4(2):1227–1233, 2010.

[161] Min Yi and Zhigang Shen. A review on mechanical exfoliation for the scalable production of graphene. *Journal of Materials Chemistry A*, 3(22):11700–11715, 2015.

[162] Ferney A Chaves, David Jiménez, Aron W Cummings, and Stephan Roche. Physical model of the contact resistivity of metal-graphene junctions. *Journal of Applied Physics*, 115(16):164513, 2014.

[163] Eduardo JH Lee, Kannan Balasubramanian, Ralf Thomas Weitz, Marko Burghard, and Klaus Kern. Contact and edge effects in graphene devices. *Nature nanotechnology*, 3(8):486–490, 2008.

[164] Eva C Peters, Eduardo JH Lee, Marko Burghard, and Klaus Kern. Gate dependent photocurrents at a graphene pn junction. *Applied Physics Letters*, 97(19):193102, 2010.

[165] Nathaniel M Gabor, Justin CW Song, Qiong Ma, Nityan L Nair, Thiti Taychatanapat, Kenji Watanabe, Takashi Taniguchi, Leonid S Levitov, and Pablo Jarillo-Herrero. Hot carrier–assisted intrinsic photoresponse in graphene. *Science*, 334(6056):648–652, 2011.

[166] Xiaodong Xu, Nathaniel M Gabor, Jonathan S Alden, Arend M Van

Der Zande, and Paul L McEuen. Photo-thermoelectric effect at a graphene interface junction. *Nano letters*, 10(2):562–566, 2010.

[167] Zhenhua Sun, Zhike Liu, Jinhua Li, Guo-an Tai, Shu-Ping Lau, and Feng Yan. Infrared photodetectors based on cvd-grown graphene and pbs quantum dots with ultrahigh responsivity. *Advanced materials*, 24(43):5878–5883, 2012.

[168] Robert W Boyd. Radiometry and the detection of optical radiation. *New York*, 1983.

[169] R Bistritzer and Allan H MacDonald. Electronic cooling in graphene. *Physical Review Letters*, 102(20):206410, 2009.

[170] Joaquim Peiró and Spencer Sherwin. Finite difference, finite element and finite volume methods for partial differential equations. In *Handbook of materials modeling*, pages 2415–2446. Springer, 2005.

[171] MK Hudait and SB Krupanidhi. Doping dependence of the barrier height and ideality factor of au/n-gaas schottky diodes at low temperatures. *Physica B: Condensed Matter*, 307(1-4):125–137, 2001.

[172] HC Casey Jr, DD Sell, and KW Wecht. Concentration dependence of the absorption coefficient for n- and p- type gaas between 1.3 and 1.6 ev. *Journal of Applied Physics*, 46(1):250–257, 1975.

[173] Yunzhi Dong and Kenneth W Martin. A high-speed fully-integrated pof receiver with large-area photo detectors in 65 nm cmos. *IEEE journal of solid-state circuits*, 47(9):2080–2092, 2012.

[174] P Chakrabarti, Vinayak Jha, Pankaj Kalra, and Gaurav Gupta. Noise modeling of an optically controlled mesfet (opfet). *Microwave and optical technology letters*, 33(2):79–83, 2002.

[175] Shih-Hao Huang, Wei-Zen Chen, Yu-Wei Chang, and Yang-Tung Huang. A 10-gb/s oeic with meshed spatially-modulated photo detector in cmos technology. *IEEE Journal of Solid-State Circuits*, 46(5):1158–1169, 2011.

[176] Yoshinori Wada. Electromigration properties of titanium/aluminum metallization and a failure mechanism for titanium/aluminum gate gaas mesfet's. *Journal of The Electrochemical Society*, 133(7):1432, 1986.

[177] JR Waldrop, RW Grant, YC Wang, and RF Davis. Metal schottky barrier contacts to alpha 6h-sic. *Journal of applied physics*, 72(10):4757–4760, 1992.

[178] O Ambacher, W Rieger, P Ansmann, H Angerer, TD Moustakas, and M Stutzmann. Sub-bandgap absorption of gallium nitride determined by photothermal deflection spectroscopy. *Solid state communications*, 97(5):365–370, 1996.

[179] Jan Kolnik, İsmail H Oğuzman, Kevin F Brennan, Rongping Wang, P Paul Ruden, and Yang Wang. Electronic transport studies of bulk zincblende and wurtzite phases of gan based on an ensemble monte carlo calculation including a full zone band structure. *Journal of Applied Physics*, 78(2):1033–1038, 1995.

[180] Sefaattin Tongay, M Lemaitre, X Miao, B Gila, BR Appleton, and AF Hebard. Rectification at graphene-semiconductor interfaces: zero-gap semiconductor-based diodes. *Physical Review X*, 2(1):011002, 2012.

[181] Y Kribes, I Harrison, B Tuck, TS Cheng, and CT Foxon. Investigation of au schottky contacts on gan grown by molecular beam epitaxy. *Semiconductor science and technology*, 12(7):913, 1997.

[182] K Kumakura, Toshiki Makimoto, N Kobayashi, T Hashizume, T Fukui, and H Hasegawa. Minority carrier diffusion length in gan: Dislocation density and doping concentration dependence. *Applied Physics Letters*, 86(5):052105, 2005.

[183] Gerd Keiser. *Optical fiber communications*, volume 2. McGraw-Hill New York, 2000.

[184] A Singh, R Ranos, S Anderson, R Purvis, DA Cardimona, S Li, JY Anderson, L Landqvist, T Faska, V Swaminathan, et al. Comparison of dark currents of quantum well infrared photodetector structures. In *Proceedings of 2nd International Conference on Long Wavelength Infrared Detectors and Arrays, Physics and Applications*, pages 114–123, 1995.

[185] Thomas Sprafke and James W Beletic. High-performance infrared focal plane arrays for space applications. *Optics and Photonics News*, 19(6):22–27, 2008.

[186] Shashikant Sharma, A Sumathi, and C Periasamy. Photodetection properties of zno/si heterojunction diode: A simulation study. *IETE Technical Review*, 34(1):83–90, 2017.

[187] M Hanzaz, A Bouhdada, F Vigue, and JP Faurie. Znse-and gan-based schottky barrier photodetectors for blue and ultraviolet detection. *J. Act. Pass. Electron. Dev*, 2:165–169, 2007.

[188] A Keffous, M Zitouni, Y Belkacem, H Menari, and W Chergui. Fabrication and characterization of au/n-si photodiode with lithium as back-surface-field. *Applied surface science*, 199(1-4):22–30, 2002.

[189] M Siva Pratap Reddy, Bong-Joong Kim, and Ja-Soon Jang. Dual detection of ultraviolet and visible lights using a dna-ctma/gan photodiode with electrically different polarity. *Optics express*, 22(1):908–915, 2014.

[190] KS Gour, OP Singh, Biplab Bhattacharyya, R Parmar, Sudhir Husale, TD Senguttuvan, and VN Singh. Enhanced photoresponse of cu2znsn (s, se) 4 based photodetector in visible range. *Journal of Alloys and Compounds*, 694:119–123, 2017.

[191] Dhinesh Babu Velusamy, Md Azimul Haque, Manas R Parida, Fan Zhang, Tom Wu, Omar F Mohammed, and Husam N Alshareef. 2d organic–inorganic hybrid thin films for flexible uv–visible photodetectors. *Advanced Functional Materials*, 27(15):1605554, 2017.

[192] Dawood Alsaedi, Mehrdad Irannejad, Khaled H Ibrahim, Abdulaziz Almutairi, Omar Ramahi, and Mustafa Yavuz. High-responsivity reduced graphene oxide gel photodetectors for visible-light detection with a large detection area and an end-contact interface. *Journal of Materials Chemistry C*, 5(4):882–888, 2017.

[193] Chaoying Zhang, Sheng Wang, Leijing Yang, Yang Liu, Tingting Xu, Zhiyuan Ning, Alla Zak, Zhiyong Zhang, Reshef Tenne, and Qing Chen. High-performance photodetectors for visible and near-infrared lights based on individual ws2 nanotubes. *Applied physics letters*, 100(24):243101, 2012.

[194] Xing Xie, So-Ying Kwok, Zhenzhen Lu, Yankuan Liu, Yulin Cao, Linbao Luo, Juan Antonio Zapien, Igor Bello, Chun-Sing Lee, Shuit-Tong Lee, et al. Visible–nir photodetectors based on cdte nanoribbons. *Nanoscale*, 4(9):2914–2919, 2012.

[195] Tianyou Zhai, Xiaosheng Fang, Meiyong Liao, Xijin Xu, Liang Li, Baodan Liu, Yasuo Koide, Ying Ma, Jiannian Yao, Yoshio Bando, et al. Fabrication of high-quality in2se3 nanowire arrays toward high-performance visible-light photodetectors. *Acs Nano*, 4(3):1596–1602, 2010.

[196] Yu Vygranenko, A Malik, M Fernandes, R Schwarz, and M Vieira. Uv–visible ito/gap photodiodes: Characterization and modeling. *physica status solidi (a)*, 185(1):137–144, 2001.

[197] Shuang-hong Wu, Wen-lian Li, Bei Chu, Zi-sheng Su, Feng Zhang, and Chun Sing Lee. High performance small molecule photodetector with broad

spectral response range from 200 to 900 nm. *Applied Physics Letters*, 99(2):134, 2011.

[198] Zhiming Bai and Yinghua Zhang. Self-powered uv–visible photodetectors based on zno/cu2o nanowire/electrolyte heterojunctions. *Journal of Alloys and Compounds*, 675:325–330, 2016.

[199] J Gary Eden, SJ Park, NP Ostrom, ST McCain, CJ Wagner, BA Vojak, J Chen, C Liu, P Von Allmen, F Zenhausern, et al. Microplasma devices fabricated in silicon, ceramic, and metal/polymer structures: arrays, emitters and photodetectors. *Journal of Physics D: Applied Physics*, 36(23):2869, 2003.

[200] Bin Li, Lingxia Zhang, Zhisheng Wu, Gang Wang, and Hao Jiang. Ingan visible photodiodes with improved performance using oxidized ir schottky contact. *IEEE Photonics Technology Letters*, 27(21):2300–2303, 2015.

[201] Emre Heves and Yasar Gurbuz. Highly responsive, solution-based al/pbs and au-ti/pbs schottky photodiodes for swir detection. *IEEE Sensors Journal*, 14(3):816–820, 2013.

[202] S Bose, Mridula Gupta, RS Gupta, et al. Analytical model for dc characteristics of gan mesfet under dark and illuminated conditions. In *APMC 2001. 2001 Asia-Pacific Microwave Conference (Cat. No. 01TH8577)*, volume 2, pages 712–715. IEEE, 2001.

[203] İsmail H Oğuzman, Ján Kolník, Kevin F Brennan, Rongping Wang, Tzu-Ning Fang, and P Paul Ruden. Hole transport properties of bulk zinc-blende and wurtzite phases of gan based on an ensemble monte carlo calculation including a full zone band structure. *Journal of applied physics*, 80(8):4429–4436, 1996.

[204] VWL Chin, TL Tansley, and T Osotchan. Electron mobilities in gallium,

indium, and aluminum nitrides. *Journal of Applied Physics*, 75(11):7365–7372, 1994.

[205] Mohammad Rezaul Huque Khan, T Detchprohm, PETER Hacke, KAZUMASA Hiramatsu, and NOBUHIKO Sawaki. The barrier height and interface effect of au-n-gan schottky diode. *Journal of Physics D: Applied Physics*, 28(6):1169, 1995.

[206] Michael Cheffena. Industrial wireless sensor networks: channel modeling and performance evaluation. *EURASIP Journal on Wireless Communications and Networking*, 2012(1):1–8, 2012.

[207] Maria Rita Palattella, Mischa Dohler, Alfredo Grieco, Gianluca Rizzo, Johan Torsner, Thomas Engel, and Latif Ladid. Internet of things in the 5g era: Enablers, architecture, and business models. *IEEE journal on selected areas in communications*, 34(3):510–527, 2016.

[208] Javier Ferrer Coll, Jose Dolz Martin De Ojeda, Peter Stenumgaard, Silvia Marzal Romeu, and José Chilo. Industrial indoor environment characterization-propagation models. In *10th International Symposium on Electromagnetic Compatibility*, pages 245–249. IEEE, 2011.

[209] Amit Gahoi, Stefan Wagner, Andreas Bablich, Satender Kataria, Vikram Passi, and Max C Lemme. Contact resistance study of various metal electrodes with cvd graphene. *Solid-State Electronics*, 125:234–239, 2016.

[210] Teresa Cusati, Gianluca Fiori, Amit Gahoi, Vikram Passi, Alessandro Fortunelli, Max Lemme, and Giuseppe Iannaccone. Understanding the nature of metal-graphene contacts: A theoretical and experimental study. In *2015 IEEE International Electron Devices Meeting (IEDM)*, pages 12–7. IEEE, 2015.

[211] Vikram Passi, Amit Gahoi, Jasper Ruhkopf, Satender Kataria, F Vaurette, Emiliano Pallecchi, Henri Happy, and Max C Lemme. Contact resistance

study of "edge-contacted" metal-graphene interfaces. In *2016 46th European Solid-State Device Research Conference (ESSDERC)*, pages 236–239. IEEE, 2016.

[212] B Krishna Bharadwaj, Digbijoy Nath, Rudra Pratap, and Srinivasan Raghavan. Making consistent contacts to graphene: effect of architecture and growth induced defects. *Nanotechnology*, 27(20):205705, 2016.

[213] Fengnian Xia, Thomas Mueller, Yu-ming Lin, Alberto Valdes-Garcia, and Phaedon Avouris. Ultrafast graphene photodetector. *Nature nanotechnology*, 4(12):839–843, 2009.

[214] Andreas Pospischil, Markus Humer, Marco M Furchi, Dominic Bachmann, Romain Guider, Thomas Fromherz, and Thomas Mueller. Cmos-compatible graphene photodetector covering all optical communication bands. *Nature Photonics*, 7(11):892–896, 2013.

[215] Tao Deng, Zhaohao Zhang, Yaxuan Liu, Yingxin Wang, Fang Su, Shasha Li, Yang Zhang, Hao Li, Houjin Chen, Ziran Zhao, et al. Three-dimensional graphene field-effect transistors as high-performance photodetectors. *Nano letters*, 19(3):1494–1503, 2019.

[216] Yifei Wang, Vinh X Ho, Zachary N Henschel, Prashant Pradhan, Leslie Howe, Michael P Cooney, and Nguyen Q Vinh. Graphene photodetectors based on interfacial photogating effect with high sensitivity. In *Infrared Sensors, Devices, and Applications X*, volume 11503, page 1150306. International Society for Optics and Photonics, 2020.

[217] Leonardo Viti, Alisson R Cadore, Xinxin Yang, Andrei Vorobiev, Jakob E Muench, Kenji Watanabe, Takashi Taniguchi, Jan Stake, Andrea C Ferrari, and Miriam S Vitiello. Thermoelectric graphene photodetectors with sub-nanosecond response times at terahertz frequencies. *Nanophotonics*, 10(1):89–98, 2021.

Publications (Journals)

[1] Gaitonde, Jaya V., and Rajesh B. Lohani, "Structural optimization and analysis of GaAs buried-gate OPFET for visible-light communication," *Optical and Quantum Electronics* 52, 512 (2020). Doi: 10.1007/s11082-020-02627-8

[2] Gaitonde, Jaya V., and R.B. Lohani "Material, Structural Optimization and Analysis of Visible-Range Back-Illuminated OPFET photodetector", *Advances in Science, Technology and Engineering Systems Journal*, vol. 4, no. 4, pp. 485-502 (2019). DOI: 10.25046/aj040459

[3] Gaitonde, Jaya V., and Rajesh B. Lohani, "Material and illumination model optimization of OPFET for visible light communication," *Optik* 232 (2021), 166519, Doi: 10.1016/j.ijleo.2021.166519

[4] Gaitonde, Jaya V., and Rajesh B. Lohani. "Analysis of Wide-Bandgap Material OPFET UV Detectors for High Dynamic Range Imaging and Communication Applications." *Communications and Network* 11, no. 4 (2019): 83-117. DOI: 10.4236/cn.2019.114007

[5] Gaitonde, Jaya V., and Rajesh B. Lohani, "Switching and frequency response of ITO-gated GaAs OPFET models for VLC applications,"

International Journal of Information Technology, 13 (2021), 1005–1017. Doi: 10.1007/s41870-021-00665-3

[6] Gaitonde, Jaya V., and R. B. Lohani. "Visible Range Characterization of Au/Graphene-GaAs Schottky Junctions in MESFET." *IETE Journal of Research* (2019): 1-11. DOI: 10.1080/03772063.2019.1676666

[7] Gaitonde, Jaya V., and Rajesh B. Lohani, "Graphene-gated GaAs OPFET photodetector and oscillator for 5G applications," in the *Proc. of the First International Conference on Advances in Smart Sensor, Signal Processing and Communication Technology (ICASSCT 2021)*, Goa, India, 19th-20th March 2021, and in *IOP Science : Journal of Physics (Conference Proceedings Journal)*, 1921 (2021) 012046, doi:10.1088/1742-6596/1921/1/012046

[8] Gaitonde, Jaya V., and Rajesh B. Lohani, "Novel graphene-based OPFET for optoelectronic applications," in the *Proc. of the Global Conference on Recent Advancements in Sustainable Materials (GC-RASM 2021)*, Mangalore, Karnataka, India, 29-30 July 2021, in *"Elsevier's Materials Today: Proceedings"*-a journal specializing in the publication of conference proceedings and indexed in SCOPUS, Web of Science (Thomson Reuter), etc, 49, Part 5 (2022), 2090-2095. doi: 10.1016/j.matpr.2021.08.312

[9] Gaitonde, J., and R. B. Lohani. "GaAs Optical Field Effect Transistor (OPFET): A High Performance Photodetector for Automotive Applications." *SAE International Journal of Passenger Cars-Electronic and Electrical Systems* 9, no. 2016-01-0094 (2016): 204-211. doi: 10.4271/2016-01-0094

Publications (Conferences)

[1] Gaitonde, Jaya V., and R. B. Lohani. "UV photodetector based on graphene-GaN Schottky junction in MESFET." In *Emerging Devices and Smart Systems (ICEDSS)*, Conference on, Namakkal, Tamil Nadu, India, 4th-5th March 2016, pp. 30-33. IEEE, 2016, doi: 10.1109/ICEDSS.2016.7587797

[2] Gaitonde, Jaya V., and R. B. Lohani. "UV photodetector based on graphene-GaAs Schottky junction in MESFET." In *Proc. of International Conference and Workshop on Electronic Technologies (ICWET 2016)*, ISBN: 978-0-9972393-0-0, Kandivali, Mumbai, Maharashra, India, 26th-27th Feb. 2016.

[3] Gaitonde, Jaya V., and R. B. Lohani. "Photovoltaic characterization of graphene-GaN schottky junction in MESFET." In *Emerging Devices and Smart Systems (ICEDSS)*, 2017 Conference on, pp. 116-119. IEEE, 2017. DOI: 10.1109/ICEDSS.2017.8073669

[4] Gaitonde, Jaya V., and R. B. Lohani. "Comparative analysis of photovoltaic, forward and reverse characteristics of graphene-GaN/GaAs and Au-GaN/GaAs Schottky junctions in MESFET for Ultraviolet (UV) photodetector applications." In *Proc. of 8th International Conference and Workshop (MULTICON-W 2017)*, ISBN-13: 978-93-5260-531-6, ISBN-10:

93-5260-531-4, Mumbai, Maharashtra, India, 24th-26th Feb. 2017, pp. 73-82.

[5] Gaitonde, Jaya V., and R. B. Lohani, "High Infrared/Visible Contrast Photodetector based on In0.53Ga0.47As Back-illuminated OPFET," In *Tata Mc-Graw Hill Proc. of 9th International Conference and Workshop (MULTICON-W 2018)*, ISBN-13: 978-93-87572-73-7, ISBN-10: 93-87572-73-0, Mumbai, Maharashtra, India, 23th-24th Feb. 2018, pp. 193-198.

[6] Gaitonde, Jaya V., and R. B. Lohani. "Back-illuminated GaAs OPFET: A High Visible/UV Contrast Photodetector." In *2018 Conference on Emerging Devices and Smart Systems (ICEDSS)*, pp. 156-161. IEEE, 2018. DOI: 10.1109/ICEDSS.2018.8544284

[7] Gaitonde, Jaya V., Sudhir Pal Singh Rawat, and R. B. Lohani. "Comparative wavelength-dependent analysis of GaAs buried-gate OPFET for visible light communication." In *2018 International Conference on Recent Innovations in Electrical, Electronics and Communication Engineering (ICRIEECE)*, pp. 3388-3390. IEEE, 2018. doi: 10.1109/ICRIEECE44171.2018.9009211

[8] Gaitonde, Jaya V., and Rajesh B. Lohani. "Operating Frequency Ranges of GaAs Back-Illuminated OPFET Detector." In *2018 International Conference on Computational and Characterization Techniques in Engineering and Sciences (CCTES)*, pp. 160-166. IEEE, 2018. DOI: 10.1109/CCTES.2018.8674093

[9] Gaitonde, Jaya V. and R. B. Lohani, "Graphene-GaN Buried-gate OPFET Ultraviolet photodetector," In *Proc the International Conference on Inno-*

vations in Engineering, Technology and Sciences (ICIETS 2018), Mysore, Karnataka, India, 20th-21st Sep. 2018.

[10] Gaitonde, Jaya V., Sudhir Pal Singh Rawat, and R. B. Lohani. "Comparative Analysis of Buried-Gate GaN OPFET Models for UV Photodetector Applications." In *2018 5th IEEE Uttar Pradesh Section International Conference on Electrical, Electronics and Computer Engineering (UPCON)*, Gorakhpur, Uttar Pradesh, India, 2-4th Nov. 2018, pp. 1-8. IEEE, 2018. DOI: 10.1109/UPCON.2018.8596854

[11] Gaitonde, Jaya V., Sunit Fulari, and R. B. Lohani, "Application-Specific Dual-Mode Buried-Gate GaAs OPFET for Visible-Light Communication," in *Proc. the International Conference on Electrical, Communication, Electronics, Instrumentation and Computing (ICECEIC-2019)*, Kanchipuram, Tamil Nadu, India, 30-31st Jan. 2019.

[12] Gaitonde, Jaya V. and R. B. Lohani, "Proposed High Performance Subtle Light Intensity Variation UV Photodetectors," in the *Tata Mc-Graw Hill Proc. 10th International Conference and Workshop (MULTICON-W 2019), International Conference on Trends in Electronics and Communications (TELCON)*, ISBN-13: 978-93-5316-754-7, ISBN-10: 93-5316-754-X, 22nd-23rd Feb. 2019, Mumbai, Maharashtra, India.

[13] Gaitonde, Jaya V., and R. B. Lohani. "Dual-Application-Mode Buried-Gate GaN OPFET for Ultraviolet Communication." In *2019 Innovations in Power and Advanced Computing Technologies (i-PACT)*, Vellore, Tamil Nadu, India, 22nd-23rd March 2019,vol. 1, pp. 1-5. IEEE, 2019. DOI:

10.1109/i-PACT44901.2019.8960111

[14] Gaitonde, Jaya V., Sunit Fulari, and R. B. Lohani. "High Performance Visible-Range Photodetector for Wide-Bandwidth Applications." In *2019 Innovations in Power and Advanced Computing Technologies (i-PACT)*, Vellore, Tamil Nadu, India, 22nd-23rd March 2019, vol. 1, pp. 1-6. IEEE, 2019 (IEEExplore Digital library). DOI: 10.1109/i-PACT44901.2019.8960139

[15] Gaitonde, Jaya V., and Rajesh B. Lohani. "Proposed GaAs and Si OPFET Photodetectors for Solar Cell Applications." In *the 2nd International Conference on Non-Conventional Energy-Nanotechnology and Nanomaterials for Energy and Environment (ICNNEE 2019)*, 18-19th October 2019, Kalyani, West Bengal, India. Doi: 10.2139/ssrn.3503782. (Elsevier Proceedings).

[16] Gaitonde, Jaya V., and Rajesh B. Lohani. "Switching Performance of GaAs OPFET," In *the Proceedings of National Conference on Computational and Characterization Techniques in Engineering and Sciences (CCTES-19)*, Ambedkar Nagar, UP, India, 6-7 Sept. 2019.

[17] Gaitonde, Jaya V., and Rajesh B. Lohani. "Characterization of GaAs OPFET Models for Switching Applications," in *the Tata Mc-Graw Hill Proc. 11th International Conference and Workshop (MULTICON-W 2020), International Conference on Trends in Electronics and Communications (TELCON)*, 28th-29th Feb. 2020, Mumbai, Maharashtra, India.

[18] Gaitonde, Jaya V., and R. B. Lohani, "OPFET under Solar (AM0) Illumina-

tion," in *the International E-Conference on Photonics and its Applications in Green Energy (ICPAGE 2020)*, Kandivali, Mumbai, Maharashtra, India, 27th-28th Nov. 2020.

[19] Gaitonde, Jaya V., and R. B. Lohani, "GaAs OPFET for 5G applications," in *the E-Proceedings of AICTE sponsored International Virtual Conference on Antenna Innovations,5G Communications and Network Technologies (ICA5NT 2020)*, Thiruvallur District, Tamil Nadu, India, ISBN-No: 978-81-909948-3-5, 6-7 Nov. 2020.

[20] Gaitonde, Jaya V., and R. B. Lohani, "Graphene FET and MESFET for Opto-electronic Applications," in the *1st International Science Exhibition Congress Symposium(SECS-2020)*, Ranchi, Jharkhand, India, 12-13 Sept. 2020 (Accepted for publication in Springer LNEE series).

Publications (Book Chapters)

[1] Gaitonde, Jaya V., and Rajesh B. Lohani, "Configurable OPFET-based Photodetector for 5G Smart Antenna Applications," in *Book, "Smart Antennas: Latest Trends in Design and Application,"* Editors: Malik, P.K., Lu, Z., Madhay, B.T.P., Kalkhambkar, G., Amit, S., ISBN 978-3-030-76636-8, Springer/EAI, 2021.

[2] Gaitonde, Jaya V., and Rajesh B. Lohani, "High-Performance 6H-SiC Buried-gate OPFET Ultraviolet Photodetector for Industrial Optically-driven 5G IoT Applications," in *Book, Security, Privacy, and Applications of the Internet of Things,"* Editors: Mishra, B. K., Borah, S., Kasturiwale, H., Saha, P., Apple Academic Press, 2021. (Submitted for review).